LA-10524-T
Thesis

UC-34C
Issued: October 1985

LA--10524-T

DE86 005881

Systematics of Pion Double Charge Exchange

Ronald Alan Gilman*

*Guest Scientist at Los Alamos. Department of Physics, University of Pennsylvania, Philadelphia, PA 19104.

Los Alamos National Laboratory
Los Alamos, New Mexico 87545

INDEX

TABLE OF CONTENTS

LIST OF TABLES

LIST OF FIGURES

ACKNOWLEDGMENTS

I am indebted to many collaborators for their assistance in this work. My advisor, Terry Fortune, provided support, advice, ideas, and numerous suggestions about additional work to be done. The experiments ran successfully with much help from John Zumbro, Peter Seidl, Chris Morris, Shaul Mordecnai, Fred Moore, Chip Laymon, Rex Kiziah, Steve Greene, John Faucett, Kalvir Dhuga, Bill Cottingame, George Burleson, and Les Bland. In particular, Peter Seidl worked much harder than anyone else, was actively involved in preparations for the experiments, and ran many midnight shifts. Also, Susan Seestrom-Morris taught me most of what I know about running EPICS experiments, and Kalvir Dhuga, Chris Morris, and Terry Fortune suffered through numerous rough drafts of this work.

I am also indebted to my theoretical collaborators, especially Mikkel Johnson and Ed Siciliano, who were always available for discussions, and without whom the work described herein would have not been possible. Thanks also to Dick Boudrie of MP-10 and Louis Rosen of MP-DO for their support of graduate students at LAMPF.

SYSTEMATICS OF PION DOUBLE CHARGE EXCHANGE

by

Ronald Alan Gilman

ABSTRACT

Differential cross sections have been measured for pion-induced double-charge-exchange (DCX) reactions leading to double-isobaric-analog states (DIAS) and low-lying nonanalog states in the residual nuclei. A description of the experimental details and data analysis is presented. The experimentally observed systematics of reactions leading to DIAS, to nonanalog ground states, and to low-lying 2^+ states are described. Lowest-order optical-model calculations of DIAS DCX are compared to the data. Efforts to understand the anomalies by invoking additional reaction-mechanism amplitudes and a higher-order optical potential are described. Calculations of nonanalog DCX reactions leading to $J^\pi = 0^+$ states were performed within a distorted-wave impulse-approximation framework. The sensitivities of these calculations to input parameters are discussed.

CHAPTER I. INTRODUCTION

A. The Pion

The pion is a light ($m_\pi/m_n \sim 1/7$), pseudoscalar ($J^\pi = 0^-$), isovector ($T = 1$) particle. Of the three charge states, π^+, π^0, and π^-, the π^+ and π^- are antiparticles, and the π^0 is its own antiparticle. The charged pions have a mass of 139.57 MeV, a lifetime of 2.60×10^{-8} s, and a dominant decay mode of $\pi^\pm \rightarrow \mu^\pm \bar{\upsilon}_\mu$ (~100%). The neutral pion has a mass of 134.96 MeV, a lifetime of $0.83 \pm 0.06 \times 10^{-16}$ s, and a dominant decay mode of $\pi^0 \rightarrow \gamma\gamma$ (~99%).

Several properties make pion scattering an interesting probe of nuclear structure. First, some properties result in an inherent simplification in scattering theories. The pion is lighter than a nucleon, thus recoil corrections are smaller. The pion is not a nucleon, thus there are no exchange corrections. The pion is a spin 0 boson, thus the angular momentum algebra and the parameterization of the basic π-nucleon (π-n) interaction both simplify. Finally, since the pion is a "fundamental" particle consisting of quarks, there are no internal structure complications (except at extremely high momentum transfers). Second, there are several features of the π-nucleus (π-A) interaction that are significantly different from the nucleon-nucleus interaction. Because the pion is a boson, single pions can be created or absorbed. Since the pion has three charge states, the single-and double-charge-exchange reactions can be studied in addition to elastic and inelastic scattering. Since the pion is the lightest meson (thus being the mediator of the long range nucleon-nucleon force), we directly study the on-shell behavior of the free π-n interaction and

its modification in the nuclear medium, hopefully leading to a better understanding of a basic interaction important to nuclear structure.

Perhaps the most significant features of the free π-n interaction are the many resonances in the π-n system. Most important is the (3,3) or Δ resonance with J, T = 3/2, 3/2 at E = 1232 MeV with a width $\Gamma \sim 110$ MeV. The Δ resonance is of particular interest because of its dominance of π-n and π-A scattering at pion kinetic energies near 180 MeV. The π-n interaction is typically parameterized with phase shifts. In the π-n center of mass (c.m.), the t-matrix is given by [Mi-76]

$$t = \frac{-1}{4\pi^2 k\omega} \sum_{LJT} (2L+1)\, \alpha_{LJT}\, P_{LJ}\, P_T\, P_L(\cos\theta).$$

In the equation, k is the c.m. momentum, and ω is an energy defined by

$$\frac{1}{\omega} = \frac{1}{E_\pi} + \frac{1}{E_n}.$$

The α_{LJT} are related to the phase shifts by

$$\alpha_{LJT} = e^{i\delta_{LJT}} \sin(\delta_{LJT}).$$

P_{LJ} and P_T are channel projection operators given by

$$P_{L,J=L+1/2} = \frac{L + 1 + \vec{\sigma} \cdot \vec{L}}{2L + 1},$$

$$P_{L,J=L-1/2} = \frac{L - \vec{\sigma} \cdot \vec{L}}{2L + 1},$$

$$P_{T=3/2} = \frac{1}{3}(1 - 2\vec{t}_\pi \cdot \vec{t}_n), \text{ and}$$

$$P_{T=1/2} = \frac{2}{3}(1 + \vec{t}_\pi \cdot \vec{t}_n).$$

It is well known that, for energies up to ~300 MeV, only the s (L = 0) and p (L = 1) wave phase shifts are important. Since all other factors in the sum are roughly equal, the relative importance of each term is given by the phase shift factor, α_{LJT}. These are displayed (with a slightly different notation) as a function of energy in Figure I-1. Both the dominance and the resonant structure of the J, T = 3/2, 3/2 partial wave are obvious. All other partial waves have real parts that are of similar size, and imaginary parts that are essentially zero.

This dominance allows the use of simple arguments to estimate relative π-n cross sections. The Δ states can be expanded into π-n states with

$$\Delta^{++} = \pi^+ p,$$

$$\Delta^{+} = \sqrt{1/3}\,\pi^+ n + \sqrt{2/3}\,\pi^0 p,$$

$$\Delta^{0} = \sqrt{2/3}\,\pi^0 n + \sqrt{1/3}\,\pi^- p, \text{ and}$$

$$\Delta^{-} = \pi^- n,$$

where the coefficients are Clebsch-Gordan coefficients, and we have

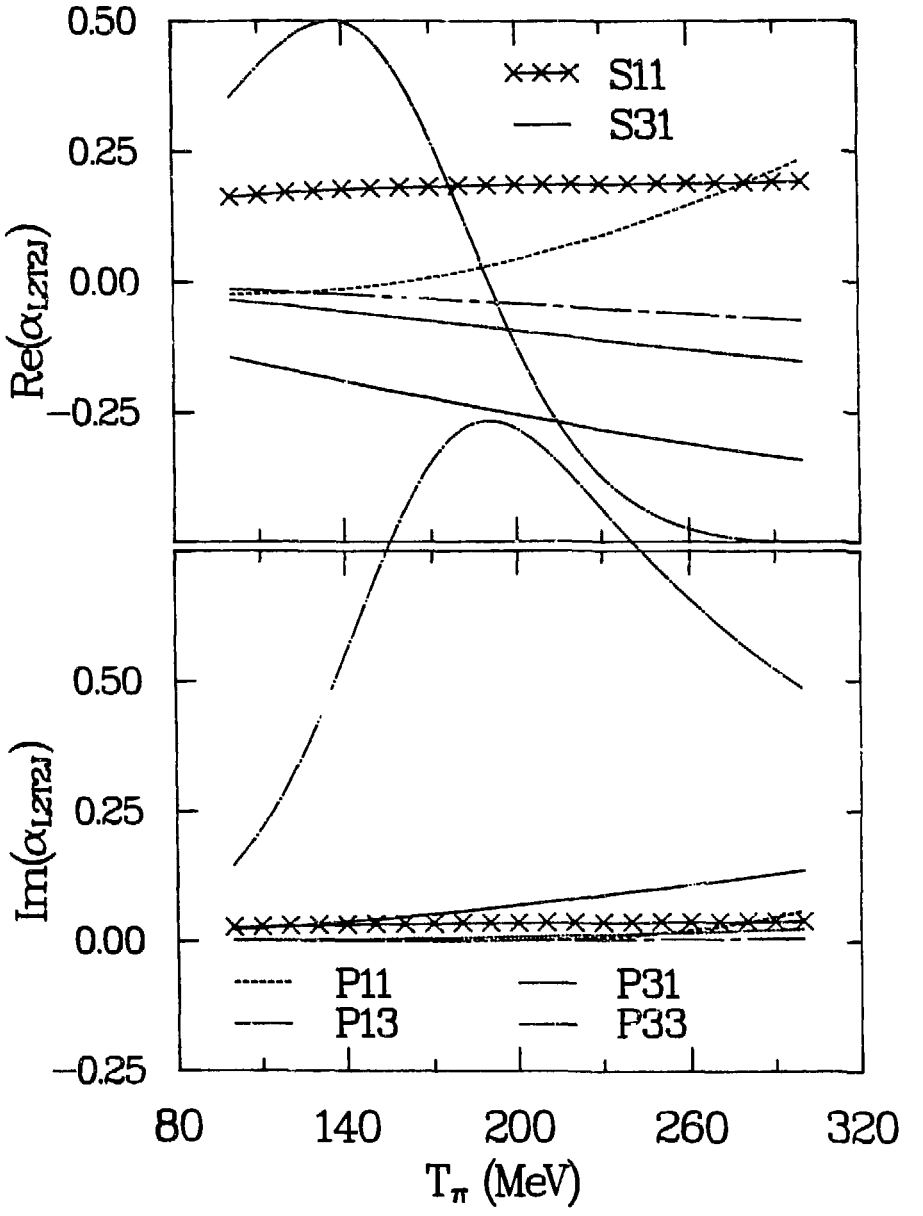

Figure I-1.
The coefficients, α_{L2T2J}, calculated from [Ro-78], as a function of energy.

used the particle physics convention, e.g., $T_z(p) = +1/2$. The relative sizes of π-n scattering processes can be estimated by, e.g.,

$$\frac{\sigma(\pi^+ n \to \pi^0 p)}{\sigma(\pi^+ p \to \pi^+ p)} = \frac{(\langle \pi^+ n | \Delta^+ \rangle \langle \Delta^+ | \pi^0 p \rangle)^2}{(\langle \pi^+ p | \Delta^{++} \rangle \langle \Delta^{++} | \pi^+ p \rangle)^2}$$

$$= \frac{(\sqrt{1/3} \times \sqrt{2/3})^2}{(\ 1 \ \times \ 1 \ )^2} = 2/9.$$

A summary of these numbers is given in Table I-1. The most striking feature is that the π^+ (π^-) interaction is dominated by elastic scattering from the proton (neutron). Thus, cross sections for pion double charge exchange are decreased by over an order of magnitude from elastic scattering by the basic π-n amplitudes. The need to interact with two nucleons decreases double charge exchange even more.

Table I-1. Relative sizes of π-n cross sections.

Reaction	Relative size
$\pi^+ p \to \pi^+ p$	1
$\pi^+ n \to \pi^+ n$	1/9
$\pi^+ n \to \pi^0 p$	2/9
$\pi^- p \to \pi^- p$	1/9
$\pi^- p \to \pi^0 n$	2/9
$\pi^- n \to \pi^- n$	1
$\pi^0 p \to \pi^0 p$	4/9
$\pi^0 p \to \pi^+ n$	2/9
$\pi^0 n \to \pi^0 n$	4/9
$\pi^0 n \to \pi^- p$	2/9

B. Double Charge Exchange

Pion double charge exchange (DCX) has long been a reaction with much promise, but few definitive results. Interest in the reaction, as a nuclear structure tool, originated in the early 1960's. All of the interest can be related to the fact that DCX changes the charge of two nucleons.

The most simple idea is the use of the reaction to produce exotic nuclei. For a target with (A,Z) the (π^+,π^-) reaction produces a residual, proton-rich nucleus, (A,Z+2), whereas the (π^-,π^+) reaction produces the residual, neutron-rich nucleus, (A,Z-2). Of particular interest to experimenters has been the search for the tetraneutron with the $^4He(\pi^-,\pi^+)$ reaction. From the earliest [Da-64] through the most recent of these experiments [Un-84], no indication of a discrete final state has been observed.

The second prospect is for the investigation of isobaric-analog states (IAS). IAS are states which have the same total isospin, spin structure, and spatial structure, but have different third component of isospin, T_z. They are states in different nuclei, of the same A, but different N and Z, which have the same numbers of nucleons in each shell-model orbit. Since elastic scattering cross sections are much larger than inelastic cross sections, it is natural to assume that elastic charge exchange, in which the charge exchanged nucleon remains in the same orbit, is much larger than inelastic charge exchange, in which the charge exchanged nucleon changes orbits. Iterating single charge exchange (SCX) leads to the double-isobaric-analog state (DIAS) via the double-isobaric-analog transition (DIAT). Although the elastic

cross section is not larger than the total inelastic cross section, one might still expect that, even in heavier nuclei, the DIAS will be selectively excited, and thus observable above a background of states of lower T.

The third consideration is that DCX necessarily involves two nucleons. Elastic and inelastic scattering are dominated by the interaction of the pion with a single nucleon. The effects of interactions with more than one nucleon enter as a higher-order correction. Since DCX requires two nucleons in lowest order, the higher-order corrections to elastic or inelastic scattering will be of similar size to the lowest-order predictions. Thus, a correct treatment of, e.g., two-nucleon correlations and pion absorption may be necessary to understand the reaction. The success, or failure, of lowest-order theory provides direct evidence of the existence of interesting higher order effects.

Early DCX experiments were hampered by small pion fluxes and poor energy resolution. Gilly et al. [Gi-65] reported a beam momentum resolution of ±8% with a pion flux of ~2.5×10^5 π/s. Boynton et al. [Bo-68] reported a flux of 6×10^4 π/s with an experimental energy resolution of 6 MeV full width at half-maximum (FWHM). Cook et al. [Co-68] obtained 3.5 MeV resolution, but a flux of only 1.5×10^4 π/s. There were two main results of early DCX experiments. First, there were no definitive measurements indicating the existence of any discrete, bound residual states. In particular, no enhancements corresponding to the DIAS were observed. Both the poor energy resolution and small pion fluxes contributed to this result. Second,

it was found that inelastic DCX processes were large. On average, nuclei were found to absorb about 60 MeV [Be-71] during DCX, resulting in multiparticle emission. Inelastic continuum cross sections were found to be much larger than cross sections to low excitation energy regions of the spectra, and in rough agreement with phase space estimates.

The theoretical development of DCX outpaced the experimental development. By the early 1970's, a second generation of DCX calculations, including improvements suggested by elastic-scattering data, began to appear. Theoretical approaches included multiple-scattering theories [Ka-74], Glauber theories [Ya-75, Li-75], and optical-model theories [Ro-71, Mi-74, Mi-76]. Because the theories used different approximations and investigated different effects, and because of the lack of data to act as a constraint, these theories predicted very different results. Predictions of $^{18}O(\pi^+,\pi^-)^{18}Ne$(DIAS) (in general, we will refer to (π^+,π^-) reactions by indicating only the target nucleus) varied by over two orders of magnitude.

The popularity of DIAT calculations probably arose from the simple theoretical consideration that DIAT DCX is much easier to calculate than nonDIAT DCX. The identical initial- and final-state structures simplify the calculational problem. In particular, it was found [Ko-69] that, assuming isospin conservation, the DIAT amplitude can be represented as a sum of elastic scattering amplitudes (with no Coulomb interaction). The explicit form of these amplitudes is [Jo-80]

$$F_{SCX} = \frac{1}{T^{1/2}(T+1)(2T+1)} \left[2Tf^{+} + (2T^2-T-1)f^{0} - (2T^2+T-1)f^{-}\right], \text{ and}$$

$$F_{DCX} = \frac{(2T-1)^{1/2}}{T^{1/2}(T+1)(2T+1)} \left[2Tf^{+} - (2T+1)f^{0} + (T+1)f^{-}\right],$$

where T is the isospin of the state, and f^{+}, f^{0}, and f^{-} are the elastic amplitudes for the channels of good isospin, T+1, T, and T-1, respectively. It should be noted that this is not the expression used by [Ge-80]. Subsequent tests [Mi-76] of this approximation, as a calculational tool, have shown it to be very accurate. Agreement with calculations that do not use the isospin identities is typically within ~2% at resonance energies. DCX models based on this simplification, however, must conserve isospin, and thus can only connect analog states. They necessarily predict zero cross section to nonanalog final states.

Experimental measurement of discrete final states was first accomplished in 1977 at the low energy pion channel (LEP) at the Clinton P. Anderson Los Alamos Meson Physics Facility (LAMPF) [Ma-77]. Cross sections at 0^{o} were measured with a pion flux of $\sim 4 \times 10^{7}$ π/s and a resolution of 4 MeV FWHM on several light targets [Co-79]. Except for these first, early measurements, and some recent measurements of DCX at low energies, essentially all measurements of DCX have been at resonance energies (T_{π} = 100 to 300 MeV) at the Energetic Pion Channel and Spectrometer (EPICS) facility at LAMPF.

When the present work started, several systematic features of DCX transitions had been found. First, DIAT angular distributions were

known to be diffractive at T_π = 292 MeV, but to have minima at very forward angles, e.g., ~21° instead of ~35° for ^{18}O, at 164 MeV. Second, excitation functions were known to rise monotonically at energies above resonance. Third, the mass dependence of DIAT DCX was known [Jo-80, Mo-80] to be

$$\frac{d\sigma}{d\Omega} \sim (N - Z)\,(N - Z - 1)\,A^{-10/3}.$$

Also, a restricted set of transitions, on self-conjugate targets leading to J^π, $T = 0^+$, 2 final ground states, had been observed to show a regular set of features. Excitation functions peaked on resonance, angular distributions at 164 MeV appeared diffractive, and the mass dependence was

$$\frac{d\sigma}{d\Omega} \sim A^{-4/3}.$$

The present work attempted to extend the systematics of DIAT and nonDIAT DCX. The nonanalog transitions were of particular interest. Measurements of ^{16}O angular distributions at 120 and 200 MeV investigated whether the energy variation of the shape was consistent with diffractive scattering. Measurements of $^{18}O(\pi^-,\pi^+)$ were intended to indicate whether the regular nonanalog characteristics were restricted to reactions on even-even, self-conjugate targets. Excitation functions on ^{56}Fe and ^{80}Se were designed to better investigate the mass dependence of nonanalog DCX. The DIAT experiments

were designed to examine the energy dependence of angular-distribution shapes in greater detail. Ten angular distributions were measured on ^{14}C, ^{18}O, and ^{26}Mg.

Chapter II presents a description of the experimental hardware. Chapter III reviews data analysis, concentrating on the software required to perform the experiments and analyze the results, and on the procedures used to calibrate the experiment, normalize the data, and extract final cross sections. Chapter IV summarizes all observed DCX systematics for both DIAT and nonanalog transitions. Chapter V presents a description of some of the theoretical approaches and models used to understand and interpret DCX measurements. Also presented is a description of some recent work, done as part of this dissertation, to calculate exotic DCX diagrams that may contribute to nonanalog and DIAT DCX. Chapter VI presents the conclusions of this work.

CHAPTER II. EXPERIMENTAL DETAILS

The data presented in this dissertation were obtained during four different experiments performed at the Energetic Pion Channel and Spectrometer (EPICS) facility at the Los Alamos Clinton P. Anderson Meson Physics Facility (LAMPF). Information about these experiments is given in Table II-1. This section describes in tedious detail the physical structure of the experimental facilities. An overview of

Table II-1. DCX experiments contributing to this work.

Experiment 749: $^{16}O(\pi^+,\pi^-)^{16}Ne$(g.s.) Angular Distribution Measurements at T_π = 120 and 200 MeV
Proposed by: L. C. Bland (University of Pennsylvania) and H. T. Fortune (University of Pennsylvania), August, 1982
Approved: A^- priority, 360 hours
Ran: October/November, 1983

Experiment 777: Angular Distributions for DCX on ^{14}C and ^{18}O
Proposed by: Peter A. Seidl (University of Texas), H. T. Fortune (University of Pennsylvania), and Helmut W. Baer (Los Alamos National Laboratory), January, 1983
Approved: B^+ priority, 200 hours
Updated: January, 1984 to A^- priority, 327 hours
Ran: September/October, 1984

Experiment 780: A Study of the DCX Reactions $^{14}C,^{18}O(\pi^-,\pi^+)^{14}Be,^{18}C$
Proposed by: Helmut W. Baer (Los Alamos National Laboratory), Peter A. Seidl (University of Texas), and R. Gilman (University of Pennsylvania), January, 1983
Approved: A priority, 206 hours
Ran: October, 1983

Experiment 826: Isospin Dependence of Nonanalog Pion DCX
Proposed by: C. L. Morris (Los Alamos National Laboratory), C. Fred Moore (University of Texas), and R. Gilman (University of Pennsylvania), January, 1984
Approved: B^+ priority, 216 hours
Ran: September/October, 1984

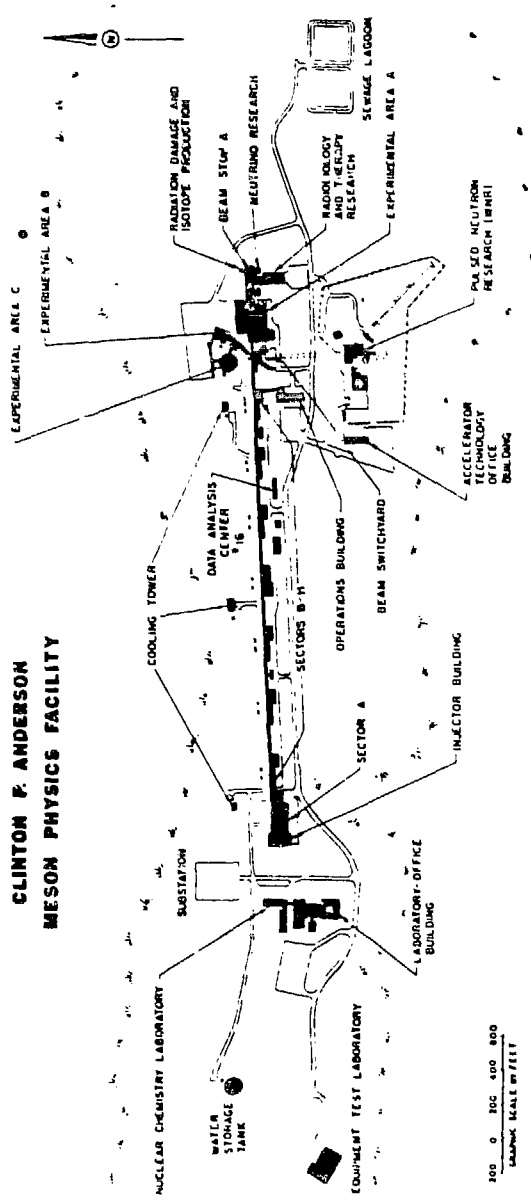

Figure II-1.
Los Alamos Meson Physics Facility.

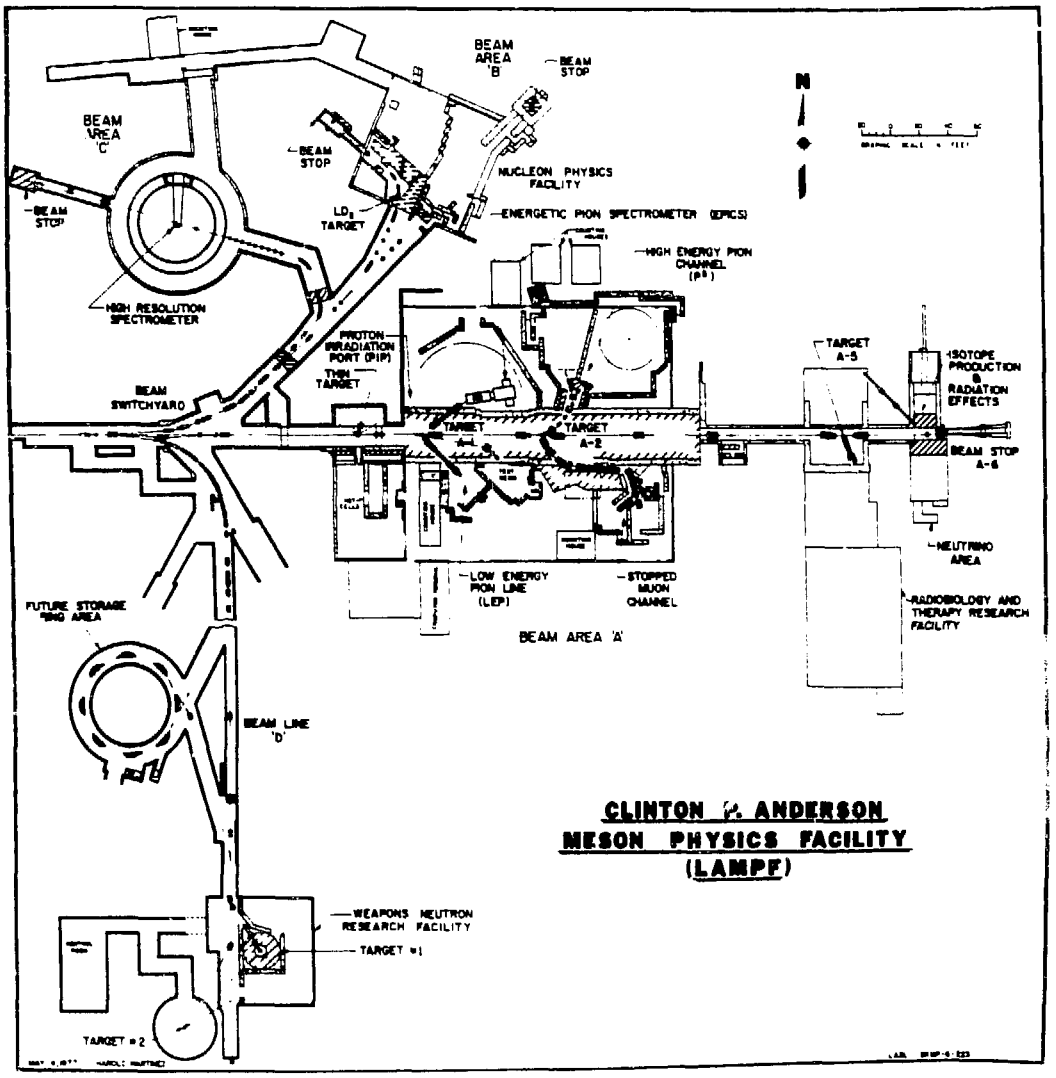

Figure II-2.
LAMPF experimental areas.

LAMPF is shown in Figure II-1. A diagram of LAMPF experimental areas is shown in Figure II-2.

A. Accelerator

The pion beam is a secondary beam produced by the passage of a pulsed primary proton beam through a pion-production target. The protons are accelerated by a ~1/2 mile long, 800 MeV linear accelerator (LINAC). The accelerator has three major sections: three 750 keV Cockroft-Walton sources, a 201.25 MHz resonant frequency (RF) Alvarez type of drift-tube LINAC that accelerates the protons to 100 MeV, and an 805 MHz RF side-coupled resonant-cavity LINAC that accelerates the protons to their final energy. When the accelerator runs well, the positive proton beam is pulsed with a repetition rate of 120 Hz, a duty factor of ~9.5%, and an average current approaching 950 μamps.

Typically, proton (H^+) and negative hydrogen (H^- or, if polarized, P^-) beams are injected into the accelerator from two of the sources and simultaneously accelerated by alternating the polarity of subsequent pulses, and injecting the two beams at opposite phases of the accelerator RF. This does not degrade accelerator performance when both beams are accelerated to the same final energy, 800 MeV. Often, however, the accelerator is run in a dual energy mode, where the last sections of the side-coupled LINAC are alternately turned off for the passage of the H^- (or P^-) beam, resulting in a lower energy, and turned back on for the H^+ beam to keep the beam energy, and thus the secondary pion spectrum, constant. In dual energy mode the H^+ pulse rate is decreased to 80 Hz, but the intensity of individual pulses is

increased, resulting in only a slight loss of average current. (Although the EPICS data acquisition system is capable of recording only one data event per primary beam pulse, this reduction in beam pulses is not a serious problem for DCX measurements. Under most experimental conditions, the number of charge-exchanged pions per primary beam pulse is much less than one. Thus, only the average beam current is of concern.)

An additional reduction of beam is caused by the Weapons Neutron Research (WNR) facility. When in operation, every tenth pulse of the H^+ beam is diverted at the beam switchyard for WNR use, reducing the H^+ beam available for pion production in Area A by 10%. The EPICS facility is located in Experimental Area A, along beam line A. There is a series of pion production targets along line A; pions for EPICS are produced at the first thick target within the Al target box.

The actual pion production target within the box is a graphite wheel that has an areal density of approximately 5 g/cm^2. The product of beam current (950 μamps) and energy (800 MeV) is the beam power (760 kwatts). The energy loss of 800 MeV protons in carbon is about 2.12 MeV-cm^2/g, resulting in a 10.6 MeV energy loss per beam particle in the Al target, or a power loss of ~10 kwatts. Although this is only a 1% loss, it is sufficient to require active heat dispersion techniques. Thus, the target wheel both rotates and is water cooled. In addition to the energy loss in the target, the Al target reduces the beam flux by about 10% (e.g., during run 210 of experiment 777, the Al current was 630 μamps, and the A2 current was 622 μamps). Almost all of the scattered protons are stopped either in the Al target box, or in

the surrounding concrete radiation shielding. This leads to an additional power deposition of ~75 kwatts in the vicinity of the Al target.

Along the primary beam line in Area A are several monitors of the H^+ beam current. As there is no monitor of the pion beam within the DCX scattering chamber, it is necessary to use these monitors for normalization of the data. Beam flux is measured by the current induced in 1ACM002 and 2ACM003, two toroidal coils located upstream and downstream, respectively, of the Al target. BOT is an ionization detector that measures scattering of the beam from the Al target. Generally, ratios of count rates in the three detectors are fairly stable; thus, all are of equal value as beam current monitors. During experiments 749/780, however, BOT was found to be stable only within about 15%. The variations were believed caused by water damage. Thus, 1ACM002 was used to normalize data. BOT was used for normalizations during experiments 777/826.

B. EPICS Channel

The EPICS channel (see Figure II-3) views the pion production target at an angle of 35o relative to the incident beam, and produces a vertically momentum dispersed beam at the EPICS scattering chamber. Pion beam characteristics, taken from [Th-77] and [LA-84], are specified in Table II-2. Physically, there are several active and inactive elements in the channel including dipole magnets, focusing magnets, a proton separator, collimating jaws, a proton absorber, and concrete and iron radiation shielding.

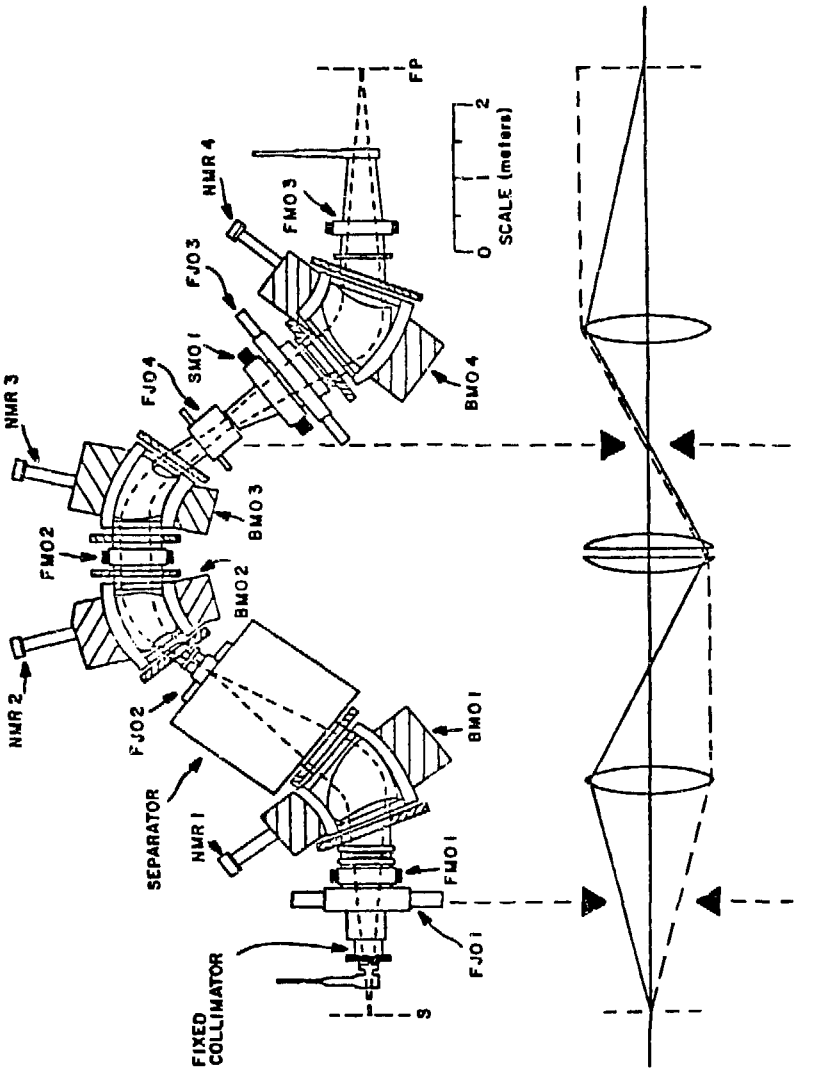

Figure II-3.
Schematic view of EPICS channel.

Table II-2. EPICS pion channel beam characteristics.

beam spot		
width	±3.2 cm (Y coordinate) includes 95% of beam	
height	±10.2 cm (X coordinate) includes 95% of beam	
vertical divergence	±77.5 mr (ϕ coordinate) includes 95% of beam	
horizontal divergence	±15.0 mr (θ coordinate) includes 95% of beam	
channel		
momentum dispersion	1.0%/10 cm in X	
momentum resolution	2.0×10^{-4} FWHM for $\Delta p/p$	
channel solid angle	3.4 msr	
pion flux (per 1 mA H^+ beam)		
50 MeV	0.11×10^8 π^+/sec	
67.5 MeV	0.22×10^8 π^+/sec	$0.07 \times 10^8 \pi^-$/sec
151.0 MeV	1.46×10^8 π^+/sec	$0.28 \times 10^8 \pi^-$/sec
200.0 MeV	2.20×10^8 π^+/sec	$0.41 \times 10^8 \pi^-$/sec
255.0 MeV	2.55×10^8 π^+/sec	$0.39 \times 10^8 \pi^-$/sec
290.0 MeV	2.54×10^8 π^+/sec	$0.34 \times 10^8 \pi^-$/sec

The dispersed beam spot is an important feature of the channel. Most importantly, it increases the pion flux over a "monochromatic" beam without degrading the resolution. Also, the large physical spot size and the capability at EPICS to project events back to the target allow data to be simultaneously obtained on several targets. Strip targets are described in detail in Appendix B3.

The four dipole magnets, BM01 - 4, momentum analyze the beam in the vertical plane. The three focusing magnets were not used in any of the experiments that contributed to this thesis. Although this is expected to degrade resolution of scattered-particle spectra, DCX targets are sufficiently thick that no effects were observed. The proton separator was designed to remove protons from the pion beam with

an E x B field, but was radiation damaged and has not been used in several years.

The sets of adjustable uranium collimating jaws, FJ01 - 4, are also generally ignored, as beam collimation reduces beam intensity, which is undesirable in low count rate experiments, and improves resolution, which is not observable given thick DCX targets. The first jaw, FJ01, determines the acceptance of the channel. It consists of only a vertical jaw, which was fixed to an opening of six inches for experiments 749/780. For experiments 777/826, pion beam intensity and experimental resolution were investigated as a function of jaw opening (see Table II-3). An initial check was done at the beginning of the experiment with a thick ^{18}O ice target in the regular scattering chamber. This determined the ratio IC1/BOT (IC1 is an ionization chamber in the regular scattering chamber that measures pion beam intensity). As it appeared that pion flux plateaued at a nine inch

Table II-3. (On-line) Resolution and count rate versus FJ01V opening.

Opening (inches)	Resolution (FWHM keV)	IC1/BOT	Relative elastic count rate
6.0	261	6.54	732 ± 22
7.0	291	7.39	882 ± 27
8.0	282	8.09	989 ± 31
9.0	285	8.64	976 ± 33
10.0	299	8.95	1026 ± 33
11.0	279	9.07	1065 ± 33
12.0	294	NA	1049 ± 34

opening, without any noticeable effect on the energy resolution for elastic scattering, this jaw opening was used at the beginning of experiments 777/826. A subsequent check was done with ^{12}C elastic scattering from a 73.68 mg/cm^2 CH_2 target in the DCX scattering chamber to better examine the experimental resolution at various jaw settings. The resolution and relative elastic count rate numbers in Table II-3 were determined by these measurements. It was decided after this to increase the jaw opening to eleven inches.

FJ02 and FJ03 were left open throughout all data acquisition runs. (FJ03 horizontal was used as a beam plug, and was closed during entries into the experimental area, until vacuum problems associated with its use developed. Then FJ03 vertical was used as a beam plug.) FJ04 was also left open during all data acquisition runs, but open for FJ04 refers to a canonical jaw setting, FJ04H = -0.1,1.2 (center and opening in inches) and FJ04V = -0.25,2.9, that does not correspond to the jaws being fully open. During calibration runs FJ04 horizontal was closed to reduce beam flux and permit measurement of $^1H(\pi^+,\pi^+)^1H$ angular distributions at forward angles. Closing FJ04H reduces the beam intensity at the target without changing the profile of the pions in the beam, and thus the acceptance of the spectrometer. All jaw positioning was controlled through CAMAC by the code, JAWS, on the EPICS data acquisition computer. Jaw positions were determined by reading potentiometer signals, and were adjusted by sending pulses to stepping motors that moved the jaws. As the stepping motors were not believed to be reliable, adjusting jaw position typically required several iterations of reading position followed by sending pulses.

The proton absorber, a 1/4 inch piece (~.65 g/cm^2) of CH_2, is located in the channel between dipole magnets BM03 and BM04. It was originally installed to allow cross-section measurements for elastic and inelastic scattering at forward angles by reducing the proton flux through the channel, and thus the count rate in the spectrometer front chambers. The different energy loss of pions and protons in the absorber result in different momenta of the particles entering BM04 (see Table II-4). The magnetic field in BM04 is adjusted to the appropriate value for the reduced energy pions, and sweeps the protons out of the beam striking the pion scattering target. The absorber was used only during experiments 777/826 when the ^{26}Mg target was used, as the loan agreement for this target stipulated that it not be exposed to protons.

In normal operation, the separate channel magnets are all set with a single power supply to a desired field setting, which is monitored by nuclear-magnetic-resonance (NMR) probes, in the final magnet, BM04. The fields in the magnets are not equal. Current shunts for each

Table II-4. Effect of 0.65 g/cm^2 proton absorber on 265 MeV/c beam.

particle	mass (MeV)	T (MeV)	dE/dx (MeV-cm^2/g)	T′ (MeV)	p′ (MeV/c)	Δp/p (%)
e	0.511	264.49	0.000	264.49	265.0	0.0
μ	105.66	179.63	2.000	178.328	263.600	-0.53
π	139.57	159.94	2.300	158.443	263.309	-0.64
p	938.17	36.71	17.460	25.359	219.604	-17.13

dipole are set to canonical values that change each field slightly relative to the average magnetic field. Thus, the procedure for adjusting the channel with the proton absorber is to set the channel, with the BM04 shunt at its canonical value, for an energy higher than desired by the energy loss in the proton absorber. Then, the BM04 shunt is increased to drop that magnet to the desired energy setting.

C. DCX Scattering Chamber

The primary constraint on forward-angle measurements at EPICS is the count rate in the front chambers (F1 - 4). To facilitate the measurement of DCX reactions at forward angles, a special DCX scattering chamber is installed on the EPICS spectrometer (see Figure II-4). This scattering chamber includes a C magnet that is used to introduce an opening angle of 20^{o} between pions of opposite polarity that are scattered at the same angle. The design and calibration of this system are described at length in a Ph.D. thesis by Steven J. Greene, [Gr-82a].

The scattering chamber is vacuum coupled to the channel with a flexible bellows. Pressure throughout the vacuum system was typically $\sim 2 \times 10^{-5}$ torr. The bellows limits the angular range of the spectrometer. For experiments 749/780, the angular range was $0^{o} \leq \theta \leq 45^{o}$. For experiments 777/826, the angular range was $0^{o} \leq \theta \leq 41^{o}$. The reasons for the decrease are unknown.

The C magnet, located immediately after the pion target, produces a uniform vertical magnetic field. The magnet field is adjusted so that pions with a momentum equal to the central momentum of the

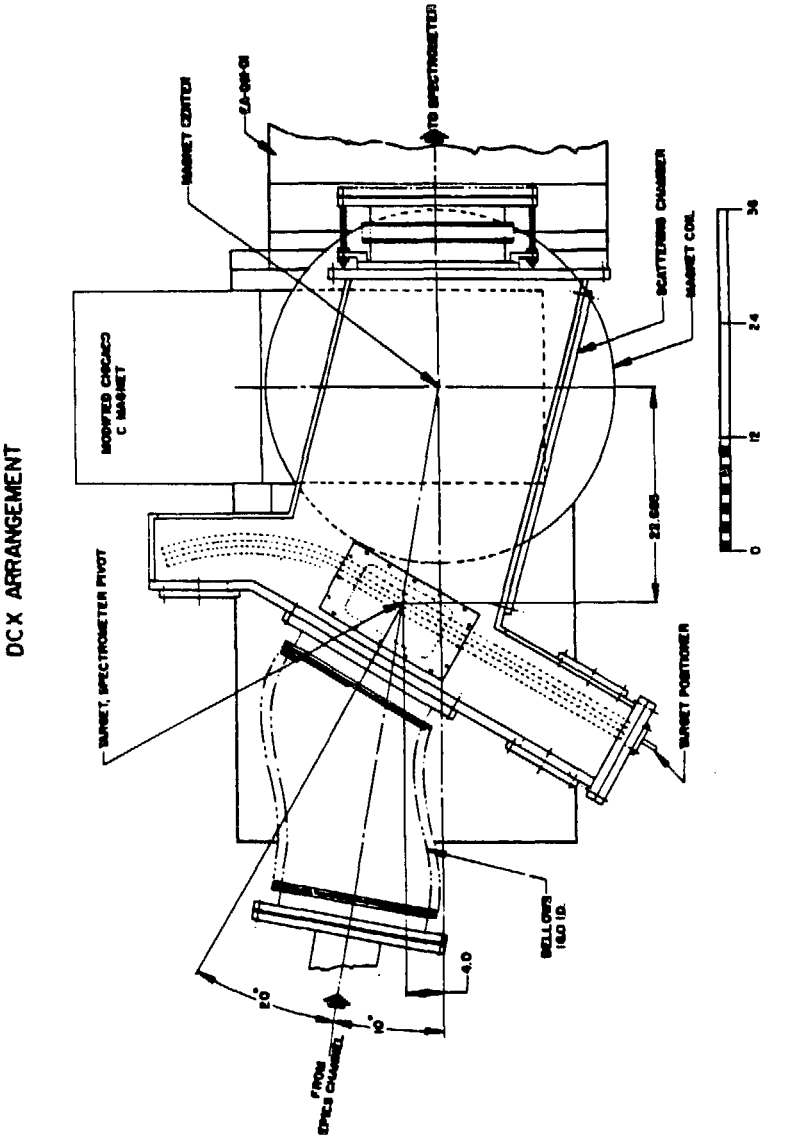

Figure II-4.
EPICS DCX scattering chamber.

spectrometer are deflected by 10° in the magnet. Because of the change in pion trajectories, the spectrometer has to be offset four inches so that the deflected charge-exchange pions enter the spectrometer on its axis. (Also, the scattering angle differs by 10° from the spectrometer floor angle.) The change of pion trajectories is sufficiently large that pions of the opposite polarity enter the spectrometer skewed. This results in most elastic (and inelastic) scattering events missing the front chambers, and reduces backgrounds significantly.

There is a momentum dependent correction to the scattering angle of about 0.1° per %. A typical pion peak with a thick DCX target is about 1 MeV wide, which corresponds, at a pion kinetic energy of 160 MeV, to a 0.4% variation in momentum, and a .04° variation in angle. This variation is insignificant compared to the ~3° (FWHM) acceptance of the spectrometer. The variation in angle across the full momentum acceptance of the spectrometer, ±7% corresponds to ±1.4°, is significant, but analyses concentrate almost exclusively on a few low-lying states.

D. EPICS Spectrometer

The EPICS spectrometer (see Figure II-5 and II-6) contains quadrupole magnets for focusing scattered pions, dipole magnets to momentum analyze scattered pions, and three types of particle detectors, wire chambers, scintillators, and a Cherenkov detector, which are divided into two sets, the front detectors before the dipole magnets, and the rear detectors after the dipole magnets.

The quadrupole triplet QM01 - 3 focuses an inverted image of the

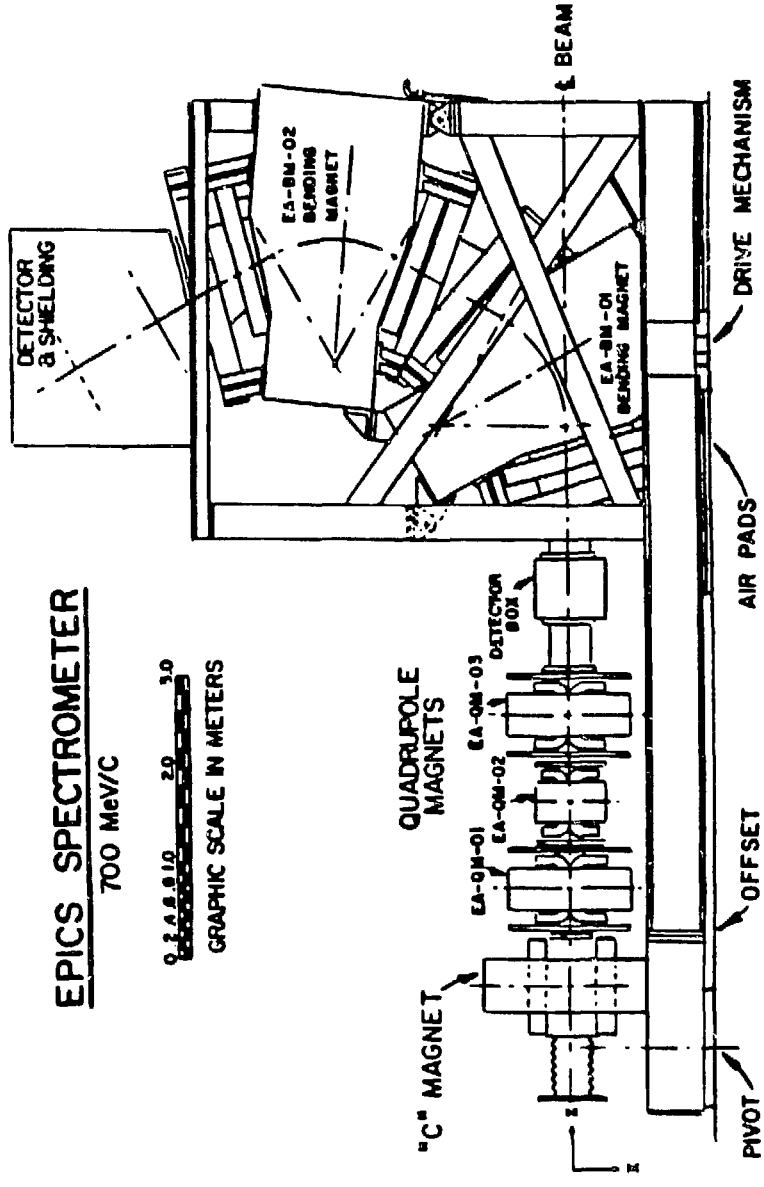

Figure II-5.
The EPICS spectrometer and coordinate system.

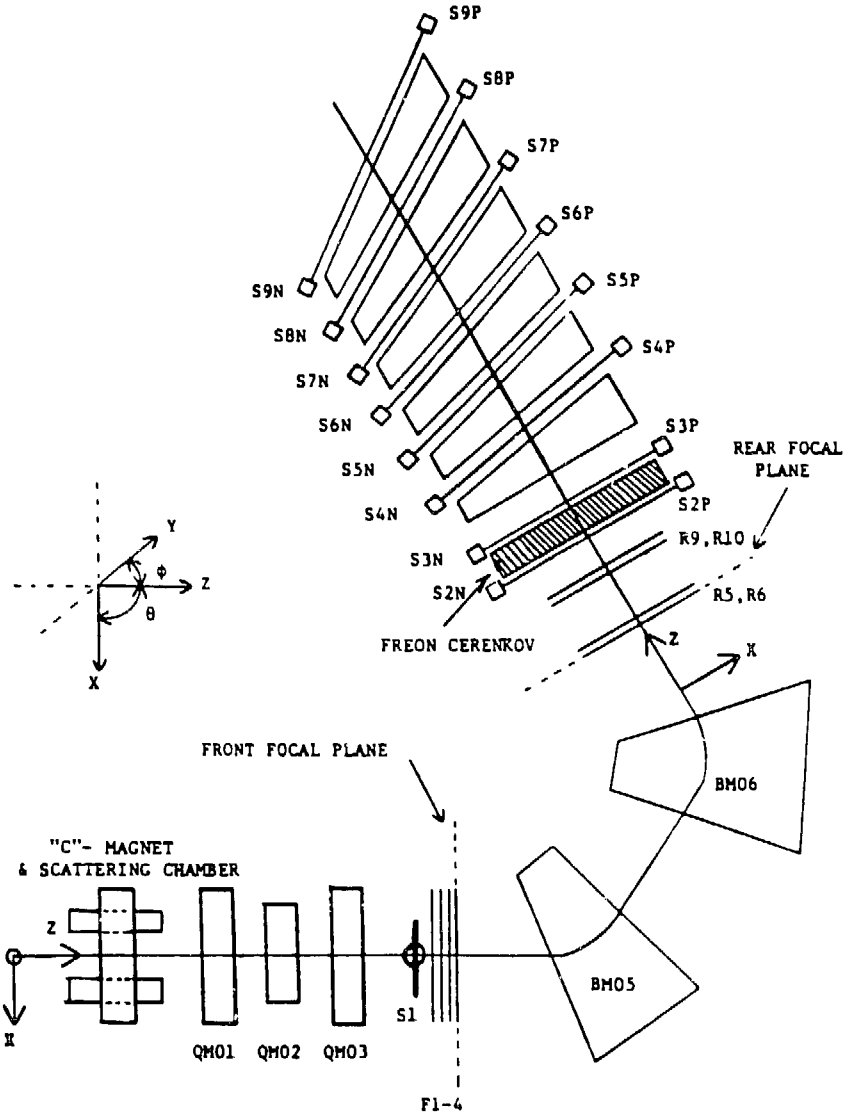

Figure II-6.
Diagram of EPICS spectrometer detectors.

target onto a set of wire chambers, F1 - 4. The wire chambers consist of four pairs of wire planes. The planes of each pair are offset by 1/2 of a wire spacing. Having a pair of planes eliminates the ambiguity (with a single plane) of on which side of a wire the detected particle passed. Two pairs of planes measure an x position; the other two pairs measure a y position. The average x and y positions and horizontal and vertical angles are calculated for each event from the four raw positions.

Before experiments 777/826, the algorithm for eliminating the left/right ambiguity was changed to allow single, rather than pairs of, wire planes. The new algorithm makes use of the fact that a wire plane consists of alternating anode and cathode wires (typically at 2100 and 0 volts, respectively). The passage of a charged particle produces anions (electrons), which are collected at the nearest anode wire, and cations (ionized gas molecules) that are collected by the nearest cathode wire. The determination of the nearest anode and cathode wires determines between which two wires the particle passed.

During DCX measurements, a scintillator, S1, is installed in the spectrometer immediately prior to the front chambers. S1 is not generally used, as, being before the other spectrometer detectors, it degrades resolution. For DCX measurements, the scintillator is an essential part of the background rejection system. S1 is used for time-of-flight data through the spectrometer. It provides sufficient timing resolution to reject electrons at all energies, and muons at lower energies.

The two spectrometer dipole magnets, BM05 and BM06, each bend

scattered particles through an angle of ~60°, transporting particles with a momentum spread of ~±8% to the focal plane. The spectrometer dispersion is 4 cm/%. Since, however, the target beam spot is 20 cm wide in X and 2% wide in momentum, counts corresponding to a particular state are spread out over 20 + 2 × 4 = 28 cm at the focal plane. The focal plane detectors include a set of rear wire chambers, a Cherenkov detector to identify electrons, two scintillators, and a muon rejector. The rear chambers, R5 - 6 and R9 - 10 (referred to as two because the four pairs of wire planes are separated into two chambers), work identically to the front chambers. The scintillators S2 and S3 are used for timing information, for pulse height information, and for the computer trigger.

The muon rejector [Mo-85] consists of scintillators S4 through S9, which are separated by graphite blocks. It is designed so that, at particular central spectrometer energies (100 MeV for S4, 140 MeV for S5, etc.), pions, with a shorter range in matter, will not trigger a particular scintillator, whereas muons will. The graphite blocks are wedge shaped to compensate for the variation of particle momenta across the focal plane. A small gap before S4 allows the insertion of aluminum plates to induce energy loss and adjust the muon rejector for intermediate energies.

E. Data Acquisition

The EPICS scintillators, wire chambers, and Cherenkov detector generate signals that are amplified and discriminated to provide pulse height, timing, scalar, and logical information. The electronic

hardware is essentially left untouched. The major exceptions occur whenever either an electronics problem develops, or it is desired to change the computer trigger. The trigger is an electronic determination that a real event has occurred. The standard EPICS trigger requires a coincidence of signals from scintillators S2 and S3, and from (some, but not all of the planes in) the front wire chambers. The trigger signal can also be put in anticoincidence with other signals to hardware reject certain types of events. Because DCX count rates are low (and not much magnetic tape is used in event recording), hardware rejection is typically not done. At lower energies, however, the electron background can be very large on certain targets (see Chapter III-E). Thus, for some data acquisition runs, the electron background was hardware rejected by using the Cherenkov detector.

CAMAC is controlled by a small computer known as a microprogrammed branch driver (MBD). If the MBD is not busy processing an event, a trigger signal causes it to read various analog-to-digital converters (ADCs) and time-to-digital converters (TDCs). These data words are then dumped into the main-acquisition-computer's core for processing.

For experiments 749/780, the main acquisition computer was an ancient PDP 11/45, which suffered from numerous hardware problems, necessitating frequent reboots and calls to computer maintenance personnel. The PDP was replaced before experiments 777/826 with a VAX 11/730, which, while more stable, exhibited a much longer response time.

F. Measurements

Data were obtained with both the (π^+,π^-) and (π^-,π^+) reactions on a variety of targets. Table II-5 presents a list of measurements completed in this work. Each data point required from as little as one hour (for, e.g., $^{18}O(\pi^+,\pi^-)$ at 292 MeV and 5^o) to as much as three days (for $^{14}C(\pi^-,\pi^+)$ at 164 MeV and 5^o) of beam time. Most of these measurements have either been published, or submitted for publication. More detailed justifications for the measurements and descriptions of the targets may be found in the articles reproduced in Appendix B. Cross sections are tabulated in the DCX data compilation in Appendix C. We summarize here the reasons for many of the measurements.

The primary purpose of experiment 780 was to extend the systematics observed for nonanalog DCX on T = 0 targets to transitions with different isospin quantum numbers. In particular, it was desired to do (π^-,π^+) on T = 1 targets leading to residual T = 3 ground states. The target ^{18}O was picked for an excitation function and an angular distribution because thick, light mass targets have high count rates. Targets of ^{14}C and ^{58}Ni were picked to examine both the mass dependence of the reaction on T = 1 targets, and the relative scale of DCX between T = 0 and T = 1 targets. An alternate target, ^{44}Ca, was intended for (π^-,π^+) measurements, if there was sufficient time, but (π^+,π^-) data were obtained because of channel magnet problems (magnet polarity could not be reversed, and the power supply could not be fixed until after the weekend). Two target materials, ^{90}Zr and ^{118}Sn, were used with the ^{44}Ca to fill out the target frame.

The primary purpose of experiment 749 was to measure the energy

dependence of the shape of $^{16}O(\pi^+,\pi^-)^{16}Ne(g.s.)$ angular distributions. It was desired to determine whether or not this variation was consistent with diffractive scattering. Extra time at the end of the experiment was used to measure the first of the $^{18}O(\pi^+,\pi^-)^{18}Ne(g.s.)$ angular distributions (at 120 MeV) proposed as part of experiment 777.

Experiment 826 measured an excitation function on ^{80}Se, and completed earlier work on ^{56}Fe. Both measurements were intended to investigate the mass dependence of the shape of nonanalog DCX excitation functions. The ^{56}Fe measurement also provided information on the lower energy shape of DIAS excitation functions.

Experiment 777 was designed to investigate the energy dependence of the shape of DIAS angular distributions. Targets used were ^{18}O, ^{14}C, and ^{26}Mg.

The experiments also had a common purpose of examining DCX mass dependence. For DIAS final states, data points were taken at energies of 292, 230, 164, and 100 MeV, at which pion single-charge-exchange data were available, and phenomenological analyses of the data could be performed. For nonanalog transitions, cross sections were measured on many nuclei at an incident pion energy of 164 MeV, near the peak of the excitation functions.

Table II-5. Measurements in this work.

Reaction	Measurement	Details
$^{14}C(\pi^-,\pi^+)^{14}Be$	single point	5^o and 164 MeV
$^{14}C(\pi^+,\pi^-)^{14}O$	angular distributions	140 and 200 MeV
	excitation function	5^o
$^{16}O(\pi^+,\pi^-)^{16}Ne$	angular distributions	120 and 200 MeV
	excitation function	5^o
$^{18}O(\pi^-,\pi^+)^{18}C$	angular distribution	164 MeV
	excitation function	5^o
$^{18}O(\pi^+,\pi^-)^{18}Ne$	angular distributions	121, 171, 180, 200, and 230 MeV
	excitation function	5^o
$^{26}Mg(\pi^+,\pi^-)^{26}Si$	angular distributions	140 and 200 MeV
	excitation function	5^o
$^{44}Ca(\pi^+,\pi^-)^{44}Ti$	two points	5^o, 164 and 210 MeV
$^{56}Fe(\pi^+,\pi^-)^{56}Ni$	excitation function	5^o
$^{58}Ni(\pi^-,\pi^+)^{58}Fe$	single point	5^o and 164 MeV
$^{80}Se(\pi^+,\pi^-)^{80}Kr$	excitation function	5^o
$^{90}Zr(\pi^+,\pi^-)^{90}Mo$	two points	5^o, 164 and 210 MeV
$^{118}Sn(\pi^+,\pi^-)^{118}Te$	two points	5^o, 164 and 210 MeV

CHAPTER III. DATA ANALYSIS

A. Q System

The Q system is a set of data acquisition programs written at LAMPF by the computing group, MP - 1, for the use of experimenters. It provides an extremely flexible (hence, somewhat slow) framework for data acquisition, event recording, and replay. The system consists of a large number of command procedures and task specific codes. The present version, written to be compatible with the Digital Equipment Corporation (DEC) PDP operating system, RSX-11M (and with some changes the VAX VMS operating system), was introduced for general use in 1983, and used for all of the experiments in this work. The 11M version of Q resulted from a several year effort to redesign the previous, 11D compatible version (since DEC was no longer supporting the 11D operating system), and create a more efficient data acquisition and replay system. Some of the more important Q procedures are listed in Table III-1.

Unfortunately, the number of Q-system tasks and their flexibility results in thick piles of documentation [Qr-83] that deter new users. Fortunately, all tasks are written to have syntax similar to RSX - 11M utilities, and all have similar grammar. Thus, the regular Q user sooner or later acquires the ability to sometimes successfully guess both unremembered task names and commands. Also, except for a change of modes when initializing the Q system (from "DATA ACQUISITION" to "REPLAY"), there are almost no changes between commands used to acquire data and those used to replay data.

Data from experiments 780/749 were replayed on a PDP 11/70 at the

Table III-1. Some Q system commands and tasks.

Command	Description
	run commands
QRU	start a run
QFI	end the run
QSU	suspend the run
QRE	resume the run
	tape commands
QNT	open a new output/input tape
QCT /OU or /IN	close the output or input tape
QDT	disable taping
QET	reenable taping
	Q initialization/termination
@QSTART	initialize Q system
@QSTOP	terminate Q system
	histogramming tasks
HSU	set up core histograms
HPL	plot histograms
HSV	save core histograms into a disk file
	testing tasks
TSU	set up test file
TPR	print out test results

LAMPF data analysis center (DAC). Prior to experiments 777/826, VMS replay was available, and allowed several simultaneous Q replays with different logical names, or QNAMES. Because replay on multiuser VAX 11/780s under VMSv4.0 was extremely slow, and data acquisition on the EPICS VAX 11/730 (VMSv3.5) used only about 10% of the CPU time during DCX runs, it was decided to replay data tapes at EPICS at a low priority (and with a different QNAME) while writing subsequent data tapes.

The Q system is designed to recognize and independently analyze different types of events. The most important types of events at EPICS (other than the start-a-run and stop-a-run events) are the data event (event 6) and the scalar event (event 8). Data event triggering has been described already. Scalar event triggering was handled differently with the PDP 11/45 and the VAX 11/730. With the PDP, a code, SLRGO, was run with a rescheduling interval (generally 30 seconds). This program existed solely to trigger scalar events. Because of obscure differences in the VAX VMS operating system, this procedure was deemed not trivially adaptable, and an electronic timer was set to trigger a scalar event every 30 seconds.

The scalar event is processed by a user-written (i.e., standard EPICS) subroutine PROC08. This processing consists mostly of Q system overhead; the function of the subroutine is simply to increment current scalar values stored in core memory by the values read.

Data event processing, by a subroutine PROC06 (also a standard EPICS subroutine), is significantly more complicated. Processing typically includes calculating various derived quantities from the data read, testing read and derived quantities according to a test file to determine if specified conditions are met, and incrementing histograms and dotplots (a two-dimensional display of data). Table III-2 presents a list of some of the quantities calculated by PROC06. Because an extensive amount of CPU time can be used in processing individual events, on line data are acquired with event 6 in "may" process mode. The availability of CPU time determines whether or not an event is processed. In a typical run (run 148 of experiment 826 was $^{56}Fe(\pi^+,\pi^-)$

Table III-2. Some parameters calculated by PROC06.

Number	Name	Description
	X	position
221	XFRONT	at front chambers
225	XREAR	at rear chambers
233	XTGT	projected back to unrotated target
	THT	angle with respect X
222	THTFR	at front chambers
226	THTRE	at rear chambers
234	THTTGT	theta target
	Y	position
223	YFRONT	at front chambers
227	YREAR	at rear chambers
235	YTGT	projected back to unrotated target
	PHI	angle with respect Y
224	PHIFR	at front chambers
228	PHIRE	at rear chambers
236	PHITGT	phi target
	CHK	calculated / measured rear angle difference
237	THTCHK	difference for THTRE
238	PHICHK	difference for PHIRE
		momenta and energy
240	DELTPA	momentum of incident beam particle
241	DELTPC	momentum of outgoing scattered particle
243	DELTA	raw spectrometer momentum
246	QEXACT	missing mass of an event
	TOF	time of flights
260	S23TOF	S23 TOF
266	S1CTOF	corrected S1 TOF
		pulse heights
251	S2DELE	
252	S3DELE	
258	CHPH	Cherenkov pulse height sum

at T_π = 120 MeV, $\theta_{scatter} = 5^o$ with a 2.5 g/cm^2 target), over 95% (181178 out of 190000) of all events were processed on line.

If higher order corrections to the spectrometer optics are ignored, the relations among many of these quantities are particularly simple. We will follow the convention of ignoring Y coordinates and angles, as they are not used in the determination of measured momentum. The incoming pion will be denoted by a subscript A, whereas the scattered pion will be denoted by the subscript C. We will use the symbol "p" for a momentum in units of MeV/c, and the symbol "δ" for a momentum in units of % difference from the central, set momentum:

$$\delta = 100 \times (p_{part} - p_{cent}) / p_{cent}.$$

The incoming momentum is measured by the position of the event at the target:

$$p_A = (1 + \delta_A/100) \times p_{ch}, \text{ where}$$

$$\delta_A = XTGT / D_{ch},$$

D_{ch} is the channel dispersion (10 cm/%), and the channel momentum, p_{ch}, is determined from the magnet field settings. The front quadrupole triplet images the target, with a magnification of -1 in X, onto the front chambers. Thus, the front chamber quantities are related to the target quantities by:

XFRONT = $-1 \times$ XTGT, and

THTFR = -1 × THTTGT.

The spectrometer optics through the dipole magnets from the front to rear detectors produce two major effects on the target image. First, there is a magnification of the image, $M_{sp} = -1$. Second, there is a momentum dependent dispersion of the scattered particles, $D_{sp} = 4$ cm/%. Thus, to lowest order, the rear position is given by

$$XREAR = M_{sp} \times XFRONT + D_{sp} \times \delta_C.$$

We do not, however, measure the scattered particle momenta directly. The front and rear positions are extracted from chamber measurements, and the spectrometer magnification and dispersion are known. Thus, the scattered momentum is extracted by inverting the equation to:

$$\delta_C = (XREAR - M_{sp} \times XFRONT) / D_{sp}, \text{ and}$$

$$p_C = (1 + \delta_C/100) \times p_{sp}.$$

Finally, the missing mass for an event (or equivalently, the excitation energy) can be extracted. Complete kinematic knowledge includes all particle masses for the reaction, energy loss in the target, scattering angle, and incoming and outgoing momenta. All of the fixed, event-independent parameters are input with a code, KINSET, which is automatically run by the QRU command. Input to KINSET consists of the reaction, target angle, energy loss in the unrotated target, scattering angle, and spectrometer and channel field settings.

The target angle and unrotated energy loss determine the total energy loss in the target. The reaction information is used to look up in a mass table masses for the target, incoming, outgoing, and residual particles. A ground-state Q value is calculated from the masses, with a 1.022 MeV (twice the electron mass) correction made for DCX to conserve electrons. The target energy loss, Q value, and recoil energy determine an energy offset that is not included in the missing mass. The spectrometer and channel fields are used in an internal calibration to determine the central momenta of the spectrometer and channel. The subroutine PROC06 calls another subroutine, CALKIN, to take the input kinematic information plus the measured momenta for each event and calculate the missing mass.

B. Calibration

Since derived quantities at EPICS are calculated with software from raw, measured input quantities, it is possible to adjust the calculation for a set of measurements to best fit a known result. The spectrometer momentum, e.g., is calibrated by examining only elastic scattering off a thin ^{93}Nb target, so that the outgoing momentum is accurately known. The pion channel momentum is varied, and a fit is performed to adjust the calculated momenta to best fit the expected values. Typically, these calibrations are examined during a development period at the start of experimental cycles.

The installation of the DCX scattering chamber with the C magnet necessitates an examination of the calibrations of target dependent quantities. Quantities that were recalibrated for DCX runs include

XTGT, YTGT, THTCHK, PHICHK, DELTA, and S1CTOF (most experiments do not use S1, as the time-of-flight information is not necessary and S1 degrades the momentum resolution; thus it is often not calibrated in development). A list of some of the recalibrated quantities and their resolution appears in Table III-3. An example of the XTGT calibration follows.

The vertical target position, XTGT, was calibrated by using a target of five horizontal, 2.0 mm diameter, graphite rods. The target is positioned so that the rods have X positions of -8.0, -4.0, 0.0, 4.0, and 8.0 cm. Spectrometer magnets are adjusted to examine quasielastic scattering. The calibration run typically extends until a few thousand XTGT good events have appeared. The actual calibration can be redone with this data either on line or in replay.

The first step in the calibration is setting up the analyzer subroutine PROC06 to write a ray file. This is done with a command

Table III-3. Some parameters recalibrated for DCX.

Quantity	Resolution (FWHM)
XTGT	3 mm at center of target, 4 mm at edges for 2 mm diameter rods
YTGT	8 mm at center of target, 11 mm at edges for 2 mm diameter rods
THTCHK	7.7 mR
PHICHK	8.6 mR
S1CTOF	1.0 ns (π/e TOF difference ranges from 8.0 ns at 100 MeV to 2.0 ns at 300 MeV)

```
;[161,20]XTARG.RDO  8-DEC-83  SJSM
;
;  DON'T FORGET TO SET INDIRECT GATES1-5 ON RODS
;  FIRST TEST FOR GATE  1
I52=81
I53=0
;  NUMBER OF RAYS TO DISK PER FILE
I55=1000
;  TEST INCLUDES GOOD CHMBRS, ANGLE CHK
I56=101
;  DATA WORDS
I57=221!XFRONT
I58=222!THTFRONT
I59=223!YFRONT
I60=224!PHIFRONT
I61=225!XREAR
I62=226!THT REAR
I63=228!PHI REAR
I64=243!CRUDE DELTA
I65=249!XDEP
I66=0
I67=0
I68=0
I69=0
;  VALUES ON XDEP
R71=-8.0
R72=-4.0
R73=0.0
R74=4.0
R75=8.0
;  LIMITS ON XDEP
R69=-8.1
R70=8.1
;  TURN ON XDEP
IFLAG(22)=0
```

Figure III-1.
Sample calibration setup file, XTARG.PRM.

file input to the Q program PRM. Figure III-1 shows the command file XTARG.PRM. The ray file contains, for events that pass particular tests, the raw quantities used to calculate the desired derived quantity and the expected value of the derived quantity. The ray file is actually written to disk by an MP - 10 program, invoked by the

command "FPO filename", where filename is usually the quantity name with an extension of .RAY (by convention, the optional choices of certain filenames are not optional). The fit, performed by the program COF, requires a second input file that specifies what polynomial terms will be used to calculate the derived quantity. Figure III-2 shows the file used for XTGT, XTARG.COF. The polynomial fit uses a matrix inversion routine. Typically, rays that are fitted very poorly (deviation greater than 3.0 σ) are eliminated, the fit is repeated, and the best-fit coefficients are written into a disk file (XTARG.POL). This file has essentially the same format as the disk file, POL.DAT, which contains all the adjustable calibrations. A portion of the file

```
;FILE=XTARG.COF
;
 0,0,0,0
 221,0,0,0
 222,0,0,0
 221,243,0,0
 222,243,0,0
 222,223,0,0
 222,224,0,0
 221,243,243,0
 222,243,243,0
 221,223,223,0
 221,223,224,0
 221,224,224,0
 221,221,221,0
 221,221,222,0
 222,222,222,0
 222,223,223,0
 222,223,224,0
 222,224,224,0
```

Figure III-2.
The file, XTARG.COF that provides polynomial terms to COF.

```
233,  18,    XTARG DCX RECALIBRATION 9/2/84 RG IN REPLAY
   0,   0,    0,   0,  -0.502199E+00,
 221,   0,    0,   0,  -0.102703E+01,
 222,   0,    0,   0,  -0.228977E-02,
 221, 243,    0,   0,  -0.336349E-02,
 222, 243,    0,   0,  -0.353094E-02,
 222, 223,    0,   0,   0.102922E-02,
 222, 224,    0,   0,  -0.144140E-04,
 221, 243, 243,   0,   0.111530E-03,
 222, 243, 243,   0,  -0.123597E-03,
 221, 223, 223,   0,  -0.237604E-03,
 221, 223, 224,   0,  -0.314516E-03,
 221, 224, 224,   0,   0.298867E-04,
 221, 221, 221,   0,   0.365179E-04,
 221, 221, 222,   0,   0.606606E-04,
 222, 222, 222,   0,   0.323498E-06,
 222, 223, 223,   0,   0.361434E-03,
 222, 223, 224,   0,  -0.126148E-03,
 222, 224, 224,   0,   0.134381E-04,
//,
```

Figure III-3.
The part of the file POL.DAT that contains the XTGT calibration.

POL.DAT is shown in Figure III-3. The largest term in the calibration is -1.027 × XFRONT (the term "221,0,0,0"), indicating a slight magnification in addition to the inversion of the target image. The next largest term is a constant term ("0,0,0,0"), indicating a 0.50 cm offset in the vertical calibration. The offset is most likely due to the positioning of the targets in the DCX scattering chamber, since the vertical alignment of the targets is not well determined, but it is possible that there are, e.g., offsets due to the front chamber calibration. All of the other, higher order terms are significantly smaller.

After editing in the changed calibration to POL.DAT, the calibrations are reinitialized. Under 11M - Q on the PDP 11/45, this

could be done with the MP-10 code POL ("POL /DF"), but this procedure failed under early versions of VMS Q because of software bugs, and it was necessary to reinitialize Q.

One additional calibration check consists of measuring a hydrogen angular distribution to check for any angle-dependent normalization effects. The angular distribution is measured with a thin CH_2 target (73.68 mg/cm^2), and with jaws FJ04H closed down (from an opening of 1.2" to an opening of 0.1") to reduce pion flux and permit measurements at forward angles. There are two effects that are believed to have occurred in the past. It is known that, during DCX runs in 1982, a weld fixing the position of the scattering chamber broke, and the scattering chamber and target positions varied slightly with angle. Also, it is possible that, at the extremes of the angular range, the edges of the pion beam can strike the bellows that vacuum couples the scattering chamber to the pion channel. Thus, a hydrogen angular distribution was measured for each experiment contributing to the present work.

Figure III-4 shows all of the hydrogen angular distributions measured. If there are no angle-dependent effects, the ratio σ_H/Y_H should be angle independent. Except for the $\theta = 45^o$ point measured for experiment 780, the data are consistent with a straight line in each case. It is believed that the increased ratio for the 45^o point was caused by the pion beam striking the bellows. A visual inspection confirmed this possibility.

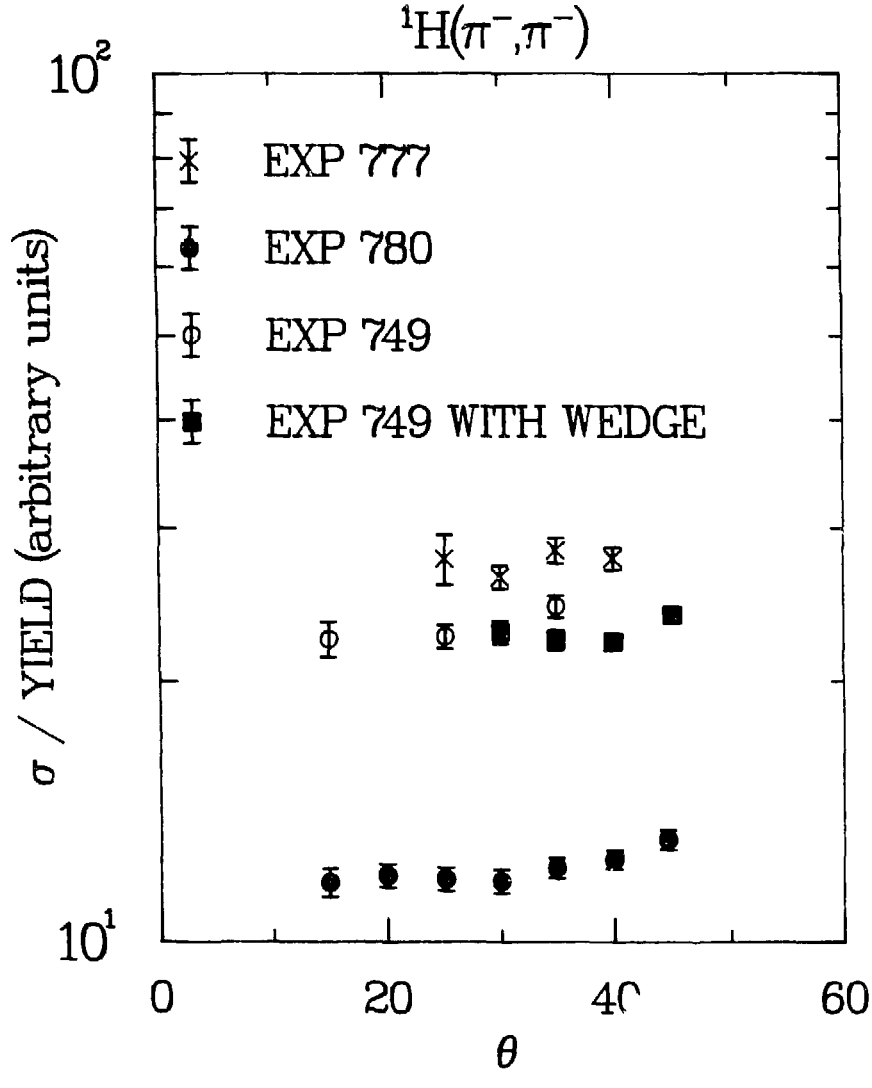

Figure III-4.
The ratio σ_H/Y_H for measured hydrogen angular distributions.

C. Normalization Procedures

Because the solid angle of the spectrometer is not accurately known (and is slightly less with the DCX scattering chamber), and absolute beam flux is not measured for DCX runs, absolute cross sections cannot be directly measured at EPICS. This problem is solved by measuring yields (the product of counts measured and a normalization factor that accounts for the amount of beam and detection efficiencies) for a reaction of known cross section. The ratio of known cross section to yield is a normalization factor that accounts for the spectrometer solid angle and the conversion of beam monitor counts to number of pions. The reaction usually picked to have a known cross section is $^1H(\pi,\pi)$, for which the known cross section is calculated from a parameterization of the pion-nucleon phase shifts [Ro-78].

This normalization factor is good at a particular energy for a particular beam polarity and outgoing momentum. The variation of normalization factor with outgoing momentum (it depends on the relative momentum, δ_C, not on the absolute momentum, p_C) is measured in an acceptance scan. In this procedure, the spectrometer fields are adjusted to look at the same peak at various values of δ_C. The relative yield for each δ_C gives the relative acceptance of the spectrometer at those momenta. Since the overall scale of the acceptance includes a factor that compensates for the number of pions of a given energy produced per amount of primary H^+ beam, the scale of the acceptance varies with pion beam polarity and energy. Figure III-5 shows measured acceptance scans from experiments 780 and 777.

There are two subtle points involving the use of acceptance scans.

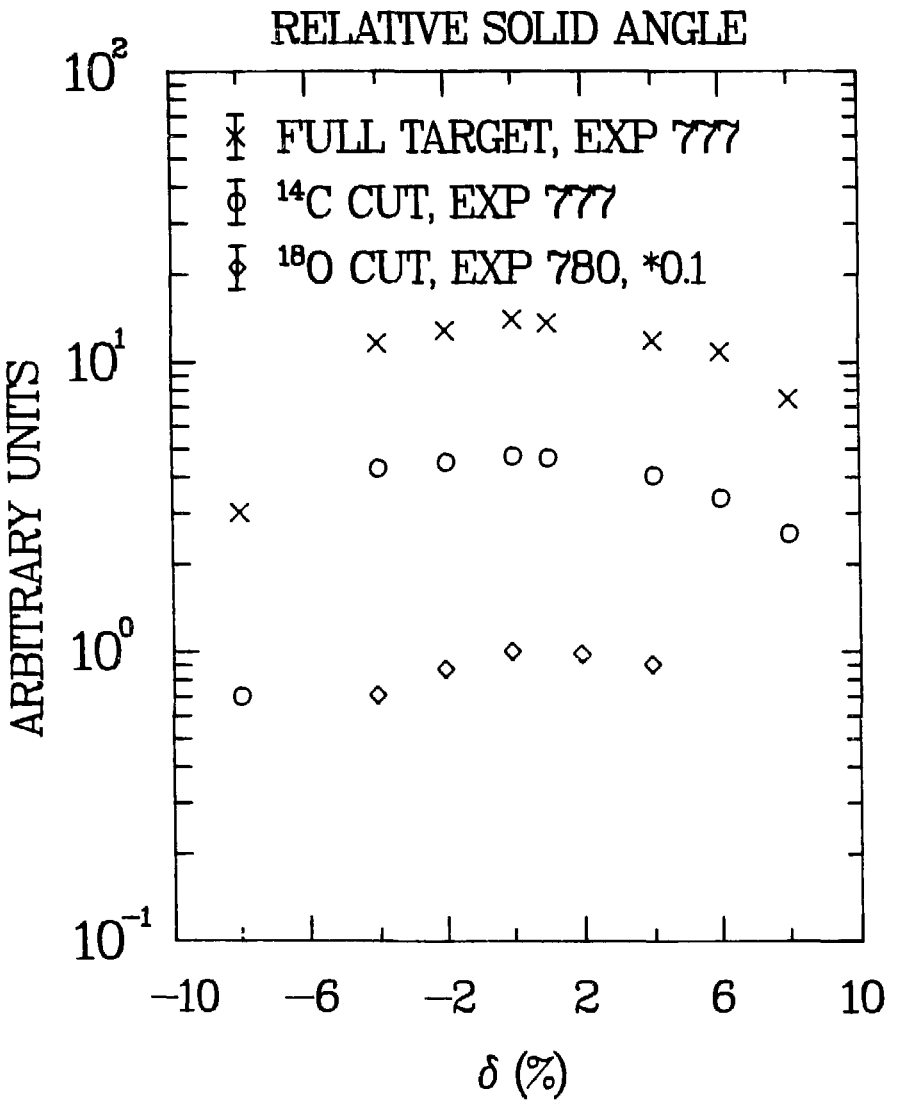

Figure III-5.
Acceptance scans measured during DCX runs.

If the π^- and π^+ beam profiles at the target are identical, than the shape of the acceptance scan is identical for both. Since the channel subtends only a small solid angle, and the differences in the pion production spectra are not large over the ±1 % momentum bite of the channel, the beam profiles and the acceptance are certainly identical within the statistical accuracy of DCX measurements. A second point is that the average scattering angle depends on the spectrometer momentum. The acceptance scan for, e.g., experiments 777/826 was done with $^1H(\pi^+,\pi^+)$ at 191.1 MeV beam energy and 40^o scattering angle. As δ_{sp} was varied from -8% to 0% to 8%, the scattering angle changed from 41^o to 40^o to 39^o, and the hydrogen cross sections changed from 26.70 mb/sr to 27.28 mb/sr to 28.05 mb/sr. This decreases the measured acceptance at 8% δ_{sp} from 50% of the maximum value to 49%, and increases the acceptance at -8% δ_{sp} from 19% of the maximum value to ~19.5%. As almost all peaks are measured at about the same δ_{sp}, this correction is typically ignored, and has not been applied to any of the cross sections within this work.

Figure III-6 shows the energy dependence of the normalization factor at δ = 2% for π^+ and π^- beams. The large rise of the normalization factors at lower energy is caused by the much smaller pion flux per unit primary proton beam at lower energies. This behavior is moderated somewhat by the decreasing π - p cross sections.

D. Good Events

The analysis of individual data events requires the determination that a valid event has occurred. It is done by performing various

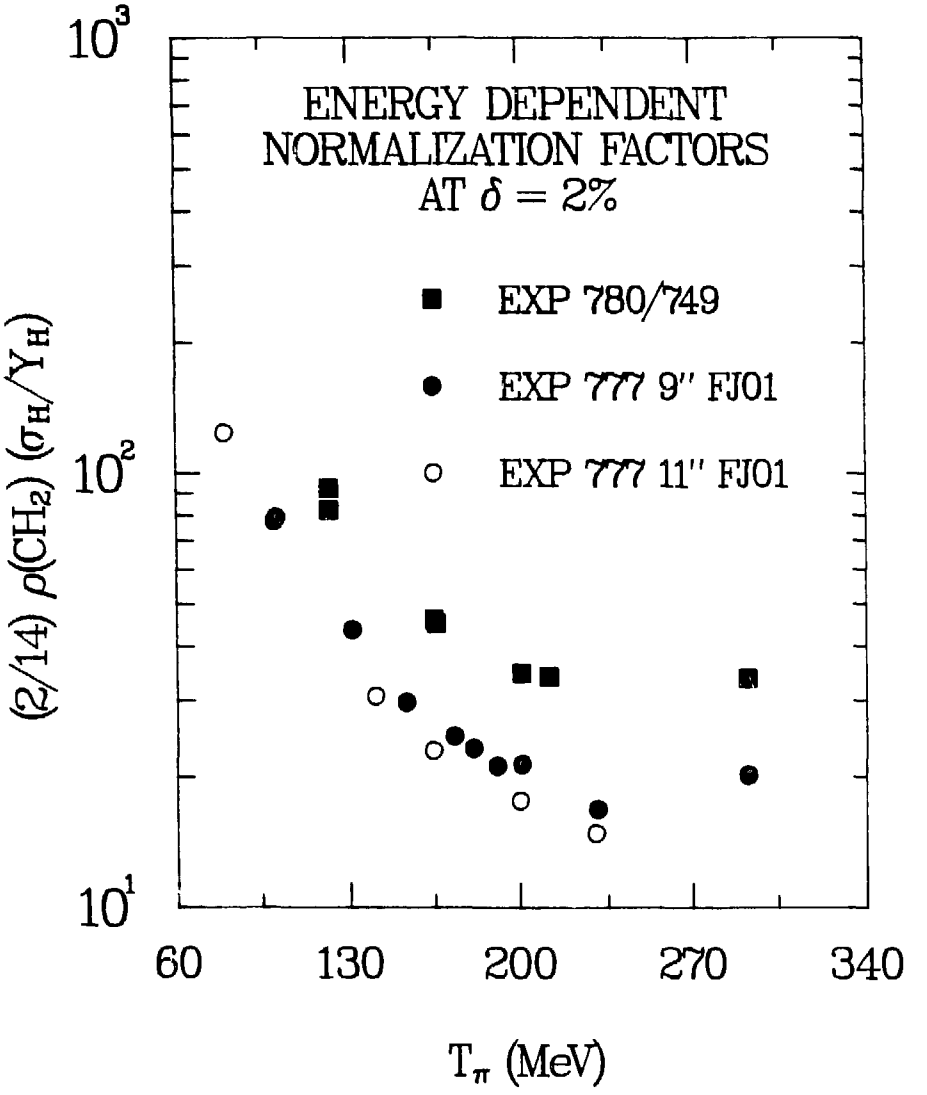

Figure III-6.
The normalization factor $(2/14)\rho(CH_2)(\sigma_H/Y_H)$ as a function of beam energy.

```
******* T E S T   R E S U L T S ******      9-SEP-84     16:43:13
VALUES FROM REPLAY OF RUN    148
[MP10REP.EXP777]EXP777.TST 25-AUG-84  CYCLE 41 L-R SETUP
;
;TE:150/SL:3/IG:10/IB:10
;
   190000 = BLOCK.1
;
;MUON REJ TESTS
;
   140917 = 1,B1,2,0,                  ;1      ;SA MUON
;
; LEFT RIGHT TESTS
;
   184616 = 2,B1,2,6,                  ;2      ;C1YL=R
   102837 = 3,B1,2,7,                  ;3      ;C1XL=R
   184184 = 4,B1,2,8,                  ;4      ;C2XL=R
    93110 = 5,B1,2,9,                  ;5      ;C2YL=R
   184479 = 6,B1,2,10,                 ;6      ;C1YL=L
    97017 = 7,B1,2,11,                 ;7      ;C1YL-L
   185457 = 8,B1,2,12,                 ;8      ;C2YL=L
    92195 = 9,B1,2,13,                 ;9      ;C2YL-L
;
;FAST CLEAR
;
       0 = 10,CAT,3,2,32001,           ;10     ;FAST CLEAR (1/10)
;
;PID
;
   184765 = 11,IBOX,1,                 ;11     ;BOX 1 ==> PID
;
;DRIFT L-R TESTS
;
   102705 = 12,AND,2,3,                ;12     ;LXI1
    93051 = 13,AND,4,5,                ;13     ;LXI2
    96921 = 14,AND,6,7,                ;14     ;LXY1
    92108 = 15,AND,8,9,                ;15     ;LXY2
   190000 = 16,IOR,1,-1,               ;16     ;LOOP1 COUNTER
;
;
   190000 = BLOCK.2,
;
; CHAMBER DRIFT TIME TESTS
;
   186091 = 17,CAT,131,-2,42,          ;17     ;DRFTHI1        ;CHAMBER LOOP 2
   185163 = 18,CAT,122,-2,42,          ;18     ;DRFTHI2
   186349 = 21,CAT,125,-2,42,          ;21     ;DRFTHI5
   188362 = 22,CAT,126,-2,42,          ;22     ;DRFTHI6
   188391 = 23,CAT,129,-2,42,          ;23     ;DRFTHI9
   184080 = 24,CAT,130,-2,42,          ;24     ;DRFTHI10
   187027 = 25,CAT,181,-2,42,          ;25     ;DRFTHY1
   186162 = 26,CAT,182,-2,42,          ;26     ;DRFTHY2
   183670 = 29,CAT,185,-2,42,          ;29     ;DRFTHY5
   183950 = 30,CAT,186,-2,42,          ;30     ;DRFTHY6
   181827 = 31,CAT,189,-2,42,          ;31     ;DRFTHY9
   181904 = 32,CAT,190,-2,42,          ;32     ;DRFTHY10
;
;DRIFT DIFFERENCES
;
   180996 = 33,CAT,222,-1500,1500,             ;33     ;TRFRONT RESONABLE
   179870 = 34,CAT,224,-800,800,               ;34     ;PRIFRONT RESONABLE
   161173 = 35,CAT,274,-9,16,          ;35     ; REAR DRF DIF PLANE X
   184640 = 36,CAT,275,-9,16,          ;36     ; REAR DRF DIF PLANE Y
   171811 = 37,AND,11,33,34,           ;37     ;FRONT ANGLES OK AND PID
   149026 = 38,AND,11,35,36,           ;38     ;REAR DRIFT DIFF OK AND PID
   139948 = 39,AND,37,38,                      ;39     ; DRIFT DIFF ALL OK(FRONT AND REAR)
;
; CHAMBER EFF TESTS
;
   180917 = 40,AND,11,25,26,           ;40     ;FRONT Y CHAMBERS OK*PID(ONLY C1 AND C2)
   179669 = 41,AND,11,17,18,           ;41     ;FRONT X CHAMBERS OK*PID(ONLY C1 AND C2)
   175925 = 42,AND,11,29,30,31,32,     ;42     ;REAR Y CHAMBERS OK*PID
   178799 = 43,AND,11,21,22,23,24,     ;43     ;REAR X CHAMBERS OK*PID
   176944 = 44,AND,40,41,              ;44     ;FRONT OK
   172131 = 45,AND,42,43,              ;45     ;REAR  OK
   161342 = 46,AND,44,45,              ;46     ;ALL OK*PID ==> CTOGRS
;
;TARGET TESTS
;
   175098 = 85,CAT,233,-999,1001,      ;85     ;ETCT   ;BACKGROUND REJECTION LOOP 1
   178571 = 86,CAT,234,-1499,1301,     ;86     ;TWTTCT
   174003 = 87,CAT,235,-800,800,       ;87     ;TTCT
   181211 = 88,CAT,236,-799,801,       ;88     ;PRITCT
   129765 = 89,CAT,237,-99,101,  ;89   ;TWTCHK
   127278 = 70,CAT,238,-99,101,  ;70   ;PRICHK
    92261 = 71,CAT,239,-273,227,       ;71     ;HARDWIRE INNER SELENIUM CELL LIMITS
   149611 = 72,CAT,240,-913,927,       ;72     ;HARDWIRE OUTER SELENIUM CELL LI
;
;GATES AND BOXES (DO WITH THESE AS YOU WISH
;
       0 = 75,IBOX,2,                  ;75     ;BOX 2
       0 = 76,IBOX,3,                  ;76     ;BOX 3
       0 = 77,IBOX,4,                  ;77     ;BOX 4
       0 = 78,IBOX,5,                  ;78     ;BOX 5
       0 = 79,IBOX,6,                  ;79     ;BOX 6
       0 = 80,IGAT,6,                  ;80     ;GATE 6
   17521 = 81,IGAT 1,                  ;81     ;PIONS BY CHERENKOV (ZERO PULSE HEIGHT)
    1194 = 82,IGAT,2,                  ;82     ;PION CUTF
  171458 = 83,IGAT,1,                  ;83     ;ELECTRON CTOF
       0 = 84,IGAT,4,                  ;84     ;180 CU BAR CUT OR SE CENTER CEL L CUT
       0 = 85,IGAT,5,                  ;85     ;OUTSIDE SE LIMITS TO CUT OUT FLUGS
  139696 = 90,AND,39,48,89,84,87,88,   ;90     ;TARGET TEST*GOOD CTOGRS ==> (TGT)
;
;VARIOUS GOOD EVENT TESTS
;
    92477 = 91,AND,39,46,69,70,         ;91     ;TWTCHK AND PRICHK*GOOD CTOGRS>=>(ANC CHK)
  134102 = 92,AND,39,46,                ;92     ;DRF*CHKSUN ==> (GOOD CHKRS)
   90891 = 93,AND,90,91,                ;93     ;TGT*ANC CHK ==> (GOOD EVENT)
;
; EXPERIMENT SPECIFIC GOOD EVENT TESTS
    87005 = 95,AND,93,-81,              ;95     ;ELECTRON ST CHRK GOOD EVENT
     1896 = 96,AND,93,81,               ;96     ;PION ST CHRK GOOD EVENT
          95 *MUON REJECT AT 184MEV....
   90891 = 100,AND,93,          ;100    ;GOOD EVENT  ==>(PION EVENT)
   92477 = 101,AND,91,          ;101    ;ANGLE CHECKS AND
  129696 = 102,AND,90,          ;102    ;TARGET CHECKS AND
  134102 = 103,AND,92,          ;103    ;GOOD CTOGRS,
       41 = 104,AND,100,81,82,-1,       ;104    ;GOOD PION EVENT W/ PION CTOF AND CHER,MUON REJ
   85886 = 105,AND,100,-81,83,  ;105    ;GOOD ELEC EVENT W/ ELEC CTOF AND CHER
   89541 = 106,AND,93,1,                ;106    ;GOOD EVENT WITH 85<=>MUONS
      17 = 107,AND,104,71,              ;107    ;INNER SE CELL GOOD PION
      23 = 108,AND,104,72,-71,  ;108    ;OUTER SE CELL GOOD PION
;
;DRIFT TIME WITH PID FOR DICK
  142101 = ,17,AND,17,11                ;117    ;DRFTHI1 AND PID
  141279 = 118,AND,18,11                ;118    ;DRFTHI2 AND PID
  142067 = 121,AND,21,11                ;121    ;DRFTHI5 AND PID
  143175 = 122,AND,22,11                ;122    ;DRFTHI6 AND PID
  141863 = 123,AND,23,11                ;123    ;DRFTHI9 AND PID
  141591 = 124,AND,24,11                ;124    ;DRFTHI10 AND PID
  142976 = 125,AND,25,11                ;125    ;DRFTHY1 AND PID
  142267 = 126,AND,26,11                ;126    ;DRFTHY2 AND PID
  141407 = 129,AND,29,11                ;129    ;DRFTHY5 AND PID
  141669 = 130,AND,30,11                ;130    ;DRFTHY6 AND PID
  141177 = 131,AND,31,11                ;131    ;DRFTHY9 AND PID
  141419 = 132,AND,32,11                ;132    ;DRFTHY10 AND PID
;
   190000 = 150,IOR,1,-1,               ;150    ;LOOP A COUNTER (WHOOPER WERE ON HE
;
;******************** GATE PARAMETERS ********************
;
;GATE   1
;              0 < OR = IDAT(256) <    40
;GATE   2
;           3340 < OR = IDAT(266) <  3740
;GATE   3
;           2600 < OR = IDAT(266) <  9000
;GATE   4
;              0 < OR = IDAT(  0) <     0
;GATE   5
;              0 < OR = IDAT(  0) <     0
;GATE   6
;              0 < OR = IDAT(  0) <     0
;
;******************** BOX PARAMETERS ********************
;
;BOX   1
;             42 < OR = IDATX(253) <   185
;            438 < OR = IDATY(260) <  2178
;BOX   2
;              0 < OR = IDATX(  0) <     0
;              0 < OR = IDATY(  0) <     0
;BOX   3
;              0 < OR = IDATX(  0) <     0
;              0 < OR = IDATY(  0) <     0
;BOX   4
;              0 < OR = IDATX(  0) <     0
;              0 < OR = IDATY(  0) <     0
;BOX   5
;              0 < OR = IDATX(  0) <     0
;              0 < OR = IDATY(  0) <     0
;BOX   6
;              0 < OR = IDATX(  0) <     0
;              0 < OR = IDATY(  0) <     0
```

Figure III-7.
A sample TPR output from a replay of run 148 of experiment 777.

tests on many of the raw and derived data words. A sample test file output from the Q program TPR is shown in Figure III-7. The output lists the tests and the number of events which have passed each test.

The test file exhibits several different tests which may be divided into two types, the tests on individual data words (often called microtests), and the tests that are logical combinations of other tests (often called macrotests). The most common microtest in the file is the gate test, written as:

GAT,iwrd,ilow,ihi,

where iwrd is the number of the data word being tested, and ilow and ihi are the limits between which the value of the data word must be for the test to be passed (or true). The other direct microtest is the bit test,

BI,iwrd,ibit,

where the test is passed if bit ibit equals 1 in data word iwrd. There are two indirect microtests,

IGAT,ngat, and

IBOX,nbox,

where ngat (nbox) is the number of the indirect gate (box) test. Indirect gates perform essentially the same function as gates, but with greater flexibility. They are set on a histogrammed parameter, and may either have their limits changed, or be set to some limits on a different parameter. Thus, they are often used for tests that will vary during the experiment, e.g., the gates on the time-of-flight test vary with energy, but can be conveniently reset after an energy change

with an IGAT test. IBOX is similar to IGAT, except that it is set simultaneously on two parameters, usually with the use of a dotplot.

The most common macrotest is the logical AND test,

AND,itst1,itst2,itst3...,

where itst1, itst2, etc. are the numbers of the tests being ANDed. In the present example, there are from one to six arguments of the AND test, all of which need to be true for the test to be true. The only other test used is the IOR test,

IOR,1,-1,

which is always true since it is always an or of a true and false result. Since cumulative test results are compiled, this test is used to count the number of times the tests are executed.

The test file is divided into two blocks. Block one includes only tests on raw data words, and is executed before any derived quantities are calculated. The most important test in this block is the PID test, which is used to identify pion events (which usually includes electron and muon events), and separate out most proton events and some events with unreasonable times or pulse heights (depending on what quantities are being tested). The test file is divided into two blocks so that, if the PID test is not true, the calculation of derived quantities and the execution of the remainder of the tests can be skipped, saving much CPU time.

There are several tests that must be passed for an event to be a good event. First, an event must produce signals in certain detectors. A computer trigger requires signals in some of the front chamber planes and scintillators S2 and S3. The group of tests from number 17 through

46 ensure that all planes in the front and rear chambers have reasonable times, and that the time differences between planes are reasonable. Cherenkov and muon rejector signals are not necessary for good events; they are used to distinguish pion events from muon or electron events. Similarly, an S1 signal is not required (unless it is put into the hardware trigger), but is used to identify pions by time-of-flight.

All good events must also pass the target tests, numbers 65 through 68. These tests check that the positions and angles that are projected back to the target have reasonable values, i.e., the x and y positions are consistent with the pion beam spot size, and the scattering angles with respect to x and y are consistent with the spectrometer acceptance.

Finally, all good events must also pass the angle check tests. These tests compare measured angles at the rear chambers with calculations from front measured quantities (in the lowest order optics, the magnitudes of measured front and rear chamber angles are the same). The primary purpose of these checks is to eliminate decays of pions in flight between the front and rear chambers. The fraction of pions that do not decay is given by:

$$SF = \exp(-dm_\pi/ctp_\pi),$$

where d is the path length between front and rear chambers (~9 meters), m_π is the pion mass, c is the speed of light, t is the pion lifetime (2.6×10^{-8} sec), and p_π is the pion momentum. For 160 MeV,

p_π = 265 MeV/c pions, the survival fraction is 0.55. As the resolution of the angle checks is about 8 mr (~0.5°), but the muon decay cone is ±8° wide, the angle checks eliminate a large fraction of the pion decays in flight.

Good events may be either pion, muon or electron events. Cherenkov, S1 time-of-flight, and muon rejection tests are used to select out the good pion events. Histograms of counts versus missing mass for good pion events are used to extract numbers of counts to residual states of interest.

E. Background

There are two primary sources of background in the DCX measurements. Individual detectors have a relatively high (compared to the low DCX rates) rate of accidental signals, caused primarily by the high radiation background in the EPICS area. These events are all rejected by good event tests. Real background events consist of a large number of electrons and a small number of muons. Both sources of background increase at lower energies. The muon increase results from a larger number of pion decays in flight. The electron increase results from the greater electron contamination of the beam. The muon background increases slightly with angle, because of the decrease in momentum of scattered particles, but the electron background is sharply peaked near 0° because of kinematics.

Although, for instance, the positive beam is ~90% protons, this cannot lead to background as protons can neither DCX nor give sufficient energy and momentum to a lighter particle for it to be

transported through the spectrometer without the proton decaying, which is an exceedingly small source of background (possibly one decay per 10^{23} DCX experiments).

The ratio of muons to pions detected is entirely consistent with the ratio observed in elastic scattering. The ratio is as large as 0.25 at 100 MeV, and decreases with energy. These muons arise from the decay of scattered DCX pions in flight through the spectrometer.

The DCX electron background can arise from several mechanisms. Since the electrons have the same momentum and more kinetic energy than incident pions, a pion-induced DCX electron event must include a pion decay. The largest cross section for this sort of event would be for a, e.g., (π^+,π^0) reaction (1000 times the DCX cross section) followed by the π^0 decay into an e^+e^- pair (1% branching ratio). This should produce about 10 times as many electrons as DCX pions, but, as the SCX cross sections increase with energy up to the Δ resonance region, this process has the wrong energy dependence to account for an electron background that increases significantly at lower energies.

DCX electrons can arise from several types of electron induced events. We will consider both 180^0 scattering of incident positrons and pair production by electrons passing through the target. Electron induced events should have the correct energy dependence. The electron contamination of the beam increases, as beam energy is decreased, to about 33% (10%) for a negative (positive) polarity beam at the lowest EPICS energies (~100 MeV), An experimental test can be made of these two mechanisms. If 180^0 electron scattering were responsible for most of the DCX electrons, we should measure no background in the (π^-,π^+)

reaction, as there are no positrons in the target. Conversely, if pair production is responsible for most of the background electrons, we should measure about equal backgrounds for both beam polarities.

The backgrounds for both polarity beams were measured with a 195 MeV/c (100 MeV π) beam on a ^{nat}Ni target. Since the positron contamination is a smaller percentage of the beam, but the positive beam is more intense, there are about equal numbers of electrons and positrons produced by each proton beam pulse. It was found that the background per incident positron was three times as large as the background per incident electron. This would indicate that, if there are no other important processes, electron knockout is responsible for about twice as much background as pair production.

F. Cross Sections

Cross sections at EPICS are calculated from a ratio to hydrogen cross section,

$$\frac{\sigma_{DCX}}{\sigma_H} = \frac{Y_{DCX} \times A_{targ} / \rho_{targ}}{Y_H / \rho_H},$$

where A is a mass number, ρ is an areal density, and Y is a yield (defined below). This ratio is more typically expressed in the form

$$\sigma_{DCX} = Y_{DCX} \times \frac{A}{\rho_{DCX}} \times \left(\frac{2}{14} \rho_{CH_2} \frac{\sigma_H}{Y_H}\right),$$

since the normalization runs are done with pion scattering from

hydrogen in CH_2 targets. The yield, Y, is the number of counts in the state of interest multiplied by a normalization factor. The normalization factors are defined by:

$$\text{norm} = \frac{\text{abs}(\cos\theta_{tgt}) \times \text{detection efficiency}}{\text{SF} \times d\Omega \times \text{beam monitor counts}},$$

and are calculated by an MP - 10 program, SHT. A sample SHT output is shown in Figure III-8. It should be noted that the survival fraction, SF, and the solid angle, $d\Omega$, are both momentum dependent. The solid angle is determined by the acceptance scan. Its absolute magnitude is unimportant, as long as the same set of solid angles is used as input for both data and normalization runs. The beam monitors used were both BOT (for which norm is called norm3) and 1ACM02 (norm2).

The DCX cross sections measured in this work varied from about 10 nb/sr to 5 μb/sr. The area of residual state peaks varied from zero (upper limits measured) to ~150 counts. For most measurements, there was essentially no nonpion background because of the background rejection tests. Pion background was also small because of either the use of isotopically enriched targets, or of targets with contaminants that have more negative Q values. Some cases with pion background are described in the publications in Appendix B.

Thus, the extraction of peak areas in most cases required only area gates with no background subtraction. In some cases, in particular the extraction of excited, DIAS cross sections, background subtraction is required. Since excited DIAS states are typically found

```
16:45:06      9-SEP-84     56FE(PI+,PI-)56NI

ALLTSTS,SCALERS,KINEMATICS FROM CORE

INPUT PARAMETERS FROM ENTEPR.DAT

RUN=  148

SPECTROMETER ANGLE=   5.00 DEG

  0.149832+ 55.920670=  0.149832+ 55.926765 EA= 1., EO= 1.
QGND=  -5.679 <-    0.014 MEV     EX=    0.000 MEV
T1= 122.480 MEV  P1= 221.788 MEV/C
P3= 210.029 MEV/C
PARTICLE DELTA MOMENTUM=  2.48 %

CHAN FIELD =  9625.6 GAUSS
SPEC FIELD =  5252.9 GAUSS

TARGET ANGLE=  -15.0 DEG
UNROT INC LOSS=  2.000 MEV, ROT LOSS=  2.071 MEV
       EX        2.000 MEV,            2.128 MEV
```

```
16:45:06      9-SEP-84     56FE(PI+,PI-)56NI

ALLTSTS,SCALER,KINEMATICS FROM CORE

RUN=  148

********** COMPUTED VALUES **********     EV NOT BUSY=   190000.

COMPUTER LT=        0.9090     EVENTS NOT BUSY/EVENTS
                               SLR( 50)/SLR( 49)
LOOP/EVENTS=        1.0000     TST LF 1/(EV NOT BUSY-FAST CLR)
                               TST( 16)/(SLR( 50)-SLR(  6))
CHAMBER EFF=        0.8976     F EFF= 0.9606
                                0.96 1.00 1.00 1.00 1.00 1.00 1.00 1.00
                               F TSTS= 46/ 45* 45/ 45* 45/ 45* 45/ 45* 45/ 45* 45
/ 45* 45/ 45* 45/ 45
                               R EFF= 0.9344
                                0.93 1.00 1.00 1.00 1.00 1.00 1.00 1.00
                               R TSTS= 46/ 44* 44/ 44* 44/ 44* 44/ 44* 44/ 44* 44
/ 44* 44/ 44* 44/ 44
DRIFT EFF  =        0.8111     0.81 1.00
                               T TSTS= 92/ 46* 46/ 46
CORR FAC   =        1.5112     1/(COMPLT*CHMBREFF*LOOP/EVENT  *DRIFT EFF)
```

```
16:45:06      9-SEP-84     56FE(PI+,PI-)56NI

ALLTSTS,SCALERS,KINEMATICS FROM CORE

RUN=  148
ACCEPTANCE SCAN FILE NOT GIVEN

EXCITATION OF STATE=   0.000 MEV      QVALUE =  -5.679 MEV

CF=(ABS(COS(TGT))*CORR FAC/(SF*DOMEGA)
NORM1=CF/(IC1     * 1.000     )      NORM2=CF/(1ACM02  * 1.000     )      NORM3=CF
/(BOT     * 1.000     )
YIELD=AREA*NORM
RATIO=HYDROGEN SIGMA(C.M.)/(YIELD(H)*JAC)
TGT THINGS=(NUM NUCLEONS)*(2/1A)*(CH2 TGTX)/(TGT TGTX)
SIGMA(C.M.)=YEILD*JAC*TGT THINGS*RATIO

        ++++++++++++++++++ TARGET ++++++++++++++++++
   THLAB     THCM      DELTA          NORM1       DOMEGA    AREA+-ERR        YIELD+-E
RR
 BINCNTR BINSIZE       JAC           NORM2
    HIST   ACCEP        SF           NORM3
-------------------------------------------------------------------------------
-------------------------------------------------------------------------------
    5.00     5.03     2.477     -0.9589E-01   -1.00
    0.00     0.00     0.9901    -0.1139E-07
       M             0.3540    -0.1121E-04
```

Figure III-8.
A sample SHT output.

in regions of excitation energy with a large level density, but are preferentially excited, the background was determined by the level of counts at excitation energies just above and below that of the DIAS.

Another type of problem occurs for measurements in which, because of the low count rates, there are no well-defined peaks. In these measurements, the expected peak position was determined by elastic scattering from the DCX target with the spectrometer magnets set identically to the data run, and the channel energy adjusted so that the elastic peak has the same δ_C. The area over which to sum counts was constrained by the width of the elastic peak shape. A complete list of the measured cross sections is given in Appendix C.

CHAPTER IV. RESULTS

The current DCX data set can be divided into three types of transitions, DIAT, nonanalog I transitions ($\Delta T = 2$, $J_i^\pi = J_f^\pi = 0^+$, gs-to-gs), and nonanalog II transitions (other). Each of these is about equally well studied experimentally, but not theoretically. In this chapter, we will summarize the experimental information about each class of transitions, and compare DIAT to lowest-order DCX calculations (see Chapter V) done with the code PIESDEX [Jo-83a]. We will concentrate on three features of the transitions, the energy dependence of forward-angle cross sections, the angular distribution shapes and their variation with energy, and the mass dependence of the reactions.

Since all cross sections are tabulated and referenced in Appendix C, we will not, in general, reference the data presented in this chapter. In the figures, all measurements from the present work will be indicated with circles, whereas measurements from other sources will be indicated with squares. The symbol "x" will be used to indicate an average of independent measurements at the same energy and angle.

A. DIAT

DIAS DCX has been measured on 13 target nuclei. Table IV-1 lists all DIAS measured, Q_{DIAS}, calculated from Coulomb energy difference formulas (below), Q_{GS}, calculated from mass tables by the relativistic kinematics program, KINREL [Oo-76], a predicted excitation energy, which is the difference between these two numbers, and the measured excitation energy. The single IAS Q value is given by [Cr-70]

Table IV-1. DIAS excitation energies.

Transition	Q(DIAS)	Q(GS)	E_x (predicted)	E_x (measured)
^{14}C -> ^{14}O	-3.541	-3.967(.01)	-	0.0
^{18}O -> ^{18}Ne	-5.071	-5.079(.01)	-	0.0
^{26}Mg -> ^{26}Si	-7.826	-8.045(.01)	-	0.0
^{42}Ca -> ^{42}Ti	-12.601	-12.397(.01)	-	0.0
^{44}Ca -> ^{44}Ti	-12.332	-2.896(.00)	9.436	9.0(.2)
^{48}Ca -> ^{48}Ti	-11.841	5.286(.01)	17.127	17.38(.02)
^{48}Ti -> ^{48}Cr	-13.430	-4.648(.02)	8.782	8.75/8.76
^{56}Fe -> ^{56}Ni	-15.534	-5.679(.01)	9.855	9.6(.2)
^{88}Sr -> ^{88}Zr	-20.475	-3.276(.20)	17.199	17.2(.1)
^{90}Zr -> ^{90}Mo	-21.575	-7.576(.01)	13.999	13.9(.1)
^{118}Sn -> ^{118}Te	-25.182	-2.796(.50)	22.386	21.9(.5)
^{208}Pb -> ^{208}Po	-35.610	-3.257(.01)	32.353	32.5(.2)
^{209}Bi -> ^{209}At	-36.032	-4.369(.01)	31.663	31.6(1.0)

$$Q(IAS) = (m_n - m_p) - E_C,$$

where the Coulomb energy difference, E_C, is calculated from

$$E_C = 1.444 \times (Z + 1/2) \times A^{-1/3} - 1.13 \text{ (MeV)},$$

where Z is the target charge. Applying this twice gives

$$Q(DIAS) = 2 \times (m_n - m_p + 1.13) - 2.888 \times (Z + 1) \times A^{-1/3}.$$

Since $Z/A^{1/3}$ increases with mass, DIAS Q values become more negative with mass. There is good agreement between the predicted and measured excitation energies. The average difference between prediction and measurement is 200 keV.

A1. Excitation Functions

The most detailed excitation-function measurements have been made with the reaction $^{18}O(\pi^+,\pi^-)^{18}Ne(gs)$. A $\theta = 5^o$ excitation function is shown in Figure IV-1. The excitation function can be divided into two energy regions, and three characteristic features should be noted. From 180 MeV to the highest measured energy, the data are consistent with a monotonic increase in the cross sections. Near 180 MeV, there is a local minimum in the excitation function. Between 100 and 180 MeV, the cross section again rises, and peaks at about 130 MeV.

The "expected" behavior of DIAS DCX does not exhibit these features. Also shown in the figure are lowest-order PIESDEX calculations with two different densities. One uses Skyrme III [Be-75] proton, neutron, and valence densities, whereas the other uses proton and neutron densities proportional to the charge density (with the finite size of the proton unfolded) measured in electron scattering [Ja-74] and a $(d5/2)^2$ excess density. Both exhibit the same qualitative feature, a monotonic rise in the cross sections from 100 to 300 MeV. The monotonic rise is typical of lowest-order calculations. The magnitude of the excitation function is reasonably well reproduced at the higher energies, but is significantly underpredicted at the lower energies.

Excitation functions on three other T = 1 nuclei are similar (see Figure IV-2). ^{42}Ca exhibits a broad minimum near T_π = 180 MeV, and larger cross sections at both higher and lower energies. ^{26}Mg is similar in shape to ^{18}O, except that the lower energy peak is much less prominent. ^{14}C is the most different of these nuclei. The excitation

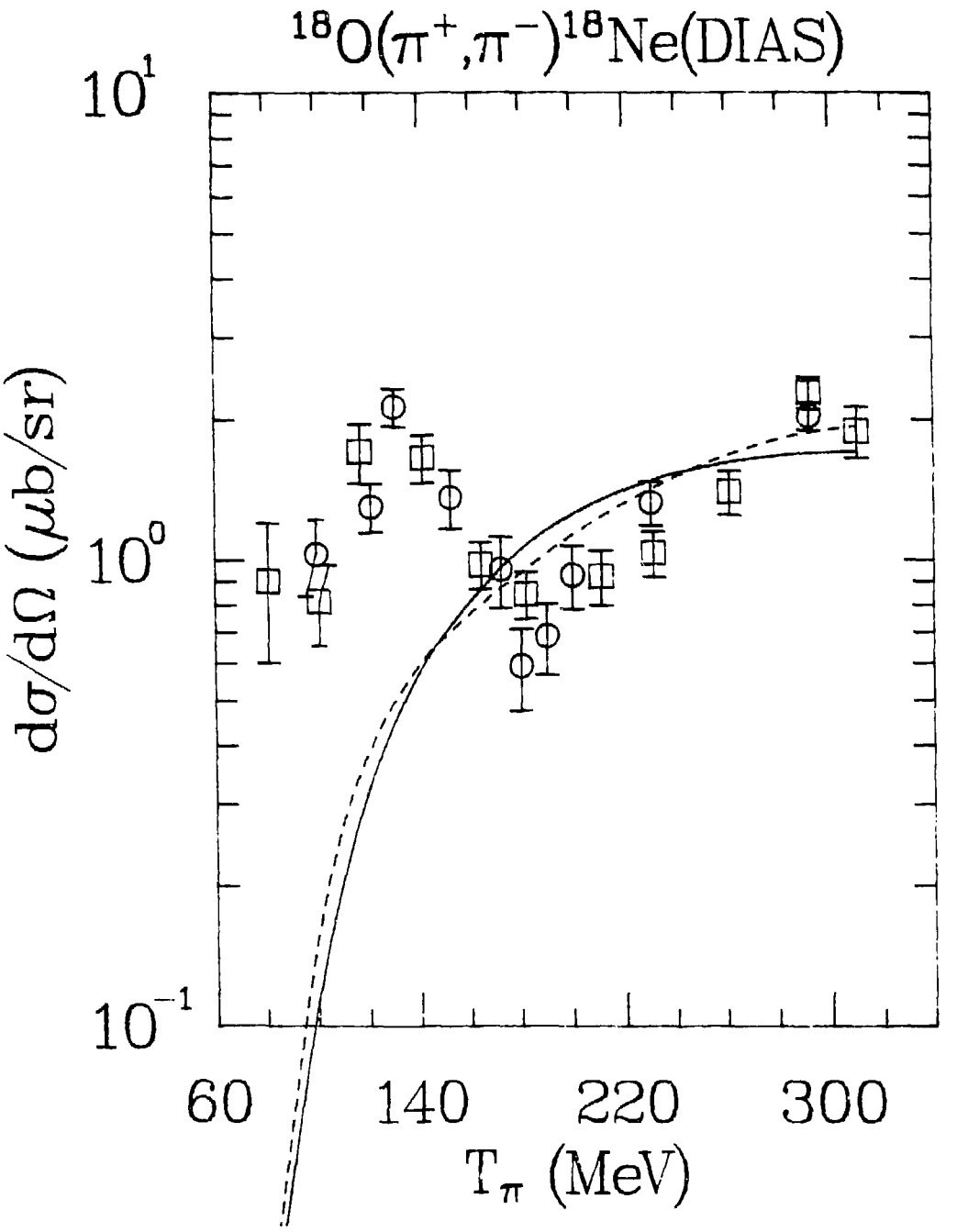

Figure IV-1.
$^{18}O(\pi^+,\pi^-)^{18}Ne(gs)$ excitation function.

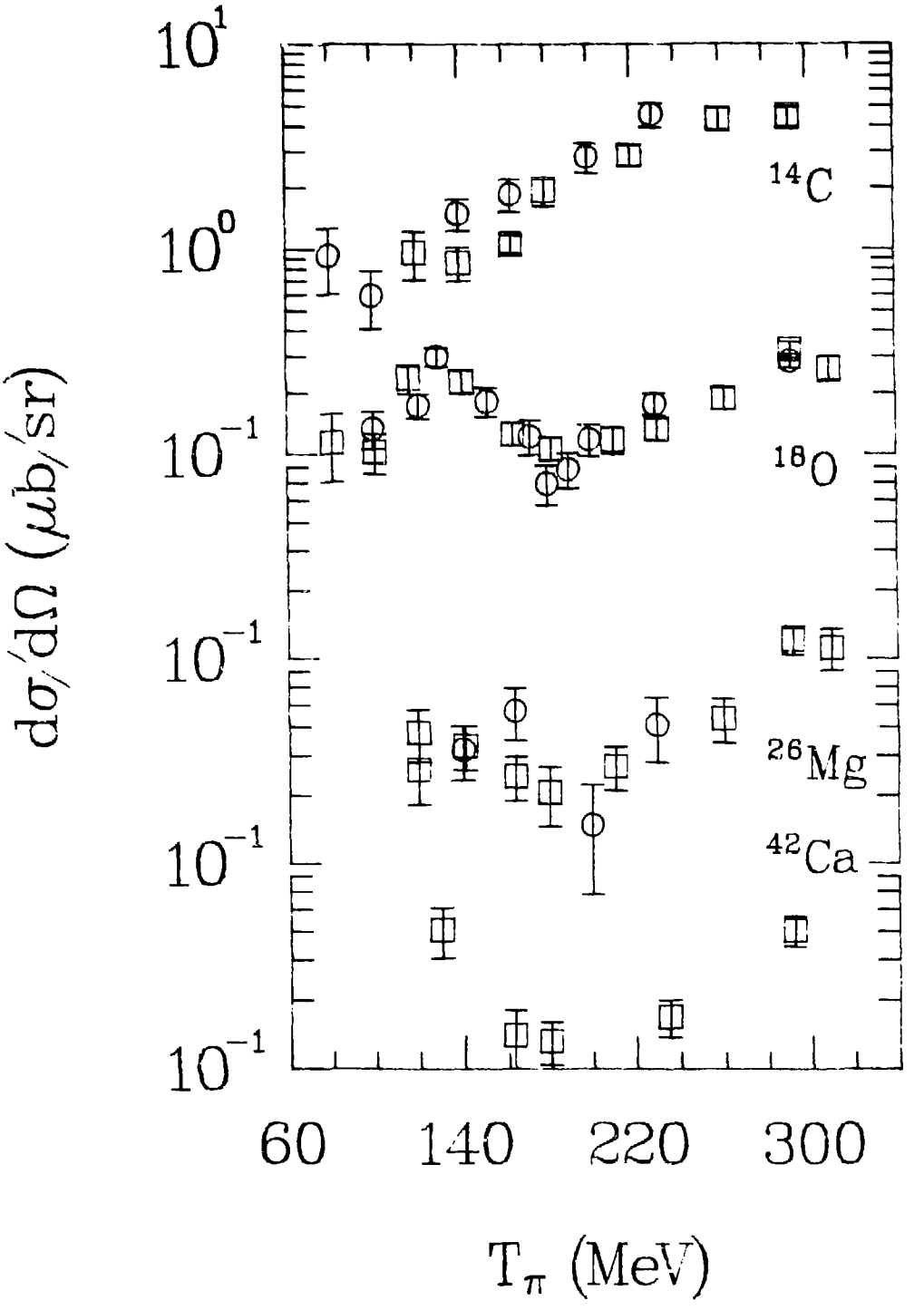

Figure IV-2.
Excitation functions on T = 1 nuclei.

function appears to monotonically increase from a somewhat lower energy, 150 rather than 180 MeV, up through 300 MeV. The cross sections below this energy show no indication of a peak.

Cross sections have been measured on both ^{14}C and ^{18}O at 50 MeV at other facilities. These measurements indicate that both excitation functions increase and become quite large, $d\sigma/d\Omega \sim 4$ or 5 μb/sr at forward angles on these nuclei. These measurements have provoked much interest and speculation, but, as the energy is below the resonance region, they will not be discussed further.

Figure IV-3 displays the four excitation functions measured on $T > 1$ nuclei. The ^{48}Ca and ^{48}Ti excitation functions both are consistent with the ^{18}O excitation function, given the poorer statistics and fewer number of data points. The cross sections at 130 and 180 MeV are about equal. The cross sections at the higher energies are larger and increasing. The ^{90}Zr excitation function is similar both in statistics and behavior. The most studied of the $T > 1$ nuclei is ^{56}Fe. It exhibits a monotonically increasing excitation function above about 160 or 180 MeV. Below this energy, the cross sections are essentially flat, although there is a hint of a peak about 120 MeV.

Thus, all measured DIAS excitation functions exhibit two energy regions. In the region above about 180 MeV, all of the excitation functions increase monotonically with energy. In the region from 100 to 180 MeV, there is a smooth range of behaviors. Cross sections on ^{18}O and ^{42}Ca targets are much larger near 130 MeV than near 180 MeV. On ^{26}Mg, there is a slight, but definite increase near 130 MeV. Data

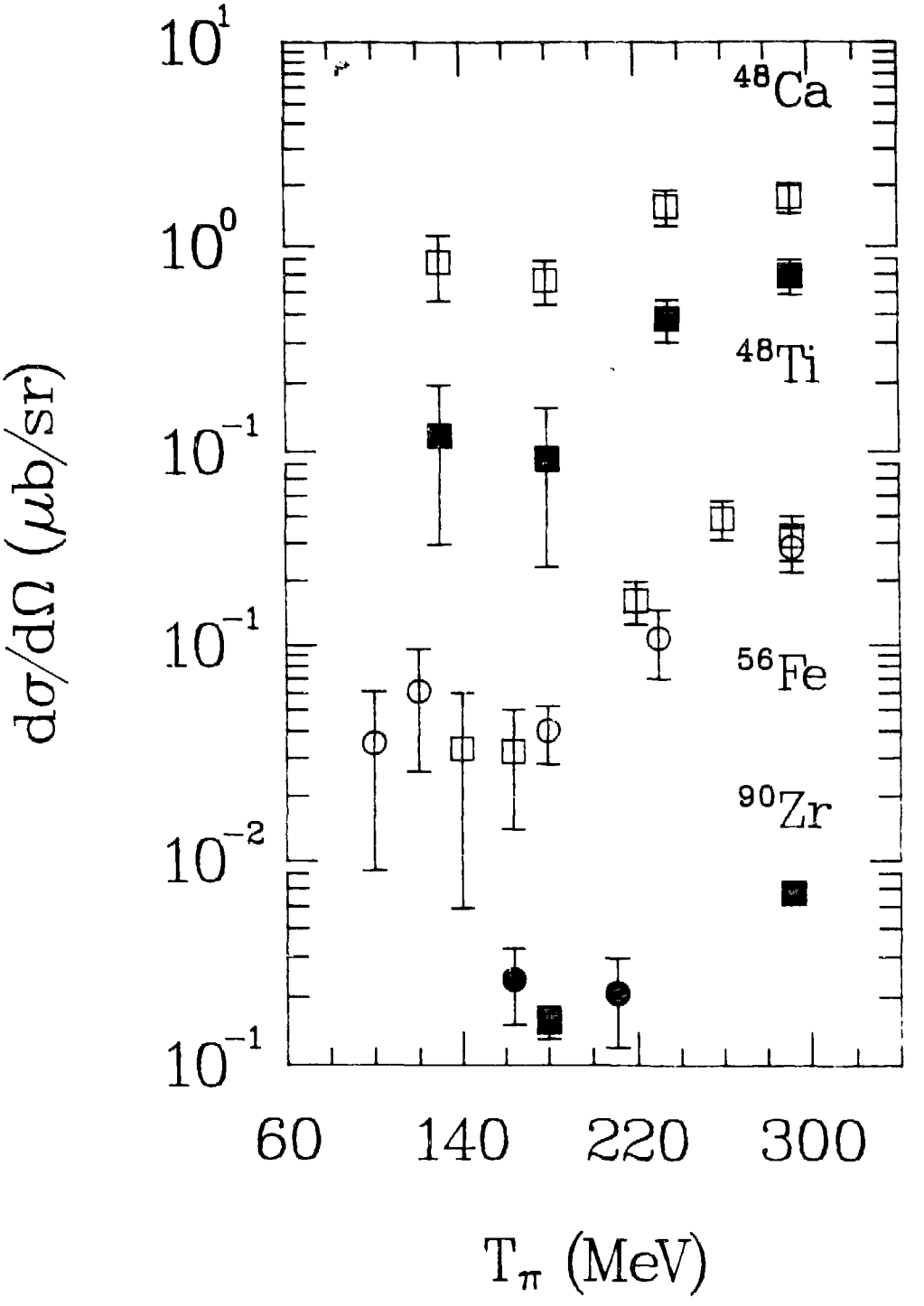

Figure IV-3.
DIAS excitation functions on T > 1 nuclei.

for ^{14}C and ^{56}Fe are consistent with being flat from 180 to 100 MeV. The other nuclei have insufficient statistics and data points to judge.

A2. Angular Distributions

The "classic" problem of DIAS DCX angular distributions has been how to explain the forward minima observed at resonance energies (see Figure IV-4), when the angular distributions are diffractive at higher energies. At 292 MeV, the ^{18}O angular distribution agrees reasonably well with the lowest-order PIESDEX calculations, both in the absolute magnitude of the forward-angle cross sections and in the position of the minimum. At 164 MeV, we see a large difference between the calculated minimum position, ~33°, and the measured position, ~21°.

These results are typical of angular distributions on T = 1 nuclei (see Figure IV-5). On all of these nuclei, 292 MeV angular distributions show forward-angle cross sections and minima that are fairly well predicted by lowest-order calculations. The major disagreement, the underprediction of the larger-angle data, is a common problem at this energy to all calculations.

At 164 MeV, ^{26}Mg exhibits a deep forward minimum, as does ^{18}O, but ^{14}C flattens out at a forward angle, and can best be described as funny-looking.

A major part of the present work consisted of the measurement of angular distributions on ^{18}O, ^{14}C, and ^{26}Mg at additional energies. Because the ^{18}O count rates are much higher than those for ^{14}C or ^{26}Mg, a set of ^{18}O angular distributions was measured across the resonance region. Figure IV-6 shows all eight angular distributions measured on

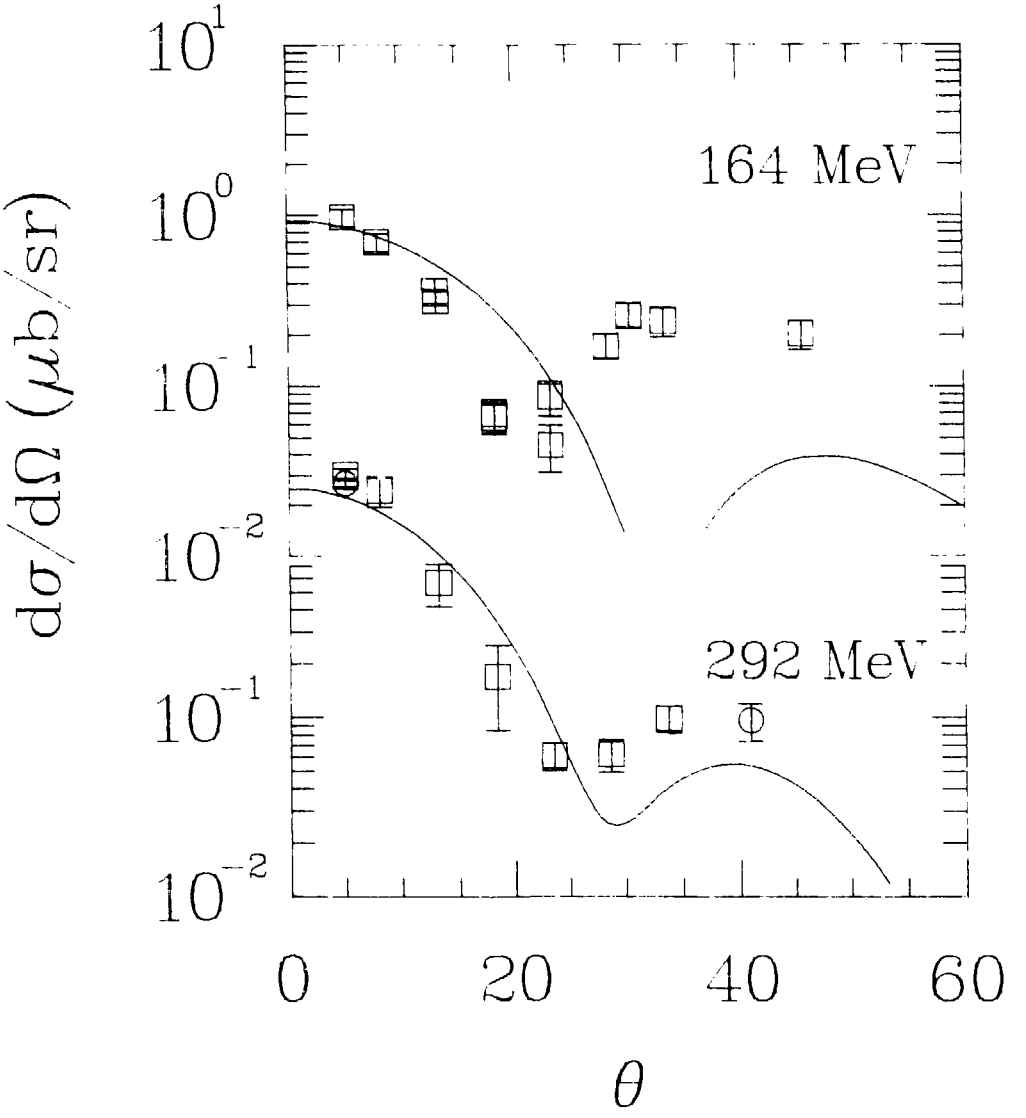

Figure IV-4.
$^{18}O(\pi^+,\pi^-)^{18}Ne(gs)$ angular distributions at 164 and 292 MeV.

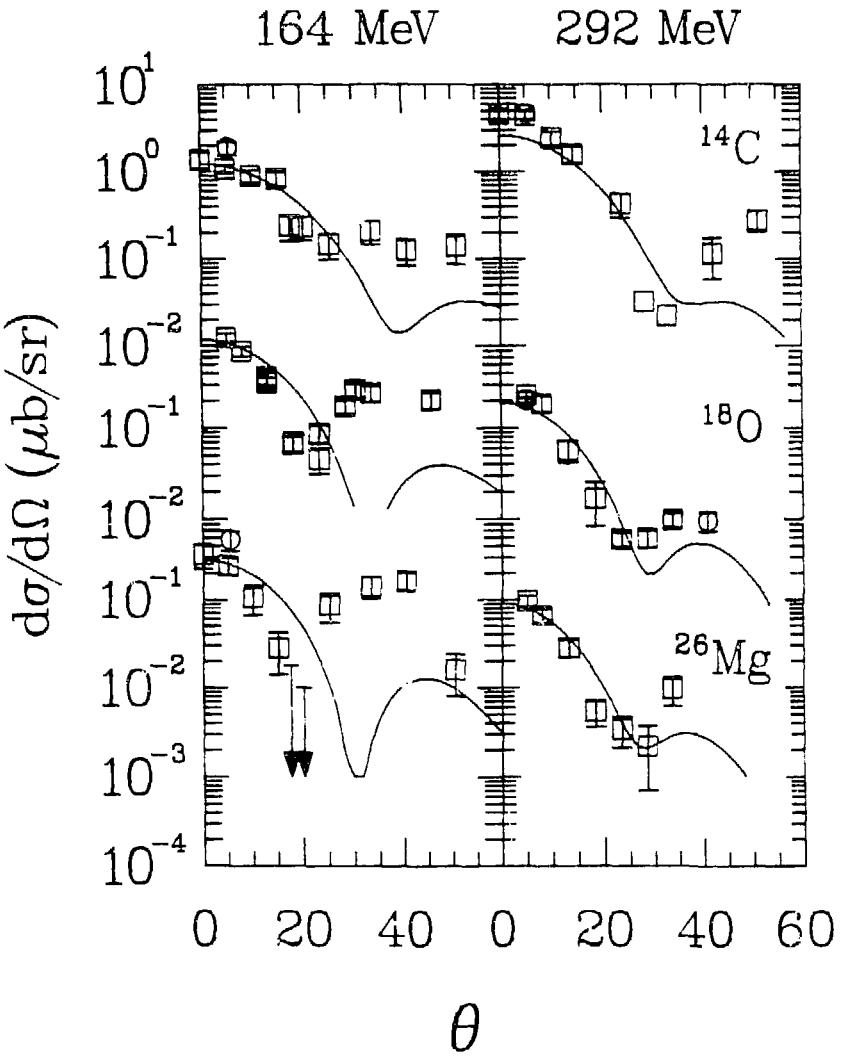

Figure IV-5.
DIAS angular distributions at 164 and 292 MeV.

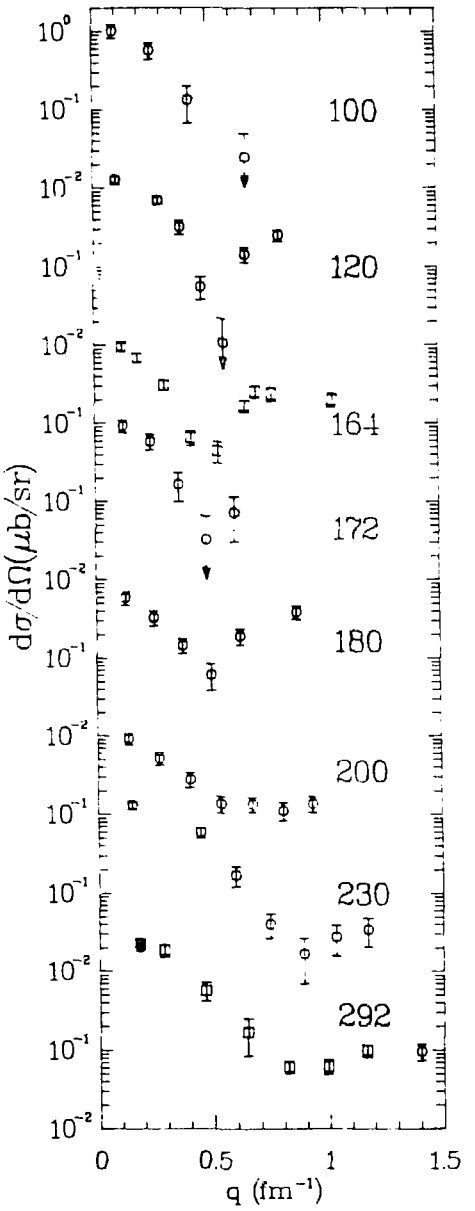

Figure IV-6.
$^{18}O(\pi^+,\pi^-)^{18}Ne(gs)$ angular distributions.

^{18}O plotted versus the momentum transfer, q. At higher energies, about and above 230 MeV, the angular distributions are simply diffractive, with a minimum at about 0.9 fm^{-1}, and large-angle cross sections are about a factor of 20 smaller than the forward angle cross sections. Near 200 MeV is a transition region, at which the larger-angle cross sections have risen to become about one-tenth of the forward angle cross sections, and the angular distribution is flat for momentum transfers greater than about 0.5 fm^{-1}. The shape is reminiscent of that for ^{14}C at 164 MeV. Across and below the resonance region, the angular distributions have deep, well-defined forward minima. At 180 MeV, the large-angle cross sections are equal to the forward-angle cross sections. By 120 MeV, the minimum has started to move to larger momentum transfer. The 100 MeV data are inadequate to make definite conclusions.

The angular distributions are compared to lowest-order calculations in Figure IV-7. The predictions are good at the higher energies, but uniformly poor near resonance.

Two angular distributions were measured on both ^{14}C and ^{26}Mg (see Figure IV-8 and IV-9). On ^{14}C at 200 MeV, it appears as if the minimum in the angular distribution has moved inward slightly from its position at 292 MeV. The shape is, however, much closer to diffractive than to the transition shape exhibited by ^{18}O at this energy. At 140 MeV, the angular distribution has a definite, forward minimum (note the upper limit at $q \sim 0.5$ fm^{-1}).

The ^{26}Mg angular distributions have poor statistics. This resulted from the use of a $^{14}C/^{26}Mg$ strip target, and from the decision

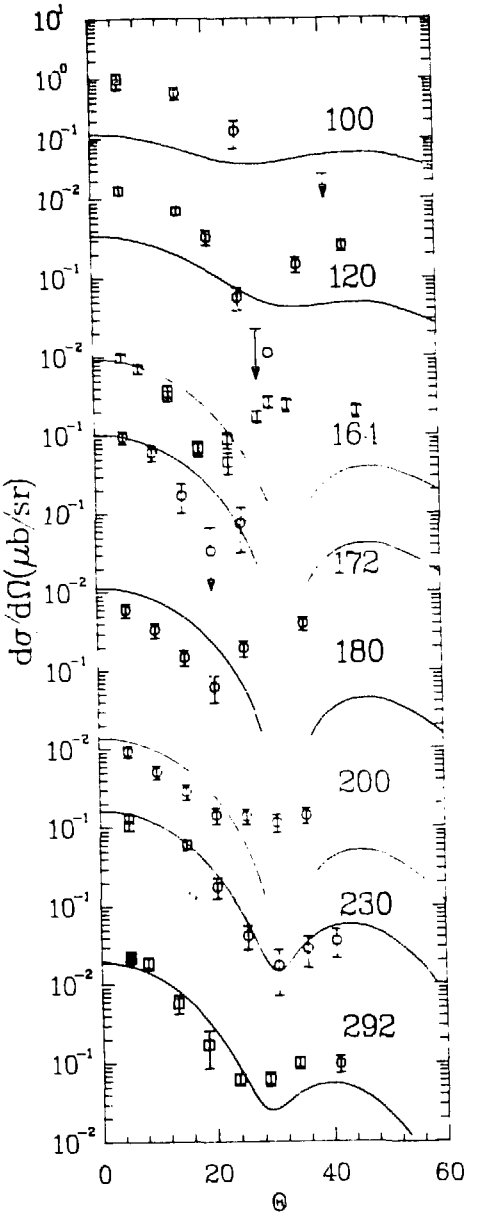

Figure IV-7.
$^{18}O(\pi^+,\pi^-)^{18}Ne(gs)$ angular distributions contrasted with lowest-order optical-model calculations.

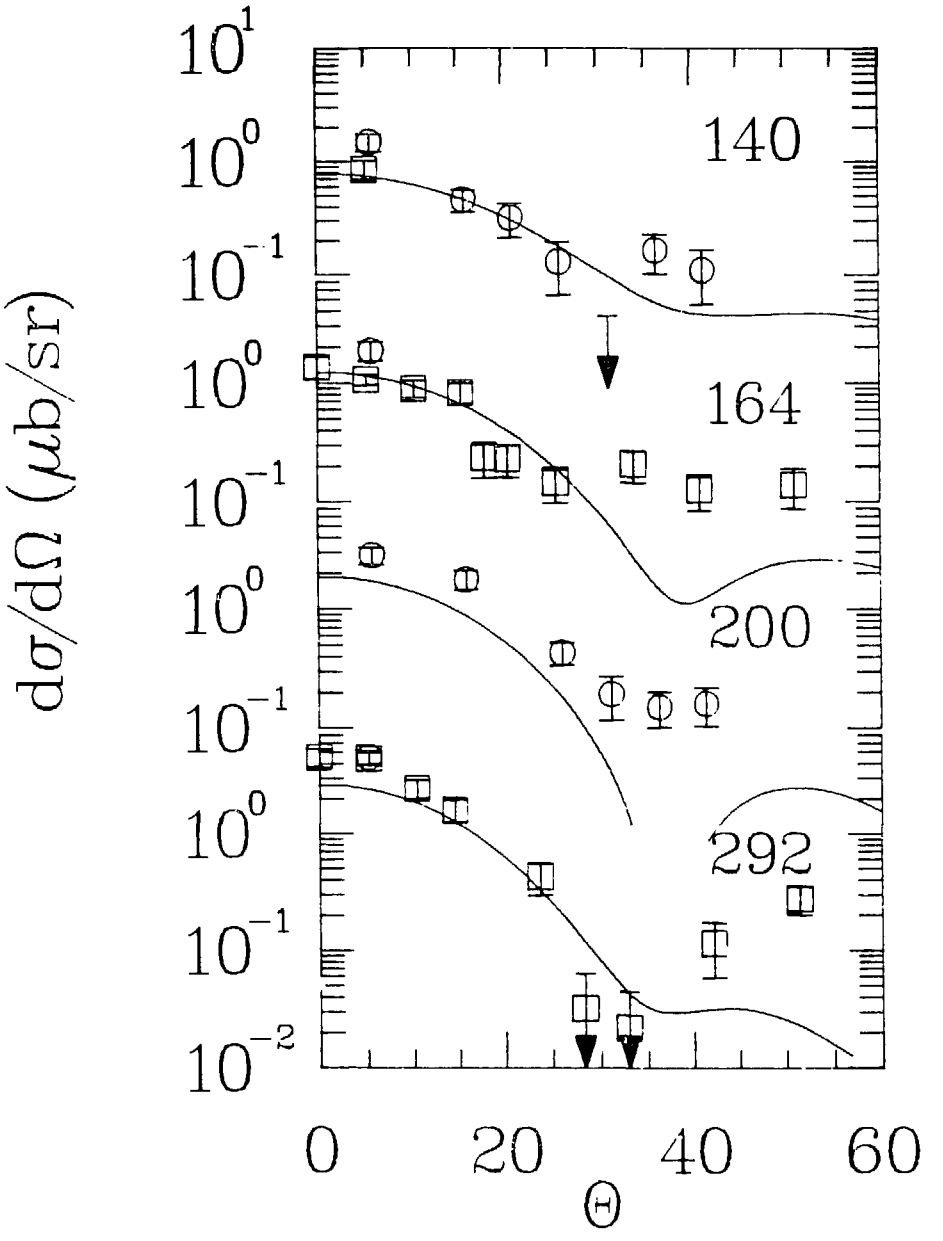

Figure IV-8.
$^{14}C(\pi^+,\pi^-)^{14}O(gs)$ angular distributions contrasted with lowest-order optical-model calculations.

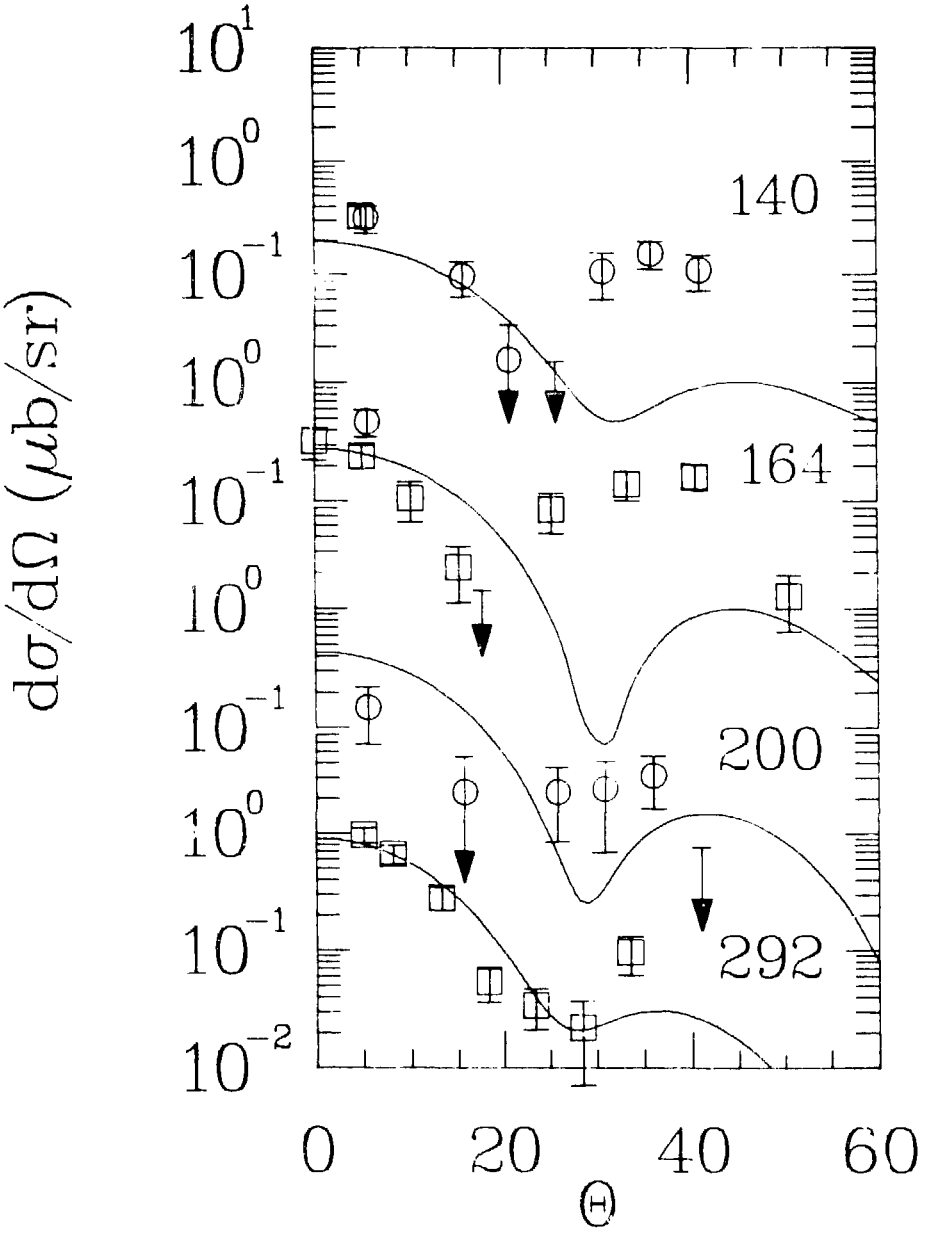

Figure IV-9.
$^{26}Mg(\pi^{+},\pi^{-})^{26}Si(gs)$ angular distributions contrasted with lowest-order optical-model calculations.

to determine run times by the ^{14}C measurements. The ^{14}C count rate averaged about four times that for ^{26}Mg, in agreement with a simple estimate based on an $A^{-10/3}$ mass dependence and the known target areal densities and relative acceptance.

All of the ^{14}C and ^{18}O resonance energy data indicate that DIAS DCX on these two nuclei is very similar, except for a 40 MeV energy shift. To illustrate this point, Figure IV-10 compares angular distributions on ^{14}C with those at 40 MeV higher energy on ^{18}O. The agreement is very good. This apparent 40 MeV shift is consistent with the observation that the minimum in the ^{14}C excitation function is shifted to an energy lower than that for ^{18}O. At present, however, no mechanism has been proposed to explain the energy shift between these two nuclei.

No angular distributions have been measured on $T > 1$ targets. Assuming that there is no isospin dependence to the angular distribution shapes, we conclude that the angular distributions exhibit two energy regions. At resonance, the excitation functions are smallest, and the angular distributions have far-forward minima. Above resonance, the shapes are simply diffractive. There is a transition region in which the angular distributions flatten out at a forward angle. The behavior as the energy is decreased below ~100 MeV is unknown.

A3. Target Mass Dependence

The target mass dependence of DIAS DCX is theoretically known [Jo-80] to be:

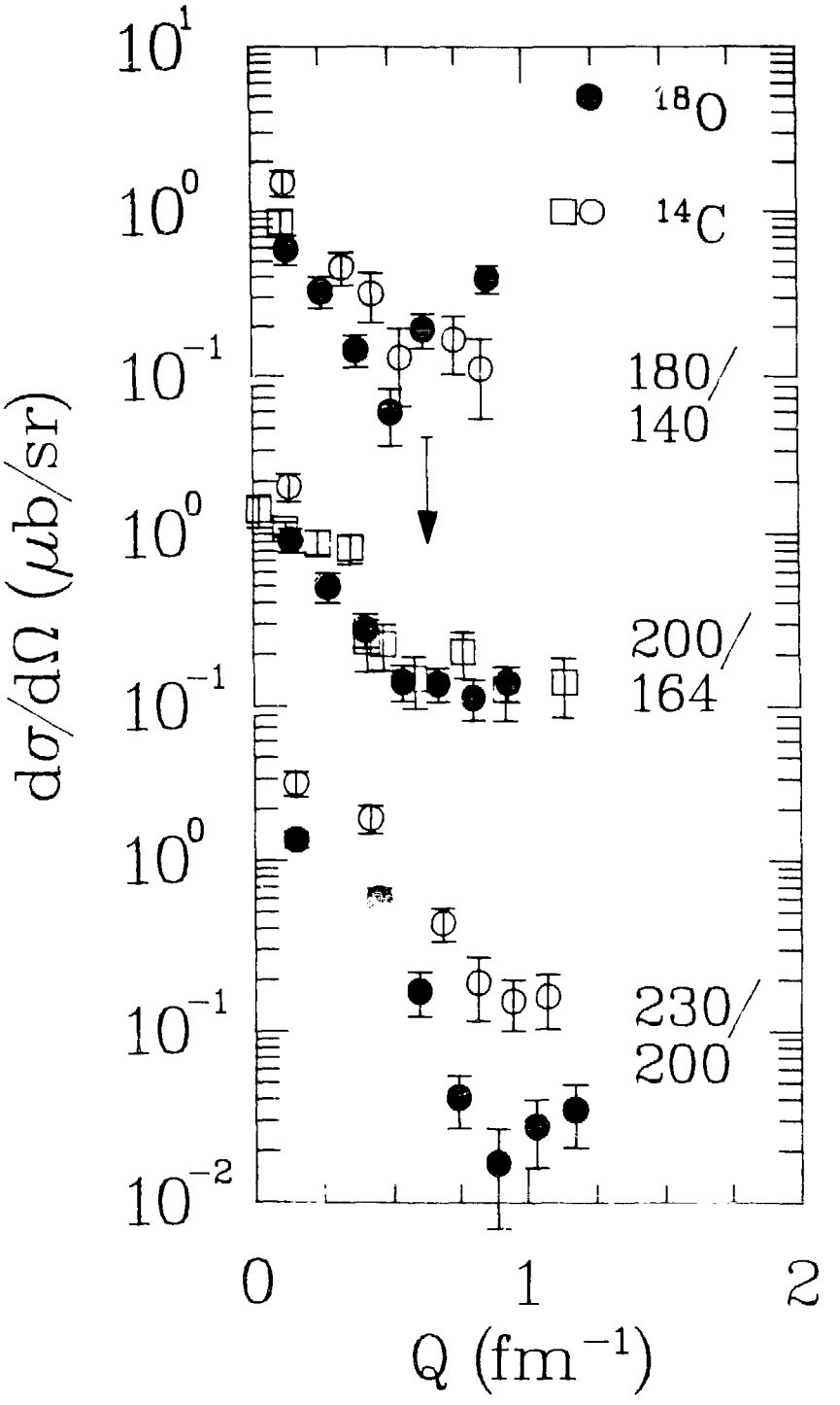

Figure IV-10.
Comparison of angular distributions on ^{14}C and ^{18}O.

$\sigma \sim (N-Z)(N-Z-1)A^{-10/3}$.

Figure IV-11 displays the A dependence of all DIAT at three energies, 292, 180, and 164 MeV. The dashed curves are proportional to $A^{-10/3}$, and provide an excellent overall description of the data. At 292 MeV, the data are extremely smooth, except that the ^{42}Ca point is large relative to the other measurements. The same is true at 180 MeV. At 164 MeV, there is much more scatter to the data, which is related to the excitation function shapes. This is the energy at which the excitation functions start to differ in shape. At higher energies, all increase monotonically. But at 164 MeV, some are increasing as the energy is decreased, whereas others are flat with energy.

Table IV-2 shows fits to the A dependence at all energies at which there are at least four data points. At all energies, the best fit A dependence is -10/3 within one or two error bars. These fits can be divided into two energy regions. At 180 MeV and above, the excitation functions are the same shape, and the A dependence is smooth and about -10/3 at all energies. Below 180 MeV, the excitation function shape varies with nucleus, and although the average A dependence is still close to -10/3, there is more scatter to the data and the chi squares are larger.

B. Nonanalog I Transitions

Nonanalog I transitions are (gs) to (gs) with $\Delta T = 2$ and $J_i^\pi = J_f^\pi = 0^+$. The data consist predominantly of measurements made on

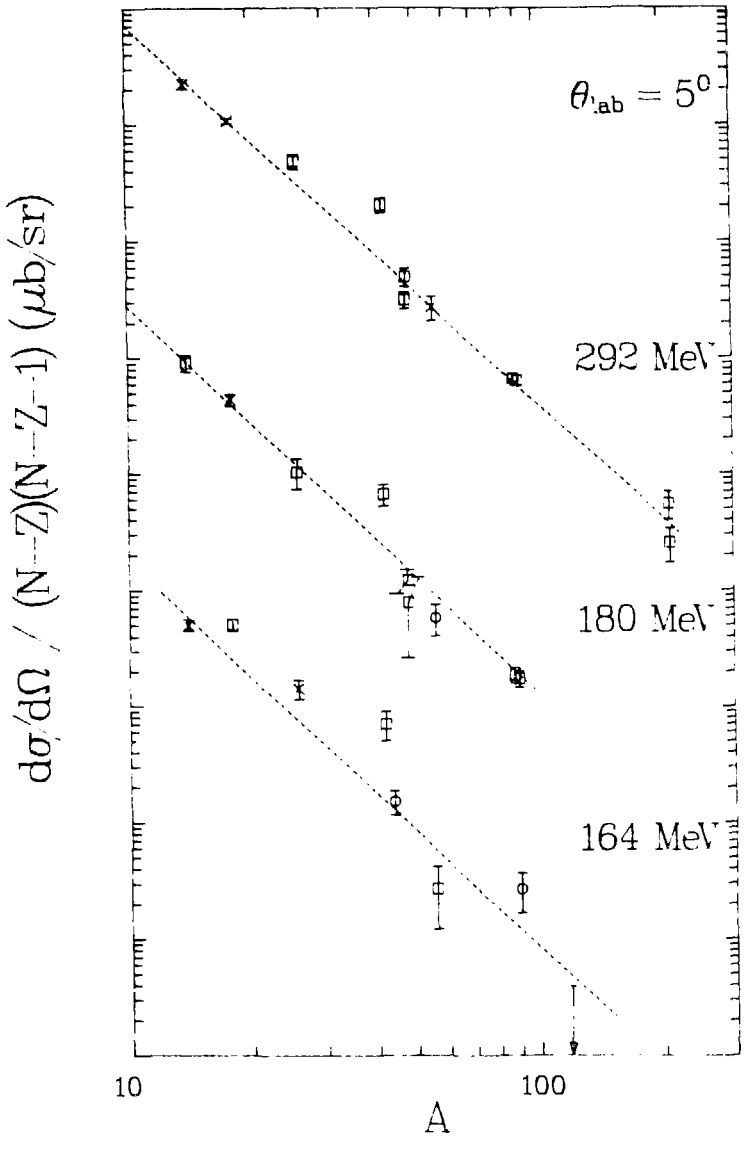

Figure IV-11.
Target mass dependence of DIAT DCX.

Table IV-2. DIAS A dependence fits at several energies.

T_π	Npts	Best Fit Exponent	$\chi^2_{reduced}$	$\chi^2_{reduced}$ for $A^{-10/3}$
120	6	-3.23(0.18)	6.59	6.54
140	6	-3.23(0.18)	8.37	8.32
164	10	-3.36(0.12)	4.68	4.68
180	10	-3.51(0.10)	3.57	3.23
210	5	-3.24(0.17)	0.08	0.02
235	8	-3.30(0.14)	3.18	3.17
260	4	-3.01(0.24)	1.90	1.55
292	14	-3.25(0.04)	3.08	2.73

solid, T = 0 targets, ^{12}C, ^{16}O (ice), ^{24}Mg, ^{28}Si, ^{32}S, and ^{40}Ca. Excitation functions have been measured on all of these nuclei, and a total of five angular distributions have been measured on three of the targets.

Most of the remaining measurements consist of DCX on T > 2 targets leading to $T_{final} = T_{initial} - 2$ ground states. No angular distributions have been measured, but excitation functions of at least four points have been measured on five targets, ^{48}Ca, ^{48}Ti, ^{56}Fe, ^{80}Se, and ^{90}Zr. Of these, the ^{48}Ca and ^{90}Zr measurements are mostly upper limits.

The remaining data have been measured with the (π^-,π^+) reaction. Except for an excitation function and angular distribution measurement on ^{18}O, these data consist solely of cross section measurements at 5° and ~164 MeV.

For brevity, we will continue to refer to (π^+,π^-) reactions by the

target nucleus. The (π^-,π^+) reaction will always be written explicitly.

B1. Excitation Functions

Figure IV-12 displays the excitation functions measured on T = 0 targets. All of the excitation functions exhibit a peak near 170 MeV. The peak is characteristically about 80 MeV wide. Cross sections off resonance are smaller than the peak by a factor of about 4. The most significant feature of the data is the lack of any major differences in the shape of the excitation functions.

Figure IV-13 displays the excitation functions measured on T ≠ 0 targets. Of these measurements, $^{18}O(\pi^-,\pi^+)$ and ^{48}Ti are consistent with the T = 0 target description, ^{48}Ca and ^{90}Zr have too poor statistics to judge, and ^{56}Fe and ^{80}Se appear slightly different. Although a peaked behavior is evident in these latter two nuclei, the peaks have shifted down in energy and become narrower.

The excitation function widths and peak energies can be extracted from fits with a Breit-Wigner function,

$$\frac{d\sigma}{d\Omega}(T) = \frac{1}{p^2} \times \frac{N}{(T-T_0)^2 + (\Gamma/2)^2},$$

where p is the pion momentum, T is the kinetic energy, and T_0 and Γ are the peak energy and width. We have absorbed all energy-independent factors into a normalization constant, N. The results to the fits are given in Table IV-3. It is difficult to judge whether the variations in the extracted parameters for the several targets is the result of a

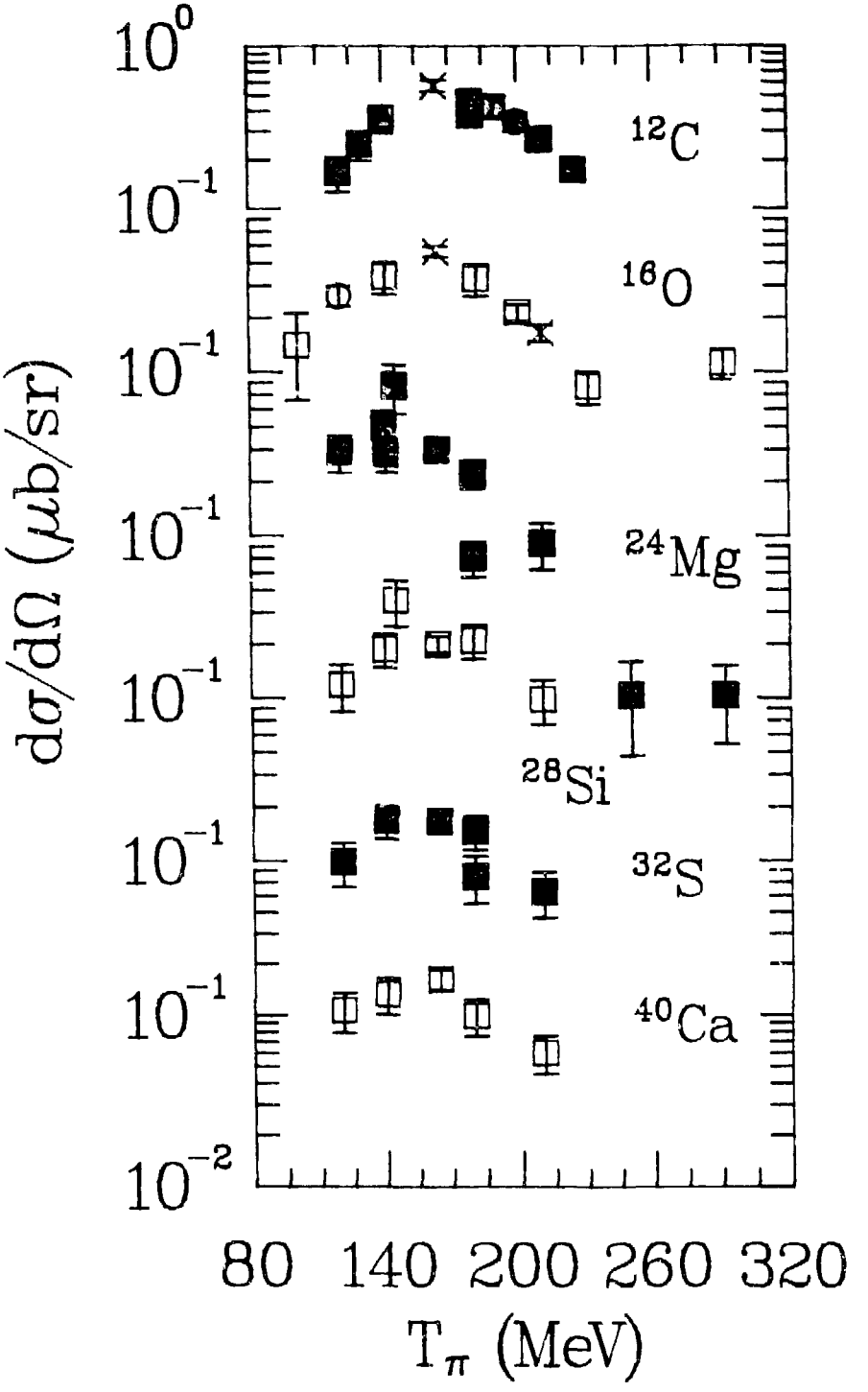

Figure IV-12.
Nonanalog DCX excitation functions on T = 0 targets.

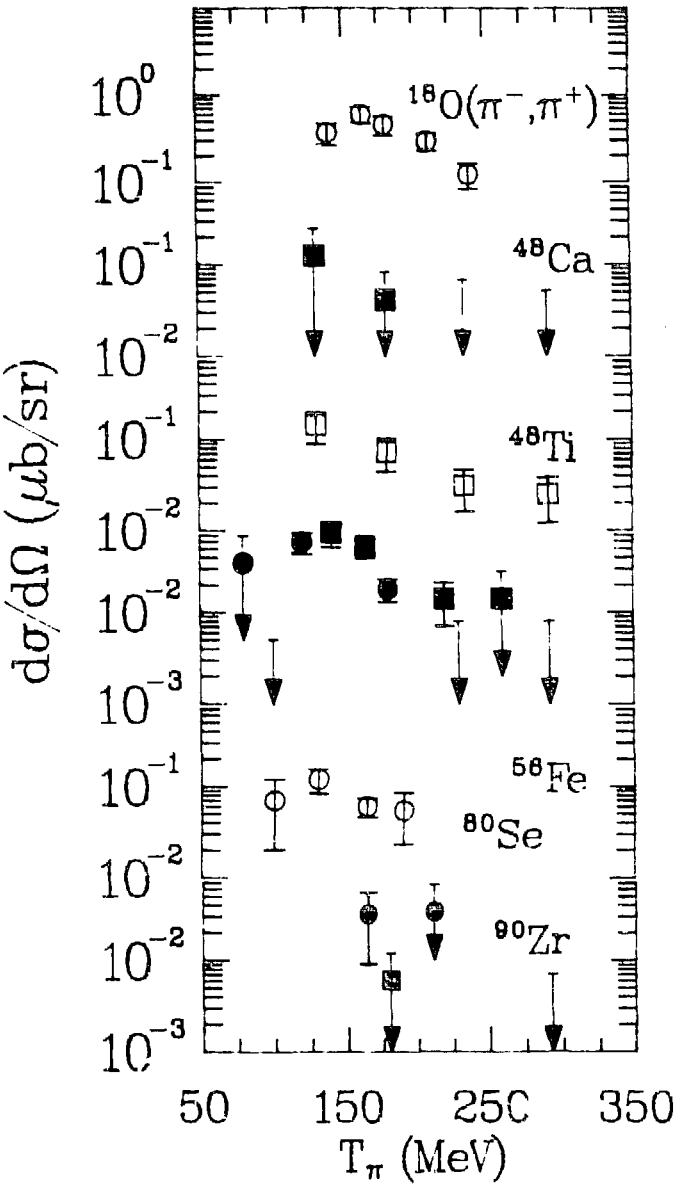

Figure IV-13.
Nonanalog I DCX excitation functions on T ≠ 0 targets.

Table IV-3. Results of Breit-Wigner fits to nonanalog I DCX excitation functions.

Target	N $\frac{\mu b \times MeV^4}{sr \times c^2}$	T_0 (MeV)	Γ (MeV)	T_{max} (MeV)	$d\sigma/d\Omega_{max}$ (μb/sr)
^{12}C	6.05E+7	181.1(2.7)	77.9(6.6)	175	.490
^{16}O	5.11E+7	170.4(2.2)	78.2(7.3)	164	.448
^{18}O	8.22E+7	179.8(6.9)	87.9(23.8)	172	.531
^{24}Mg	2.00E+7	147.7(4.2)	60.0(13.9)	144	.359
^{28}Si	3.24E+7	176.5(7.0)	90.1(19.5)	168	.205
^{32}S	1.96E+7	163.1(6.2)	82.5(23.5)	156	.165
^{40}Ca	2.14E+7	165.7(6.7)	88.6(22.2)	157	.153
^{56}Fe	1.19E+6	151.6(2.0)	23.4(5.1)	151	.133
^{80}Se	1.02E+7	139.7(9.4)	81.1(50.1)	131	.111

smooth change in the parameters with mass, or is related to the changes that occur in nuclear structure with increasing mass. It is clear, however, that all nonanalog I excitation functions exhibit the same general features.

B2. Angular Distributions

Six nonanalog I DCX angular distributions have been measured. Three of the angular distributions, for ^{16}O at 120 and 200 MeV, and for $^{18}O(\pi^-,\pi^+)$ at 164 MeV, were measured as part of the present work. All of the angular distributions appear consistent with simple, diffractive scattering. Figure IV-14 displays the four angular distributions measured at 164 MeV plotted versus qR, the momentum transfer multiplied by an appropriate strong-absorption radius, for which we have used the one-tenth density point (calculated from charge distributions

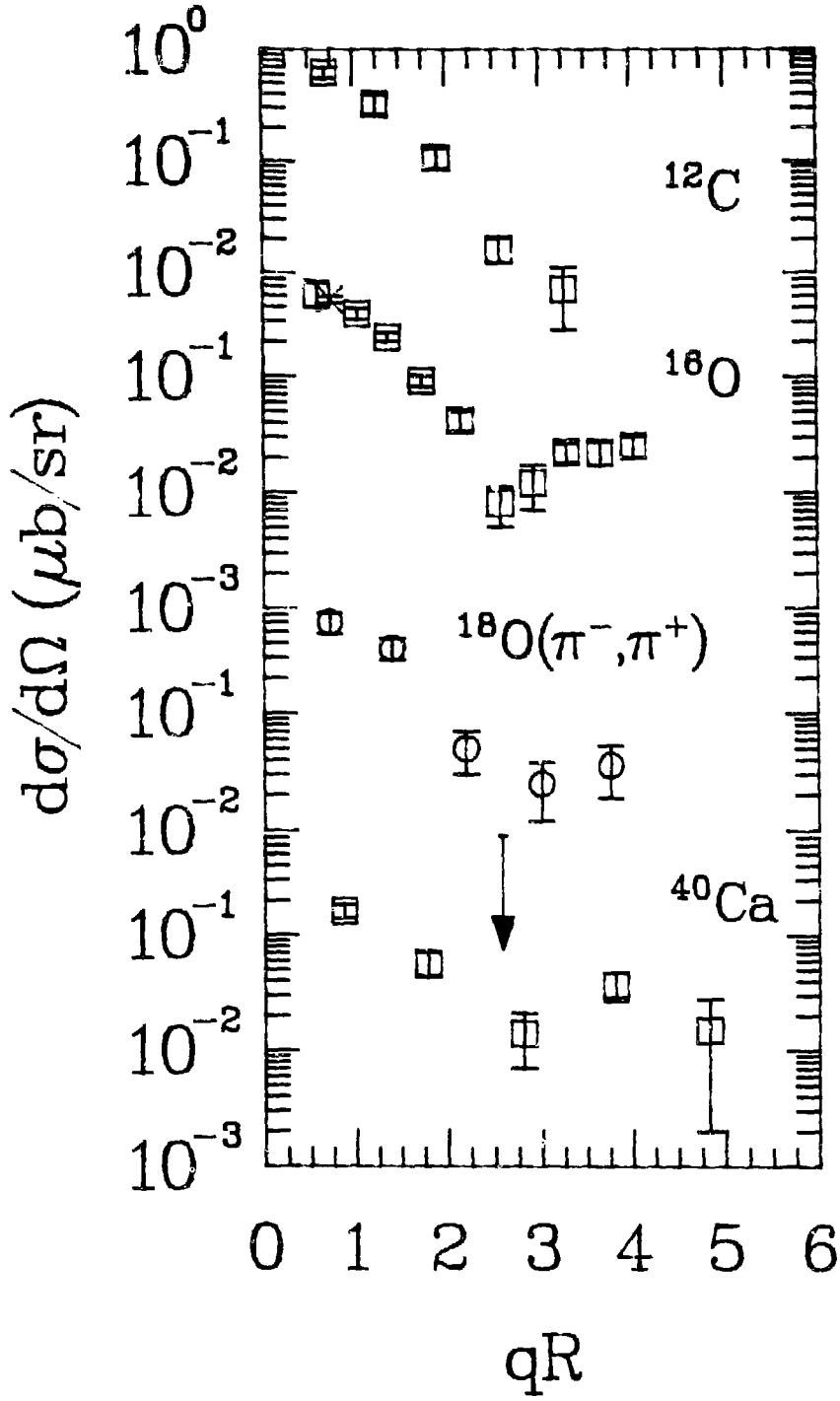

Figure IV-14.
Nonanalog I DCX angular distributions at 164 MeV.

determined by electron scattering [Ja-74]). The fact that the minima are all at the same qR indicates that the angular distributions merely reflect the nuclear size. This is further demonstrated in Figure IV-15, where the three ^{16}O angular distributions at 120, 164, and 200 MeV are plotted versus the momentum transfer. Again, the minima occur at the same momentum transfer, independent of the energy, indicating that the angular distributions are all identical functions of qR, except for an overall scale factor. Since the 5^{0} excitation function is peaked, the similarity in angular distribution shapes indicates that the entire angular distribution goes up and down with energy, and thus the total cross section is peaked. A more complete discussion is given in Appendix B1.

B3. Mass Dependence

The $A^{-10/3}$ mass dependence predicted for DIAT is derived specifically for a sequential charge exchange mechanism connecting analog states. It does, however, apply to other mechanisms leading to the DIAS [Ki-83]. The A dependence of nonanalog DCX need not be the same. Since all of the nonanalog I excitation functions display the same shape, we show, in Figure IV-16, the mass dependence of the reactions at three energies, 140, 164, and 180 MeV, near the peak of the excitation functions. The smoothness of the data is apparent. Table IV-4 lists the mass dependence fit parameters at these three energies. The $\sim A^{-4/3}$ mass dependence is significantly slower than that for DIAT. At present, there is no generally accepted explanation for the mass dependence of nonanalog I DCX.

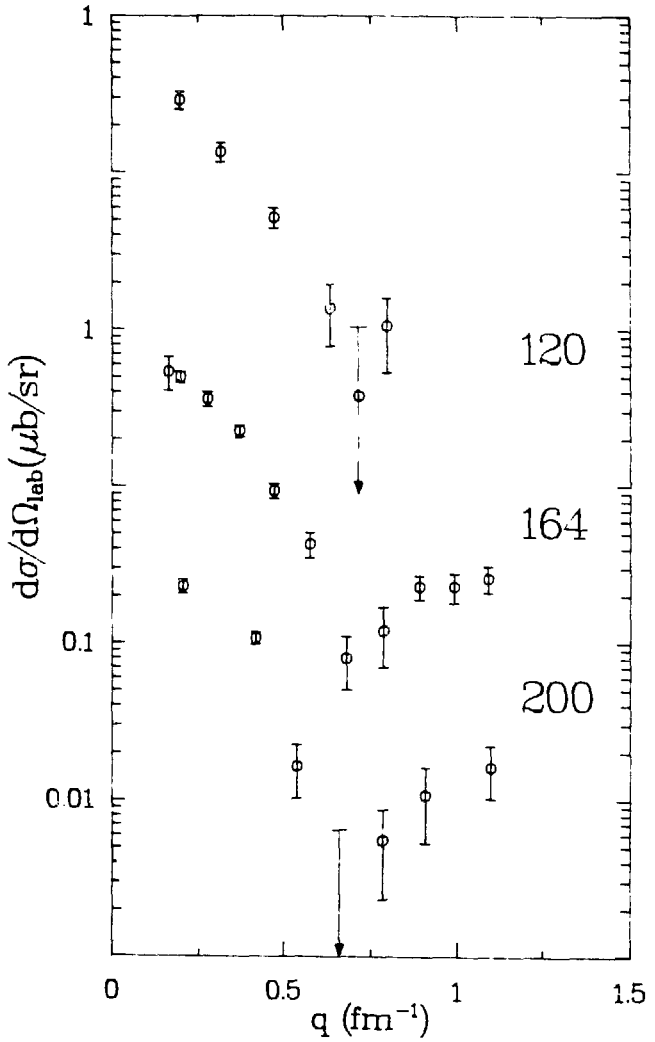

Figure IV-15.
$^{16}O(\pi^+,\pi^-)^{16}Ne(gs)$ angular distributions at three energies.

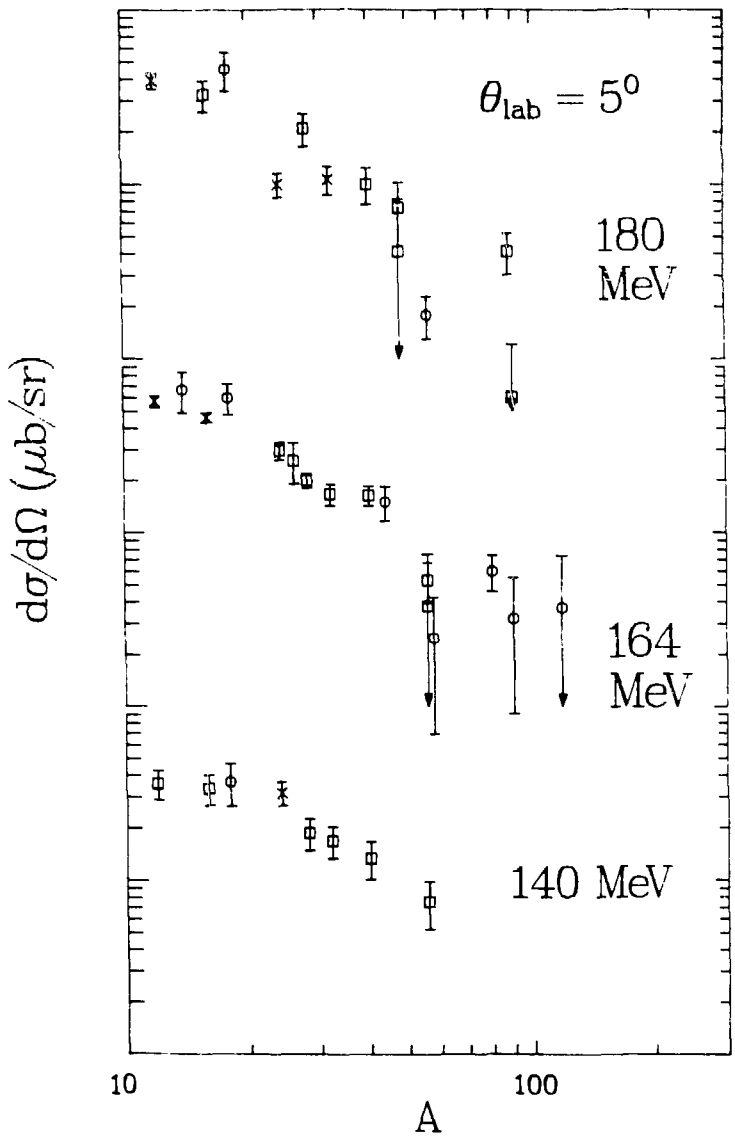

Figure IV-16.
Mass dependence of nonanalog I DCX at three energies.

Table IV-4. Nonanalog I A dependence fits at three energies.

T_π	Npts	Best Fit Exponent	$\chi^2_{reduced}$	$\chi^2_{reduced}$ for $A^{-4/3}$
140	9	-0.96	0.82	1.52
164	18	-1.38	1.61	1.64
180	15	-1.78	3.33	4.55

It is clear that the systematics of nonanalog I DCX are much more regular than those of DIAT. Whereas DIAT exhibits simple features above resonance, but complicated features at and below resonance, nonanalog I DCX is simple at all energies. The excitation function peaks are reminiscent of the underlying Δ resonance amplitude, which, in most reactions, is washed out by the pion distortions (see Chapter V). All angular distributions are diffractive. The A dependence is smooth, although unexpected.

C. Nonanalog II Transitions

Other DCX data include measurements on T = 1/2 targets and some nonDIAS excited state cross sections that have been extracted. In general, nonDIAS excited state cross sections cannot be extracted in DCX measurements. DIAS and nonanalog I transitions dominate most spectra at forward angles, and are used to determine the acquisition time requirements. Also, thick targets are used to enhance count rates, thus increasing the difficulty of observing particular excited final states. Most of the data that could be mentioned in this section consists of unique measurements, thus it will not be discussed. We

will describe only the transitions to first-excited 2^+ states. Excitation functions and angular distributions have been extracted for DCX on ^{16}O and ^{18}O leading to the first-excited 2^+ states of ^{16}Ne, ^{18}Ne, and ^{18}C.

Figure IV-17 contrasts the excitation function for each residual 2^+ state with that for the corresponding 0^+ gs. For ^{16}O and $^{18}O(\pi^-,\pi^+)$, for which $T_f \neq T_i$, the shapes of the excitation functions are very similar. It is unclear whether the similarities or differences of the ^{18}Ne(gs, DIAS) and $^{18}Ne(2^+)$ should be emphasized. The 2^+ exhibits a very dramatic minimum near 160 MeV, but otherwise is consistent with being flat. It is unclear whether there is any relation between the structure in the 2^+ excitation function and that in the DIAT, or between the $^{18}Ne(2^+)$ and the other 2^+ states.

Angular distributions for the $\Delta T = 2$ 2^+ states are shown in Figure IV-18. The behavior is almost that of an exponential decrease in angle. Whereas the gs angular distributions can be simply parameterized (see Appendices B2 and B3) with

$$\frac{d\sigma}{d\Omega}(q) = N\, J_0^2(qR)\, e^{-qd},$$

where q is the momentum transfer, R is the strong-absorption radius, and d is proportional to the diffusivity, no similar parameterization works for the 2^+ states with reasonable, physical values for R.

Figure IV-19 shows the $^{18}Ne(2^+)$ angular distributions at several energies. It is clear that the excitation function minimum results from the vanishing of only the forward-angle cross sections near

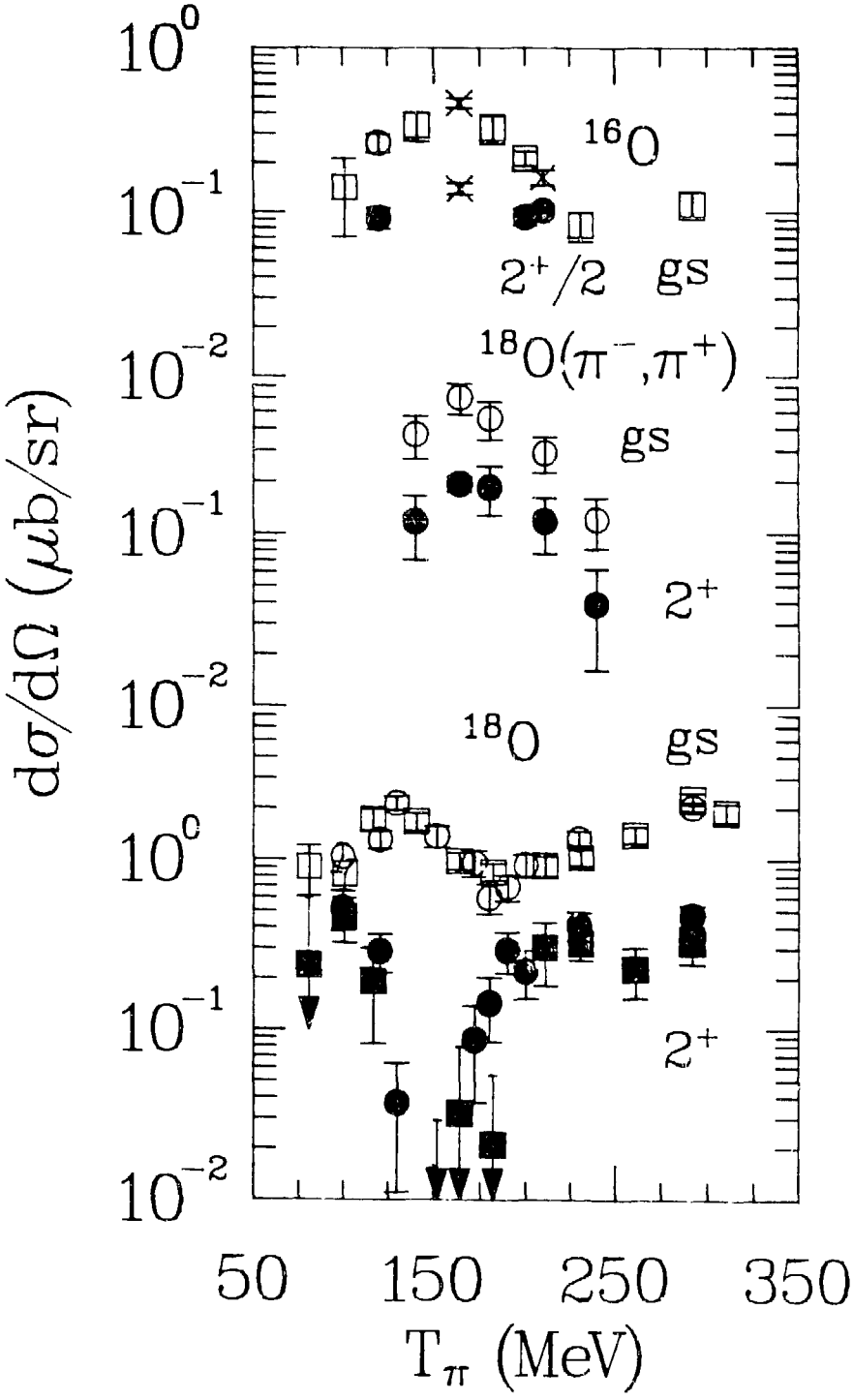

Figure IV-17.
2^+ excitation functions contrasted with those of corresponding gs.

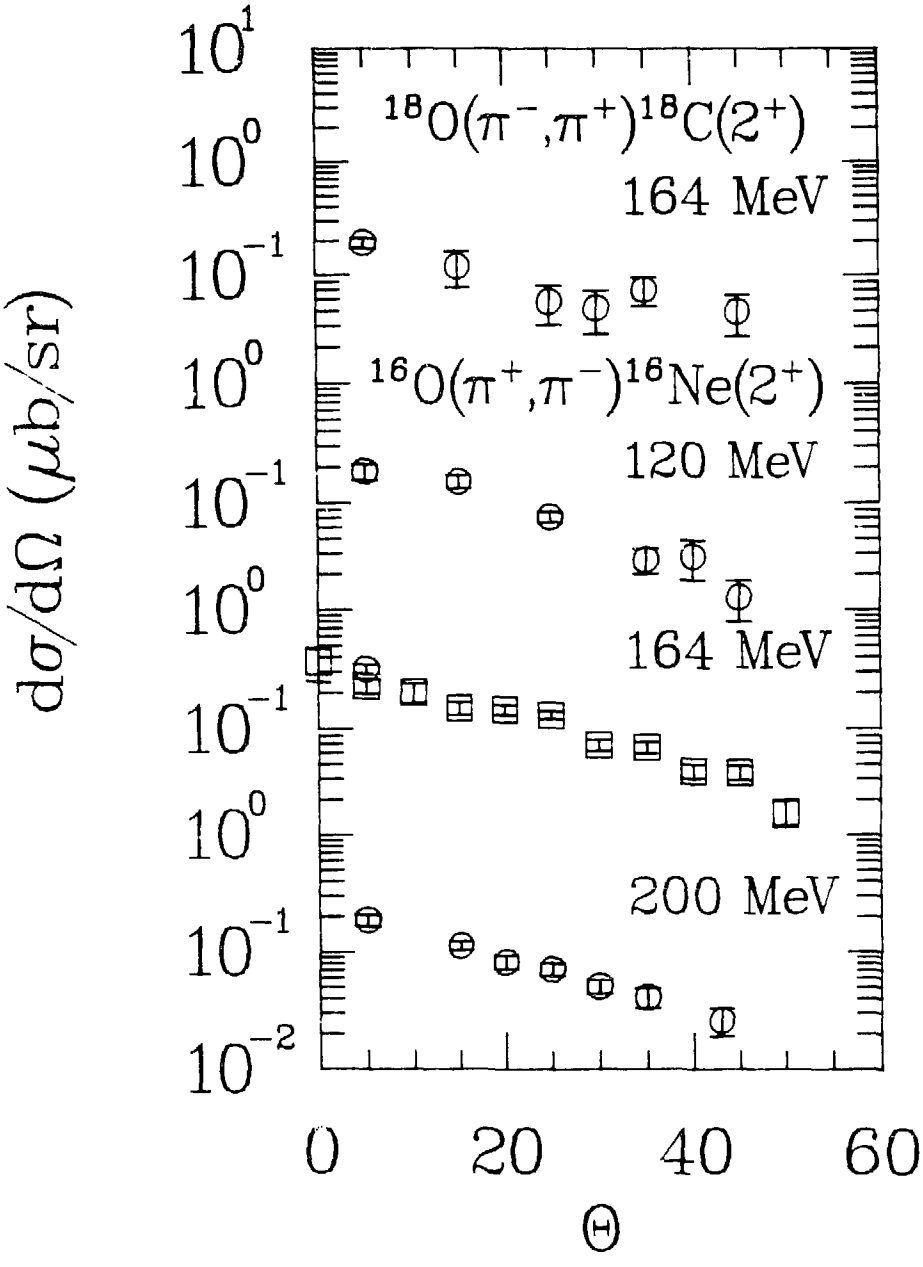

Figure IV-18.
Angular distributions for $\Delta T = 2$ 2^+ states.

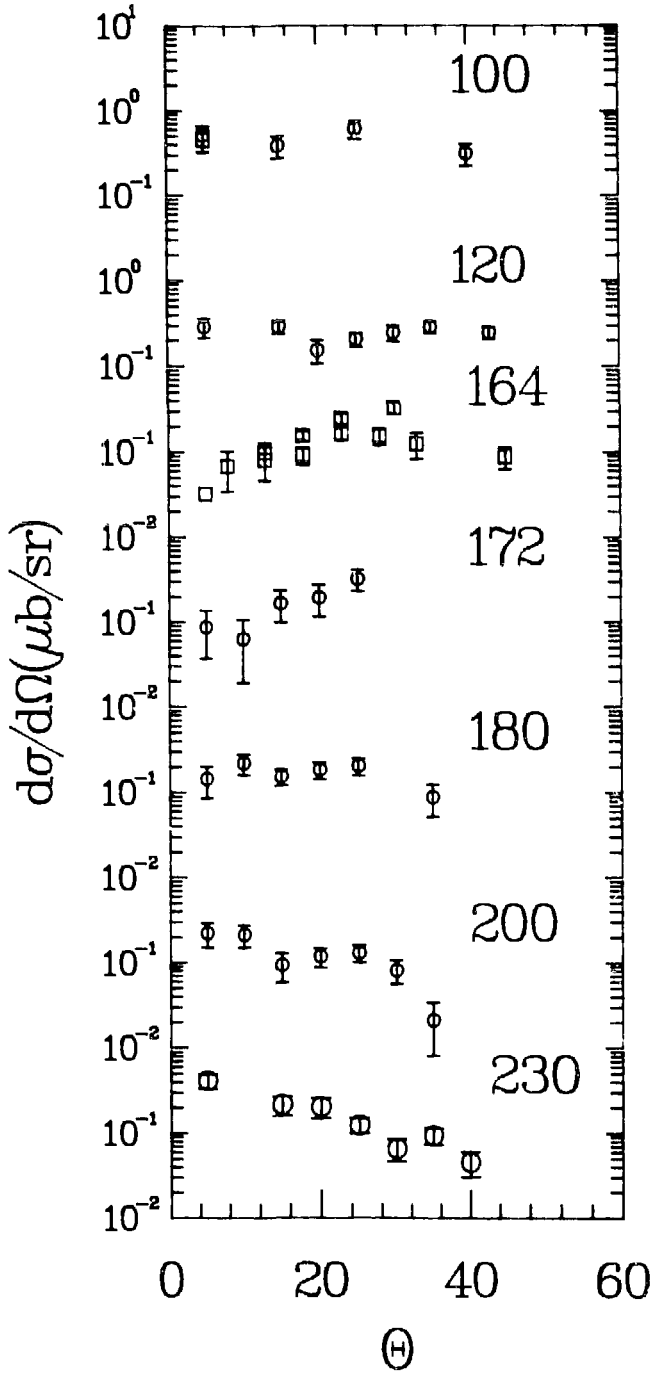

Figure IV-19.
Angular distributions for $^{18}O(\pi^+,\pi^-)^{18}Ne(2^+)$.

160 MeV. Cross sections at larger angles appear to be essentially constant. Attempts to fit the angular distributions with a simple parameterization, as above, failed.

Given the partial angular distributions, a comparison can be made of the angle-integrated cross sections for the region in which data has been obtained. These results are presented in Table IV-5. These numbers were obtained by fitting the angular distributions with a sum of Legendre polynomials, then integrating the fit ($2\pi\int d(\cos\theta)$) from 0° to 50°, and from 0° to 180°. In general, the 2^{+} total cross sections appear larger than the gs total cross sections.

Table IV-5. Comparison of angle-integrated cross sections.

Residual Nucleus	T_{π} (MeV)	gs integral $0^{\circ} \rightarrow 50^{\circ}$	gs integral $0^{\circ} \rightarrow 180^{\circ}$	2^{+} integral $0^{\circ} \rightarrow 50^{\circ}$	2^{+} integral $0^{\circ} \rightarrow 180^{\circ}$
^{16}Ne	120	5.9	1290.0	7.5	208.0
	164	8.3	85.3	11.4	283.0
	200	3.5	22.7	7.4	99.4
^{18}C	164	12.2	203.0	9.2	104.0
^{18}Ne	100	21.0	54.0	48.6	90.0
	120	33.0	101.0	32.4	123.0
	164	74.1	1850.0	17.0	105.0
	172	20.0	131.0	126.0	17400.0
	180	18.5	82.0	15.1	87.1
	200	46.3	225.0	7.2	43.0
	230	17.4	52.0	14.5	105.0

CHAPTER V. DCX THEORIES

Some qualitative features expected of DCX, e.g., the expected dominance of DIAT, were presented in the Introduction (see Chapter I). Results of some numerical calculations of DIAT DCX in lowest-order were contrasted with data in Chapter IV. Although the calculations adequately explain the data for energies above $T_\pi \sim 230$ MeV, the large disagreements between calculations and data near resonance has resulted in numerous efforts to investigate various effects and to create more complicated models of the reaction. Several works, e.g. [Le-77, Oo-77, Li-83], have emphasized the importance of treating the initial-and final-state nuclear structures correctly. Other works, e.g. [Sp-78, Li-81], have emphasized the importance of nonanalog intermediate states. Some works, e.g. [Li-83, Jo-83a] have emphasized the importance of higher-order terms in the π-A optical potential. Other works, e.g. [Mo-82, Jo-84], have suggested the importance of additional, nonsequential, reaction mechanisms.

In this chapter, we will describe a procedure for calculating DCX in lowest order. We will then proceed to describe three more complicated models. These are the two-amplitude model (TAM) of H. T. Fortune [Gr-82b, Fo-83, Gi-85a], the higher-order optical potential of Johnson and Siciliano [Jo-83a, Gr-84], and the double-delta calculations of Johnson, Siciliano, Toki, and Wirzba [Jo-84, Gi-85b, Wi-85]. Several other approaches to DCX will be discussed briefly in the final section.

A. DIAT Calculations in Lowest Order

We have previously indicated (see Chapter I) that DCX amplitudes

are simply related to the amplitudes for pion elastic scattering in channels of good total isospin. The elastic amplitudes in channels of good isospin are related [Jo-80] to the amplitudes for elastic scattering of the π^+, π^0, and π^-. Thus, the calculation of both elastic scattering and DCX involve identical procedures, except for the summing of amplitudes for DCX. Thus, we will restrict the description to the calculation of elastic scattering.

Pion elastic scattering is calculated by solving the coordinate-space Klein-Gordon equation. Neglecting the Coulomb potential (since we assume isospin symmetry), the radial part of the Klein-Gordon equation is given by

$$\left[\frac{-d^2}{dr^2} + \frac{\ell(\ell+1)}{r^2}\right]\frac{u_\ell}{r} = \left[\kappa^2 - 2EV_{op}\right]\frac{u_\ell}{r},$$

and the pion wave function by

$$\psi = \sum_\ell \frac{u_\ell(r)}{r} i^\ell P_\ell(\cos\theta),$$

and κ is the c.m. momentum.

The optical potential V_{op} can be derived (see, e.g., [Ki-84]) in a proper, tedious, and formal manner from the free π-n interaction. We will instead summarize the salient features of this derivation, emphasizing the physically-motivated approximations that are made. The transition operators and potentials are formally related by the operator equation,

$$T = V + VG_0T,$$

where G_0 is an appropriate pion propagator. In particular, the π-n t matrix in free space is

$$t_i = v_i + v_i g_0 t_i,$$

whereas the π-n t matrix in the nuclear medium is

$$\tau_i = v_i + v_i G_0 \tau_i.$$

The free-space propagator g_0 is given by

$$g_0 = \frac{1}{\omega - K_\pi - K_n + i\eta} \qquad \eta \to 0^+$$

with ω the total collision energy and K the the kinetic energy. A similar expression exists for the propagator G_0. The standard approximation is to assume that the difference between g_0 and G_0 is small, and thus $t_i \sim \tau_i$. This is called the impulse approximation. (Often, however, the entire set of approximations that will be made is collectively called the impulse approximation.) Physically, it is assumed that the π-n t matrix in the nucleus is the same as in free space.

In multiple scattering theory, the π-A transition matrix is then given as a series of multiple scatterings,

$$T = \sum_{i=1}^{A} t_i + \sum_{i=1}^{A} t_i G_0 \sum_{j \neq i}^{A} t_j + \ldots$$

With these approximations, the momentum-space optical potential is given by the matrix elements of the transition operator,

$$V_{op} = \langle \chi(\vec{\kappa})\psi(\vec{p}) | T | \chi(\vec{\kappa}')\psi(\vec{p}') \rangle,$$

in which χ (ψ) is the pion (nucleon) wave function, $\vec{p}$ is the nucleon momentum, and the nucleus is in its ground state. The potential can also be expressed as a multiple-scattering series, in which all intermediate states are constrained to be the ground state. The simplest approximation to the series is given by the first term,

$$T = \sum_{i=1}^{A} t_i,$$

which represents scattering of the pion from a single nucleon in the presence of the nucleus. This is called the single-scattering approximation. The optical potential may now be written as:

$$= \sum_{i=1}^{A} \langle \chi(\vec{\kappa})\psi(\vec{p}) | t_i | \chi(\vec{\kappa}')\psi(\vec{p}') \rangle.$$

The optical potential results from an integral over the nucleon momentum distribution of the π-n transition operator. Clearly, the optical potential depends on the model used to describe the nucleon momentum distribution. The standard assumption for most coordinate-space calculations is that the nuclear momentum distribution is sharply

peaked. Then, the matrix element may be evaluated at some appropriate, fixed value of $\vec{p}$. The optical potential becomes a product of a t-matrix element that depends only on a fixed, relative π-n momentum, and a nuclear form factor that is the overlap of the nuclear momentum distributions. One common choice for the nucleon momentum is to use the fixed-nucleon (or frozen-target) approximation, in which one assumes that all nucleons have no Fermi momentum,

$$\vec{p}_i = \vec{p}_A/A.$$

Defining $\vec{q}$ to be the momentum transfer ($\vec{q} = \vec{p}' - \vec{p} = \vec{\kappa} - \vec{\kappa}'$), the potential then may be expressed as a product,

$$V_{op} = \sum_i \langle \chi(\vec{\kappa}) | t_i | \chi(\vec{\kappa}') \rangle \rho(\vec{q}).$$

Ignoring the dependence of the matrix element on the nucleon momentum is the factorization approximation.

We have now expressed the momentum space optical potential in terms of the π-n t matrix in the π-A c.m. The π-n t matrix is known, however, in the π-n c.m. A transformation between the two frames is required.

The free π-n interaction t matrix is parameterized as:

$$t = \frac{-1}{4\pi^2 k\omega} \sum_{LJT} (2L+1)\, \alpha_{LJT}\, P_{LJ}\, P_T\, P_L(\cos\theta).$$

All symbols have been defined in the introduction (see Chapter I). For

resonance-energy calculations, it is standard to keep only the s- and p-wave terms (d waves are unimportant below some energy which is about 300 MeV), and to ignore spin-flip contributions to elastic scattering (which are small compared to the spin non-flip contribution). The t matrix in the π-n c.m. may then be written as:

$$t_{\vec{k},\vec{k}'} = t_0 + t_1(\vec{t}_\pi \cdot \vec{t}_n)$$

in which

$$2\omega t_0 = A + Ck^2\cos(\theta),$$

$$2\omega t_1 = B + Dk^2\cos(\theta), \text{ and}$$

$$A = \frac{-1}{6\pi^2 k}(2\alpha_3+\alpha_1)$$

$$B = \frac{-1}{6\pi^2 k}(2\alpha_3-2\alpha_1)$$

$$C = \frac{-1}{6\pi^2 k^3}(4\alpha_{33}+2\alpha_{31}+2\alpha_{13}+\alpha_{11})$$

$$D = \frac{-1}{6\pi^2 k^3}(4\alpha_{33}+2\alpha_{31}-4\alpha_{13}-2\alpha_{11}).$$

Here, we have shortened the notation for the s- and p-wave coefficients to α_{2T} and $\alpha_{2T,2J}$, respectively. The symbol θ is the scattering angle in the π-n c.m.

Elastic π-n scattering, however, corresponds to quasifree π-A scattering, not elastic π-A scattering. Thus, it is necessary to

extrapolate the on-shell behavior of the t matrix to off-shell kinematics. There are many possible extrapolations. The standard prescription for coordinate-space calculations is from [Ki-55],

$$2\omega t_0 = A + C\vec{k}\cdot\vec{k}', \text{ and}$$

$$2\omega t_1 = B + D\vec{k}\cdot\vec{k}'.$$

The t matrix must then be transformed from the π-n c.m. to the π-A c.m. The Lorentz invariance of probability flux requires that the t matrix in the π-A c.m. is related to that in the π-n c.m. by a factor γ,

$$\gamma^2 = \frac{E_\pi(k)E_\pi(k')E_n(k)E_n(k')}{E_\pi(\kappa)E_\pi(\kappa')E_n(p)E_n(p')}.$$

Assuming on-shell kinematics, and neglecting the motion of the nucleon in the π-A c.m., we find

$$\gamma = \frac{E_\pi(k)E_n(k)}{E_\pi(\kappa)M_n} = \frac{\omega S^{1/2}}{E_\pi(\kappa)M_n}.$$

The symbol $S^{1/2}$ represents the total energy $(E_\pi(\kappa) + E_n(\kappa))$. Employing the relation

$$\frac{\kappa}{k} = \frac{\kappa'}{k'} = \frac{S^{1/2}}{M_n}$$

then yields

$$2\omega t_0(\vec{\kappa},\vec{k}') = \frac{\kappa}{k}A + \frac{k}{\kappa}C\vec{k}\cdot\vec{k}', \text{ and}$$

$$2\omega t_1(\vec{\kappa},\vec{k}') = \frac{\kappa}{k}B + \frac{k}{\kappa}D\vec{k}\cdot\vec{k}'.$$

The momentum space optical potential (summed over all nucleons) now becomes

$$2\omega V_{op}(\vec{\kappa},\vec{k}') = (N+Z)\left[\frac{\kappa}{k}A + \frac{k}{\kappa}C\vec{k}\cdot\vec{k}'\right]\rho_0(q)$$

$$-T\left[\frac{\kappa}{k}B + \frac{k}{\kappa}D\vec{k}\cdot\vec{k}'\right]\rho_1(q),$$

in which N and Z are the neutron and proton numbers, and T = (N-Z)/2. The Fourier transform of the optical potential to coordinate space gives:

$$2\omega V_{op}(r) = (2\pi)^3(N+Z)\left[\frac{\kappa}{k}A\rho_0(r) - \frac{k}{\kappa}C\nabla\rho_0(r)\nabla\right]$$

$$-(2\pi)^3\frac{(N-Z)}{2}\left[\frac{\kappa}{k}B\rho_1(r) - \frac{k}{\kappa}D\nabla\rho_1(r)\nabla\right].$$

One additional approximation that has been neglected is the "angle transformation". The scattering angle in the π-n c.m. is not the same as the scattering angle in the π-A c.m. Thus, the $\vec{k}\cdot\vec{k}'$ term in the t-matrix is sometimes replaced by [Mi-74]

$$\vec{k}\cdot\vec{k}' = \vec{\kappa}\cdot\vec{\kappa}' - \frac{\omega}{2M_n} q^2.$$

The q^2 term becomes a Laplacian term, $\nabla^2\rho$, in the coordinate-space potential. In general, however, the effects of the correction are small, and some authors have found better agreement without this correction [Co-80].

It is perhaps appropriate at this point to discuss the philosophy of the lowest-order optical potential. It is certainly possible to do complete, microscopic calculations of some of the effects for which simple approximations have been made. The utility of the coordinate-space optical-model approach is in its ability to reproduce the qualitative features of the data over wide angular ($\theta \sim 20^o$ to 90^o) and energy ($T_\pi \sim 100$ to 300 MeV) regions in a short calculation time. Certainly, simple approximations that work adequately should be employed until superior calculational models are introduced. There are many momentum-space models that can provide superior predictions by including some effects explicitly (e.g., Δ propagation in the nucleus, medium corrections to the t matrix) at the cost of calculation time. There are also various efforts (e.g., [Jo-83b], see Chapter V-C) to introduce higher-order corrections to the optical model, so that the benefit of reduced calculation time may be retained.

The description of the lowest-order optical potential given above is consistent with that used in the code PIESDEX [Jo-83a], which has been used for all DIAT calculations presented in this work. One

difference should be noted. The frame transformation factor, $S^{1/2}/M_n$, is replaced by a factor,

$$Pl = \frac{1+\epsilon}{1+\epsilon/A},$$

with $\epsilon = E_\pi/M_n$. These two quantities are nearly equal. To lowest order in ϵ, we find

$$Pl = (1+\epsilon)\ (1+\epsilon/A)^{-1}$$

$$\sim (1+\epsilon)\ (1-\epsilon/A...)$$

$$\sim 1 + \epsilon\ \frac{A-1}{A}\ ...$$

whereas, using

$$S = m_\pi^2 + M_n^2 + 2E_\pi M_n$$

gives

$$\frac{S^{1/2}}{M_n} = (\ 1 + m_\pi^2/M_n^2 + 2e_\pi/1M_n)^{1/2}$$

$$\sim (\ 1 + 2\epsilon)^{1/2}$$

$$\sim 1 + \epsilon...$$

Clearly, the factor (A-1)/A is unimportant in lowest order, and the two transformation parameters are equivalent.

Calculations of DCX are obviously sensitive to the input density. In particular, the transition is driven by the density of the excess neutrons (the excess density) rather than the difference in neutron and proton densities (the valence density). The DIAT calculations presented in the present work have used two types of densities. Some calculations use mass densities derived from electron-scattering charge parameterizations, with excess densities calculated (with harmonic-oscillator radial wave functions) from the expected shell-model configuration of the target nucleus. Other calculations use Skyrme III proton, neutron, and excess densities. These two prescriptions usually result in similar predictions (see Figure IV-1).

Calculations of DCX arising from sequential charge exchanges through the intermediate analog state exhibit certain features. The typical energy dependence of lowest-order calculations is a monotonic rise in forward-angle cross sections from 100 to 300 MeV. At resonance energies, the typical angular dependence exhibits a deep, diffractive minimum, e.g., at $\theta = 30^{o}$ for ^{18}O at 164 MeV. As the energy is varied either higher or lower, the minimum becomes increasingly shallow, and, for certain densities, essentially disappears by 292 MeV. The mass dependence, investigated with Skyrme III densities for consistency, exhibits slight variations about $A^{-10/3}$.

It is possible, under certain assumptions, to derive analytic expressions for both SCX and DCX [Jo-80]. With a potential of the form given above, and the relations between elastic-scattering and DCX amplitudes, it was shown that the angular-distribution shape is approximately given by

$$\frac{d\sigma}{d\Omega} \sim J_0(qR) - \frac{a}{R}\,(J_0(qR) - qRJ_1(qR)),$$

with R and a an appropriate nuclear radius and diffusivity, and J a cylindrical Bessel function. With the additional assumption that the radial dependence of the proton, neutron, total, and valence densities are the same, the forward-angle (q = 0) N, Z, and A dependence was expressed as

$$\frac{d\sigma}{d\Omega} \sim (N-Z)(N-Z-1)A^{-10/3}.$$

B. TAM

The physical basis of the TAM is quite simple, and can best be illustrated with an example. The nuclear structure of ^{18}O may be reasonably-well approximated by

$$^{18}O \sim {}^{16}O \times 2n.$$

Thus, DCX on ^{18}O will consist of the usual sequential DCX mechanism on the valence neutrons, plus DCX on the ^{16}O core. Since DCX on ^{16}O is small at energies above the Δ_{33} resonance, we observe the simple, expected features of DCX at higher energies. On resonance, at which ^{16}O DCX is large, the core amplitude interferes with the valence amplitude, resulting in the observed nondiffractive angular

distribution. In addition, there may be nonsequential reaction mechanisms contributing to the core DCX that also contribute to, e.g., $d^2 \rightarrow d^2$ transitions of the valence neutrons.

Until recently, all calculations [Le-77, Xi-81, Li-81] of nonanalog DCX assumed that the reaction also proceeded through sequential charge exchanges. The problem with this assumption is that it should result in the same energy and angle dependences for $^{16,18}O$ DCX. This is clearly inconsistent with the experimental results. Since sequential transfer dominates DCX at higher energies, it is more reasonable to assume that the ratio of cross sections at 292 MeV, viz.,

$$\frac{d\sigma(^{16}O)}{d\sigma(^{18}O)} \sim 0.05,$$

represents an approximate limit on the relative importance of the sequential mechanism in ^{16}O to that in ^{18}O.

The regular systematics of nonanalog DCX, combined with the above discussion, suggest that nonanalog DCX is dominated by a single, nonsequential reaction mechanism. The diffractive angular distributions could result from any strong-absorption process. The energy dependence is similar to that of the underlying Δ_{33} resonance, although, in most calculations, one of the effects of distortions is to wash out this underlying energy dependence. Finally, the $A^{-4/3}$ mass dependence is the same as that for SCX, and suggests that DCX is caused by a single-step reaction. The only possible single-step reaction that would result in a double charge transfer is

$\pi^+ n \rightarrow \pi^- \Delta^{++}$.

Thus, it was suggested [Mo-82] that nonanalog DCX is sensitive to Δ components of final-state wave functions.

Although this explanation of nonanalog DCX is often identified with the TAM, it is not necessary for the model. Presumably, any reaction mechanism causing nonanalog DCX will also contribute to DIAT. The spirit of the model has been that, lacking a microscopic description of nonanalog DCX, the contribution of the unknown nonanalog amplitude to analog DCX can be taken from the nonanalog data. In [Gr-82b], the ^{18}O excitation function was fitted with a sum of a lowest-order DIAT calculation and an amplitude taken from the ^{16}O excitation function. The model was subsequently extended (see Appendix B4) to simultaneously explain both the ^{18}O angular-distribution and excitation-function shapes.

The model presents a reasonable basis for understanding DCX. Any explanation of DIAT that does not explain nonanalog DCX is incomplete. Present work on the model concentrates on providing it with a microscopic basis (see Chapter V-D). Some recent calculations of DCX (e.g., [Mi-84]) indicate, however, that there may be several important nonsequential mechanisms that contribute to DIAT. Thus, a complete understanding of DCX may require a detailed, microscopic, multiple-amplitude model.

C. Higher-Order Optical Potential

In the derivation of the optical potential for elastic scattering,

we assume that the incident pion interacts with only a single nucleon. For elastic scattering at small angles, this is a reasonable assumption (reflected in reasonable agreement between lowest-order elastic calculations and data). The DCX reaction, however, necessarily involves interactions with two nucleons. Thus, two-nucleon effects, which are a small correction to elastic scattering, can be of the same size as the usual sequential amplitude. Among the more commonly mentioned effects are two-nucleon correlations, pion absorption, and Pauli blocking effects.

The lowest-order optical potential results from interactions with a single nucleon. Thus, it has terms proportional to the density, ρ, and the excess density, $\Delta\rho$. Higher-order effects requiring two nucleons result in terms proportional to the two-nucleon probability. These terms, commonly called ρ^2 terms, are of the forms ρ^2, $\rho\Delta\rho$, and $(\Delta\rho)^2$.

No adequate microscopic understanding exists of many of the higher-order processes that can contribute to the optical potential. Thus, calculations that use ρ^2 terms typically use some model for the form of the higher-order terms, and adjust the magnitude of the terms phenomenologically to fit some data set. For example, [Li-83] use ρ^2 terms that were fitted to elastic scattering.

The approach of Johnson and Siciliano [Gr-84] is somewhat different. The most general isospin-dependent form of the optical potential is given by

$$U = u_0 + u_1(\vec{t}\cdot\vec{T}) + u_2(\vec{t}\cdot\vec{T})^2,$$

where $\vec{t}$ ($\vec{T}$) is the pion (nuclear) isospin. The lowest-order optical potential has only isoscalar and isovector terms. There are, however, isoscalar, isovector, and isotensor ρ^2 terms. The approach is (again) to adjust the magnitude of the ρ^2 terms to fit data, but it is believed necessary to simultaneously fit elastic-scattering, SCX, and DCX data. The elastic scattering should be insensitive to the isovector and isotensor ρ^2 terms, whereas the SCX and DCX should be insensitive to the isoscalar ρ^2 term. Although the form of the optical potential has been generalized, calculations are still performed assuming isospin invariance, and using the relations between elastic, SCX, and DCX amplitudes.

An additional parameter that is fitted is the energy shift, which arises for both kinematic and dynamic reasons. For example, in the choice of an energy at which to evaluate the t-matrix, the interaction between the nucleon and the core was ignored. This effect, as well as a poor prescription for choosing the nucleon momentum, could result in a poor choice of the energy at which to evaluate the π-N t matrix. Shifting the energy at which the phase shifts are evaluated can correct for these assumptions. One dynamic effect is the possible shifting in the Δ resonance width and energy due to interactions with the nucleus. Many calculations partially correct for the poor lowest-order prescription by including a phenomenological energy shift. The convention of [Co-80] is to evaluate the π-n phase shifts at an energy reduced by ~28 MeV. The convention of these ρ^2 fits is to include a phenomenological complex energy shift that accounts for the change in the Δ resonance energy and width.

A theoretical investigation of various effects [Jo-83b] showed that the ρ^2 terms are approximately independent of A, but strongly dependent on the pion kinetic energy. For resonance energies, it is assumed that the s-wave ρ^2 terms are unimportant. Thus, the procedure is to fit a set of data, all obtained at the same energy. The energy shift and isoscalar ρ^2 term are first adjusted to fit elastic-scattering angular distributions. The isovector and isotensor ρ^2 terms are then adjusted to simultaneously fit forward-angle SCX and DCX. Thus, data determine four complex parameters at each incident energy. To insure a consistent treatment of the nuclear structures, Skyrme III densities are used for all nuclei. The theory can be tested by predictions of SCX and DCX angular distributions and by predictions of cross sections on targets not used in the fits.

The theory and its application to data at 164 MeV are described in [Gr-84]. Figure V-1, taken from that work, displays the predicted 164-MeV DCX angular distributions. While the agreement between data and prediction is excellent, several difficulties remain. First, the theory is not applicable for nonanalog transitions, since isospin invariance is built into the calculations. Second, the microscopic origin of the values determined for the ρ^2 parameters is not adequately understood. Third, there are cases (^{42}Ca, see [Se-84]) where nuclear-structure effects which are not properly represented by the Skyrme densities are important, and result in enhanced cross sections. Thus, although ρ^2 effects are important, it is not possible to claim that DIAT DCX is understood. It is possible that the ρ^2 parameters determined may be different from the "correct" values by amounts that

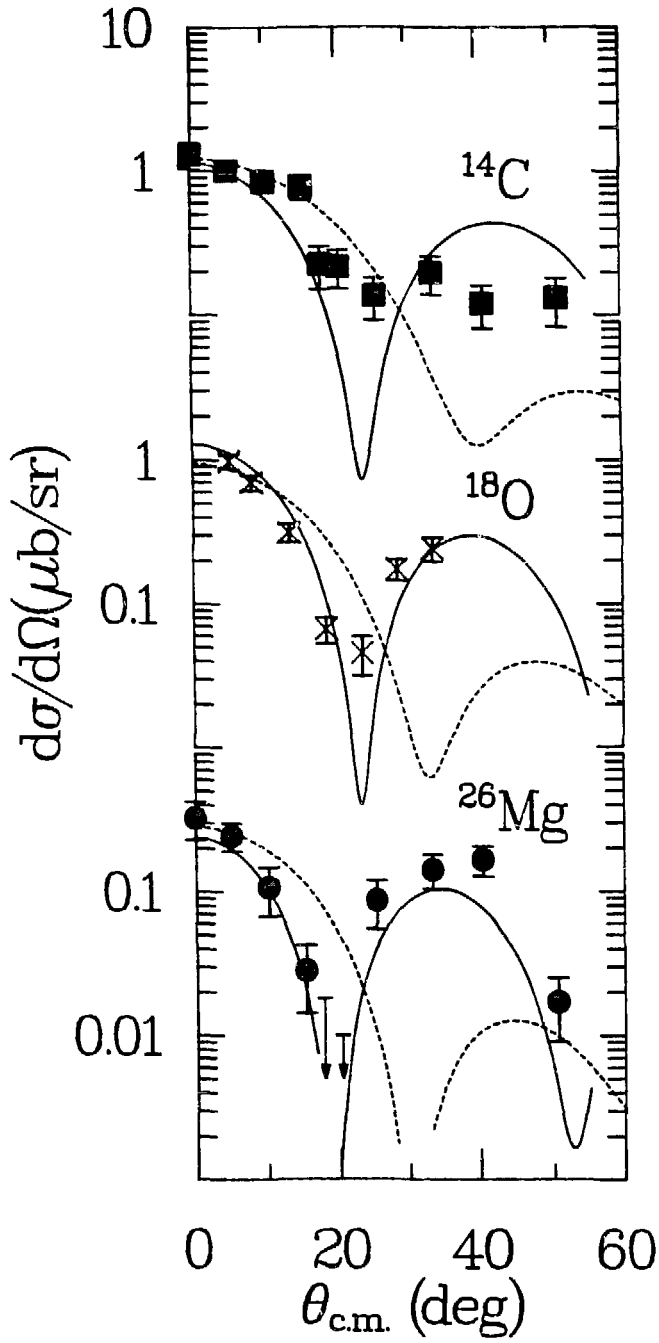

Figure V-1.
Predictions from [Gr-84] of DCX angular distributions. The dotted lines are lowest-order calculations. The solid lines include ρ^2 terms.

compensate for the effects of, e.g., additional reaction mechanisms and inadequacies in the Skyrme description of nuclear structure.

In an effort to learn about the variation of ρ^2 terms, we have repeated the fitting procedure at 230 (with Peter A. Seidl) and 292 MeV. The fits were performed with a version of the code PIESDEX linked to the MINUIT optimizing program [Ja-75]. These are the only other energies, at present, with data for elastic scattering, SCX, and DCX. (Data is becoming available at 50 MeV, but additional adjustments to the optical potential are required at lower energies, and the π-n

Table V-1. SCX and DCX data fitted with ρ^2 parameters.

230 MeV χ^2 =		2.55	292 MeV χ^2 =		2.13	2.61
data	$d\sigma/d\Omega$[a]	fit	data	$d\sigma/d\Omega$[a]	fit 1	fit 2
SCX			SCX			
^{7}Li	2.64(.16)	2.182	^{7}Li	2.15(.11)	1.963	1.937
^{14}C	2.19(.36)	2.053	^{14}C	1.89(.30)	1.929	1.857
^{90}Zr	1.23(.12)	1.473	^{90}Zr	1.48(.16)	1.473	1.445
^{120}Sn	2.10(.25)	2.339	^{120}Sn	1.74(.21)	2.202	2.434
^{208}Pb	2.17(.36)	2.273	^{208}Pb	2.28(.33)	2.190	2.243
DCX			DCX			
^{14}C	3.060(.36)	2.291	^{14}C	4.44(.39)	4.377	3.966
^{18}O	1.073(.211)	1.327	^{18}O	2.132(.110)	2.197	2.257
^{26}Mg	0.344(.075)	0.462	^{26}Mg	0.966(.138)	0.995	0.941
^{42}Ca	0.166(.047)	0.119	^{42}Ca	0.404(0.61)	0.239	0.257
^{48}Ca	1.494(.359)	1.781	^{48}Ca	1.746(.290)	1.944	2.168
^{56}Fe	0.218(.042)	0.160	^{56}Fe	0.323(.058)	0.115	0.194
			^{90}Zr	0.572(.058)	0.585	0.536

[a] SCX cross sections are at 0^{o} in (mb/sr). DCX cross sections are at 5^{o} in (μb/sr).

phase shifts are not as well determined.) Table V-1 lists the SCX and DCX data that were fitted at each energy with the best fit results. The resulting ρ^2 parameters at all three energies are given in Table V-2.

Although the lowest-order calculations of DCX assume the transition proceeds through the intermediate analog state, the ρ^2 fits are done with a closure approximation. The contributions to DCX from all intermediate states are summed. This requires an additional parameter, λ_4^2, to prevent double counting the contribution from the

Table V-2. Values of fitted ρ^2 parameters at three energies.

parameter	164 MeV	230 MeV	292 MeV 1	292 MeV 2
energy shift ES				
Re(ES)	35.0	19.96	19.24	19.24
Im(ES)	0.3	9.67	4.91	4.91
isoscalar ρ^2 λ_0^2				
Re(λ_0^2)	0.75	3.06	1.68	1.68
Im(λ_0^2)	3.67	0.85	2.38	2.38
isovector ρ^2 λ_1^2				
Re(λ_1^2)	7.71	-1.02	5.32	-2.77
Im(λ_1^2)	15.5	5.96	5.54	-0.60
isotensor ρ^2 λ_2^2				
Re(λ_2^2)	1.66	-1.62	-2.04	-2.68
Im(λ_2^2)	10.8	4.20	2.38	0.93
double-counting parameter λ_4^2				
Re(λ_4^2)	2.89	0.19	-0.63	-0.63
Im(λ_4^2)	-1.13	1.72	0.39	0.39

intermediate analog state. It is included in Table V-2 for completeness.

The success of the lowest-order sequential-charge-exchange model at higher energies qualitatively indicates that the ρ^2 terms are less important at these energies. Thus, one would expect to see that the fitted values are smaller above resonance than at resonance. This is indeed the case for the tabulated values. The magnitudes of the parameters are of similar size at 230 and 292 MeV. The isoscalar coefficient decreases by about 25% from its 164-MeV value, whereas the isovector and isotensor coefficients decrease by roughly 50%. Efforts to interpret the derived values of the ρ^2 parameters with microscopic mechanisms are in progress [Jo-85].

At 292 MeV, the sensitivity of the fit to the chosen starting value was investigated for five distinct starting values. Case I started with the values of the 164-MeV ρ^2 parameters. Case II started with ρ^2 values from an estimate of Pauli-blocking effects. Case III started with ρ^2 parameters set to 0. Case IV started with the same values as case II, except that the isotensor term had the opposite sign. Case V started with the 230-MeV ρ^2 parameters. All cases, except II, converged into a single fit. Case II resulted in a slightly worse χ^2 and slightly different angular-distribution predictions at 292 MeV (see Figure V-2). It is not clear, however, that one fit is definitely superior to the other. As at 164 MeV, the predictions are an improvement over the lowest-order calculation, although the differences are not as significant as at the lower energy. Fit 1 consistently predicts the minimum at a slightly smaller angle than that

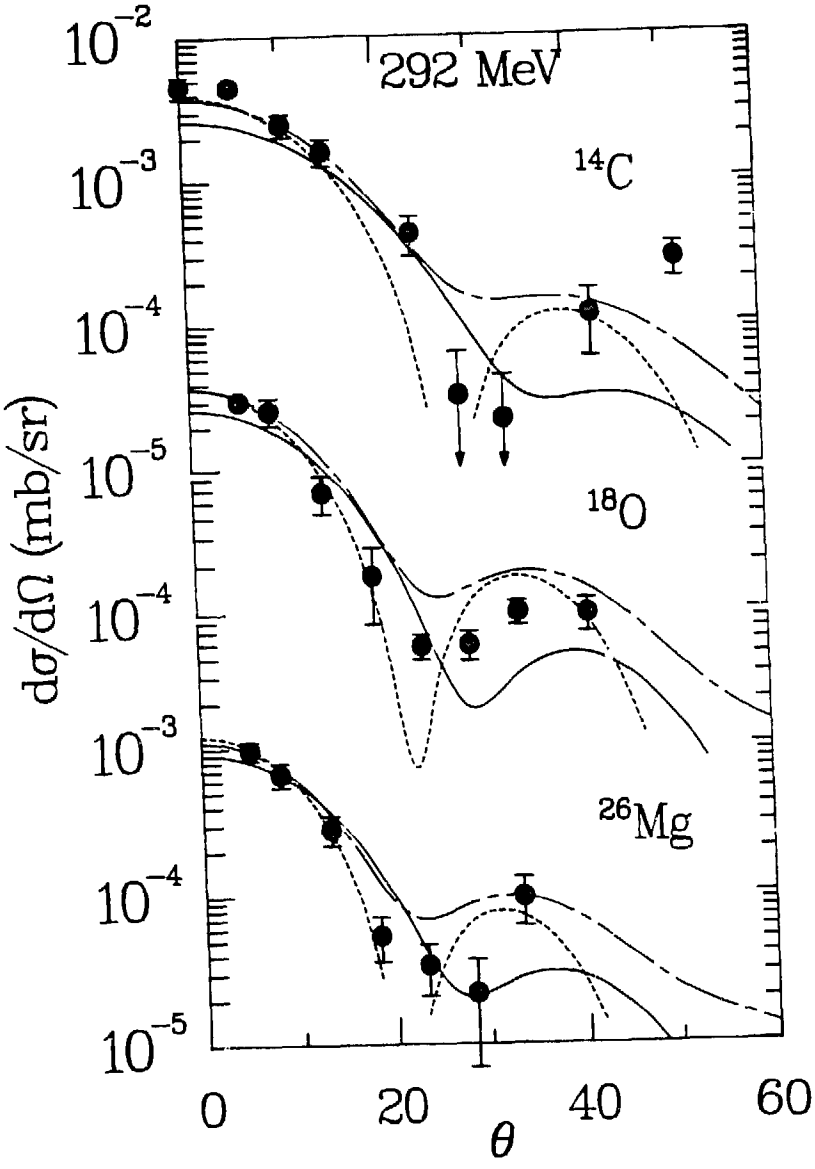

Figure V-2.
Predictions of 292-MeV DCX angular distributions with no ρ^2 terms (solid line), and ρ^2 fits (dashed line for fit 1, long-short dashed line for fit 2).

exhibited by the data. Fit 2 predicts a shallow minimum at about the correct position, but does not adequately reproduce the fall off of the angular distribution with angle.

Although the ρ^2 parameters are independent of mass [Jo-83b], they enter the optical potential in an isospin dependent way (see [Gr-84]). Thus, there is an isospin dependence to the shape of the predicted angular distributions. Figures V-3 and V-4 shown angular distribution predictions for DCX on ^{44}Ca, a T=2 target, and on ^{18}O, a T = 1 target. The differences are most pronounced at 164 MeV, where the minimum is moved inward on the T = 1 target, but outward on the T = 2 target. This prediction will be subjected to experimental verification [Fo-84]. At the higher energies, the minimum in the angular distribution is not shifted much. The prediction, however, of the 230 MeV ^{18}O angular distribution is certainly worse than the lowest-order calculation.

An effort was made at 230 MeV to examine whether small changes in the fitted parameters could result in improved agreement with the angular distributions without a significant degradation in the forward-angle cross-section fits. The isovector and isotensor ρ^2 parameters were adjusted to fit the ^{18}O angular distribution, but were constrained to not vary from the forward-angle fitted values by more than 10% of the error estimated by MINUIT. The results are shown in Table V-3. The forward-angle fit is almost unaffected, but the poor fit to the angular distribution remains. There is little change in the predicted shape. It is puzzling how to interpret the success of the ρ^2 terms in fitting the 230 MeV forward-angle SCX and DCX data, and the failure of

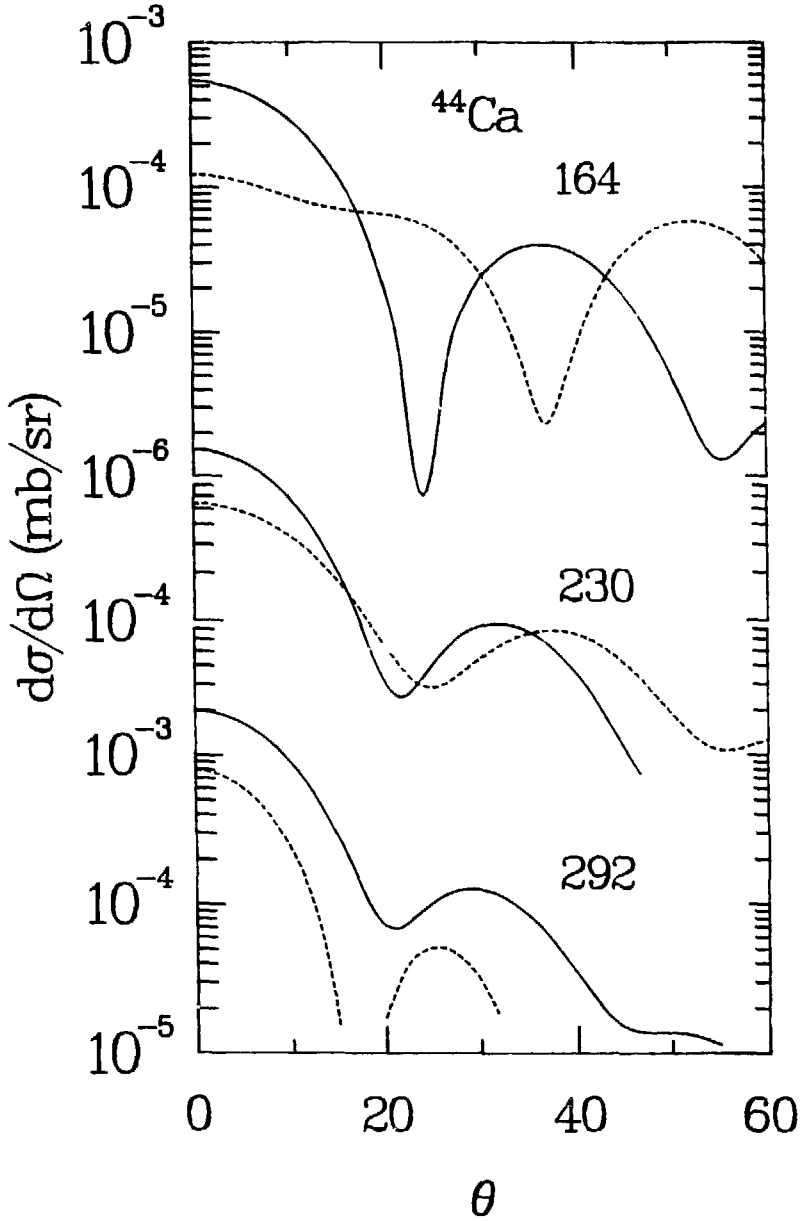

Figure V-3.
Predictions of ^{44}Ca angular distributions with (dashed line) and without (solid line) ρ^2 terms.

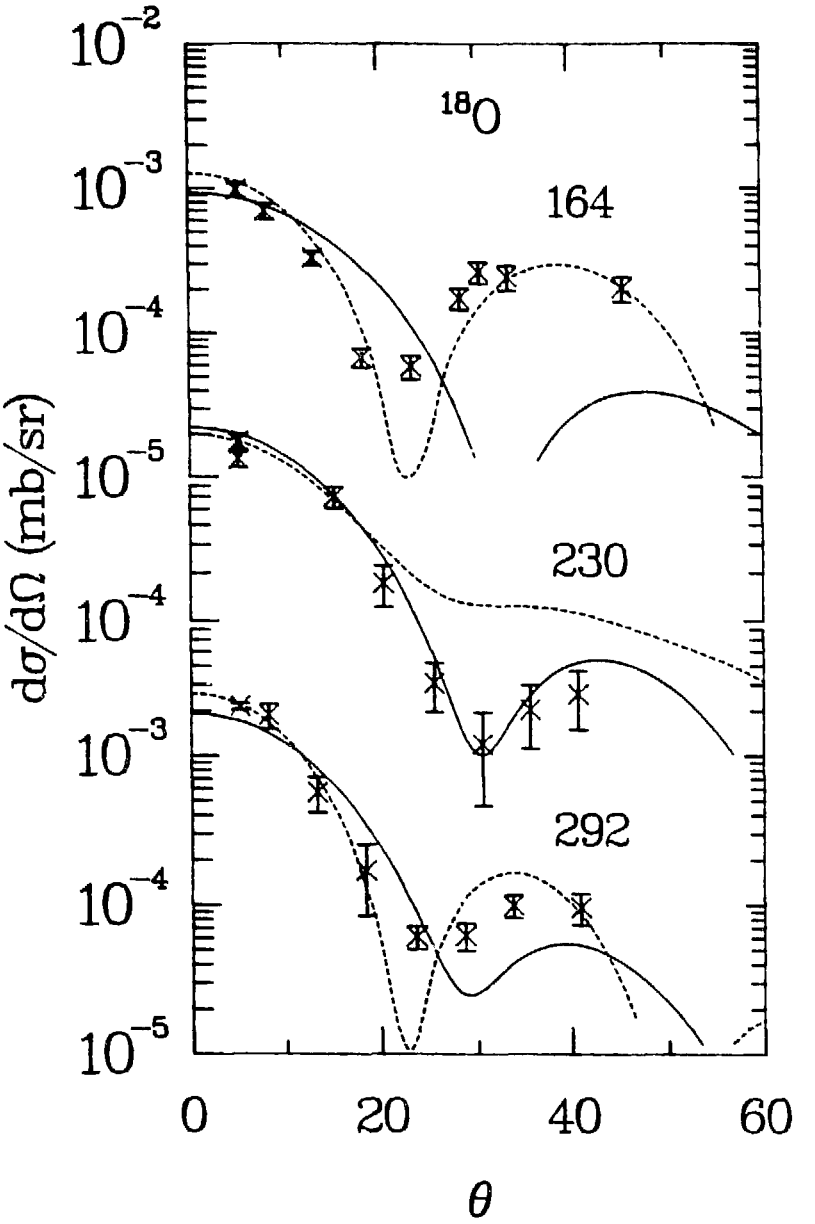

Figure V-4.
Predictions of ^{18}O angular distributions with (dashed line) and without (solid line) ρ^2 terms.

Table V-3. Adjusted values of ρ^2 parameters at 230 and 292 MeV.

quantity	230 MeV value unadjusted	adjusted
$\underline{\chi^2}$		
forward-angle	2.547	2.917
angular-distribution	40.7	32.7
isovector ρ^2 λ_1^2		
$\mathrm{Re}(\lambda_1^2)$	-1.02	-0.41
$\mathrm{Im}(\lambda_1^2)$	5.96	5.70
isotensor ρ^2 λ_2^2		
$\mathrm{Re}(\lambda_2^2)$	-1.62	-1.49
$\mathrm{Im}(\lambda_2^2)$	4.20	4.09

the ^{18}O DCX angular distribution prediction, especially given the success of the model at 164 and 292 MeV.

D. Double-Delta Calculations

Interest in double-delta mechanisms arose in part due to the suggestion [Mo-82] that nonanalog DCX was sensitive to final-state Δ-admixed components of the nuclear wave function. Diagrams for the standard sequential mechanism, final- and initial-state deltas, and for a delta-interaction mechanism are shown in Figure V-5. Calculations [Jo-84] of these mechanisms were initially performed for the DIAT on ^{18}O. Two important results were obtained. First, the Δ-admixture mechanism (DWF) was found to be relatively small compared to the usual sequential mechanism, even though the estimated size of the Δ admixture was 3-5%. Second, the delta-interaction mechanism (DINT) was found to

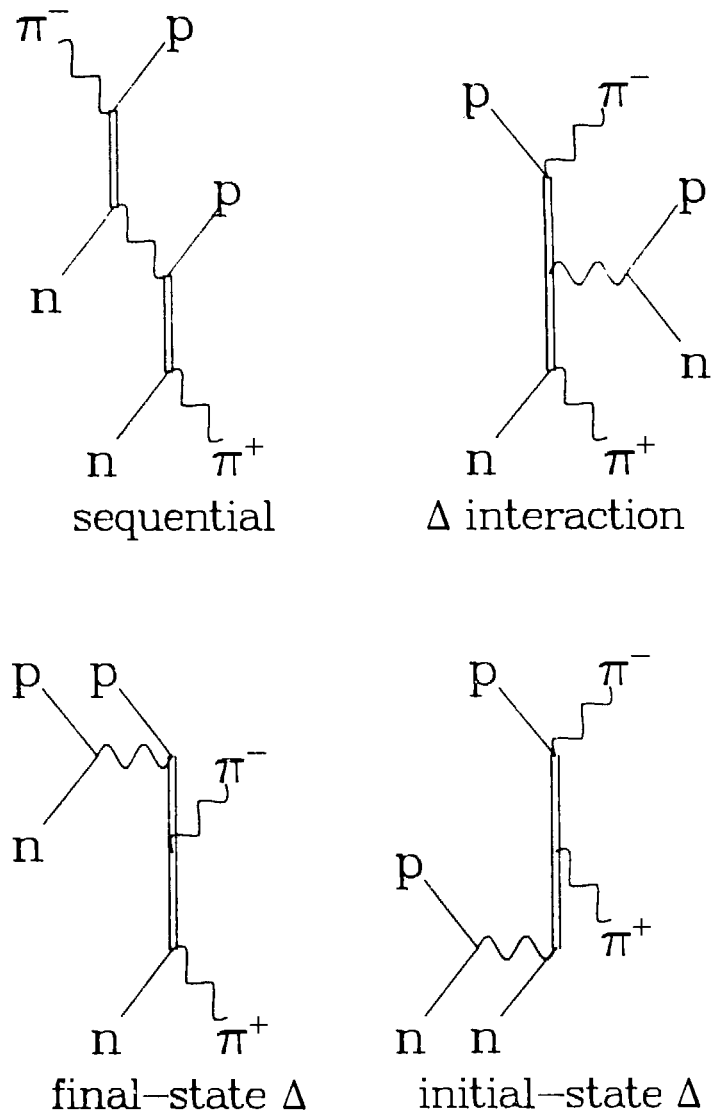

Figure V-5.
Diagrams of some processes that can contribute to DCX.

be large, of about the same size as the sequential mechanism, and to have about the same energy dependence as nonanalog DCX.

The calculations were, however, restricted to analog transitions by the method of evaluation. It was assumed that the diagrams all have transition densities proportional to the square of the excess neutron density, which drives sequential DCX. Since the same operators appear in all three mechanisms, the matrix elements of all the mechanisms are simply related by the Wigner-Eckart theorem. The amplitudes for all the diagrams are proportional to each other. Thus, the isospin relations can be used in a simple calculation for transitions between analog states to calculate all three of the mechanisms. For nonanalog transitions, the isospin relations no longer apply, and a more general calculational procedure must be employed.

The theory has been generalized [Wi-85] to apply to nonanalog transitions in an inelastic, distorted-wave impulse-approximation (DWIA) framework. As part of this work, we have encoded some of the theory, and performed many preliminary calculations investigating the sensitivities of the calculations to the input parameters that describe the reaction mechanism. Some calculations are shown in Appendix B6.

The basic elements of the theory have been presented in [Jo-84] and Appendix B6, and a detailed description of the theory [Wi-85] is to be published. Here we restrict the discussion to a brief description of the theory, a detailed description of the construction of the transition density, and a description of the sensitivities of the calculation to input parameters.

The DWIA calculations are performed with an optical potential

identical to that generated for elastic scattering. The amplitude of the inelastic transition is given by the matrix element of the perturbing operator (or potential) that induces the transition,

$$T \sim \langle \chi(\vec{\kappa})\psi(\vec{p}) | \; H' \; | \chi(\vec{\kappa}')\psi(\vec{p}') \rangle$$

where χ (χ') is the initial (final) pion wave function, Ψ (Ψ') is the initial (final) nuclear wave function, H' is the operator that induces the transition, and T is the T-matrix element connecting initial and final states. The factorization approximation is used so that the π-n t matrix is evaluated independent of the nucleon momentum. The calculation involves an integral of the product of distorted-wave pion wave functions and a nuclear transition density.

The transition density is calculated microscopically for transitions between specified shell-model configurations. Here, we will discuss only illustrative calculations of ^{16}O DCX. It was assumed that ^{16}O is a closed core, and ^{16}Ne is $\upsilon(p1/2)^{-2}\pi(d5/2)^2$. Thus, the reaction proceeds solely via a $\upsilon(p1/2)^{-2} \rightarrow \pi(d5/2)^2$ transition.

The transition density is calculated assuming both intermediate π and ρ exchange. It is a sum over five possible tensors, M_U, each of which results from a contraction of tensors in the pion momenta and nuclear spins. Transitions between $J^\pi = 0^+$ analog states are dominated by two of the tensors (see Appendix B6). Thus we neglect the other three tensors in the present calculations. In addition, the derivation of the transition density assumes that the transition involves only nucleon pairs coupled to $J^\pi = 0^+$. (Estimates with shell-model codes

indicate that this includes roughly 90% of the total transition strength.) Thus, both initial (and both final) nucleons are in the same orbit. The initial and final orbits may, however, be different.

Each tensor is also summed over all possible intermediate states. The explicit form of the transition density is given by:

$$\rho_X(\ (n11lj1 \to n1'11'j1'),\ \lambda,\ \alpha,\ \lambda',\ R) =$$

$$\sum \Big[\ (-1)^{S+S'+j1+j1'+11+11'+s1+s1'+L+1}$$

$$\times \langle n111n111;S|NLn1;S\rangle\ \langle n1'11'n1'11';S'|N'L'n'1';S'\rangle$$

$$\times \hat{S^2}\ \hat{j1}\ \hat{j2}\ \hat{S'}\ \hat{L}\ \hat{L'}\ \hat{1}\ \hat{1'}\ \hat{\lambda}\ \hat{\alpha}$$

$$\times \begin{pmatrix} L & \lambda & L' \\ 0 & 0 & 0 \end{pmatrix} \begin{pmatrix} 1 & \alpha & 1' \\ 0 & 0 & 0 \end{pmatrix} \begin{Bmatrix} L & L' & \lambda \\ 1 & 1' & \alpha \\ S & S' & \lambda' \end{Bmatrix}$$

$$\times \begin{Bmatrix} 11 & 11 & S \\ s1 & s1 & j1 \end{Bmatrix} \begin{Bmatrix} 11' & 11' & S' \\ s1' & s1' & j1' \end{Bmatrix}$$

$$\times \langle (s1,\ s1)S|(\sigma_1 \times \sigma_2)^{\lambda'}|(s1',\ s1')S'\rangle$$

$$\times R_{NL}(R)\ R_{N'L'}(R) \int r^2 dr\ R_{n1}(r)\ R_{n'1'}(r)\ H_\alpha(r)\ \Big].$$

The sum is over the parameters N, N', n, n', L, L', 1, 1', S, and S', all of which represent intermediate-state quantum numbers. Except for the quantity λ', the unprimed (primed) variables indicate initial (final) state quantities. The tensors are specified by three quantum numbers, λ, α, and λ'. The two tensors of interest both have $\lambda = 0$. One tensor has $\alpha = \lambda' = 0$, specifying a scalar interaction between the intermediate meson and nucleon. The other tensor has $\alpha = \lambda' = 2$, specifying a tensor interaction. Certain overall factors and phases in the sum have been suppressed.

The sum involves a product of initial- and final-state Moshinsky

brackets, which transform the harmonic-oscillator wave functions from particle 1 / particle 2 coordinates to relative / c.m. coordinates. The symbol $\hat{x}$ represents the quantity $\sqrt{2x+1}$. The angular momentum factors consist of the usual 3J, 6J, and 9J coefficients. In the matrix element of $\sigma\times\sigma$, the object in the center is a spherical tensor of order λ'. The radial dependence of the transition density arises from the product of the initial-and final-state c.m. radial wave functions. It should be noted that the function R_{nl} is the harmonic-oscillator radial wave function, and the coordinates R and r are the c.m. and relative nuclear coordinates, respectively. The wave function phase convention is real and positive at the origin for all ℓ, with a normalization given by

$$4\pi\int r^2 dr\ R_{nl}^2(r) = 1.$$

The radial matrix element involves an integral over a function H_α that depends on the meson-nucleon potential, and is discussed further below. To account for the strong, short-ranged, repulsive nucleon correlations, the integral is done only over radii larger than 0.5 fm.

Several quantities specifying the reaction mechanism are input to the calculation. Since the intermediate meson is allowed to be either a π or ρ meson, the overall magnitude of the calculation is proportional to

$$f_{\pi n\Delta}^2 \times f_{\pi n\Delta}^2 \times f_{\pi\Delta\Delta}^2 \times f_{\pi nn}^2$$

for the π, and to

$$f^2_{\pi n\Delta} \times f^2_{\pi n\Delta} \times f^2_{\rho\Delta\Delta} \times f^2_{\rho nn}$$

for the ρ. Thus, only the ratio

$$\frac{f^2_{\rho\Delta\Delta} \times f^2_{\rho nn}}{f^2_{\pi\Delta\Delta} \times f^2_{\pi nn}}$$

is important to the relative size of the π and ρ terms. The strengths of the couplings have been taken from [Jo-84]. The numerical value of the ratio is 4. The effect of varying the ratio has not been studied in detail; however, calculations without the ρ, corresponding to a ratio of 0, have been performed. In addition, the π and ρ are assumed to have form factors given by, e.g.,

$$\upsilon_\pi(k) = (1+k^2/\Lambda_\pi^2)^{-1}.$$

The values for the cutoff parameters, Λ_π and Λ_ρ, are controversial, model-dependent, and poorly determined. Estimates range from about 2 to 10 fm^{-1}, but some calculations have been performed with large values for Λ_π and Λ_ρ. We have investigated the effects of varying the Λ_π and Λ_ρ.

Figure V-6 shows transition densities calculated with $\Lambda_\pi = \Lambda_\rho = 6.07$ fm^{-1}, both with and without the ρ meson, for the $(p1/2)^2 + (d5/2)^2$ transition on ^{16}O. The solid curve is the sum of all terms in the transition density. The dashed curve is the scalar term $\lambda = \alpha = \lambda' = 0$, with the initial and final nucleon pairs coupled to

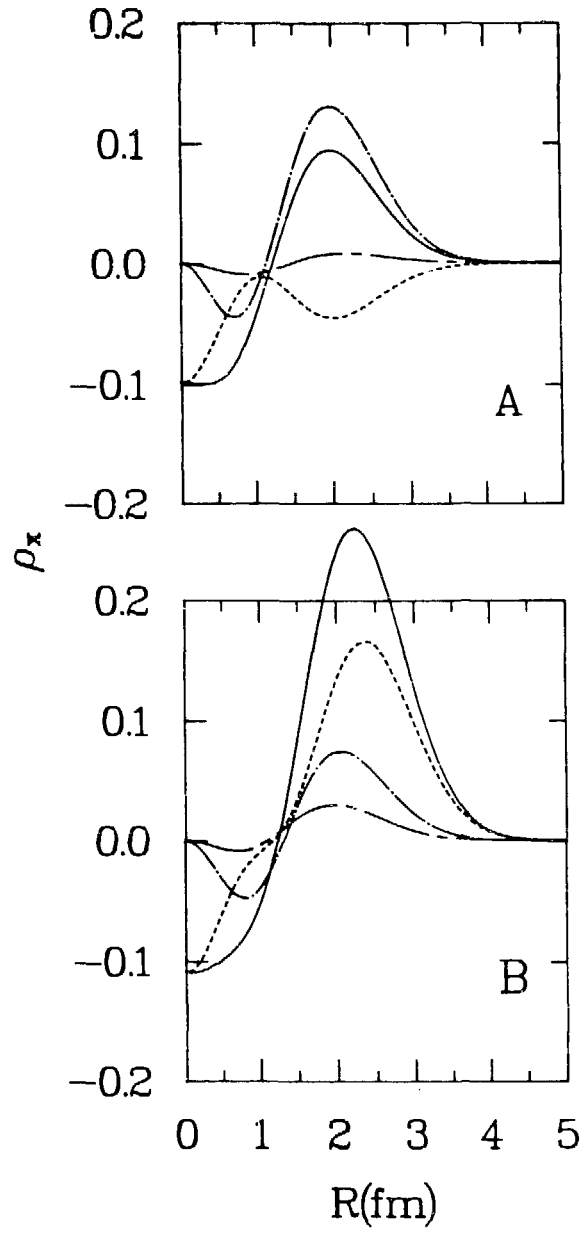

Figure V-6.
Transition densities without (A) and with (B) the ρ meson. The curves are described in the text.

S = L = 0. The chaindash curve is the same term for the nucleon pairs coupled to S = L = 1. The chaindot curve is the contribution from the tensor $\lambda = 0$, $\alpha = \lambda' = 2$ term, for which the nucleon pairs must couple to S = L = 1. We will hereafter ignore the scalar S = L = 1 term, as it is typically small for all input parameters.

The relative size of the scalar and tensor term depends strongly on the input parameters. Some of the features of the terms in the transition density can be qualitatively understood by examining the Moshinsky transformation and the meson-nucleon interaction. Assume we have two particles in the same state coupled to S = L = 1. Since the particles are in the same state, the total number of quanta is even. In the relative/c.m. system, either each wave function has an even number of quanta, or an odd number of quanta. To have a nonzero wave function at the origin, one requires an s state. But an s state and another L-even state cannot couple to S = L = 1, whereas an s state and an L-odd state cannot add to an even number of quanta. Thus, s states are not allowed for S = L = 1. This causes the transition densities to be 0 at the origin for these cases. The only allowed intermediate states are p states for S = L = 1, and s states for S = L = 0.

The π and ρ interactions (H_α) are displayed in Figure V-7. The ρ meson interaction is much shorter range than that of the π meson due to the form-factor cutoff parameters. The π and ρ tensor forces are of opposite sign, resulting in contributions to the transition density of opposite sign. With only a relative p state, which enhances the π contribution relative to the ρ contribution, and a stronger π

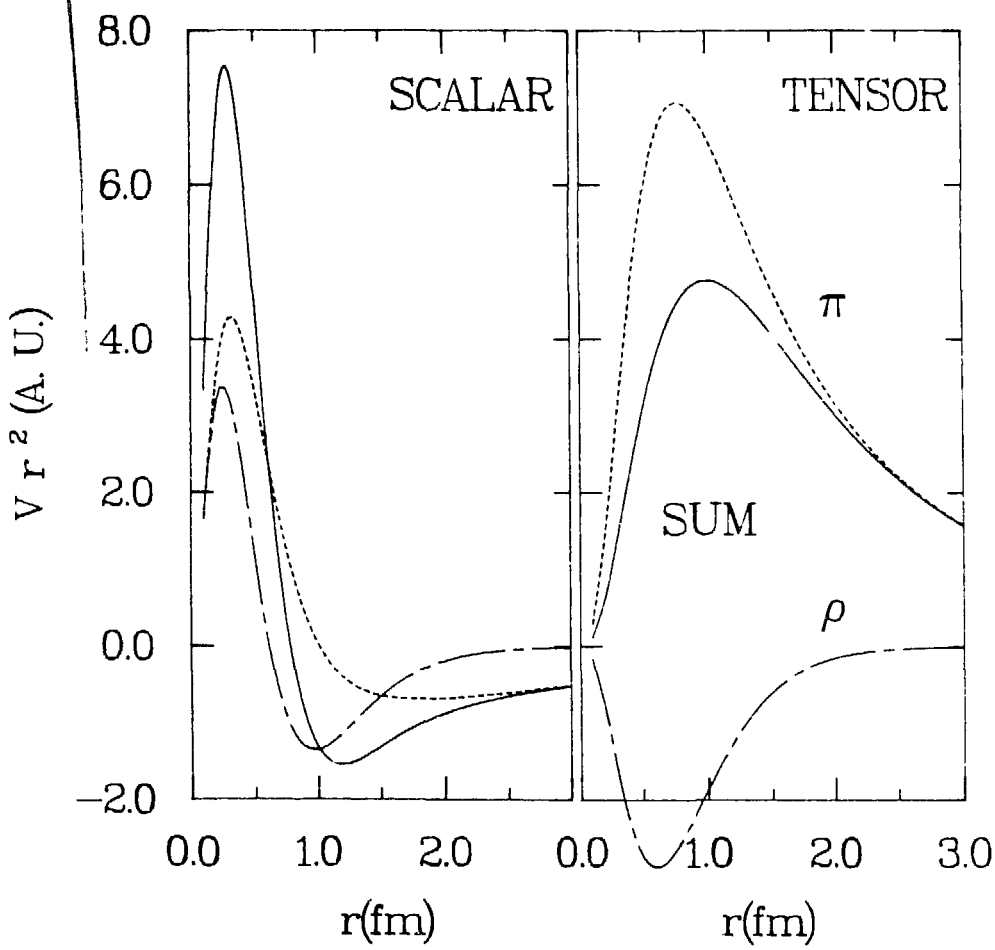

Figure V-7.
The π and ρ interaction potential H_α. The absolute normalization is arbitrary.

interaction, the inclusion of the ρ meson results in only a slight decrease of the tensor term.

No such simple arguments can be applied to the scalar term. There are five possible combinations of relative s wave functions (1s1s, 1s2s, 1s3s, 2s2s, 2s3s). The phase and magnitude of each of these five terms varies due to the product of Moshinsky brackets. Also, each term has a different radial dependence. Thus, even though the π and ρ interactions are of similar shape and magnitude, each is integrated over a sum of terms that can delicately cancel to 0 at some radii, but add in phase at other radii. Thus, the slight differences in the π and ρ meson ranges can significantly change the c.m. radial dependence.

Calculations of excitation functions and angular distributions are shown in Appendix B6. In general, we have found that the predicted shapes of the excitation functions and angular distributions are fairly insensitive to the values of the form-factor cutoff parameters, and to the inclusion of the intermediate ρ meson. The energy dependence appears to be dominated by the effects of the intermediate delta propagators and the effects of distortions. A plane-wave calculation results in a predicted excitation function that is roughly fifty times as large as the distorted-wave calculation, and has an energy dependence that is much more similar to the Δ resonance. The angular dependence reflects the nuclear size and the effects of distortions. It should be noted that plane-wave calculations do not exhibit a diffractive pattern (minima).

Because of the excellent agreement in the shapes of the excitation-function and angular-distribution predictions, and the close

agreement between the magnitudes of the data and the calculation with the best-guess values of the form factor cutoffs ($\Lambda_\pi = \Lambda_\rho = 6.07\ fm^{-1}$), we believe that this mechanism may explain nonanalog DCX. Thus, work is in progress to calculate this diagram for several target nuclei with realistic wave functions. One major unexplained feature of nonanalog DCX is the observed $A^{-4/3}$ mass dependence. Initial estimates of the mass dependence have been made with calculations for ^{16}O and ^{40}Ca with simple wave functions. These indicate a ratio of ~6 for $d\sigma(^{16}O)/d\sigma(^{40}Ca)$, rather than the ratio of ~3 measured experimentally, or the $A^{-10/3}$ ratio of ~10.

E. Other DCX Theories

There are numerous possible reaction mechanisms that can contribute to DCX besides the conventional sequential-charge-exchange mechanism and the double-delta calculations described above. The effects of, e.g., meson-exchange currents on DCX has been examined [Os-83] for DIAT transitions, and found to be small. Some speculative calculations of the contributions to DCX from six-quark bags have found that the contributions are either larger than the data [Mi-84], or smaller than the data [Ki-85], and probably can not be either calculated correctly, or extracted from the data correctly, given other uncertainties in the reaction mechanism.

One of the most successful DIAT DCX theories has been formulated by L. C. Liu [Li-83, Se-84]. Calculations are performed within a momentum-space coupled-channels framework with realistic wave functions. The optical potential is fully covariant, and includes

second-order isoscalar, isovector, and isotensor ρ^2 terms. These terms are included in the optical potential phenomenologically. The form of the terms is appropriate for either pion-absorption effects or two-nucleon short-range correlation effects. The latter, however, are believed to be small for pion scattering in the resonance region. The magnitude of the ρ^2 terms is adjusted to fit elastic scattering. Thus, DCX is predicted, rather than being fitted. It should be noted that Fermi motion and binding energy effects are treated microscopically. Thus, no additional phenomenological energy shift is included in the calculations.

Calculations have been performed for the T = 1 nuclei ^{14}C, ^{18}O, ^{26}Mg, and ^{42}Ca. The ρ^2 terms have two major effects on the predictions. First, at energies near the Δ resonance, the minima of the angular distributions are moved inward. Second, all excitation functions exhibit a peak just below the Δ resonance, although the amount of peaking and the position of the peak vary for different nuclei. For ^{18}O, the peak is at ~140 MeV, whereas for ^{14}C, the peak rises until ~70 MeV. The peak in ^{18}O is about twice the cross section of the near-resonance minimum, whereas in ^{14}C the ratio is about 5.

The predicted shapes of the excitation functions and angular distributions are in qualitative agreement with the data. Quantitative differences range from less than ~10% to a factor of ~2. Comparisons of angular distributions on T = 1 nuclei from Liu's theory and the ρ^2 fitting procedure described above show that the predicted shapes are very similar, and overall magnitudes agree within ~20%. We cannot compare T = 2 predictions, as no calculations have been performed

within Liu's model. It should be noted that, with the exception of lowest-order calculations and the DINT calculations described above, Liu's theory is the only modern DCX theory that has predicted excitation functions.

Another recent approach to DCX is the Δ-hole-model calculation of T. Karapiperis and collaborators [Ka-84]. The most significant feature of this model is its treatment of the intermediate Δ-particle, nucleon-hole states. The resonance is treated in a nonstatic manner. The effects of the intermediate-state Δ-nucleon potential are evaluated. The calculation also includes both nonanalog intermediate states, and the DINT mechanism (although in a phenomenological manner). No investigation of DCX energy dependence has been performed within this model. Calculations of ^{18}O at 164 MeV fail to explain the forward-minimum, but agree better with the data than does any other theory without ρ^2 terms. Additional calculations have been performed [Ka-85] on resonance for ^{16}O DCX. These reproduce both the magnitude and shape of the angular distribution. As yet, it is unknown whether the energy and mass dependence of nonanalog DCX could be reproduced as well.

CHAPTER VI. CONCLUSIONS

It has already been indicated in Chapter IV that a large body of data now exists for the pion DCX reaction. Over 500 data points, about 200 of them from this work, are tabulated in Appendix C. The systematic features of three classes of transitions have been described in Chapter IV. We emphasize here the conclusions of the description.

DIAT are well described at higher energies by simple sequential charge exchanges. Lowest-order DCX calculations provide predictions accurate to a ~20% level in overall magnitude, energy dependence, and angular distribution shape. At energies below ~200 MeV, the lowest-order model fails, and more complicated models are necessary to understand the reaction.

Nonanalog I transitions show a particularly simple, regular set of features. The energy dependence is similar to that of the underlying Δ resonance. The angular dependence is diffractive. The mass dependence is a smooth, but unexpected, $A^{-4/3}$. The strength of these transitions (of similar size to DIAT transitions in T = 1 nuclei of similar mass) is much larger than anticipated.

Nonanalog II transitions have the same energy dependence as nonanalog I transitions. Transitions on T = 0 targets to first-excited 2^+ states appear to have a larger total cross section than the corresponding ground state transition. Only a few cases of this sort have been investigated, however.

The systematics of the data are on a much firmer basis than the theoretical interpretations. We have described in Chapter V several of the many approaches to understanding aspects of DCX. While some

theories present complementary results, others present conflicting interpretations. We believe that an adequate understanding of DCX requires simultaneous understanding of several reactions. We have stated in Chapter V that a consistent explanation for both analog and nonanalog DCX is necessary, since reaction mechanisms contributing to one will, in general, contribute to the other.

In addition, an explanation of DCX will require an understanding of both analog and nonanalog SCX. It is clear that sequential charge exchanges through the intermediate analog state are the dominant reaction mechanism for high energy DCX. Both the success of lowest-order calculations and the small cross sections measured for nonDIAS discrete states support this conjecture. At lower energies, it is not yet known whether an improved treatment of sequential charge exchange will suffice to explain DCX quantitatively, or whether other mechanisms contribute significantly to the reaction. If the first step of a two-step reaction cannot be correctly predicted, there can be little confidence in the prediction for the final state.

Many SCX cross sections have been measured. The A dependence has been found to be $\sim A^{-4/3}$, as expected. The angle dependence has been found to be diffractive near resonance, as expected. The major disagreement has been in the absolute magnitude of the data. At energies near 200 MeV, SCX data are consistently larger than predicted by lowest-order theories, whereas at 292 MeV, the data are consistently smaller than predicted. In the unified-analysis approach of Johnson and Siciliano, these differences can be induced by large isovector ρ^2 terms, but that requires large isotensor ρ^2 terms to rescale the DCX

back to the values predicted by lowest-order theory, which are close to the measured cross sections.

It is also clear that DCX, as well as any other nonelastic reaction, requires an understanding of elastic scattering for valid predictions to be made. In a DWIA formalism, the distorted pion waves are generated with the same potential used to describe elastic scattering. If isospin identities are used, the DCX amplitude is a sum of elastic amplitudes. At present, there are many approaches to elastic scattering which are successful at a several per cent level, and some that are successful at a few percent level. The major disagreements at resonance energies are for predictions of large angle ($\theta > 90^{o}$) elastic scattering.

At present, there appear to be two possible approaches that might explain both analog and nonanalog DCX. The simpler possibility is that sequential charge exchange with realistic wave functions and a higher-order optical potential will account for nonanalog DCX. The more complicated possibility is that this mechanism must be added to various other nonsequential mechanisms to explain both analog and nonanalog DCX. Due to the much simpler features of nonanalog DCX data, we will discuss the possible explanations of these transitions first.

As has been shown in Chapter V and Appendix B6, the energy and angle dependence of nonanalog DCX can be explained by the delta-interaction diagram. Almost any reaction model for nonanalog DCX has to get about the correct angle dependence. This results simply from the fact that it is a 0^{+} to 0^{+} inelastic transition in a strong-absorption interaction region. Calculations will reflect the input

nuclear size, which will be similar in all cases. The correct prediction of the energy dependence is, however, a new and significant result. Most significant is the as yet unexplained A dependence. If, with the use of realistic wave functions, the DINT calculations manage to reproduce the nonanalog mass dependence, then there will be a complete explanation of nonanalog I DCX.

It should be noted, however, that several calculations of the ratio of ^{16}O DCX to ^{18}O DCX have been performed. These indicate that, with the use of realistic wave functions, the sequential cross section for ^{16}O should be roughly one-third that for ^{18}O. This would indicate a sequential cross section of 200 → 500 nb/sr for ^{16}O at 5° and 164 MeV, in agreement with the data. These predictions would, of course, predict the ^{16}O angle dependence correctly. There are no published calculations, however, of, e.g., the ^{16}O energy dependence, nor any indication in published works that the cross section ratios should be energy dependent. If we assume the energy dependence should be similar to that for ^{16}O, we conclude that the calculations are inconsistent with the data, and probably wrong. Recent unpublished calculations by C. L. Morris [Mo-85] confirm that nonanalog sequential charge exchange routes should exhibit a similar energy dependence to lowest-order sequential calculations. Thus, there are no indications that, in the absence of ρ^2 terms, sequential charge exchange can explain nonanalog DCX data. It should be noted that calculations of nonanalog DCX are possible within Liu's model, but have not been performed in the past due to the lack of adequate wave functions. Work on these calculations is underway at present. Since the effects of the

ρ^2 terms are largest at energies near the Δ resonance, these calculations may result in a peaked energy dependence.

The unexplained feature is still the mass dependence of nonanalog DCX. It is more logical to assume that the smooth mass dependence results from a reaction mechanism property independent of the details of nuclear structure. No proper calculations have been done for either the DINT or sequential mechanisms, however. Thus, it cannot be concluded that either of these mechanisms is responsible for nonanalog DCX. The regular features of the data do, however, seem to imply domination by a single reaction mechanism. Since calculations of both are of similar size to the data, we conclude that at least one set of calculations is probably wrong.

DIAS DCX is at least as complicated as nonanalog DCX at lower energies. If nonanalog DCX results from sequential charge exchanges, there will be similar transitions leading to the analog state plus a large transition through the intermediate analog state, plus the effects of the higher-order optical potential. If DINT were to explain nonanalog DCX, there is the interference of this mechanism as well.

The only models that have correctly predicted the forward minima in the ^{18}O angular distribution have been the higher-order optical-potential models of Liu and of Johnson and Siciliano. Given the accuracy of their predictions, it must be questioned whether we actually do understand DIAT DCX. If they are the correct explanation for analog DCX, then either the two-amplitude model is wrong, or the DINT mechanism does not contribute to analog DCX, or nonanalog DCX results from sequential charge exchanges.

One possible explanation is that the DINT mechanism is much smaller than has been estimated in this work, and sequential charge exchange explains DCX. "Correct" values for the coupling coefficients and form-factor cut-off parameters would result in a much smaller contribution to DCX that would not be noticeable because of much larger sequential contributions. Three calculations of analog DCX with the DINT mechanism have been performed. Hoodboy et al. [Ho-83] investigated the interference of sequential DCX and DINT, adjusting the strength of the latter, in an effort to explain the forward minimum in the ^{18}O angular distribution at 164 MeV. They found it was impossible to simultaneously reproduce both the forward minimum in the angular distribution and the overall magnitude of the data. Karapiperis et al. [Ka-85], in a similar effort (see Chapter V-E), achieved essentially the same results. Johnson et al. [Jo-84], in an earlier version of the present DINT calculations, found that the overall magnitude of the data was adjusted without much change to the shape of the angular distribution. No phenomenological investigation was made. We have, within the present framework, performed DINT calculations for the ^{18}O reaction. We find that DINT and sequential mechanisms have a similar angular dependence. Apparently, the phase between them is such that the minima is not shifted. Clearly, one future project, given that the DINT mechanism is important, is to interfere DINT and sequential mechanisms with realistic wave functions and a higher-order optical potential.

It is important at this point to note some of the inconsistencies in various DCX calculations. While, for example, three calculations of

the contributions of DINT to analog DCX have found similar results, the estimated sizes of DINT and the sequential contribution to nonanalog DCX appear inconsistent. Similarly, although both Liu and Johnson and Siciliano find similar effects from the higher-order optical potential on T = 1 nuclei near resonance, their predictions for T = 2 nuclei and their interpretations of what mechanisms result in the ρ^2 terms appear inconsistent.

We conclude that a consistent explanation of both nonanalog and DIAT DCX is possible in the near future. It requires a predominantly theoretical effort. Two possible forms that this explanation could take have been suggested. There could, however, be additional, unanticipated, important reaction mechanisms and higher-order effects.

APPENDIX A. COMPILATION OF DCX PUBLICATIONS

Following is a less than comprehensive listing of pion DCX articles either submitted to or published in refereed journals since 1973. They are ordered inversely to the date of publication. An excellent additional source of information is the as yet unpublished "Proceedings of the LAMPF Workshop on Pion Double Charge Exchange", held January 10 - 12, 1985, at Los Alamos. Also, three Ph.D. theses based on EPICS DCX measurements have been issued as Los Alamos reports. These are:

Steven J. Greene, University of Texas (1981); LA-8891-T (1981).

Mark O. Kaletka, Northwestern University (1983); LA-9947-T (1984).

Peter A. Seidl, University of Texas (1984); LA-10338-T (1985).

The articles follow.

"Delta-Hole Approach to Pion Double Charge Exchange" by T. Karapiperis and M. Kobayashi, SIN preprint (1985).

"Disentangling N, A Dependence of Non-Analog Double Charge Exchange" by H. T. Fortune, L. C. Bland, C. L. Morris, and C. Fred Moore, accepted by Nucl. Phys.

"Observation of the Double Isobaric Analog Transition $^{18}O(\pi^+,\pi^-)^{18}Ne$ at 50 MeV" by A. Altman, R. R. Johnson, U. Wienands, N. Hessey, B. M. Barnett, B. M. Forster, N. Grion, D. Mills, F. M. Rozon, G. R. Smith, R. P. Trelle, D. R. Gill, G. Sheffer, and T. Anderl, Phys. Rev. Lett. 55, 1273 (1985).

"Systematics of Continuum Pion Double Charge Exchange on T=0

Nuclei" by S. Mordechai, Peter A. Seidl, C. Fred Moore, L. C. Bland, R. Gilman, Kalvir S. Dhuga, H. T. Fortune, C. L. Morris, and S. J. Greene, Phys. Rev. C 32, 999 (1985).

"Calculations of Nonanalog Pion Double Charge Exchange" by R. Gilman, H. T. Fortune, Mikkel B. Johnson, E. R. Siciliano, H. Toki, and A. Wirzba, Phys. Rev. C 32, 349 (1985).

"Observation of Double Analog States in ^{88}Zr and ^{90}Mo and the Neutron Excess and Mass Systematics of Pion Double Charge Exchange" by Kamal K. Seth, M. Kaletka, D. Barlow, D.Kielczewska, A. Saha, L. Casey, D. Godman, R. Seth, and J. Stuart, Phys. Lett. 155B, 339 (1985).

"The Double Analog Transition $^{14}C(\pi^+,\pi^-)^{14}O$ at 50 MeV" by M. J. Leitch, E. Piasetzky, H. W. Baer, J. D. Bowman, R. L. Burman, B. J. Dropesky, P. A. M. Gram, F. Irom, D. Roberts, G. A. Rebka, J. N. Knudson, J. R. Comfort, V. A. Pinnick, D. H. Wright, and S. A. Wood, Phys. Rev. Lett. 54, 1482 (1985).

"Multiple-Scattering Approach to Pion Double Charge Exchange at 50 MeV" by T. Karapiperis and M. Kobayashi, Phys Rev. Lett. 54, 1230 (1985).

"The Energy Dependence of $^{18}O(\pi^+,\pi^-)^{18}Ne(gs)$", by Peter A. Seidl, C. Fred Moore, S. Mordechai, R. Gilman, Kalvir S. Dhuga, H. T. Fortune, J. D. Zumbro, C. L. Morris, J. A. Faucett, and G. R. Burleson, Phys. Lett. 154B, 255 (1985).

"Properties of the $^{208}Po(0^+, T = 22)$ Double Isobaric Analog Resonance", by C. L. Morris, R. L. Boudrie, Steven J. Greene, R. Gilman, H. T. Fortune, J. D. Zumbro, J. A. Faucett, G. R. Burleson,

Kalvir S. Dhuga, Peter A. Seidl, S. Mordechai, and C. Fred Moore, Phys. Rev. Lett. 54, 775 (1985).

"Two-Amplitude Model of Pion DCX Applied to ^{18}O Angular Distribution and Excitation Function" by R. Gilman, L. C. Bland, Peter A. Seidl, C. Fred Moore, C. L. Morris, Steven J. Greene, and H. T. Fortune, Nucl. Phys. A432, 610 (1985).

"Quasi-α-Particle Mechansm of Pion Double Charge Exchange on Light Nuclei" by R. I. Jibuti and R. Ya. Kezerashvili, Nucl. Phys. A430, 573 (1984).

"Six-Quark Cluster Components of Nuclear Wave Functions with the Pion-Nucleus Double-Charge-Exchange Reaction" by Gerald A. Miller, Phys. Rev. Lett. 53, 2008 (1984).

"Pion Charge Exchange from Oriented, Deformed Nuclei" by H.-C. Chiang and Mikkel B. Johnson, Phys. Rev. Lett. 53, 1996 (1984).

"Search for the Tetraneutron by the Double-Charge-Exchange of Negative Pions" by J. E. Ungar, R. D. Mckeown, D. F. geesaman, R. J. Holt, J. R. Specht, K. E. Stephenson, B. Zeidman, and C. L. Morris, Phys. Lett. 144B, 333 (1984).

"A Unified Analysis of Pion Single- and Double-Charge-Exchange Scattering in the Resonance Region" by Steven J. Greene, C. J. Harvey, P. A. Seidl, R. Gilman, E. R. Siciliano, and Mikkel B. Johnson, Phys. Rev. C 30, 2003 (1984).

"$^{13}C(\pi^+,\pi^-)^{13}O$ Near the Δ_{33} Resonance" by Peter A. Seidl, Mark D. Brown, Rex R. Kiziah, C. Fred Moore, Helmut Baer, Christopher L. Morris, G. R. Burleson, W. B. Cottingame, Steven J. Greene, L. C. Bland, R. Gilman, and H. T. Fortune, Phys. Rev. C 30, 1076 (1984).

"Pion Double Charge Exchange on T=1 Nuclei" by Peter A. Seidl, Mark D. Brown, Rex R. Kiziah, C. Fred Moore, Helmut Baer, C. L. Morris, G. R. Burleson, W. B. Cottingame, Steven J. Greene, L. C. Bland, R. Gilman, and H. T. Fortune, Phys. Rev. C 30, 973 (1984).

"Nonanalog (π^-,π^+) Double Charge Exchange on ^{18}O" by R. Gilman, H. T. Fortune, L.C. Bland, Rex R. Kiziah, C. Fred Moore, Peter A. Seidl, C. L. Morris, and W. B. Cottingame, Phys. Rev. C 30, 962 (1984).

"^{14}Be via Pion Double Charge Exchange" by R. Gilman, H. T. Fortune, L. C. Bland, Rex R. Kiziah, C. Fred Moore, Peter A. Seidl, C. L. Morris, and W. B. Cottingame, Phys. Rev. C 30, 958 (1984).

"Delta-Hole Description of the Double Charge Exchange Reaction $^{18}O(\pi^+,\pi^-)^{18}Ne$(g.s.)" by T. Karapiperis, M. Kobayashi, and M. Hirata, Phys. Lett. 144B, 23 (1984).

"Energy Dependence of Angular Distributions in the Nonanalog Pion Double-Chage-Exchange Reaction $^{16}O(\pi^+,\pi^-)^{16}Ne$(g.s.)" by R. Gilman, H. T. Fortune, Kalvir S. Dhuga, Peter H. Kutt, L.C. Bland, Rex R. Kiziah, C. Fred Moore, Peter A. Seidl, C. L. Morris, and W. B. Cottingame, Phys. Rev. C 29, 2395 (1984).

"Core-Excitation Effects in Pion Double Charge Exchange" by Kamal K. Seth, M. Kaletka, S. Iversen, A. Saha, D. Barlow, D. Smith, and L. C. Liu, Phys. Rev. Lett. 52, 894 (1984).

"Δ_{33} Dynamics in Pion Double Charge Exchange" by Mikkel B. Johnson, E. R. Siciliano, H. Toki, and A. Wirzba, Phys. Rev. Lett. 52, 593 (1984).

"Pion Double Charge Exchange at 50 MeV on ^{14}C" by I. Navon, M. J. Leitch, D. A. Bryman, T. Numao, P.Schlatter, G.Azuelos, R. Poutissou,

R. A. Burnham, M. Hasinoff, J. M. Poutissou, J. A. Macdonald J. E. Spuller, C. K. Hargrove, H. Mes, M. Blecher, K. Gotow, M. Moinester, and H. Baer, Phys. Rev. Lett. 52, 105 (1984).

"Meson-Exchange Currents in Pion-Nucleus Double-Charge-Exchange Reactions" by E. Oset, D. Strottman, M. J. Vicente-Vacas, and Ma Wei-Hsing, Nucl. Phys. A408, 461 (1983).

"Systematics of Pion Double-Charge-Exchange Reactions on T=0 Nuclei" by L. C. Bland, R. Gilman, M. Carchidi, K. Dhuga, Christopher L. Morris, H. T. Fortune, S. J. Greene, Peter A. Seidl, and C. Fred Moore, Phys. Lett. 128B, 157 (1983).

"Diffractive Angular Distribution for $^{16}O(\pi^+,\pi^-)^{16}Ne(g.s.)$" by S. J. Greene, W. B. Cottingame, G. R. Burleson, L. C. Bland, R. Gilman H. T. Fortune C. L. Morris, D. B. Holtkamp, and C. Fred Moore, Phys. Rev. C 27, 2375 (1983).

"Observation of Analog and Nonanalog Transitions in the Reaction $^{56}Fe(\pi^+,\pi^-)^{56}Ni$" by Peter A. Seidl, Rex R. Kiziah, Mark D. Brown, C. Fred Moore, C. L. Morris, Helmut Baer, Steven J. Greene, G. R. Burleson, W. B. Cottingame, L. C. Bland, R. Gilman, and H. T. Fortune, Phys. Rev. Lett. 50, 1106 (1983).

"Theory of Pion Single and Double Charge Exchange in the Resonance Region II: Dynamical Corrections" by Mikkel B. Johnson and E. R. Siciliano, Phys. Rev. C 27, 1647 (1983).

"Diffraction Theory and the Double-Charge-Exchange Reaction $^{18}O(\pi^+,\pi^-)^{18}Ne$" by L. C. Liu, Phys. Rev. C 27, 1611 (1983).

"Pion-Nucleus Charge-Exchange Reactions with Isobar Dynamics" by

Pervez Hoodbhoy, Roger A. Freedman, Gerald A. Miller, and Ernest M. Henley, Phys. Rev. C 27, 277 (1983).

"Energy Dependence of Pion-Induced Isotensor Double Charge Exchange" by L. C. Bland, H. T. Fortune, S. J. Greene, C. Fred Moore, C. L. Morris, J. Phys. G 8, L173 (1982).

"Target Mass Dependence of Isotensor Double Charge Exchange: Evidence for Deltas in Nuclei" by C. L. Morris, H. T. Fortune, L. C. Bland, R. Gilman, S. J. Greene, W. B. Cottingame, D. B. Holtkamp, G. R. Burleson, C. Fred Moore, Phys. Rev. C 25, 3218 (1982).

"Pion Double Charge Exchange on Ca Isotopes" by H. T. Fortune, S. J. Greene, C. F. Moore, and C. L. Morris, Phys. Rev. C 25, 2142 (1982).

"Systematics in Pion Double Charge Exchange" by S. J. Greene, W. J. Braithwaite, D. B. Holtkamp, W. B. Cottingame, C. F. Moore, G. R. Burleson, G. S. Blanpied, A. J. Viescas, C. H. Daw, C. L. Morris, and H. A. Thiessen, Phys. Rev. C 25, 927 (1982).

"Interference Effects in Pion Double Charge Exchange" by S. J. Greene, D. B. Holtkamp, W. B. Cottingame, C. Fred Moore, G. R. Burleson, C. L. Morris, H. A. Thiessen, and H. T. Fortune, Phys. Rev. C 25, 924 (1982).

"Pion Double Charge Exchange on ^{4}He and Meson Exchange Currents" by A. Stetz, L. W. Swenson, J. Davis, J. Kallne, R. C. Minehart, R. R. Whitney, V. Perez-Mendez, A. Sagle, J. Carroll, J. B. Mcclelland, and J. Faucett, Phys. Rev. Lett. 47, 782 (1981).

"Elastic Pion Double Charge Exchange Reactions" by Gerald A. Miller, Phys. Rev. C 24, 221 (1981).

"π^+ - ^{16,18}O Double Charge Exchange Reaction" by Liu Xianhui, Wu Zongen, Huang Zhaohui, and Li Yangguo, Sci. Sin. 24, 789 (1981).

"A Closure Approximation Calculation of a Pion Double-Charge-Exchange Reaction" by Guang-Lie Li, Chu-Hsia Li, and T.-S. H. Lee, Phys. Lett. 99B, 200 (1981).

"Double Charge Exchange and One-Pion Production in π^+ ^{4}He Collisions at 1.7 GeV/c" by J. B. Jeanneret, M. Bogdanski, and E. Jeannet, Nucl. Phys. A350, 345 (1980).

"Limitations of Pion Double Charge Exchange Calculations Using Isospin Identities" by WilLiam A. Gerace, Morton M. Sternheim, Kwang-Bock Yoo, and David A. Sparrow, Phys. Rev. C 22, 2497 (1980).

"Identification and Measurement of the Mass of ^{26}Ne(g.s.) by the ^{26}Mg(π^-,π^+)^{26}Ne Reaction" by H. Nann, Kamal K. Seth, S. G. Iversen, M. O. Kaletka, D. B. Barlow, and D. Smith, Phys. Lett. 96B, 261 (1980).

"Observation of A Double Isobaric Analog State in the Reaction ^{209}Bi(π^+,π^-)^{209}At" by C. L. Morris, H. A. Thiessen, W. J. Braithwaite, W. B. Cottingame, S. J. Greene, D. B. Holtkamp, I. B. Moore, C. Fred Moore, G. R. Burleson, G. S. Blanpied, G. H. Daw, and A. J. Viescas, Phys. Rev. Lett. 45, 1233 (1980).

"Isospin Quintets in the 1P and S-D Shells" by G. R. Burleson, G. S. Blanpied, G. H. Daw, A. J. Viescas, C. L. Morris, H. A. Thiessen, S. J. Greene, W. J. Braithwaite, W. B. Cottingame, D. B. Holtkamp, I. B. Moore, and C. F. Moore, Phys. Rev. C 22, 1180 (1980).

"Analytical Theory of Pion Single and Double Charge Exchange in Resonance Region. I. Geometrical Limit" by Mikkel B. Johnson, Phys. Rev. C 22, 192 (1980).

"Inelastic Pion Double Charge Exchange on ^{16}O at 240 MeV" by R. E. Mischke, A. Blomberg, P. A. M. Gram, J. Jansen, J. Zichy, J. Bolger, E. Boschitz, C. H. Q. Ingram, and G. Probstle, Phys. Rev. Lett. 44, 1197 (1980).

"New Results in Nuclear Structure from Pion Inelastic Scattering and Reactions Near 180 MeV" by H. A. Thiessen, Nucl. Phys. A335, 329 (1980).

"Studies of the Pion Double-Charge-Exchange Reaction $^{18}O(\pi^+,\pi^-)^{18}Ne$" by S. J. Greene, W. J. Braithwaite, D. B. Holtkamp, W. B. Cottingame, C. F. Moore, C. L. Morris, H. A. Thiessen, G. R. Burleson, and G. S. Blanpied, Phys. Lett. 88B, 62 (1979).

"Angular Distributions for the Reaction $^{18}O(\pi^+,\pi^-)^{18}Ne$ and Pion Double-Charge-Exchange Form Factors" by Kamal K. Seth, S. Iversen, H. Nann, M. Kaletka, J. Hird, and H. A. Thiessen, Phys. Rev. Lett. 43, 1574 (1979); ibid 45, 147 (1980).

"Pion Double Charge Exchange Reactions in ^{12}C and $^{40,44,48}Ca$" by J. Davis, J. Kallne, J. S. Mccarthy, R. C. Minehart, C. L. Morris, H. A. Thiessen, G. Blanpied, G. R. Burleson, K. Boyer, W. Cottingame, C. F. Moore, and C. A. Goulding, Phys. Rev. C 20, 1946 (1979).

"Pion-Nucleus Charge Exchange Reactions" by Jonas Alster and Jaime Warszawski, Phys. Rep. 52, 87 (1979).

"Mass of ^{18}C by Pion Double-Charge-Exchange Reaction" by Kamal K. Seth, H. Nann, S. Iversen, M. Kaletka, J. Hird, and H. A. Thiessen, Phys. Rev. Lett. 41, 1589 (1978).

"Pion-Induced Double Charge Exchange on ^{18}O" by D. A. Sparrow and A. S. Rosenthal, Phys. Rev. C 18, 1753 (1978).

"Pion Double-Charge Exchange on ^{16}O and ^{18}O" by R. L. Burman, M. P.Baker, M. D. Cooper, R. H. Heffner, D. M. Lee, R. P. Redwine, J. E. Spencer, T. Marks, D. J. Malbrough, B. M. Preedom, R. J. Holt, and B. Zeidman, Phys. Rev. C 17, 1774 (1978).

"Nuclear Structure Effects in Pion Double Charge Exchange" by E. Oset, D. Strottman, and G. E. Brown, Phys. Lett. 73B, 393 (1978).

"Nuclear-Structure Effects in Pion Double Charge Exchange" by T.-S. H. Lee, D. Kurath, and B. Zeidman, Phys. Rev. Lett. 39, 1307 (1977).

"Observation of the ^{18}Ne Ground State in the Pion Double-Charge-Exchange Reaction $^{18}O(\pi^+,\pi^-)^{18}Ne$" by C. Perrin, J.-P. Albanese, R. Corfu,J.-P. Egger, P. Gretillat, C. Lunke, J. Piffaretti, E. Schwarz, J. Jansen, and B. M. Preedom, Phys. Lett. 69B, 301 (1977).

"Pion Non-Analog Double Charge Exchange: $^{16}O(\pi^+,\pi^-)^{16}Ne$" by R. J. Holt, B. Zeidman, D. J. Malbrough, T. Marks, B. M. Preedom, M. P. Baker, R. L. Burman, M. D. Cooper, R. H. Heffner, D. M. Lee, R. P. Redwine, and J. E. Spencer, Phys. Lett. 69B, 55 (1977).

"Pion Double Charge Exchange on ^4He" by W. R. Gibbs, B. F. Gibson, A. T. Hess, and G. J. Stephenaon, Jr., Phys. Rev. C 15, 1384 (1977).

"Observation of the Pion Double-Charge-Exchange Reaction $^{18}O(\pi^+,\pi^-)^{18}Ne$" by T. Marks, M. P. Baker, R. L. Burman, M. D. Cooper, R. H. Heffner, R. J. Holt, D. M. Lee, D. J. Malbrough, B. M. Preedom, R. P. Redwine, J. E. Spencer, and B. Zeidman, Phys. Rev. Lett. 38, 149 (1977).

"Cross-Section for the Double-Charge-Exchange Reaction $\pi^+ + {}^4He \rightarrow \pi^- + 4p$ at Pion Energies of 98, 135, 145, and 156 MeV" by I. V.

Falomkin, V. I. Lyashenko, G. B. Pontecorvo, Yu. Shcherbakov, M. Albu, T. Angelescu, O. Balea, A. Mihul, F. Nichitiu, A. Sararu, F. Balestra, R. Garfagnini, G. Piragino, C. Guaraldo, and R. Scrimaglio, Lett. Nuo. Cim. 16, 525 (1976).

"A Survey of Pion Charge-Exchange Reactions with Nuclei" by Gerald A. Miller and James E. Spencer, Ann. Phys. 100, 562 (1976).

"Exchange Current Effects in Pion Double Charge Exchange from ^{4}He" by J. F. Germond and C. Wilkin, Lett. Nuc. Cim. 13, 605 (1975).

"Double Charge Exchange Scattering of Pions by ^{18}O" by L. C. Liu and Victor Franco, Phys. Rev. C 11, 760 (1975).

"π^- Nucleus Charge Exchange Reactions" by Li Yang-Kuo, Liu Hsien-Hui, and Ma Wei-Hsing, Sci. Sin. 18, 38 (1975).

"Pion Charge-Exchange Reactions with Nuclei" by Gerald A. Miller and J. E. Spencer, Phys. Lett. 53B, 329 (1974).

"Double-Charge Exchange and Inelastic Scattering in π^- + ^{3}He" by John Sperinde, Don Fredrickson, and Victor Perez-Mendez, Nucl. Phys. B78, 345 (1974).

"Total Cross-Section for the Double Charge Exchange Reaction π^+ + ^{4}He - π^- + 4p at 100 MeV" by I. V. Falomkin, M. M. Kulyukin, V. I. Lyashenko, G. B. Pontecorvo, Yu. A. Shcherbakov, C. Georgescu, A. Mihul, F. Nichitiu, A. Sararu, and G. Piragino, Nuo. Cim. 22, 333 (1974).

"Charge-Exchange Reactions on Light Nuclei in a Multiple-Scattering Formalism" by William B. Kaufmann, Jane C. Jackson, and W. R. Gibbs, Phys. Rev. C 9, 1340 (1974).

APPENDIX B. PAPERS RESULTING FROM THIS WORK

Following are copies of six articles resulting from this work that have been published in refereed physics journals. Articles B1, B2, and B3 were published in Physical Review C (Phys. Rev. C 29, 2395 (1984), Phys. Rev. C 30, 958 (1984), and Phys. Rev. C 30, 962 (1984) respectively, all copyright 1984 The American Physical Society). Article B4 was published in Nuclear Physics (Nucl. Phys. A432, 610 (1985), copyright 1985 North-Holland Publishing Company). Article B5 was published in Physics Letters (Phys. Lett. 154B, 255 (1985), copyright 1985 North-Holland Publishing Company). Article B6 was published in Physical Review C (Phys. Rev. C 32, 349 (1985), copyright 1985 The American Physical Society).

RAPID COMMUNICATIONS

PHYSICAL REVIEW C VOLUME 29, NUMBER 6 JUNE 1984

Energy dependence of angular distributions in the nonanalog pion double-charge-exchange reaction $^{16}O(\pi^+,\pi^-)^{16}Ne$(g.s.)

R. Gilman, H. T. Fortune, Kalvir S. Dhuga, and Peter H. Kutt
University of Pennsylvania, Philadelphia, Pennsylvania 19104

L. C. Bland, Rex R. Kiziah, C. Fred Moore, and Peter A. Seidl
University of Texas at Austin, Austin, Texas 78712

C. L. Morris
Los Alamos National Laboratory, Los Alamos, New Mexico 87545

W. B. Cottingame
New Mexico State University, Las Cruces, New Mexico 88003

(Received 5 March 1984)

Previous measurements have shown that pion double-charge-exchange angular distributions between nonanalog $J^\pi = 0^+$ states at $T_\pi = 164$ MeV are consistent with simple diffractive scattering, whereas angular distributions between analog $J^\pi = 0^+$ states at $T_\pi = 164$ MeV are not. We present measurements of angular distributions for the nonanalog reaction $^{16}O(\pi^+,\pi^-)^{16}Ne$(g.s.) at two additional energies and compare the energy dependence with that expected for diffractive scattering.

All reported measurements of $J^\pi = 0^+$ to 0^+, (g.s.) to (g.s.) pion double-charge-exchange (DCX) transitions in which the initial and residual nuclear states are not analogs show a consistent set of characteristics. Those characteristics, summarized for $T = 0$ to $T = 2$ transitions in Ref. 1, have been confirmed in more recent measurements.[2,3] Of those characteristics, the most pertinent to this Rapid Communication is that angular distributions at $T_\pi = 164$ MeV are all consistent with a diffractive scattering (strong absorption) process. In contrast, all measured analog DCX angular distributions[4-6] are inconsistent with simple diffractive scattering (but can be explained with a more complex model[7,8]). Four nonanalog angular distributions at $T_\pi = 164$ MeV have been reported: $^{16}O(\pi^+,\pi^-)^{16}Ne$(g.s.),[9] $^{12}C(\pi^+,\pi^-)^{12}O$(g.s.),[1] $^{40}Ca(\pi^+,\pi^-)^{40}Ti$(g.s.),[1] and $^{18}O(\pi^-,\pi^+)^{18}C$(g.s.).[3] We have measured angular distributions for $^{16}O(\pi^+,\pi^-)^{16}Ne$(g.s.) at two additional energies, $T_\pi = 120$ and 200 MeV, to investigate the energy dependence of nonanalog DCX angular distributions.

There is no general theory for nonanalog transitions. The work of Liu[7] is not restricted to analog transitions, but calculations of nonanalog transitions require final-state wave functions for exotic nuclei, e.g., ^{16}Ne(g.s.), and have not been done. A calculation[10] of the ratio of cross sections for $^{16,18}O(\pi^+,\pi^-)^{16,18}Ne$(g.s.) at $T_\pi = 140$ MeV agrees roughly with the measured ratio (calculated to be -3, but measured recently[11] to be 4.9 ± 1.6 at $\theta = 5°$), but fails to account for the rapid variation of the ratio with energy[11] or the difference in shape of angular distributions for the two reactions at $T_\pi = 164$ MeV.[9] It should be noted that both of the above models assume that DCX on $T = 0$ targets proceeds via a sequential charge transfer (SCT) mechanism [see Fig. 1(a)], and that both are sensitive to nuclear structure effects (core excitation). The work of Johnson and Siciliano,[3] also based on the diagram in Fig. 1(a), explicitly assumes isospin invariance; only analog transitions are calculated. It has been speculated,[12] as transitions between analog and nonanalog states have different energy dependence, angle dependence at $T_\pi = 164$ MeV, and target mass dependence (see Refs. 1 and 6), that the dominant reaction mechanisms are different in the two cases. In particular, it was suggested[12] that diagram (c) of Fig. 1 is responsible for nonanalog DCX. Calculations of DCX from all the non-SCT mechanisms [diagrams (b), (c), and (d)] of Fig. 1 are underway by Johnson *et al.*[13]

Data were obtained with the DCX modifications[5] to the Energetic Pion Channel and Spectrometer (EPICS) at the Clinton P. Anderson Meson Physics Facility (LAMPF). Three ^{16}O targets were used. All targets were water (of natural isotopic purity) frozen in a copper frame. The areal densities, types of entrance and exit windows, and data points obtained with each target are specified in Table I. The "two-gram" target was used initially for enhanced count rates. It was replaced by the "one-gram" target to improve energy resolution. The "Mylar" target was used to reduce background in the spectra that arose from continuum DCX on the copper windows.

Background became an important problem at larger angles, at which the ^{16}O cross sections are small. The background from the aluminized Mylar was much smaller than that from the copper for two reasons. First, the number of copper atoms was much larger than the number of aluminum atoms (the ratio was ~ 100). Second, Mylar consists of hydrogen (on which there is no DCX), oxygen (a negligibly small amount compared with the full target), and carbon (99% ^{12}C, which has a more negative DCX Q value than ^{16}O). There was, in addition, background from continuum DCX on ^{18}O in the natural isotopic purity water target. Background problems from the ^{18}O and copper windows were of similar size, as (with the one-gram target) the ratio of copper atoms to ^{18}O atoms was ~ 4. The DCX Q values (in MeV) are -28.38 for ^{16}O, -7.85 for ^{63}Cu, -3.59 for ^{65}Cu, -16.38 for ^{27}Al, -31.96 for ^{12}C, and -5.08 for ^{18}O.

Absolute normalization factors were determined by measuring $^1H(\pi^+,\pi^+)^1H$ yields on a CH_2 target at 40° (laboratory) at all energies at which data were taken. The

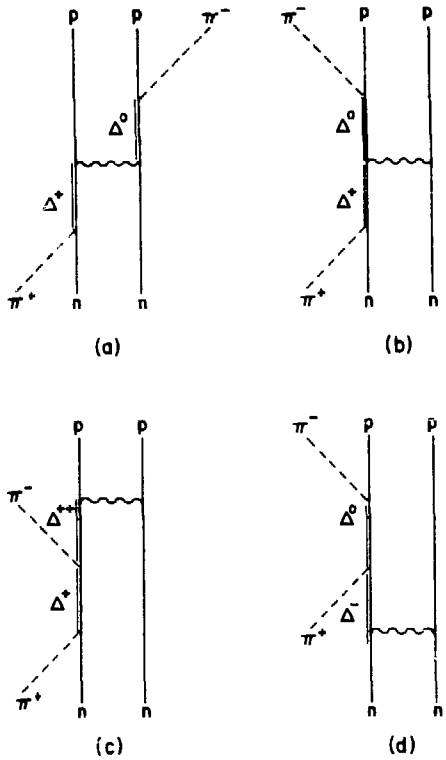

FIG 1. diagrams for pion DCX Diagram (a) is the usual sequential charge transfer mechanism It has been speculated (Ref 12) that diagram (c) is the dominant mechanism of nonanalog DCX. Work is in progress (Ref. 13) to evaluate diagrams (b), (c), and (d) for nonanalog transitions

ratio of hydrogen cross section, calculated from the phase shifts of Rowe, Salomon, and Landau,[14] to yield is a normalization factor that accounts for the product of the solid angle of the spectrometer and the number of pions in the incident beam. The absolute normalization factors are believed accurate to -10%. This uncertainty is the sum of several errors, each of -3%, that include statistical errors on measuring the yield of $^1H(\pi^+,\pi^+)^1H$, uncertainties in monitoring the primary beam flux, and uncertainties in calculating various correction factors such as the pion survival fraction and detection efficiencies. Typically, repeated normalization runs agree within statistical errors. Three normalization runs at $T_\pi = 200$ MeV, including one at 43°, yielded the same normalization factor, within statistical errors. A weighted average of these factors was used to normalize the $T_\pi = 200$ MeV data. Four runs at $T_\pi = 120$ MeV, including one at 43°, however, did not agree as well. The normalization factors were divided into two pairs. Agreement within each pair was better than 3%, but the pairs differed by -13%. Although there is evidence of some differences between the two pairs of runs, there is no evidence that any of the measurements is wrong. Thus we have used a weighted average of the four runs to normalize the $T_\pi = 120$ MeV data.

As a check on physically measured target thicknesses, $^1H(\pi^+,\pi^+)^1H$ yields were measured with two of the three targets. This measurement gives a ratio of hydrogen in the water targets to hydrogen in the CH_2 target. Since the CH_2 target areal density is accurately known (73.69 mg/cm^2 CH_2), a water target areal density can be calculated. The result for the two-gram target, 1.66 ± 0.07 g/cm^2 of ^{16}O, is slightly lower than the physically measured value of 1.78 g/cm^2 given in Table I. It is believed that this slight difference arises from the high count rates at which the H_2O measurement was made (-0.5×10^6/sec). The result for the Mylar target, 0.755 ± 0.021 g/cm^2 of ^{16}O, agrees well with the value in Table I.

As a check on angle-dependent effects, hydrogen yields were measured as a function of angle. For part of the experiment, a wedge was inserted between the scattering chamber and the bellows that couples the scattering chamber to the pion beam channel to allow measurements at slightly larger scattering angles. Ratios of hydrogen cross sections, calculated as above, to yields measured from 15° to 40° without the wedge, and from 30° to 45° with the wedge, were constant within error bars (-3%).

As a final check on our overall normalization, a four-point excitation function at $\theta_{lab} = 5°$ was measured. Figure 2 shows the overlap between this work and previous measurements.[9,11] The repeated point at 164 MeV agrees well with the previous measurement, whereas the new point at 210 MeV is higher than the previously measured value,[11] but not inconsistent given the statistical uncertainties. The two new points at $T_\pi = 120$ and 200 MeV fit smoothly into the excitation function.

TABLE I Target properties.

Target (Label)	$x\rho(^{16}O)$ (g/cm^2)	Window foils	Data obtained T_π (MeV)	Data obtained θ (deg)
"Two-gram"	1.78	Copper	120	5,15,25,35,45
			164	5
			200	15
			210	5
"One-gram"	0.75	Copper	200	5,15,25,35,43
"Mylar"	0.75	Aluminized Mylar	120	40
			200	5,20,30,43

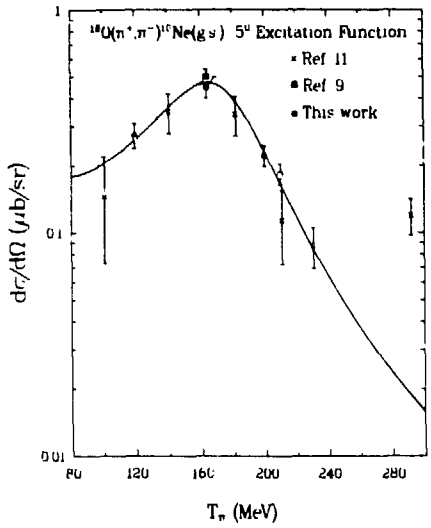

FIG. 2. Excitation function at $\theta = 5°$ (laboratory) for $^{16}O(\pi^+,\pi^-)^{16}Ne(g.s.)$. The curve is a Breit Wigner fit to all the data (except the 292-MeV point) with parameters $T_{res} = 171$ MeV and width $\Gamma = 75$ MeV.

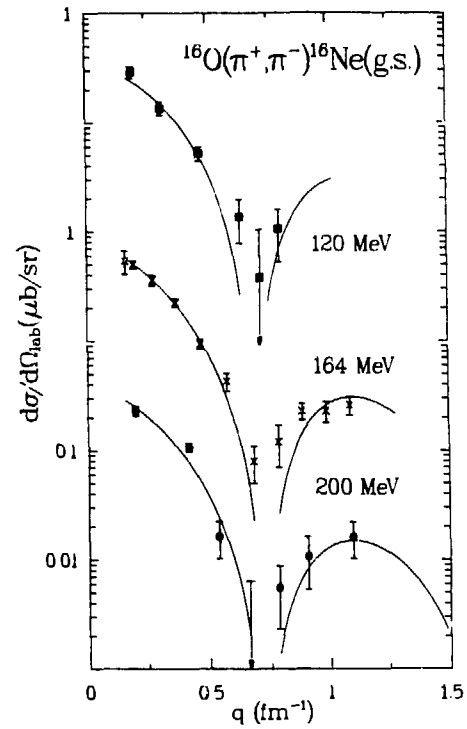

FIG. 3. Angular distributions for $^{16}O(\pi^+,\pi^-)^{16}Ne(g.s.)$ at three energies. The angular distribution at $T_\pi = 164$ MeV is from Ref. 9. The curves displayed are the damped Bessel functions, calculated from $\sigma = NJ_\delta^2(qR)e^{-qd}$, that best fit the data. All curves extend over the same angular range, $0° \leq \theta \leq 60°$. Fit parameters are given in Table II.

Angular distributions for $5° \leq \theta_{lab} \leq 45°$ ($5° \leq \theta_{lab} \leq 43°$) were measured at $T_\pi = 120$ (200 MeV). These angular distributions, along with a previous measurement[9] at $T_\pi = 164$ MeV, are plotted versus the momentum transfer in Fig. 3. It is apparent that the minima occur at about the same momentum transfer at all energies, as is expected for simple diffractive scattering. The curves displayed are damped Bessel functions, calculated from $\sigma = NJ_\delta^2(qR)e^{-qd}$, with parameters that best fit the data. These parameters are given in Table II. Both the radius R and damping factor d are, within uncertainties, independent of energy. Thus, except for an overall scale factor, the angular distributions are essentially the same at all energies. The large uncertainties in d merely reflect the insensitivity of the fit to the value of d. However, these uncertainties in d contribute insignificantly to the uncertainties in R.

It should be noted that the radius we have extracted, $R \sim 3.4$ fm, is a reasonable value for the strong-absorption radius of ^{16}O. The one-tenth (two-tenths) density point of ^{16}O, calculated from the parametrizations of Ref. 15, is about 3.7 fm (3.3 fm). Of course, as the energy is varied across the $\Delta_{3,3}$ resonance, the validity of the strong-absorption assumption varies, and the effective radius is expected to be a function of energy. Estimates of the strong-absorption radius from the values of σ_{tot} in Ref. 16 indicate that this radius is nearly constant between $T_\pi = 120$ and 164 MeV, and is 5% smaller at 200 MeV. Our measurements are not sensitive to an effect of that magnitude.

In Table III we list, for the three bombarding energies, the 5° cross section, the normalization factor from the

TABLE II. Best fit parameters $[\sigma(q) = NJ_\delta^2(qR)e^{-qd}]$ for ^{16}O angular distributions

T_π (MeV)	χ^2	N (μb/sr)	R (fm)	d (fm)
120	3.17	0.334	3.48 ± 0.23	0.51 ± 1.19
164	2.31	0.810	3.30 ± 0.16	1.28 ± 0.44
200	4.30	0.411	3.31 ± 0.19	1.32 ± 0.39

TABLE III. Energy dependence of the cross sections.

T_π (MeV)	$\sigma(5°)$ (nb/sr)	N (nb/sr)	$\sigma_{tot}(0°-50°)$ (nb)
120	273 ± 35	334	92
164	449 ± 49	810	140
200	222 ± 23	411	60

angular-distribution fits, and the angle-integrated ($\theta = 0°-50°$) cross section. The three quantities all exhibit the same trend—a peak at 164 MeV with a rapid falloff on either side. With a damping factor d as large as 1.0 fm, if the angular distributions are of the form $\sigma = NJ_0^2(qR)e^{-qd}$, then the 0°–50° integrated cross section is more than half of that for 0°–180°. Hence it is clear that the peak in the excitation function is not an artifact of an anomalous 5° behavior. The angular distribution as a whole goes up and down rapidly with increasing bombarding energy.

In conclusion, angular distributions for the $^{16}O(\pi^+,\pi^-)^{16}Ne(g.s.)$ reaction are functions of the momentum transfer q, which are independent of energy (except for an overall scale factor) within the accuracy of our measurement. This energy dependence is consistent with strong-absorption scattering, in sharp contrast to the observed behavior of angular distributions for analog DCX transitions,[6] for which the minima at $T_\pi = 164$ MeV (292 MeV) are at $qR \sim 1.7$ (3.5). Minima for $^{16}O(\pi^+,\pi^-)^{16}Ne(g.s.)$ are at $qR = 2.4$ at all measured energies. Any correct theory of nonanalog DCX must predict diffractive angular distributions at all energies, forward angle excitation functions that peak near $T_\pi = 160$ MeV, and a smooth $A^{-4/3}$ mass dependence for $T = 0$ to $T = 2$ transitions.

We thank Andrew Harvier of the MP-10 technical staff for preparation of the ice targets, and acknowledge several discussions with Mikkel Johnson. This work was supported in part by the U.S. Department of Energy, The Robert A. Welch Foundation, the National Science Foundation, and the Natural Sciences and Engineering Research Council of Canada.

[1] L. C. Bland, R. Gilman, M. Carchidi, K. Dhuga, Christopher L. Morris, H. T. Fortune, S. J. Greene, Peter A. Seidl, and C. Fred Moore, Phys. Lett. 128B, 157 (1983).

[2] Peter A. Seidl, Rex R. Kiziah, Mark K. Brown, C. Fred Moore, C. L. Morris, Helmut Baer, Steven J. Greene, G. R. Burleson, W. B. Cottingame, L. C. Bland, R. Gilman, and H. T. Fortune, Phys. Rev. Lett. 50, 1106 (1983).

[3] R. Gilman, H. T. Fortune, L. C. Bland, Rex R. Kiziah, C. Fred Moore, Peter A. Seidl, C. L. Morris, and W. B. Cottingame (submitted to Phys. Rev. C).

[4] Kamal K. Seth, S. Iversen, H. Nann, M. Kaletka, J. Hird, and H. A. Thiessen, Phys. Rev. Lett. 43, 1574 (1979), 45, 147 (1980).

[5] S. J. Greene, W. J. Braithwaite, D. B. Holtkamp, W. B. Cottingame, C. Fred Moore, C. L. Morris, H. A. Thiessen, G. R. Burleson, and G. S. Blanpied, Phys. Lett. 88B, 62 (1979).

[6] Peter A. Seidl, Rex R. Kiziah, Mark K. Brown, C. Fred Moore, C. L. Morris, Helmut Baer, Steven J. Greene, G. R. Burleson, W. B. Cottingame, L. C. Bland, R. Gilman, and H. T. Fortune (submitted to Phys. Rev. C).

[7] L. C. Liu, Phys. Rev. C 27, 1611 (1983).

[8] Mikkel B. Johnson and E. R. Siciliano, Phys. Rev. C 27, 730 (1983); 27, 1647 (1983).

[9] S. J. Greene, W. B. Cottingame, G. R. Burleson, L. C. Bland, R. Gilman, H. T. Fortune, C. L. Moris, D. B. Holtkamp, C. Fred Moore, Phys. Rev. C 27, 2375 (1983).

[10] T.-S. H. Lee, D. Kurath, and B. Zeidman, Phys. Rev. Lett. 39, 1507 (1977).

[11] S. J. Greene, W. J. Braithwaite, D. B. Holtkamp, W. B. Cottingame, C. Fred Moore, G. S. Blanpied, A. T. Viescas, G. H. Daw, C. L. Morris, and H. A. Thiessen, Phys. Rev. C 25, 927 (1982).

[12] C. L. Morris, H. T. Fortune, L. C. Bland, R. Gilman, S. J. Greene, W. B. Cottingame, D. B. Holtkamp, G. R. Burleson, and C. Fred Moore, Phys. Rev. C 25, 3218 (1982).

[13] Mikkel B. Johnson *et al.* (unpublished).

[14] G. Rowe, M. Salomon, and Rubin H. Landau, Phys. Rev. C 18, 584 (1978).

[15] C. W. de Jager, H. de Vries, and C. de Vries, At. Data Nucl. Data Tables 14, 479 (1974).

[16] J. P. Albanese, J. Arvieux, J. Bolger, E. Boschitz, C. H. Q. Ingram, J. Jansen, and J. Zichy, Nucl. Phys. A350, 301 (1980).

PHYSICAL REVIEW C VOLUME 30, NUMBER 3 SEPTEMBER 1984

^{14}Be via pion double charge exchange

R. Gilman and H. T. Fortune
University of Pennsylvania, Philadelphia, Pennsylvania 19104

L. C. Bland, Rex R. Kiziah, C. Fred Moore, and Peter A. Seidl
University of Texas at Austin, Austin, Texas 78712

C. L. Morris
Los Alamos National Laboratory, Los Alamos, New Mexico 87545

W. B. Cottingame
New Mexico State University, Las Cruces, New Mexico 88003

(Received 29 March 1984)

The ^{14}Be nucleus has been produced in the reaction ^{14}C(π^-,π^+). The cross section for the reaction is roughly that which would be expected from the $A^{-4/3}$ mass dependence observed for nonanalog (π^+,π^-) reactions on self-conjugate nuclei. If it is the ground state that we observe, the mass excess of ^{14}Be is $\sim$600 keV smaller (more bound) than expected from systematics.

A recent measurement[1] of the nonanalog pion double-charge-exchange (DCX) cross section at T_π=164 MeV and θ=5° (lab) for the reaction ^{18}O(π^-,π^+)^{18}C(g.s.) gave a value that was larger (by a factor of about 1.5) than expected from the systematic behavior[2] of DCX cross sections on T=0 targets leading to ground states of T=2 nuclei. The only T=1 nucleus lighter than ^{18}O on which a similar measurement can be carried out is ^{14}C. Its location is midway between ^{12}C and ^{16}O, for which DCX cross sections have been measured, whereas ^{18}O lies between ^{16}O and ^{20}Ne, the latter of which has not been used as a target in DCX. Because the ^{14}C target presents special problems, we report in detail on the experimental procedure.

It is important to note that (π^-,π^+) DCX on *any* stable nucleus will have a Q value less negative than that expected for the ^{14}C(π^-,π^+)^{14}Be(g.s.) reaction. With the estimated mass excess of ^{14}Be (Ref. 3; unless otherwise noted, all Q values are calculated with all mass excesses taken from Ref. 4), $\Delta\sim$40.69 MeV, the ^{14}C(π^-,π^+)^{14}Be(g.s.) Q value is

$$Q=\Delta_{^{14}\mathrm{C}}-\Delta_{^{14}\mathrm{Be}}-2m_e=-38.69\ \mathrm{MeV}\ .$$

All stable nuclei have Q values less negative than -35 MeV. Thus, all contaminants cause background problems.

Data were obtained at a pion kinetic energy of 164 MeV and a laboratory angle of 5° with the DCX modifications[5] to the Energetic Pion Channel and Spectrometer (EPICS) at the Clinton P. Anderson Meson Physics Facility (LAMPF). The channel[6] focuses the pion beam to a beam spot on target that is 6 cm wide (by convention, the y coordinate) by 20 cm high (the x coordinate). The beam is momentum dispersed in x with a dispersion of 10 cm/%. Wire chambers in the spectrometer measure both positions and angles of scattered particles, enabling software to ray trace each event and construct a target image. This capability enables simultaneous measurements on multiple targets. The targets are typically horizontal strips of materials, both because of the greater vertical width of the beam and because of the superior resolution in x ($\sim$4 mm in x for a 3.2 mm diameter horizontal rod vs $\sim$9 mm in y for a 3.2 mm vertical rod).

The ^{14}C target[7] consists of 9.17±0.05 g of carbon powder sealed with 1 cm long CH_2 plugs into two copper cells, each with external dimensions $\sim$6.0 cm ×5.0 cm ×0.6 cm and 0.0051 cm thick walls. The areal density of carbon powder in each cell is 187±4 mg/cm^2. The ^{14}C in the carbon powder has been enriched to a ratio of 4.6±0.4 atoms of ^{14}C per atom of ^{12}C. A recent analysis[8] of elastic and inelastic pion scattering from the ^{14}C target indicates the presence of several contaminants in addition to the ^{12}C. We list in Table I the isotopic composition of the target (taken from Ref. 8) and the Q value for (π^-,π^+) DCX on each isotope.

Figure 1(a) shows the strip target that was used during the first part of the experiment. About 40% of the data were taken with this target configuration. The copper (areal density 1460 mg/cm^2) and ^{12}C (graphite with areal density 516 mg/cm^2) strips were used to estimate background in the ^{14}C target spectrum. The target configuration of Fig. 1(b) was used for the second part of the experiment. With the ^{14}C target oriented vertically, all of the carbon powder was illuminated by the beam, resulting in an $\sim$20% increase of the count rate.

The procedure for calculating absolute normalization factors by measuring ^{1}H(π^-,π^-) yields on a CH_2 target has been described previously.[1] The use of two different target configurations required measuring the relative acceptance for the two configurations. The acceptance for the first target configuration was measured by replaying data from a full CH_2 target run with software target cuts on x that corresponded to the physical dimensions of the ^{14}C target. For the DCX data runs, slightly wider x target cuts were used because of the finite x resolution and

TABLE I. Composition of carbon powder [the areal density of copper is 107 mg/cm^2; the Q value for ^{63}Cu (^{65}Cu) is -4.75 (-9.11) MeV (Ref. 13)] in a ^{14}C target (Ref. 8).

Isotope	% (by weight)	areal density (mg/cm^2)	Q value (MeV)
^{14}C	73.5±2.2	137.4±7.1	−38.69
^{12}C	16.9±1.8	31.6±4.0	−26.05
^{16}O	4.5±0.5	8.4±1.1	−19.45
^{24,26}Mg	3.1±0.5	5.8±1.1	−9.00, −17.04
Other[a]	2.1±2.9	3.9±5.5	

[a]Other contaminants include ^{13}C, Na, Al, Si, Cl, and Mo.

the gaps between the strip targets. No y target cuts were needed, as both the CH_2 and ^{14}C targets were wider than the beam. For the second target configuration, the acceptance was determined by measuring ^{1}H(π^-,π^-) yields on a CH_2 target that had been cut to the physical dimensions of the ^{14}C target. Software target cuts on x were identical for both the DCX and normalization runs.

Figure 2 shows both the ^{14}C target spectrum and a background spectrum. The background spectrum is the sum of renormalized spectra obtained with the copper and ^{12}C targets. The renormalization factors accounted for the relative amounts of material in the background targets versus in the ^{14}C target, and for the relative acceptance of the spectrometer (at $Q\sim-38$ MeV) for the background targets versus for the ^{14}C target. The contribution of other contaminants to the background is not known. It is not expected to be large, however, as ~90% of the contaminant atoms are either ^{12}C or copper. Also, the background spectra were not shifted to compensate for the differing energy losses in the three targets. These energy losses were measured with elastic scattering to be 1.2 MeV for the copper target, 0.91 MeV for the ^{12}C target, and 0.46 MeV for the ^{14}C target.

The eight counts centered in our spectrum at $Q=-26.20\pm0.18$ MeV (we quote only statistical errors for peak positions, unless otherwise specified) are from the ^{12}C(π^-,π^+)^{12}Be(g.s.) reaction, which has a known Q value of -26.05 MeV. This agreement is surprisingly good, as the g.s. peak was at the edge of the acceptance of the spectrometer ($\delta=p/p_{spec}-1=+8.5\%$), where errors in measuring momentum would be expected to be largest. This peak is not seen in the background spectrum because the acceptance of the spectrometer for the ^{12}C background target is reduced at higher outgoing momenta, as the ^{12}C was at the higher incident momentum end of the target. There are no obvious peaks significantly above background until the large peak (23 counts) centered at $Q=-38.10\pm0.13$ MeV. We identify this as a state in ^{14}Be.

With background subtraction, we estimate a net yield of 19±5 counts in the ^{14}Be peak, giving a cross section of 733±193 nb/sr. Just to the left of the peak in the spectrum there does appear to be an excess of counts above

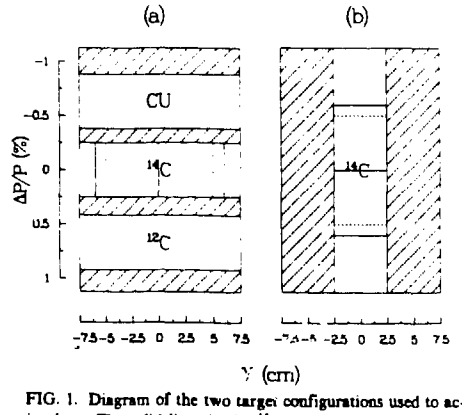

FIG. 1. Diagram of the two target configurations used to acquire data. The solid lines in the ^{14}C target indicate the extent of the copper cells. The dashed lines indicate the inner edge of the CH_2 plugs. The cells were fastened to aluminum holders which were attached to the target frame

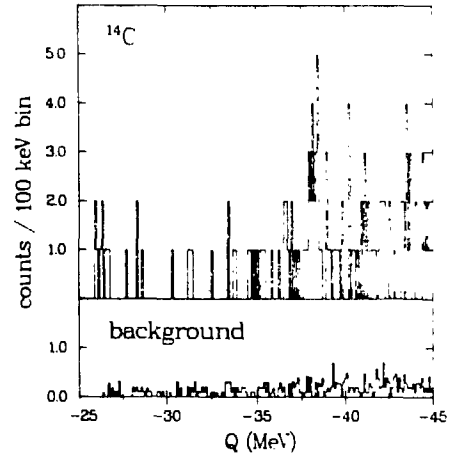

FIG. 2. Spectrum for (π^-,π^+) on a ^{14}C target (top) and copper and ^{12}C background spectrum (bottom). The method used to generate the background spectrum is described in the text.

what would be expected by comparison with the background spectrum. Specifically, in the 2.5 MeV wide region from $Q=-34.5$ to -37.0 MeV, we observe 14 counts, whereas we would have expected about five background counts from ^{12}C and Cu. It may be that the excess of nine counts is a statistical fluctuation, or they may arise from DCX on contaminants in the ^{14}C target that are not present in the background targets. If all the excess counts correspond to a state (or states) in ^{14}Be, the cross section is less than about 350 ± 120 nb/sr.

Ignoring nuclear structure effects, the cross section expected for the ^{14}C$(\pi^-,\pi^+)^{14}$Be(g.s.) reaction, based on the mass dependence[1,2] of $T=0$ to $T=2$ transitions, and ignoring kinematic differences between (π^-,π^+) and (π^+,π^-) reactions, is 591 nb/sr. It is thus likely that the large peak is the ^{14}Be(g.s.) because of the lack of a statistically significant peak at a more positive Q value, a measured Q value that approximately agrees with that expected (-38.10 ± 0.13 vs -38.69 MeV), and a cross section that approximately agrees with that expected (733 ± 193 vs 591 nb/sr).

Assuming that this peak is the ^{14}Be(g.s.), we can now proceed to compare cross sections of $T=1$ to $T=3$ transitions with those of $T=0$ to $T=2$ transitions. This comparison is shown in Fig. 3. The ^{12}C and ^{16}O cross sections have been converted from (π^+,π^-) to (π^-,π^+) by shifting the incident pion kinetic energy by the Coulomb energy difference between π^+ and π^- to $T_{\pi^-}=164$ MeV. (This change is about ten percent, and causes the data points to fall below the curve.) It appears from this comparison that (π^-,π^+) cross sections on $T=1$ target nuclei, leading to ground states of $T=3$ residual nuclei, are larger than those for $T=0$ targets.

The observed ^{14}Be Q value is 0.59 MeV more positive than that calculated for the g.s. from the estimated ^{14}Be mass excess.[3,4] As the primary emphasis of the experiment was on measuring a cross section, no attempt was made to calibrate the absolute energy scale of the spectrometer. This does not imply any large systematic error. We note that, in a recent measurement[1] of ^{18}O$(\pi^-,\pi^+)^{18}$C(g.s.) with a similar setup (channel and spectrometer magnet field settings differed by $<0.6\%$), the Q value (mass excess) was observed to be -26.69 ± 0.06 MeV (24.89 ± 0.06 MeV). This is in good agreement with reported mass excess measurements of $\Delta=24.82\pm0.30$ MeV (Ref. 9) and 24.91 ± 0.15 MeV (Ref. 10) for ^{18}C.

We have estimated the contributions of several sources of uncertainty in this Q value. The largest source of uncertainty is the statistical error in determining the peak centroid (130 keV). The second largest source of uncertainty is in the determination of the beam energy. Because of preamplifier problems, the nuclear magnetic resonance (NMR) probe usually used to set channel fields was accurate to only ~2 G. The channel energy was set with a different NMR that measures the field of a different dipole magnet in the channel. The relative calibration of these two magnets was known to ~2 G. We estimate an uncertainty of 60 keV in setting the channel. Additional uncertainties include channel magnet stability (60 keV), spectrometer magnet stability (40 keV), and the determination of energy loss in the target (20 keV). Adding these in quadrature gives a total uncertainty of 0.16 MeV.

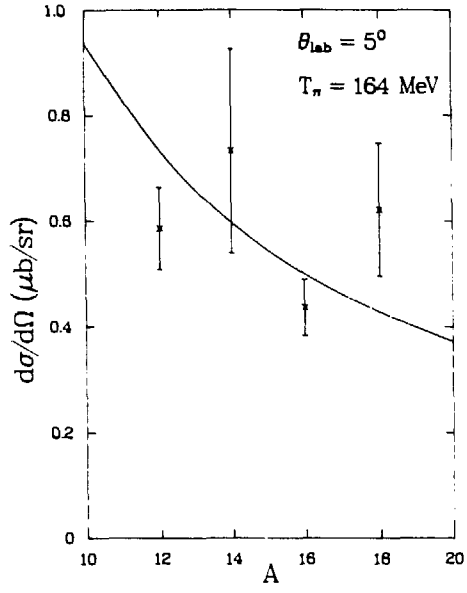

FIG. 3. Measured nonanalog cross sections for light nuclei, $10\le A\le20$, at $T=164$ MeV and $\theta=5°$ (lab). The ^{16}O point is from Ref. 1. The ^{12}C point has been extrapolated from data in Ref. 2, and the ^{16}O point has been extrapolated from data in Refs. 11 and 12. The curve is a best fit to the A dependence of (π^+,π^-) DCX on self-conjugate targets.

In conclusion, in the reaction ^{14}C(π^-,π^+) at an incident kinetic energy of 164 MeV and a laboratory angle of 5°, the ^{14}Be(g.s.) has been observed with a DCX cross section of 733 ± 193 nb/sr, which is slightly larger than expected, but consistent with population of a 0^+ g.s. The mass excess of ^{14}Be is 40.10 ± 0.16 MeV, which is about 0.6 MeV more bound than expected.

We thank Helmut Baer for the loan of the ^{14}C target and his assistance in preparing the target for use during the experiment, and also J. van Dyke for his assistance in preparing the target. We also thank R. Gill-Dhuga for her assistance in acquiring the data. This work was supported in part by the U.S. Department of Energy, The Robert A. Welch Foundation, the National Science Foundation, and the Natural Sciences and Engineering Research Council of Canada.

[1]R. Gilman, H. T. Fortune, L. C. Bland, Rex. R. Kiziah, C. Fred Moore, Peter A. Seidl, C. L. Morris, and W. B. Cottingame, Phys. Rev. C. **30**, 962 (1984).

[2]L. C. Bland, R. Gilman, M. Carchidi, K. Dhuga, Christopher L. Morris, H. T. Fortune, S. J. Greene, Peter A. Seidl, and C. Fred Moore, Phys. Lett. **128B**, 157 (1983).

[3]C. Thibault and R. Klapisch, Phys. Rev. C **9**, 793 (1974).

[4]Nuclear Wallet Cards, edited by V. S. Shirley and C. M. Lederer, 1979.

[5]S. J. Greene, W. J. Braithwaite, D. B. Holtkamp, W. B. Cottingame, C. Fred Moore, C. L. Morris, H. A. Thiessen, G. R. Burleson, and G. S. Blanpied, Phys. Lett. **88B**, 62 (1979).

[6]H. A. Thiessen, J. C. Kalline, J. F. Amann, R. J. Peterson, S. J. Greene, S. L. Verbeck, G. R. Burleson, S. G. Iversen, A. W. Obst, Kamal K. Seth, C. F. Moore, J. E. Bolger, W. J. Braithwaite, D. C. Slater, and C. L. Morris, Los Alamos Scientific Laboratory Report LA-6663-MS, 1977 (unpublished).

[7]Helmut W. Baer (private communication).

[8]Carol J. Harvey (private communication); also, Carol J. Harvey, Helmut W. Baer, C. L. Morris, S. J. Seestrom-Morris, D. Dehnhard, D. B. Holtkamp, and S. J. Greene (unpublished).

[9]F. Naulin, C. Detraz, M. Roy-Stephan, M. Bernas, J. de Boer, D. Guillemaud, M. Langevin, F. Pougheon, and P. Roussel, Phys. Rev. C **25**, 1074 (1982).

[10]Kamal K. Seth, H. Nann, S. Iversen, M. Kaletka, J. Hird, and H. A. Thiessen, Phys. Rev. Lett. **41**, 1589 (1978).

[11]S. J. Greene, W. B. Cottingame, G. R. Burleson, L. C. Bland, R. Gilman, H. T. Fortune, C. L. Morris, D. B. Holtkamp, and C. Fred Moore, Phys. Rev. C 27, 2375 (1983).

[12]S. J. Greene, W. J. Braithwaite, D. B. Holtkamp, W. B. Cottingame, C. Fred Moore, G. S. Blanpied, A. T. Viescas, G. H. Daw, C. L. Morris, and H. A. Thiessen, Phys. Rev. C **25**, 927 (1982).

[13]R. T. Kouzes and D. Mueller, Nucl. Phys. **A307**, 71 (1978).

PHYSICAL REVIEW C VOLUME 30, NUMBER 3 SEPTEMBER 1984

Nonanalog (π^-,π^+) double charge exchange on ^{18}O

R. Gilman and H. T. Fortune
University of Pennsylvania, Philadelphia, Pennsylvania 19104

L. C. Bland, Rex R. Kiziah, C. Fred Moore, and Peter A. Seidl
University of Texas at Austin, Austin, Texas 78712

C. L. Morris
Los Alamos National Laboratory, Los Alamos, New Mexico 87545

W. B. Cottingame
New Mexico State University, Las Cruces, New Mexico 88003

(Received 20 April 1984)

We present measurements of the nonanalog pion double charge exchange reaction, $^{18}O(\pi^-,\pi^+)^{18}C$(g.s.), a transition between a $T=1$ state and a $T=3$ state, and compare the results to earlier measurements on self-conjugate targets.

In the simplest models of pion double charge exchange (DCX), transitions to the analog state in the residual nucleus are expected to dominate the reaction because of the large overlap of the initial- and final-state wave functions. Yet, at energies near the $\Delta_{3,3}$ resonance, it has been found that cross sections to certain nonanalog states are about as large as the analog cross sections.[1,2] In particular, a large body of data exists for transitions between $J^\pi,T=0^+,0$ target ground states and $J^\pi,T=0^+,2$ residual ground states. The regular characteristic features[3] of these transitions ($A^{-4/3}$ mass dependence, diffractive angular distributions, and excitation functions that are peaked near the $\Delta_{3,3}$ resonance) are in sharp contrast to the irregular features of analog DCX transitions (irregular $A^{-10/3}$ mass dependence at 164 MeV, nondiffractive angular distributions, and excitation functions that either monotonically increase across the $\Delta_{3,3}$ resonance, or that have a minimum near $T_\pi=164$ MeV).

No theory exists for nonanalog DCX. Published speculation[4,5] has centered on a model in which a single-step reaction leads to $\Delta_{3,3}$ components of the residual nuclear wave function. If this, or some other exotic reaction mechanism,[6] is responsible for nonanalog DCX on self-conjugate targets, similar transitions should be seen on $T\neq 0$ targets. There is, however, no unambiguous evidence of nonanalog DCX transitions on other than $T=0$ targets that have all the features found in DCX on $T=0$ targets. Transitions with some, but not all, of the characteristic features have been seen on targets of ^{9}Be (Ref. 7), ^{13}C (Ref. 8), ^{14}C (Ref. 9), and ^{56}Fe (Ref. 12). Also, the observed anomalies in $^{18}O(\pi^+,\pi^-)^{18}Ne$(g.s.) (Ref. 2) can be explained by the interference of analog and nonanalog amplitudes[10] (or alternatively by a second order calculation[11] including core excitation).

As self-conjugate targets are a special class of nuclei, nonanalog DCX on these targets may exhibit systematic features that are not generally characteristic of the reaction. In particular, we note that the experimental A dependence of nonanalog DCX on self-conjugate targets, $\sigma\sim A^{-4/3}$, disagrees with the $A^{-10/3}$ mass dependence expected for any DCX diagram. The best-fit A dependence[3,5] is

$$\sigma(5^\circ,\ 164\ \text{MeV})\simeq 21.06A^{-1.354}\ (\mu\text{b/sr})\ .$$

Constraining the mass dependence to be $A^{-10/3}$ increases the χ^2 per point from ~ 1 to ~ 40. Thus, it became of interest to unambiguously demonstrate the existence (or nonexistence) of the systematic features of nonanalog DCX on other than a self-conjugate target, and to examine the mass dependence of the reaction. To ensure the absence of the analog amplitude, but to still connect ground states, the fact that stable nuclei have $N>Z$ requires [unless T (target)$=2$, as in ^{56}Fe] the use of the (π^-,π^+) reaction. We have investigated the reaction $^{18}O(\pi^-,\pi^+)^{18}C$(g.s.), which has quantum numbers

$$J_i^\pi,T(J_f^\pi,T)=0^+,1(0^+,3)\ .$$

This reaction has been used to measure the mass excess of ^{18}C (but a cross section was not measured[13]).

Data were obtained with the standard DCX modification[14] of the EPICS spectrometer at the Clinton P. Anderson Meson Physics Facility (LAMPF). The ^{18}O target was 0.94 g/cm^2 H_2O, of which 94% (by number of molecules) was $H_2{}^{18}O$. The water was frozen in a copper frame with copper entrance and exit windows, and was wrapped with aluminized Mylar for insulation. Because the Q values for DCX on ^{63}Cu (-4.85 MeV), ^{65}Cu (-9.11 MeV), aluminum (-12.59 MeV), ^{12}C (-25.97 MeV), and ^{16}O (-19.45 MeV) are more positive than the Q value for $^{18}O(\pi^-,\pi^+)^{18}C$(g.s.) ($-26.70$ MeV), the spectra include some background at more positive Q values than that corresponding to the ^{18}C(g.s.) peak.

Absolute normalizations of the cross sections were determined by measuring $^1H(\pi^-,\pi^-)$ yields with a CH_2 target at $\theta=40^\circ$ and at all energies at which data were

taken. The ratio of yield to cross section, calculated from the phase shifts of Rowe, Salomon, and Landau,[15] gives a normalization factor that compensates for the solid angle of the spectrometer and the flux of pions in the incident beam. Two additional checks of the absolute normalization were made. First, hydrogen yields were measured with the H_2O target. This gives a ratio of the H_2O target thickness to a CH_2 target whose thickness is more accurately determined. The resulting H_2O thickness, 0.91 ± 0.07 g/cm^2, agrees well with the physically measured thickness given above. Second, a measurement was made of $^{18}O(\pi^+,\pi^-)^{18}Ne(g.s.)$ at $\theta=5°$ and $T_\pi=292$ MeV to check our absolute normalization against that of Greene *et al.*[2] Our measurement yielded $\sigma=2.14\pm0.15$ μb/sr, which is slightly less than their value of $\sigma=2.41\pm0.19$ μb/sr, but agrees within the uncertainties.

In addition, as a check on any angle-dependent effects, yields were measured for $^1H(\pi^+,\pi^+)$ as a function of angle, and compared with cross sections calculated from phase shifts as above. No statistically significant effects were found except for a 10% increase in the ratio of hydrogen cross section to measured yield at the largest angle, $\theta=45°$. It is believed that this effect was caused by part of the pion beam striking the bellows that vacuum couples the scattering chamber to the beam channel. The $\theta=45°$ ^{18}O data point has been renormalized.

The spectrum shown in Fig. 1 is the sum of all raw $^{18}O(\pi^-,\pi^+)$ spectra at all energies and angles. It has not been corrected for either the acceptance of the spectrometer or the relative normalizations of the data acquisition runs at various angles and energies. There are clear signals (above an irregular background) for both the ground state and an excited state at $E_x=1.55$ MeV. We note that most shell model calculations give the excitation energy of the first 2^+ state as 1.8 MeV $< E_x <$ 2.1 MeV, and that, in weak coupling, where $^{18}C=^{20}O\otimes^{14}C$, the excitation energy of $^{18}C(2^+)$ would be the same as $^{20}O(2^+)$, 1.67 MeV. Background subtraction has been done for the ground state cross sections presented, although the estimated number of background counts in the ground state peak in all spectra (133 total counts at all energies and angles) is only ten counts.

The $\theta=5°$, $^{18}O(\pi^-,\pi^+)^{18}C(g.s.)$ excitation function is compared in Fig. 2 to those for the previously measured[2]

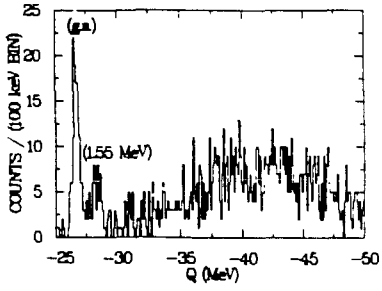

FIG. 1. Sum of all raw $^{18}O(\pi^-,\pi^+)$ spectra at all energies and angles.

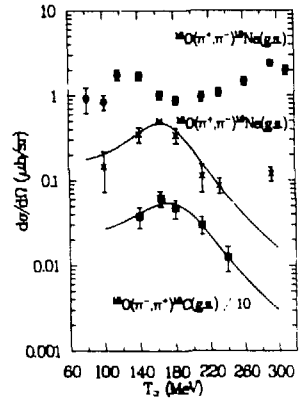

FIG. 2. Excitation function for $^{18}O(\pi^-,\pi^+)^{18}C(g.s.)$ at $\theta=5°$ (lab) contrasted with previously measured excitation functions for $^{16,18}O(\pi^+,\pi^-)^{16,18}Ne(g.s.)$ (Ref. 2). The curves are Breit-Wigner fits to the nonanalog transitions.

nonanalog and analog transitions,

$$^{16,18}O(\pi^+,\pi^-)^{16,18}Ne(g.s.)\ .$$

The new data are clearly similar to those for the pure nonanalog $^{16}O(\pi^+,\pi^-)$ case. At energies above 160 MeV, the nonanalog excitation functions decrease with energy, whereas the analog excitation function increases. The maximum cross section of the new excitation function occurs at about the same incident pion energy as for the ^{16}O data. There is no known significance, however, to the energy at which the maximum cross section occurs. A fit with a Breit-Wigner expression to the new excitation function gives a width of 88 MeV, which is slightly larger than the results presented in Ref 3.

The 164-MeV, $^{18}O(\pi^-,\pi^+)^{18}C(g.s.)$ angular distribution is shown in Fig. 3, along with 164-MeV angular distributions for the reactions $^{16,18}O(\pi^+,\pi^-)^{16,18}Ne(g.s.)$. The new data exhibit a minimum near $\theta=30°$. The new angular distribution is much more similar to the nonanalog ^{16}O angular distribution than the analog ^{18}O angular distribution. Both the nonanalog angular distributions exhibit minima consistent with the nuclear size, whereas the analog angular distribution does not. The damped-Bessel-function curves through the new data and the ^{16}O data are, aside from a scale factor and kinematic differences, identical.

Finally, we discuss the mass dependence on nonanalog DCX. The expected $^{18}O(\pi^-,\pi^+)^{18}C(g.s.)$ cross section calculated from the best fit formula given above (evaluated at mass 18), is -421 nb/sr. This is significantly less than the measured cross section, 621 ± 126 nb/sr. All data points on self-conjugate targets are within 17% of the best fit curve; the new point is larger by 48%. The new data point has an insignificant effect on the fit parameters since the six points on self-conjugate targets all have better statistics. Thus, an $A^{-6/3}$ mass dependence represents all the data well, but the $^{18}O(\pi^-,\pi^+)^{18}C(g.s.)$ cross section appears to be enhanced by 50% over cross

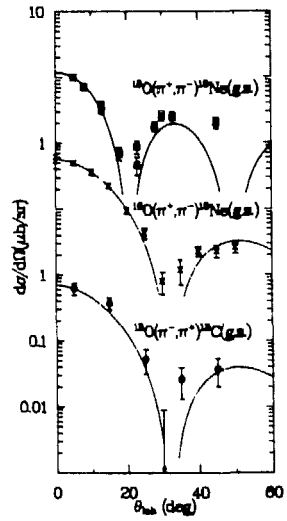

FIG. 3. Angular distribution for $^{18}O(\pi^-,\pi^+)^{18}C(g.s.)$ at $T_\pi = 164$ MeV contrasted with previously measured angular distributions for $^{16}O(\pi^+,\pi^-)^{16}Ne(g.s.)$ (Ref. 16) and $^{18}O(\pi^+,\pi^-)^{18}Ne(g.s.)$ (Refs. 2 and 17). All curves are of the form $J_0^2(qR)e^{-qd}$, and have been normalized to the $\theta = 5°$ points. The dashed curves were calculated with $R = 3.3$ fm and $d = 1.2$ fm. The solid curve was calculated with $R = 4.9$ fm and $d = 0.0$ fm.

sections measured on self-conjugate targets.

With only one data point on a non-self-conjugate target, it is impossible to determine whether the enhancement is caused by nuclear structure effects or reaction mechanism effects. There may be isospin-dependent reaction mechanism effects that increase the cross sections of all $T = 1$ to $T = 3$ transitions relative to $T = 0$ to $T = 2$ transitions. Measurement of additional $T = 1$ to $T = 3$ transitions could settle this question. There is no evidence that nuclear structure effects significantly affect cross sections on self-conjugate targets. All data agree with the best fit within error bars. All but one (^{24}Mg) of the self-conjugate targets, however, have (in a simple picture) completely filled shell model orbits. If nonanalog DCX is analogous to two-particle transfer reactions, amplitudes are proportional to two-particle coefficients of fractional parentage. These are unity for targets with filled orbits, but greater than unity for targets with partially empty orbits. For example, if neutrons in ^{16}C, ^{18}C, and ^{18}O are all in the $1d_{5/2}$ orbital, the cross section for $^{18}O(\pi^-,\pi^+)^{18}C(g.s.)$ would be 1.33 times that for $^{16}O(\pi^-,\pi^+)^{16}C(g.s.)$. More realistic wave functions can give larger enhancements.

In conclusion, we have shown that the nonanalog DCX systematics observed in $T = 0$ to $T = 2$ transitions are a general feature of pion DCX, rather than an anomaly on a special class of target nuclei. The observed $A^{-4/3}$ mass dependence fits all observed data well, although the $^{18}O(\pi^-,\pi^+)^{18}C(g.s.)$ appears enhanced over cross sections on self-conjugate targets. This suggests that (1) it would be interesting experimentally to measure nonanalog mass dependence on heavier nuclei (especially $T = 1$ targets), and (2) it would be interesting theoretically to do a microscopic calculation of the proposed reaction mechanism.

We thank Noby Tanaka and the MP-10 technical staff at LAMPF for installing the DCX modifications to the spectrometer and preparing the ice target. This work was supported in part by the U. S. Department of Energy, The Robert A. Welch Foundation, the National Science Foundation, and the Natural Sciences and Engineering Research Council of Canada.

[1]R. L. Burman, M. P. Baker, M. D. Cooper, R. H. Heffner, D. M. Lee, R. P. Redwine, J. E. Spencer, T. Marks, D. J. Marlbrough, B. M. Preedom, R. J. Holt, and B. Zeidman, Phys. Rev. C 17, 1774 (1978).

[2]S. J. Greene, W. J. Braithwaite, D. B. Holtkamp, W. B. Cottingame, C. Fred Moore, G. S. Blanpied, A. T. Viescas, G. H. Daw, C. L. Morris, and H. A. Thiessen, Phys. Rev. C 25, 927 (1982).

[3]L. C. Bland, R. Gilman, M. Carchidi, K. Dhuga, Christopher L. Morris, H. T. Fortune, S. J. Greene, Peter A. Seidl, and C. Fred Moore, Phys. Lett. 128B, 157 (1983).

[4]C. L. Morris, H. T. Fortune, L. C. Bland, R. Gilman, S. J. Greene, W. B. Cottingame, D. B. Holtkamp, G. R. Burleson, and C. Fred Moore, Phys. Rev. C 25, 3218 (1982).

[5]L. C. Bland, H. T. Fortune, S. J. Greene, C. Fred Moore, and C. L. Morris, J. Phys. G 8, L173 (1982).

[6]M. B. Johnson, E. R. Siciliano, H. Toki, and A. Wirzba, Phys. Rev. Lett. 52, 593 (1984).

[7]Kamal K. Seth in Intermediate-Energy Nuclear Chemistry Workshop, Los Alamos National Laboratory Report LA-8835-C, 250, 1980.

[8]Peter A. Seidl *et al.* (unpublished).

[9]Peter A. Seidl *et al.*, submitted to Phys. Rev. C.

[10]R. Gilman, L. C. Bland, Peter A. Seidl, C. Fred Moore, C. L. Morris, Steven J. Greene, and H. T. Fortune (unpublished).

[11]L. C. Liu, Phys. Rev. C 27, 1611 (1983); M. B. Johnson *et al.* (unpublished).

[12]Peter A. Seidl, Rex R. Kiziah, Mark K. Brown, C. Fred Moore, C. L. Morris, Helmut Baer, Steven J. Greene, G. R. Burleson, W. B. Cottingame, L. C. Bland, R. Gilman, and H. T. Fortune, Phys. Rev. Lett. 50, 1106 (1983).

[13]Kamal K. Seth, H. Nann, S. Iversen, M. Kaletka, J. Hird, and H. A. Thiessen, Phys. Rev. Lett. 41, 1589 (1978).

[14]S. J. Greene, W. J. Braithwaite, D. B. Holtkamp, W. B. Cottingame, C. Fred Moore, C. L. Morris, H. A. Thiessen, G. R. Burleson, and G. S. Blanpied, Phys. Lett. 88B, 62 (1979).

[15]G. Rowe, M. Salomon, and Rubin H. Landau, Phys. Rev. C 18, 584 (1978).

[16]S. J. Greene, W. B. Cottingame, G. R. Burleson, L. C. Bland, R. Gilman, H. T. Fortune, C. L. Morris, D. B. Holtkamp, and C. Fred Moore, Phys. Rev. C 27, 2375 (1983).

[17]Kamal K. Seth, S. Iversen, H. Nann, M. Kaletka, J. Hird, and H. A. Thiessen, Phys. Rev. Lett. 43, 1574 (1979); 45, 147 (1980).

Article B4

Nuclear Physics A432 (1985) 610-618

TWO-AMPLITUDE MODEL OF PION DCX APPLIED TO THE ^{18}O ANGULAR DISTRIBUTION AND EXCITATION FUNCTION†

R. GILMAN and L.C. BLAND*

University of Pennsylvania, Philadelphia, PA 19104, USA

PETER A. SEIDL and C. FRED MOORE

University of Texas at Austin, Austin, TX 78712, USA

C.L. MORRIS

Los Alamos National Laboratory, Los Alamos, NM 87545, USA

STEVEN J. GREENE**

New Mexico State University, Las Cruces, NM 88003, USA

and

H.T. FORTUNE***

Los Alamos National Laboratory, Los Alamos, NM 87545, USA
and
University of Pennsylvania, Philadelphia, PA 19104, USA

Received 20 March 1984
(Revised 11 July 1984)

Abstract: An earlier model developed to fit the DCX excitation function of ^{18}O has been extended to account for the $T_\pi = 164$ MeV ^{18}O DCX angular distribution in terms of that for ^{16}O and a double-isobaric-analog transition.

E NUCLEAR REACTIONS $^{18}O(\pi^+, \pi^-)$, π^-, two-amplitude fit to previously published data.

In pion-induced double charge exchange[1,2] (DCX) on $^{16,18}O$ leading to the ground states of $^{16,18}Ne$, the forward-angle cross sections exhibit very different behavior with pion energy (see fig. 1). Of course, ^{18}Ne (g.s.) is the double-isobaric-analog state (DIAS) of ^{18}O(g.s.), and DCX $^{18}O \rightarrow {}^{18}Ne$ can proceed via a double-isobaric-analog transition (DIAT). On the other hand, ^{16}O(g.s.) is $T = 0$, whereas ^{16}Ne(g.s.) is $T = 2$, and no DIAT connects the two. In virtually all published models

† Supported in part by US National Science Foundation, US Department of Energy, and The Robert A. Welch Foundation.

* Present address: IUCF, Milo B. Sampson Lane, Bloomington, IN, USA.
** Present address: Los Alamos National Laboratory, Los Alamos, NM 87545, USA.
*** Permanent address: University of Pennsylvania, Philadelphia, PA 19104, USA.

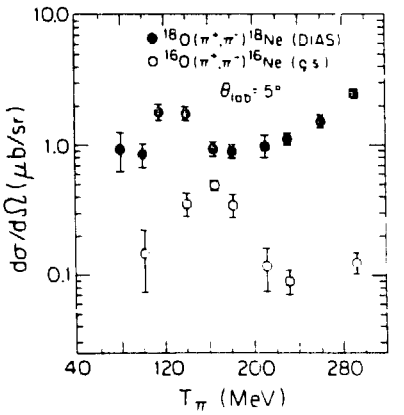

Fig. 1. Excitation functions measured at 5° (lab) for $^{18}O(\pi^+,\pi^-)^{18}Ne$(g.s.) (closed circles) and $^{16}O(\pi^+,\pi^-)^{16}Ne$(g.s.) (open circles). The data are from refs. [1,2])

of DCX, the cross section for ^{16}O should be zero, while, in fact, it is seen to be comparable to that for ^{18}O, especially near $T_\pi = 160$ MeV.

Furthermore, the most sophisticated calculation [3]) available to date for the energy dependence of $^{18}O(\pi^+,\pi^-)^{18}Ne$ fails to account for the data (see fig. 2). Deviations between data and calculation are minimal above 200 MeV, but substantial below that energy, i.e. in the region in which the ^{16}O cross section is largest.

At 164 MeV, angular distributions [1,4]) (fig. 3) for ^{16}O and ^{18}O are also quite different, and it is the ^{18}O shape that is anomalous – the first minimum appears at a much-too-forward angle. Fig. 4 compares the ^{18}O data [1]) with results of an eikonal calculation [5]). Other DIAT calculations give similar results.

The ^{16}O angular distribution, however, is regular. Its shape is well reproduced [4]) with a damped Bessel function, using reasonable parameters. At 292 MeV, the ^{18}O angular distribution [1]) is no longer irregular, but has the expected shape. Thus, at high energies, both the excitation function and the angular distribution behave as expected for ^{18}O, whereas near 160 MeV the excitation function and angular distribution for ^{18}O are both anomalous. It is at these latter energies that the ^{16}O cross section is the largest.

Because the ^{16}O DCX processes necessarily involves non-double-analog routes, we postulate that the unusual behavior of the ^{18}O DCX arises also from such non-double-analog processes. Hence, we expect we can express the ^{18}O DCX cross section as

$$\sigma_{1R}(E,\theta) = |f_{DIAT}(E,\theta) + f_{NA}(E,\theta)|^2 ,$$

where the DIAT amplitude is e.g. that from Miller [3]), or from an eikonal calculation [5]). As there is some question concerning the overall magnitude of the DIAT

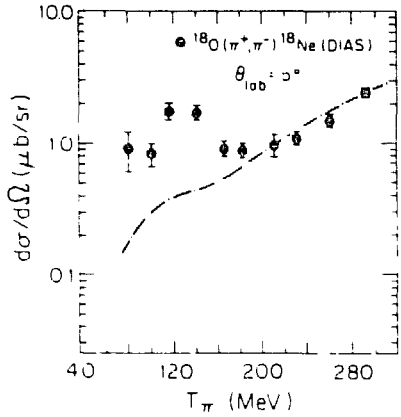

Fig. 2. Excitation function for ^{18}O [from ref. [1]] compared with a DIAT calculation [ref. [4]].

amplitude, we allow an enhancement factor, A_{DIAT}, which is independent of both energy and angle and is defined such that $A_{DIAT} = 1$ corresponds to $\sigma_{DIAT} = 0.56\ \mu b/sr$ at 164 MeV and 5° (lab).

For the non-analog amplitude, we take

$$f_{NA} = A_{NA} f_{16}(E, \theta),$$

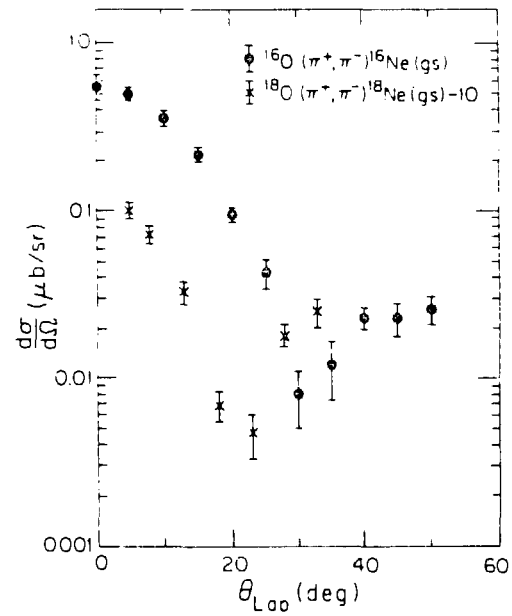

Fig. 3. Angular distributions at $T_\pi = 164$ MeV for $^{16}O(\pi^+,\pi^-)^{16}Ne$(g.s.) [dots, from ref. [4]] and $^{18}O(\pi^+,\pi^-)^{18}Ne$(g.s.) [crosses, from ref. [1]].

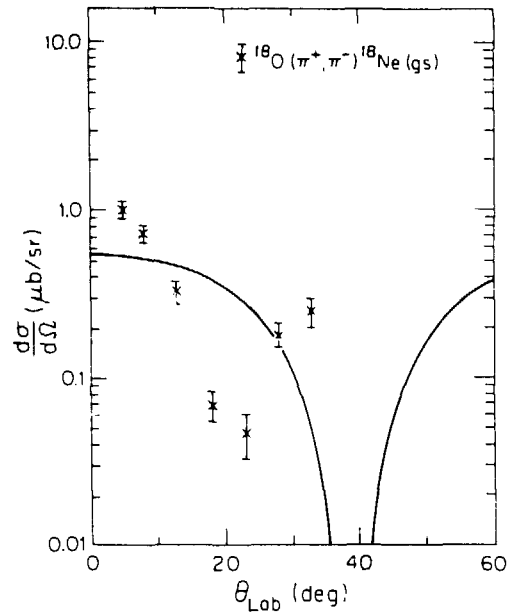

Fig. 4. Angular distribution for $^{18}O(\pi^+, \pi^-)^{18}Ne$(g.s.) at T_π = 164 MeV [ref. [1]] compared with eikonal-model calculation of ref. [4]).

where

$$|f_{16}(E, \theta)|^2 = \sigma_{16}(E, \theta),$$

i.e. $|f_{16}|^2$ fits the angle and energy dependence of DCX on ^{26}O. Again, A_{NA} is independent of both energy and angle. As [2,4]) $\sigma_{16} = 0.50\ \mu$b/sr at 164 MeV and 5°(lab), $A_{NA} = 1$ corresponds to that cross section for the non-analog route.

We have no theoretical calculation for the non-analog process, and are hence forced to use a parameterized form of the data for that amplitude. We have used two analytic forms that have some intuitive, physical basis. The Bessel-function form, $f_{16} = N\, e^{-qd} J_0^2(qR)\, e^{i\phi_0}$, is an eikonal approximation, with a damping factor e^{-qd} added to simulate surface effects. The phase ϕ_0 is independent of angle but will depend on energy. This expression gives a good fit [4]) to the 164 MeV $^{16}O(\pi^+, \pi^-)^{16}Ne$(g.s.) data, with $N = 0.885\ (\mu b/sr)^{1/2}$, $d = 0.60$ fm and $R = 3.3$ fm.

A Legendre-polynomial expansion

$$f_{NA}(E, \theta) = \sum_{l=0}^{L} b_l(E) P_l(\cos\theta),$$

with complex b's, is a standard partial-wave expansion of the reaction amplitude. The coefficients b_l that are required to fit the ^{16}O data at 164 MeV are not unique,

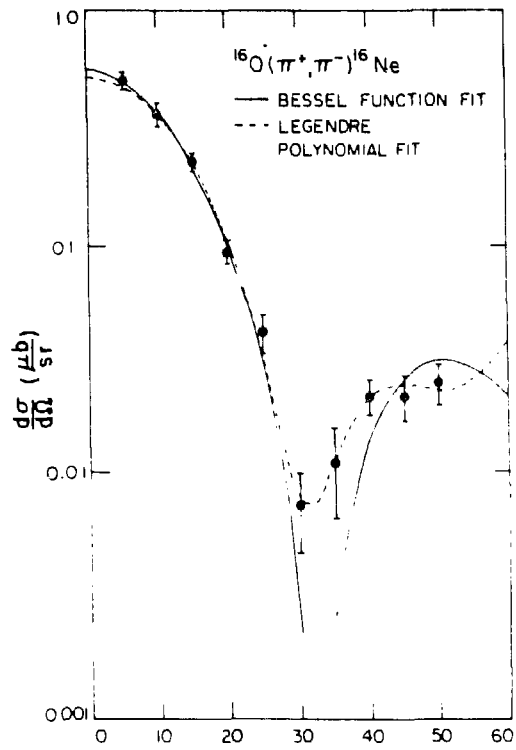

Fig. 5. Angular distribution, at T_π = 164 MeV, for $^{16}O(\pi^+, \pi^-)^{16}Ne(g.s.)$ [from ref. [4]]. The solid curve is the Bessel-function fit of ref. [4]; the dashed curve is a Legendre-polynomial fit using coefficients listed in table 1.

but all require a large b_4 and b_5 - not surprising since the grazing partial wave for $\pi^- + {}^{16}O$ at 164 MeV is about 4.5. The fit displayed in fig. 5 was calculated with the coefficients listed in table 1.

For the DIAT amplitude to be used in fitting the ^{18}O 164 MeV angular distribution, we employ the eikonal-model result of Johnson [5]) displayed in fig. 4. We combine

TABLE 1

Coefficients of the Legendre-polynomial fit to the $^{16}O(\pi^+, \pi^-)^{16}Ne(g.s.)$ angular distribution

l	b_l	
	magnitude	phase [deg]
0	0.91	13
4	0.536	−59
5	0.574	52

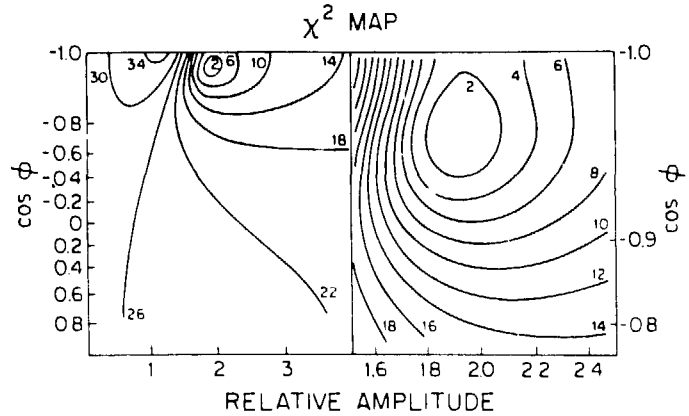

Fig. 6. A χ^2 map of cos ϕ versus A_{NA}/A_{DIAT} obtained in fitting the 164 MeV angular distribution for $^{18}O(\pi^+, \pi^-)^{18}Ne$(g.s.). The region of the χ^2 minimum is shown in more detail in the right half of the figure.

this amplitude with each of the two non-analog amplitudes discussed above to fit the ^{18}O angular distribution. The two fitting parameters are A_{NA}/A_{DIAT} and the relative phase between analog and non-analog amplitude. The absolute magnitude of the measured cross section then fixes the overall magnitude of the fit.

A χ^2 map of cos ϕ versus A_{NA}/A_{DIAT} is displayed in fig. 6 for the case in which the Bessel-function form was used for the non-analog amplitude. We find only one minimum. This minimum occurs at cos $\theta = -0.98$, i.e. $\phi = 169°$ or 191°, and $A_{NA}/A_{DIAT} = 1.90$. These parameters provide the fit displayed as a solid curve in fig. 7, and correspond to $A_{NA} = 3.11$ and $A_{DIAT} = 1.64$, i.e. the non-analog amplitude needed in ^{18}O is 3.11 times that needed in ^{16}O, and the analog amplitude needed is 1.64 times that calculated by Miller. The relative phase between the two amplitudes, at 164 MeV and 5°(lab), is 169°, i.e. near 180°.

We display as a dashed curve the fit obtained separately with the Legendre-polynomial form for the non-analog amplitude, using the amplitudes and phases listed in table 2.

We turn now to a fit to the ^{18}O excitation function measured at 5° (lab). In ref. [6]), the assumption was made that $A_{DIAT} = A_{NA} = 1$. This assumption led to an acceptable fit to the excitation function, with a relative phase that was energy dependent and was near 90° at 164 MeV. We display in fig. 8 a new fit to the 5° excitation function, with enhancement factors constrained to be those of table 2. In this fit the non-analog amplitude, f_{NA}, was taken to be given by the ^{16}O data [2]), f_{16}, times the enhancement factor, A_{NA}, and the analog amplitude, f_{DIAT}, taken to be given by the calculation of Miller [3]), f_{Miller}, times the enhancement factor, A_{DIAT}. The only free parameter in the fit was the relative phase between the analog and non-analog amplitudes. This relative phase is plotted versus energy in fig. 9, where it is compared with the

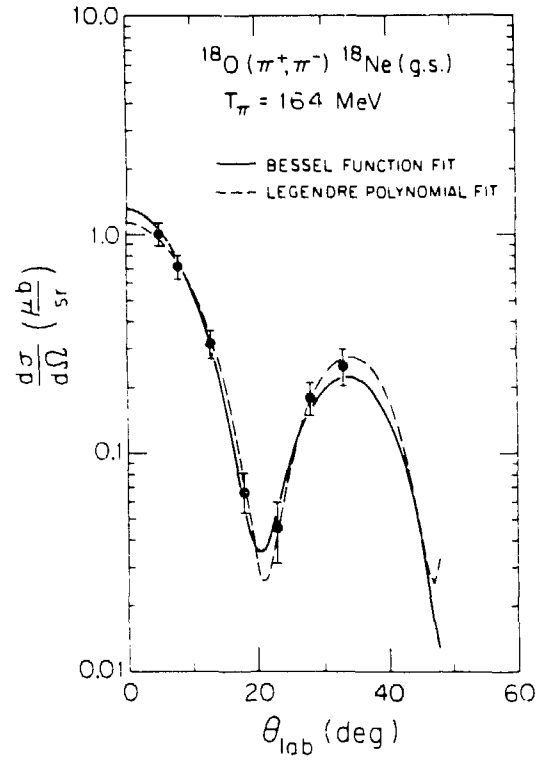

Fig. 7. Angular distribution, at 164 MeV, for $^{18}O(\pi^+, \pi^-)^{18}Ne(g.s.)$. The solid curve is a fit using $A_{DIAT} = 1.63$, $A_{\sim A} = 3.12$, $\phi = 169°$, with the Bessel-function form of $f_{\sim A}$; the dashed curve uses the Legendre-polynomial form for $f_{\sim A}$, arnd $A_{DIAT} = 1.30$, $A_{\sim A} = 2.82$, $\phi = 175°$.

earlier results of ref. [6]). Except for an overall shift of about 90°, the energy dependence of the phase is about the same as previously observed.

Thus, excellent agreement is obtained for both the 164 MeV angular distribution and the 5° excitation function for $^{18}O(\pi^+, \pi^-)^{18}Ne(g.s.)$ if the amplitude is taken to be the sum of a DIAT and a non-DIAT amplitude. The DIAT amplitude needed

TABLE 2

Parameters of two-amplitude fits to ^{18}O data

^{18}O representation	A_{DIAT}	$A_{\sim A}$	ϕ [deg] [a])
Bessel	1.632	3.117	169
Legendre	1.301	2.823	185

[a]) Relative phase at 164 MeV and 5°.

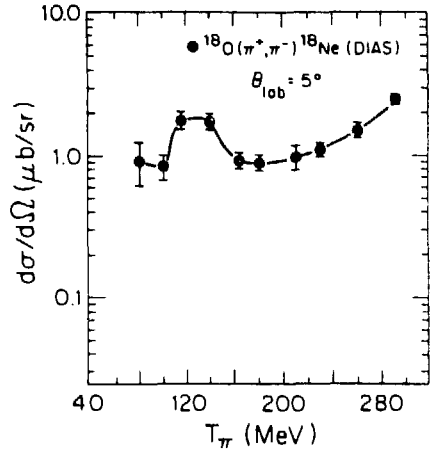

Fig. 8. Fit to the $^{18}O(\pi^+, \pi^-)^{18}Ne$(g.s.) 5° excitation function, using f_{NA} from ^{16}O data and f_{DIAT} from ref. [1]). The amplitudes are those of table 2 and relative phase that plotted in fig. 9.

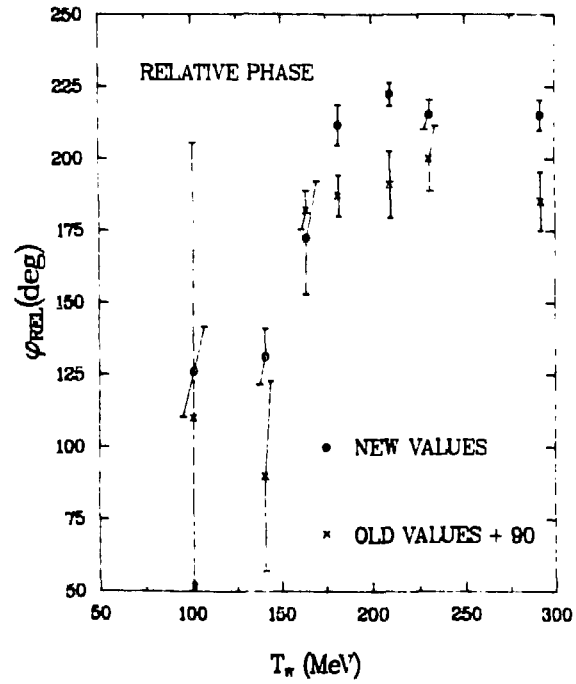

Fig. 9. Plot versus energy of the relative phase between analog and non-analog amplitudes needed to fit ^{18}O DCX excitation functions. The dots are from the present work, the crosses from ref. [1]).

is about 1.5 times that calculated by Miller, the non-DIAT amplitude is about 3.0 times that needed to describe the ^{16}O data, and their relative phase is about 180°.

An enhancement of about 1.5 for DIAT is extremely reasonable, as the use of realistic wave functions for ^{18}O produces, for DIAT alone, a cross section roughly twice [7] that of Miller, who used a simple wave function. As to the non-DIAT enhancement, the $T = 1$ nature of ^{18}O and ^{18}Ne allows the "non-analog" mechanism to take place on a Δ in the target, as well as leading to a Δ in the final state, giving an immediate enhancement of a factor of 2. If the mechanism prefers transitions in which initial and final configurations are equal over orbit-changing transitions, the non-DIAT enhancement will be still larger. Thus a value of 3.0 for this factor is also reasonable.

References

[1] S.J. Greene, W.J. Braithwaite, D.B. Holtkamp, W.B. Cottingame, C.F. Moore, G.R. Burleson, G.S. Blanpied, A.J. Viescas, G.H. Daw, C.L. Morris and H.A. Thiessen, Phys. Rev. C25 (1982) 927.

[2] L.C. Bland, H.T. Fortune, S.J. Greene, C.F. Moore and C.L. Morris, J. of Phys. G8 (1982) L173.

[3] G.A. Miller, Phys. Rev. C24 (1981) 221.

[4] S.J. Greene, W.B. Cottingame, G.R. Burleson, L.C. Bland, R. [illegible]an, H.T. Fortune, C.L. Morris, D.B. Holtkamp and C.F. Moore, Phys. Rev. C27 (1983) 2375.

[5] M.B. Johnson, Phys. Rev. C22 (1980) 192.

[6] S.J. Greene, D.B. Holtkamp, W.B. Cottingame, C.F. Moore, G.R. Burleson, C.L. Morris, H.A. Thiessen and H.T. Fortune, Phys. Rev. C25 (1982) 924.

[7] E. Oset, D. Strottman and G.E. Brown, Phys. Lett. 73B (1978) 393.

Article B5

The Energy Dependence of $^{18}O(\pi^+,\pi^-)^{18}Ne(gs)$

Peter A. Seidl, C. Fred Moore, and S. Mordechai[a]
University of Texas at Austin, Austin, TX 78712

R. Gilman, Kalvir S. Dhuga[b], H. T. Fortune, and J. D. Zumbro
University of Pennsylvania, Philadelphia, PA 19104

C. L. Morris
Los Alamos National Laboratory, Los Alamos, NM 87545

J. A. Faucett and G. R. Burleson
New Mexico State University, Las Cruces, NM 88003

ABSTRACT

Eight angular distributions measured for $^{18}O(\pi^+,\pi^-)^{18}Ne(gs)$ across the Δ_{33} resonance show the details of the energy dependence of the reaction. At higher energies, the minimum is at $q = 0.85$ fm^{-1}, in agreement with simple sequential scattering models, but at lower energies it is at $q = 0.5$ fm^{-1}, with the transition occuring over a narrow energy range.

[NUCLEAR REACTIONS: $^{18}O(\pi^+,\pi^-)^{18}Ne(g.s., E_x = 1.89$ MeV) $T_\pi = 100$ to 310 MeV, $\theta_{lab} = 5^\circ$ to 40°; measured $\sigma(T_\pi,\theta_{lab})$.]

PACS Numbers: 25.80.Fm, 21.10.Re

In pion-nucleus scattering, the qualitative (and often quantitative) features of many strong inelastic transitions are well explained within models which take nuclear structure information from data on reactions such as (e,e′) and (p,p′) data and treat the π-nucleus interaction in the distorted wave impulse approximation.[1] However, this approach significantly underestimates single-charge-exchange (SCX) differential cross sections,[2] and its extension to double-charge-exchange (DCX) reactions fails at Δ_{33} resonance energies.[3] In particular, DCX angular distributions leading to double isobaric analog states (DIAS) at resonance energies have been shown to exhibit forward minima at angles that are, within the simpler models (sequential charge exchange through the free pion-nucleon amplitude), inconsistent with the nuclear size.[4,5] At higher energies, the same reactions exhibit angular distributions that agree with simple calculations.

The anomalous angular distributions have often been interpreted as evidence for interference of the simple DCX amplitude with a second amplitude of similar size. In Ref. 6, it was suggested that this second amplitude arises from whatever reaction mechanism is responsible for the equivalently large differential cross sections observed for (necessarily non-analog) DCX on self-conjugate targets. In Ref. 7, the anomalous position of the minima is attributed to interference with higher-order (two-nucleon, usually called ρ^2) terms in the pion-nucleus optical potential. In that approach, the magnitudes of the isovector and isotensor ρ^2 terms are adjusted to fit the 0° SCX and 5° DCX data, and the resulting parameters provide good predictions of the angular-distribution shapes. The model of Liu[8,9] gives good predictions of both angular distributions and excitation functions by using core-excitation nuclear

wave functions and ρ^2 terms. The latter are obtained from an analysis of π-A elastic scattering data and reflect the effects of true pion absorption.

In this letter, we report six new angular distributions for the reaction $^{18}O(\pi^+,\pi^-)^{18}Ne(gs)$, which, when combined with previous measurements,[4,10] show the change in shape of the angular distributions as a function of energy. This is the most extensive study of DCX on a single nucleus, and identifies the energy regions in which the simple DCX amplitude is adequate to describe the data, and the energy regions in which higher order processes become important.

The measurements were made with the Energetic Pion Channel and Spectrometer (EPICS) at the Clinton P. Anderson Meson Physics Facility (LAMPF). Descriptions of the spectrometer, channel, and the modifications installed for forward-angle DCX measurements have been presented elsewhere.[11] A copper frame with 0.25-mil aluminized mylar windows contained the H_2O ice target which was enriched to 94% isotopic purity $H_2{}^{18}O$. The frame was constructed with a centered horizontal copper bar to enhance cooling of the ice. Physical measurement of the target thickness indicated an areal density of 0.95 ± 0.01 g/cm^2 H_2O, assuming a density of 1.12 g/cm^3. This value agreed well with an areal density obtained by comparing yields for $^1H(\pi^+,\pi^+)$ measured with a CH_2 target (73.68 mg/cm^2) and with the H_2O target, of xρ = 0.93 ± 0.03 g/cm^2 H_2O.

Background muon and electron events were eliminated from pion spectra by a combination of time-of-flight tests, a Freon-12 threshold Cherenkov detector to reject electrons, and a range-nuclear-interaction absorber that was adjusted to identify muon events.[12] No background events under the states of interest were expected from DCX events in the target windows, frame, or contaminants. The Q values for ^{16}O (-28.38 MeV), ^{12}C (-31.96 MeV), and ^{27}Al (-16.38 MeV) are much

more negative than that for ^{18}O (-5.08 MeV). The copper Q values (-7.85 MeV for ^{63}Cu, -3.59 MeV for ^{65}Cu) are similar to that for ^{18}O, but the greater pion energy loss in the copper frame (8.33 MeV) than in the ice (1.32 MeV) removes this background from under the states of interest. (Computer software gates were, however, used to eliminate scattering events occuring in the copper bar.) The data were normalized by measuring yields for $^{1}H(\pi^+,\pi^+)$ at $\theta = 40^\circ$ and comparing them to cross sections based on the phase shift fits of Rowe, Saloman, and Landau[13]. Yields measured for $^{1}H(\pi^+,\pi^+)$ at $\theta = 20$, 30, and 40° indicated that, within the statistical uncertainty of the yield and uncertainty of the π-p cross sections, the normalization factors are angle independent. The error bars shown in the figures represent the statistical uncertainty of the ^{18}Ne peak areas.

The new $^{18}O(\pi^+,\pi^-)^{18}Ne(gs)$ excitation function data are shown in Fig. 1, along with the data from Ref. 4. Where overlap points exist the agreement with previous measurements is, in general, good. The new and old measurements within two MeV of 100, 180, 230, and 292 MeV differ from their means by 1.4 standard deviations.

An excitation function for the $^{18}Ne(2^+,1.89$ MeV) state is also displayed in Fig. 1. We note that these cross sections are almost independent of energy, except between 130 and 170 MeV, where cross sections are at least a factor of ten smaller, a larger decrease than in the transition to the $^{18}Ne(gs)$ state.

The new ground-state angular distributions are shown in Fig. 2, along with previously measured 164- and 292-MeV data,[4,10] plotted as a function of the momentum transfer, q. The shape of the 230-MeV angular distribution is nearly identical to that of the 292-MeV data, with a broad diffraction minimum at $q = 0.85$ fm^{-1}. The larger-angle data are suggestive of a second maximum a

factor of 20 lower than the 5^{o} datum. At 200 MeV the data are roughly constant for $q \geq 0.5$ fm^{-1}, and the cross section at the largest angle measured has increased to be only a factor of 10 smaller than the forward-angle values. These features provide a smooth transition in shape between 230 and 180 MeV.

At 180 MeV the minimum is at $q = 0.5$ fm^{-1}. The cross sections for $q > 0.5$ MeV are indicative of a relatively large second maximum. The shapes of the angular distribution at 164, 172, and 180 MeV are very similar, and are clearly different from those at higher energies. Below the Δ_{33} resonance, at 120 MeV, the minimum is at a slightly larger momentum transfer. Because of the lower pion flux at lower energies and the limited angular range of the DCX setup ($\theta < 42^{o}$), it was impossible to determine the location of the first minimum of the 100-MeV angular distribution.

In an energy region just above the Δ_{33} resonance (from $200 < T_{\pi} < 230$ MeV) up to at least 292 MeV the ^{18}O angular distribution is normal in the sense that the position of the minimum is consistent with a simple diffractive process. Thus, at these energies the reaction would appear to be dominated by sequential SCX via the intermediate analog state. Figure 3 shows angular distribution calculations for the higher energy region. The curves are from lowest-order calculations with the code PIESDEX[7] using Hartree-Fock[14] (Skyrme-III effective interaction) neutron, proton, and excess neutron densities, and represent sequential charge exchange through the intermediate analog state. The theory correctly predicts angular-distribution shapes at 230 and 292 MeV, and the departure from the dominance of the lowest order reaction mechanism is apparent at 200 and 180 MeV. Not shown are calculations with a ground state density generated from electron scattering parameterizations and a $(d_{5/2})^2$ harmonic oscillator valence neutron density that predict minima at angles a few degrees

larger than the solid curve and similar overall magnitudes. Thus, reasonable variations in the densities do not significantly alter these calculations.

For energies across the Δ_{33} resonance, down to 120 MeV, the angular distributions clearly exhibit forward minima, evidence for additional dynamical effects. The nature of these effects is uncertain, but some possibilities are discussed in Ref. 8 and 15. There is no evidence in our data to indicate whether or not there exists a lower-energy region where the reaction will again agree with lowest-order DCX calculations. Recent measurements[16] of DCX on ^{14}C at 50 MeV would seem to indicate that no such region exists. At 50 MeV, $d\sigma/d\Omega(0^o) = 3.9 \pm 0.5$ μb/sr for the $^{14}C(\pi^+,\pi^-)^{14}O(gs)$ reaction, roughly 20 times that calculated in a sequential charge-exchange calculation in which the intermediate state is the single analog in ^{14}N, and the angular distribution is forward peaked, rather than exhibiting the shallow forward minimum predicted by the calculation.

The shape of the $^{18}O(\pi^+,\pi^-)^{18}Ne(gs)$ 200 MeV angular distribution is similar to the $^{14}C(\pi^+,\pi^-)^{14}O(gs)$ angular distribution[5] at T = 164 MeV, where the cross section is roughly constant for $q > 0.4$ fm^{-1}. The ^{14}C data have been perplexing because all other 164 MeV DCX angular distributions exhibit well-defined, deep, forward minima. It is interesting to speculate that ^{14}C and ^{18}O have similar features shifted by ~40 MeV. This speculation is supported by the shape of the excitation functions, which also exhibit similar shapes, shifted by ~40 MeV with respect to each other. The cause for this shift is unknown.

In conclusion, these new $^{18}O(\pi^+,\pi^-)^{18}Ne(gs)$ data show that the onset of interesting dynamical effects occur over a 30 MeV incident kinetic energy range, which dramatically change the shape of the angular distributions. The completeness of this measurement will hopefully distinguish between varied theoretical approaches to the perplexing DCX problem.

This work has been supported in part by The Robert A. Welch Foundation, The National Science Foundation, and The US Department of Energy.

REFERENCES

a) permanent address: Ben Gurion University of the Negev, Beer-Sheva, Israel.

b) present address: New Mexico State University, Las Cruces, NM 88003

[1] J. A. Carr, F. Petrovich, D. Halderson, D. B. Holtkamp, W. B. Cottingame, Phys. Rev. C27, 1636 (1983).

[2] A. Doron, J. Alster, A. Erell, S. Gilad, M. A. Moinester, R. A. Anderson, H. W. Baer, J. D. Bowman, M. D. Cooper, F. H. Cverna, C. M. Hoffman, N. S. P. King, M. J. Leitch, J. P. Piffaretti, P. R. Bevington, E. Winkelmann, and C. D. Goodman, Phys. Rev. Lett. 48, 989 (1982); A. Doron, J. Alster, A. Erell, M. A. Moinester, R. A. Anderson, H. W. Baer, J. D. Bowman, M. D. Cooper, F. H. Cverna, C. M. Hoffman, N. S. P. King, M. J. Leitch, J. P. Piffaretti, and C. D. Goodman, Phys. Rev. C26, 189 (1982).

[3] Gerald A. Miller, Phys. Rev. C24, 221 (1981).

[4] S. J. Greene, W. J. Braithwaite, D. B. Holtkamp, W. B. Cottingame, C. F. Moore, G. R. Burleson, G. S. Blanpied, A. J. Viescas, G. H. Daw, C. L. Morris, and H. A. Thiessen, Phys. Rev. C 25, 927 (1982).

[5] Peter A. Seidl, M. D. Brown, Rex R. Kiziah, C. Fred Moore, Helmut Baer, C. L. Morris, G. R. Burleson, W. B. Cottingame, Steven J. Greene, L. C. Bland, R. Gilman and H. T. Fortune, Phys. Rev. C30, 973 (1984).

[6] S. J. Greene, D. B. Holtkamp, W. B. Cottingame, C. F. Moore, G. R. Burleson, C. L. Morris, H. A. Thiessen, and H. T. Fortune, Phys. Rev. C25, 924 (1982); R. Gilman, L. C. Bland, Peter A. Seidl, C. Fred Moore, C. L. Morris, Steven J. Greene, H. T. Fortune, Nuc. Phys. A, (to be published).

[7] Mikkel B. Johnson and E. R. Siciliano, Phys. Rev. C27, 1647 (1983); S. J. Greene, C. J. Harvey, P. A. Seidl, R. Gilman, E. R. Siciliano, and Mikkel B. Johnson, Phys. Rev. C (to be published).

[8] L. C. Liu, Phys. Rev. C27, 1611 (1983).

[9] Kamal K. Seth, M. Kaletka, S. Iversen, A. Saha, D. Barlow, D. Smith, and L. C. Liu, Phys. Rev. Lett. 52, 894 (1984).

[10] Kamal K. Seth, S. Iversen, H. Nann, M. Kaletka, J. Hird, and H. A. Thiessen, Phys. Rev. Lett. 43, 1574 (1979).

[11] H. A. Thiessen, J. C. Kallne, J. F. Amann, R. J. Peterson, S. J. Greene, S. L. Verbeck, G. R. Burleson, S. G. Iverson, A. W. Obst, Kamal K. Seth, C. F. Moore, J. E. Bolger, W. J. Braithwaite, D. C. Slater and C. L. Morris, Los Alamos Scientific Laboratory Report No. LA-6663-MS, (1977); S. J. Greene, W. J. Braithwaite, D. B. Holtkamp, W. B. Cottingame, C. F. Moore, C. L. Morris, H. A. Thiessen, G. R. Burleson, and G. S. Blanpied, Phys. Lett. 88B, 62 (1979); G. R. Burleson, G. S. Blanpied, G. H. Daw, A. J. Viescas, C. L. Morris, H. A. Thiessen, S. J. Greene, W. J. Braithwaite, W. B. Cottingame, D. B. Holtkamp, I. B. Moore, and C. F. Moore, Phys. Rev. C22, 1180 (1980); S. J. Greene, PhD thesis, The University of Texas at Austin, Los Alamos National Laboratory Report No. LA-8891-T, (1981).

[12] C. L. Morris, J. F. Amann, R. L. Boudrie, N. Tanaka, S. J. Seestrom-Morris, L. C. Bland, P. A. Seidl, and R. Kiziah, (to be published).

[13] Glenn Rowe, Martin Salomon and Rubin H. Landau, Phys. Rev. C 18, 584 (1978).

[14] M. Beiner, H. Flocard, Nguyen Van Giai, and P. Quentin, Nucl. Phys. A238, 29 (1975).

[15] Mikkel B. Johnson, E. R. Siciliano, H. Toki, and A. Wirzba, Phys. Rev. Lett. 52, 593 (1984); E. Oset, D. Strottman, M. J. Vicente-Vacas, and Ma Wei-Hsing, Nuc. Phys. A408, 461 (1983); T. Karapiperis, M. Kobayashi, and M. Hirata, Phys. Lett. 144B, 23 (1984); Pervez Hoodbhoy, Roger A. Freedman, Gerald A. Miller, and Ernest M. Henley, Phys. Rev. C27, 277 (1983).

[16] M. J. Leitch, E. Piasetzky, H. W. Baer, J. D. Bowman, R. L. Burman, B. J. Dropesky, P. A. M. Gram, F. Irom, D. Roberts, G. A. Rebka, J. N. Knudson, J. R. Comfort, V. A. Pinnick, D. H. Wright, and S. A. Wood, submitted to Phys. Rev. Lett. (1984) and Los Alamos National Laboratory Report LA-UR 84-2754; I. Navon, M. J. Leitch, D. A. Bryman, T. Numao, P. Schlatter, G. Azuelos, R. Poutissou, R. A. Burnham, M. Hasinoff, J. M. Poutissou, J. A. Macdonald, J. E. Spuller, C. K. Hargrove, H. Mes, M. Blecher, K. Gotow, M. Moinester, H. Baer, Phys. Rev. Lett. 52, 105 (1984).

FIGURE CAPTIONS

Fig. 1. Center-of-mass cross sections ($\theta_{lab} = 5^{o}$) for $^{18}O(\pi^{+},\pi^{-})^{18}Ne(gs)$ (crosses from this work and circles from Ref. 4) and $^{18}O(\pi^{+},\pi^{-})^{18}Ne(2^{+}, 1.89\ MeV)$ are plotted versus the pion energy in the lab frame. The $^{18}Ne(2_{1}^{+})$ data from both Ref. 4 and from this work are represented by squares.

Fig. 2. Center-of-mass cross sections for $^{18}O(\pi^{+},\pi^{-})^{18}Ne(0\ MeV)$, are plotted versus the momentum transfer, q. The incident energies in MeV are indicated on the graph. Data for q = 0.70 and 1.03 fm^{-1} ($\theta = 30^{o}$ and 45^{o}) at $T_{\pi} = 164$ MeV are from Ref. 10. The datum for $T_{\pi} = 292$ MeV, q = 1.40 is from this work, and all remaining data for $T_{\pi} = 164$ and 292 MeV are from Ref. 4.

Fig. 3. Center-of-mass cross sections for $^{18}O(\pi^{+},\pi^{-})^{18}Ne(gs)$ are compared to lowest order PIESDEX calculations.

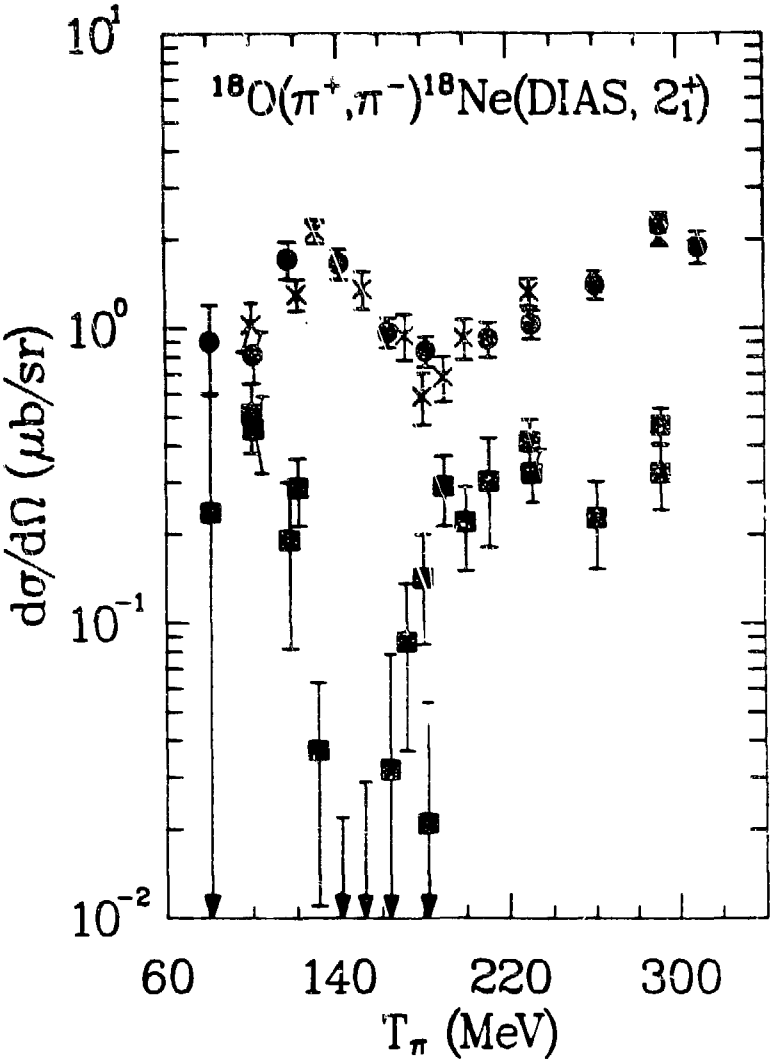
$^{18}O(\pi^+,\pi^-)^{18}Ne(DIAS, 2_1^+)$
$d\sigma/d\Omega$ (μb/sr)
10^1
10^0
10^{-1}
10^{-2}
60
140
220
300
T_π (MeV)

Figure 1

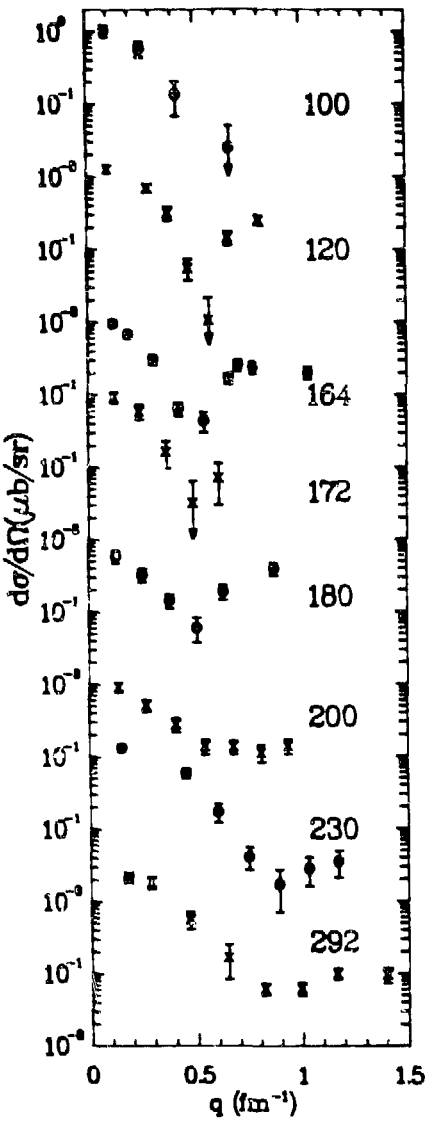

Figure 2

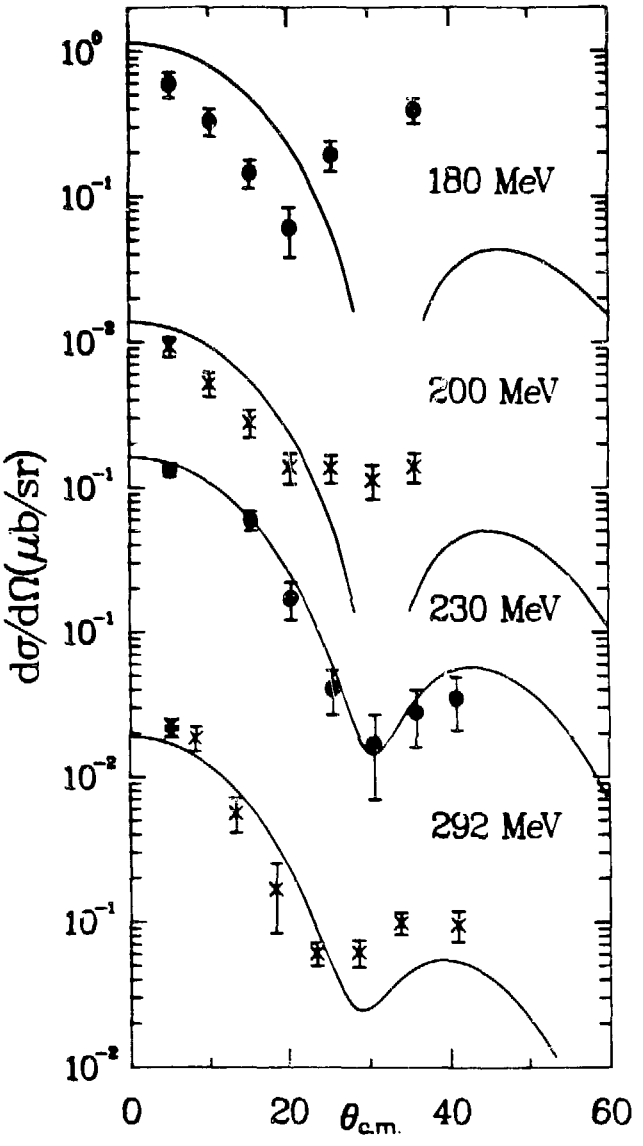

Figure 3

Article B6

Calculations of Nonanalog Pion Double Charge Exchange

R. Gilman and H. T. Fortune
University of Pennsylvania, Philadelphia, PA 19104

Mikkel B. Johnson
Los Alamos National Laboratory, Los Alamos, NM 87545

E. R. Siciliano
University of Georgia, Athens, GA 30602

H. Toki
Tokyo Metropolitan University, Tokyo, Japan

and
A. Wirzba
State University of New York, Stony Brook, NY 11794

ABSTRACT

Numerical results of calculations of pion double-charge-exchange (DCX) arising from Δ-mediated forces have been obtained. Calculations of DCX excitation functions and angular distributions for the reaction $^{16}O(\pi^+,\pi^-)^{16}Ne(gs)$ are presented. The sensitivity of the calculations to quantities specifying the reaction mechanism is shown.

[PACS Number 25.80.Fm]

The large cross sections and simple systematics of pion double-charge exchange (DCX) on T = 0 targets[1] are among the most surprising features of DCX. The systematics of these $\Delta T = 2$, $\Delta J = 0$ transitions (excitation functions peaked at Δ_{33} resonance energies, diffractive angular distributions, and an $A^{-4/3}$ mass dependence) were not anticipated, and have not been explained in any model. Several calculations of the ratio,

$$\frac{d\sigma(^{16}O(\pi^+,\pi^-)^{16}Ne(gs))}{d\sigma(^{18}O(\pi^+,\pi^-)^{18}Ne(gs))},$$

have been performed[2-4] within models in which both transitions proceed via sequential single-charge exchanges, but none of these has reproduced the energy and angle dependencies of the experimental data. The energy dependence of the nonanalog data strongly suggests a simple Δ-dominated mechanism shown in Fig. 1.

In this Letter, we describe the results of new calculations of nonanalog DCX through this reaction mechanism. In an earlier Letter,[5] the contribution of two nonsequential charge-exchange processes to the analog reaction, $^{18}O(\pi^+,\pi^-)^{18}Ne(gs)$, was examined. The direct Δ_{33}-nucleus interaction process (DINT), displayed in Figure 1, was found to be of similar size to the standard sequential charge-exchange mechanism at energies near the Δ_{33} resonance ($T_\pi \sim 180$ MeV). A process involving Δ_{33} components of the initial-and final-state wave functions (DWF) was found to have little effect on the calculated cross sections. This work has been generalized and extended[6] to describe nonanalog DCX reactions. Since the theory was described earlier,[5] we present here only a brief description of its main features, and

concentrate on the modifications between the previous and present works. A full description of the theory will be published in an upcoming article.[6]

DCX cross sections are calculated within a distorted-wave impulse approximation framework using a version of the code DWPI[7] built around an optical potential of the form given in Ref. 8. The input transition density is constructed microscopically for transitions between specific shell model configurations. For illustrative purposes, we have assumed that ^{16}O is a closed core, and that ^{16}Ne is $\upsilon(p1/2)^{-2}\pi(d5/2)^2$. Then, the $^{16}O(\pi^+,\pi^-)^{16}Ne(gs)$ reaction proceeds solely via a $\upsilon(p1/2)^2 \rightarrow \pi(d5/2)^2$ transition.

The DINT process in Fig. 1 is calculated from π + ρ exchange interactions. As in Ref. 5 it consists of five tensors, M_υ, which are contractions of the nuclear spins and the momenta of the mesons. Coefficients of the terms are specified in Ref. 5. Input parameters to the calculations include several coupling constants, e.g., $f_{\pi nn}$, which have been fixed at the values specified in Ref. 5. The π and ρ meson form factors are taken to be

$$\upsilon(k) = (1+k^2/\Lambda^2)^{-1}.$$

Since there are no generally accepted values for Λ_π and Λ_ρ, we have investigated the effects of variations in these parameters for values near $\Lambda_\pi = \Lambda_\rho = 6.07$ fm^{-1}. Two of the tensors (υ = 2 and 6) lead to transition densities that are scalars in the pion initial and final momenta, $T_0(\hat{k}',\hat{k})$. Three (υ = 4, 5, and 7) lead to second-rank tensors in the pion momenta, $T_2(\hat{k}',\hat{k})$. DINT and DWF have the same tensor terms in k and k', but only DINT has the scalar terms. Since DINT is much larger than DWF, we conclude

that the scalar terms dominate, and do not evaluate the tensor pieces.

The most significant difference between the calculation presented here and that in Ref. 5 is the nuclear structure. We use harmonic-oscillator wave functions coupled to $J = 0$, and perform the Moshinsky transformation to relative and center-of-mass (cm) coordinates. (In contrast to Ref. 5, we do not approximate the radial dependence of the transition density as proportional to the square of the valence neutron density.) An integral over relative wave functions is performed only for $r > 0.5$ fm to account for short-range, repulsive nuclear correlations.

Transition densities for $^{16}O(\pi^+,\pi^-)^{16}Ne(gs)$ are shown as solid curves in Figure 2. As we have stated, the scalar transition density has contributions from tensors M_2 and M_4. We show separately the contributions to M_2 from nucleon pairs coupled to $S = L = 0$ (the short dashed curve) and to $S = L = 1$ (the long-short dashed curve). The chaindot curve is the tensor term, M_4, for which the nucleon pairs must be coupled to $S = L = 1$. The inclusion of the ρ meson results in a change in the relative magnitude of each term, which depends on the input parameters for Λ_π and Λ_ρ. This causes a shift in the position of the peak in the transition density.

In general, we find we are insensitive to the shape of the transition density inside R ~ 2.5 fm. We also find (see Figure 3) that the resulting excitation-function and angular-distribution shapes are insensitive to the input parameters. The energy dependence is dominated by the intermediate Δ_{33} propagators and the effects of distortions. The angular dependence reflects the nuclear size and the effects of distortions. We emphasize that, for wide variations in Λ_π and Λ_ρ, only the absolute magnitude of the calculations is changed. The sensitivity to Λ_π and Λ_ρ suggests the need for the explicit introduction of a model for the nucleon and Δ_{33} and its coupling to mesons.

Figs. 3 and 4 contrast calculations with the experimental data for $^{16}O(\pi^+,\pi^-)^{16}Ne(gs)$. The agreement in shape of both excitation function and angular distribution is excellent. The angular distribution agreement is not surprising. It has been shown that all nonanalog DCX angular distributions reflect the nuclear size.[1,9] This is, however, the first calculation to correctly reproduce the energy dependence of nonanalog DCX.

Preliminary indications are that the excitation-function and angular-distribution shapes are also insensitive to the specified shell-model transition. Because these features look very much like the data, we are encouraged to make additional calculations with more realistic nuclear wave functions for several nuclei. This extension is necessary in order to compare to the observed $A^{-4/3}$ mass dependence of nonanalog DCX.[1]

In conclusion, calculations of nonanalog DCX through the $\Delta_{3/2}$-nucleus interaction process reproduce the angular and energy dependence of nonanalog DCX. Both the absolute magnitude and the mass dependence of the calculations require additional investigation. We do, however, appear close to a quantitative explanation of nonanalog DCX.

This work was supported in part by the U. S. Department of Energy and the National Science Foundation.

REFERENCES

[1] L. C. Bland, R. Gilman, M. Carchidi, K. Dhuga, Christopher L. Morris, H. T. Fortune, S. J. Greene, Peter A. Seidl, and C. Fred Moore, Physics Letters 128B, 157 (1983).

[2] T.-S. H. Lee, D. Kurath, and B. Zeidman, Phys. Rev. Lett. 39, 1307 (1977).

[3] Guang-Lie Li, Chu-Hsia Li, and T.-S. H. Lee, Phys. Lett. 99B, 200 (1981).

[4] Liu Xianhui, Wu Zongen, Huang Zhaohui, and Li Yangguo, Sci. Sin. 24, 789 (1981).

[5] M. B. Johnson, E. R. Siciliano, H. Toki, and A. Wirzba, Phys. Rev. Lett. 42, 593 (1984).

[6] A. Wirzba, H. Toki, E. R. Siciliano, and M. B. Johnson, unpublished.

[7] R. A. Eisenstein and G. A. Miller, Comp. Phys. Comm. 11, 95 (1976).

[8] M. B. Johnson and E. R. Siciliano, Phys. Rev. C 27, 730 (1983).

[9] R. Gilman, H. T. Fortune, Kalvir S. Dhuga, Peter H. Kutt, L. C. Bland, Rex. R. Kiziah, C. Fred Moore, Peter A. Seidl, C. L. Morris, and W. B. Cottingame, Phys. Rev. C 29, 2395 (1984).

FIGURE CAPTIONS

Fig. 1. Feynman diagram for DCX through direct Δ_{33}-nucleus interaction.

Fig. 2. Transition density for $^{16}O(\pi^+,\pi^-)^{16}Ne(gs)$. The assumed transition is $\upsilon(p1/2)^2 \rightarrow \pi(d5/2)^2$. A is calculated assuming only virtual π exchange. B is calculated with virtual π and ρ exchange. The solid curve is the sum of all terms in the transition density. The individual terms are described in the text.

Fig. 3. Energy dependence of calculations of $^{16}O(\pi^+,\pi^-)^{16}Ne(gs)$ for several values of Λ_π and Λ_ρ (values given in fm^{-1}) contrasted with data from Ref. 9.

Fig. 4. Angle dependence of calculations of $^{16}O(\pi^+,\pi^-)^{16}Ne(gs)$ contrasted with angular distributions from Ref. 9. The calculations used $\Lambda_\pi = \Lambda_\rho = 5.2\ fm^{-1}$.

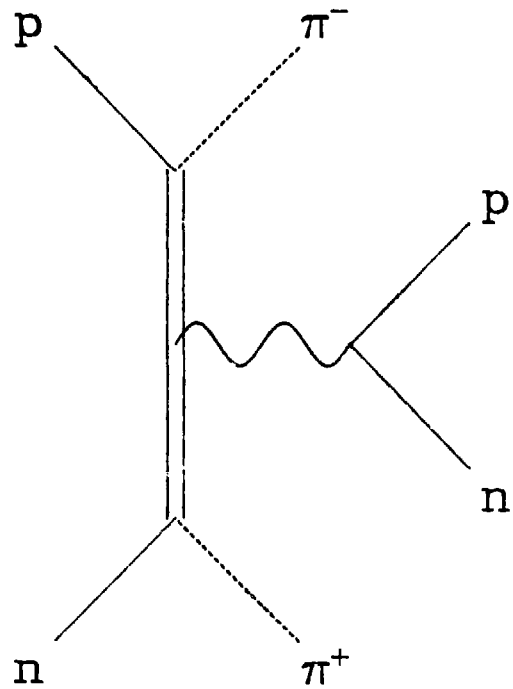

Figure 1

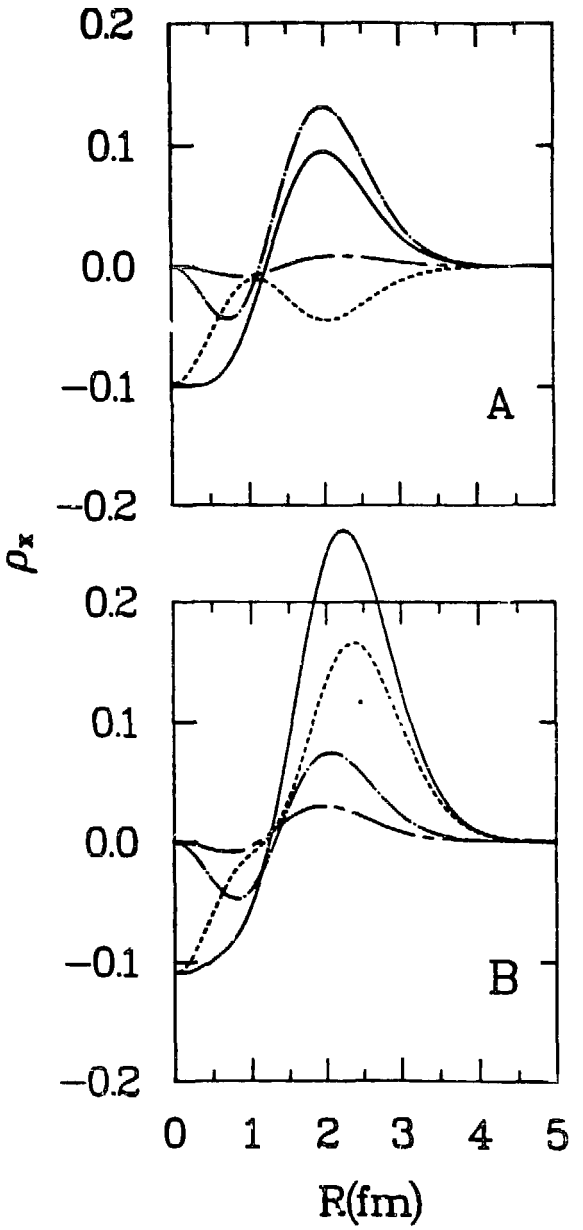

Figure 2

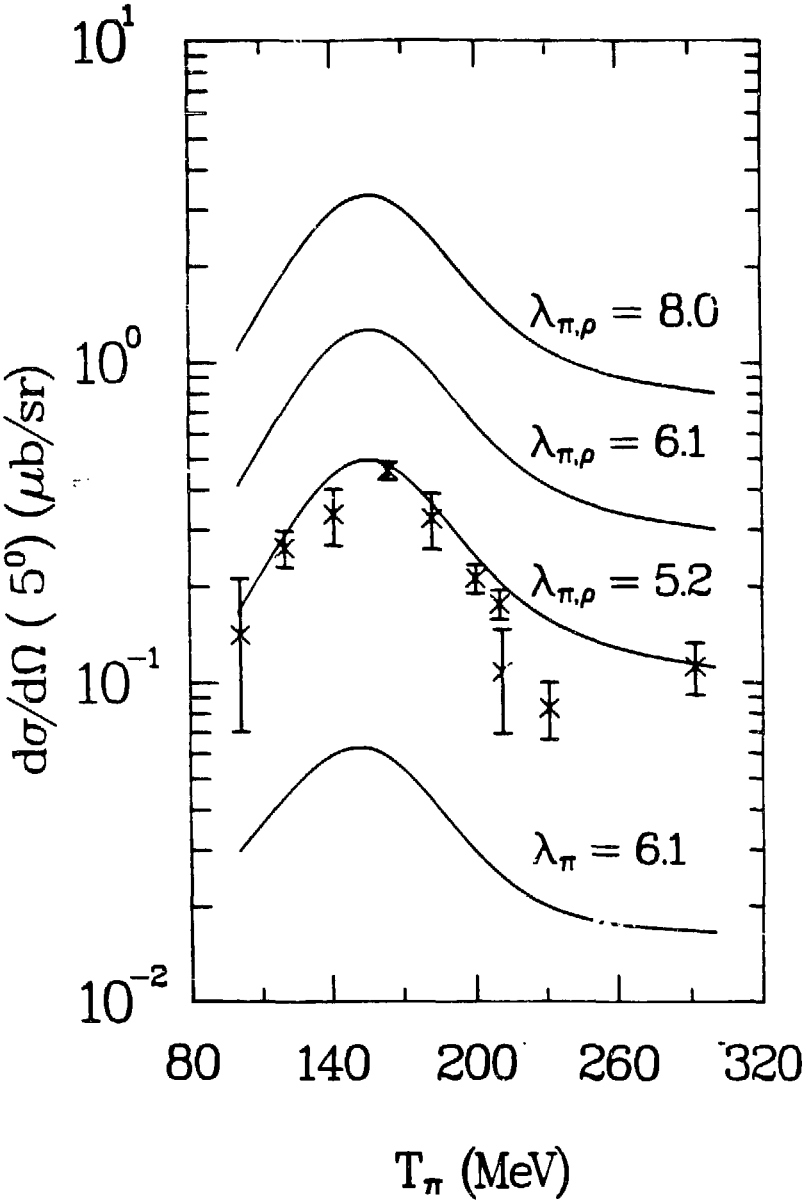
10^1
10^0
10^{-1}
10^{-2}
$d\sigma/d\Omega$ (5°) (μb/sr)
$\lambda_{\pi,\rho} = 8.0$
$\lambda_{\pi,\rho} = 6.1$
$\lambda_{\pi,\rho} = 5.2$
$\lambda_{\pi} = 6.1$
80
140
200
260
320
T_π (MeV)

Figure 3

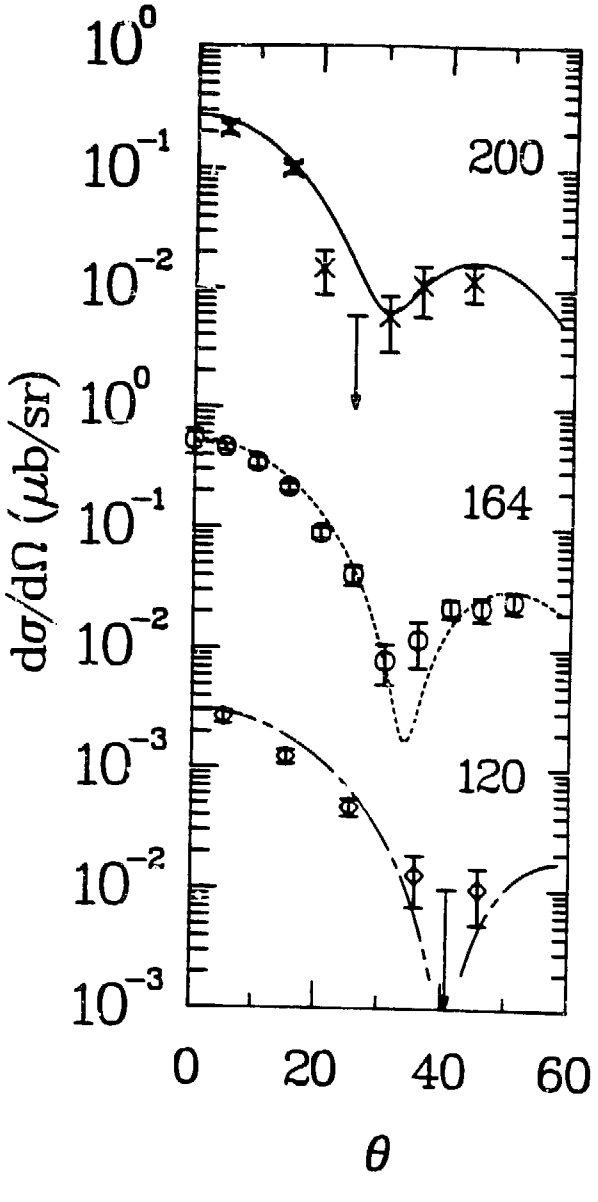
10^0
10^{-1}
10^{-2}
10^0
10^{-1}
10^{-2}
10^{-3}
10^{-2}
10^{-3}
$d\sigma/d\Omega$ (μb/sr)
200
164
120
0
20
40
60
θ

Figure 4

APPENDIX C. DCX DATA COMPILATION

Following are the contents of the data file [mp10rag.dat]data.dat, which is a compilation of DCX data.

```
* FILE=MPFGO::DRA2:[MP10RAG.DAT]DATA.DAT
*
* DCX DATA COMPILATION: PRESENT SOURCES OF DATA INCLUDE:
*  LEP COLLABORATION - LP: LEP NUMBERS FROM COOPER TALK IN
*INT-ENERGY NUCL CHEM WRKSHP, LA-8835-C (1979)
*  TRIUMPF GROUP - NV: NAVON ET AL, PHYS REV LETT 52, 105 (1984)
*  NEW LEP GROUP - LE: LEITCH ET AL, PHYS REV LETT 54, 1482 (1985)
*  NORTHWESTERN COLLABORATION - KS: PHYS REV LETT 45, 147 (1980).
*MK: MARK KALETKA PHD THESIS, LA-9947-T (1984); 42CA ALSO IN
*    K. SETH ET AL., PHYS REV LETT 52, 894 (1984)
*NA: H. NANN ET AL, PHYS LETT 96B, 261 (1980)
*NC: K. SETH  ALK IN INT-ENERGY NUCL CHEMI WRKSHP, 250 LA-8835-C,
*    250 (1980)
*SE: K. SETH ZR/MO PREPRINT, PHYS LETT 155B, 339 (1985).
*  TODCXG - BG: GREENE ET AL, PHYS REV C27, 2375 (1983).
*LB: BLAND ET AL, PHYS LETT 128B, 157 (1982)
*PS: PETER SEIDL ET AL, PHYS REV C30, 973 (1984); IBID,
*    1076 (1984); ALSO PHD THESIS, LA REPORT, LA-10338-T (1985).
*RG: ASST'D RG DATA, SOME UNPUBLISHED, SOME IN RG ET AL
*    PHYS REC C29, 2395 (1984); PHYS REV C30, 958 (1984);
*    PHYS REV C30, 962 (1984)
*PR: PAS/RG DATA FROM 777/826, FALL 1984, SOME UNPUBLISHED,
*    SOME IN 180 ARTICLE, SEIDL ET AL, PHYS LETT 154B, 255 (1985).
*SG: STEVE GREENE PHD THESIS, LA-8891-T (1981), AND NUMEROUS
*    ARTICLES, INCL GREENE ET AL, PHYS REV C25, 927 (1982);
*    MORRIS ET AL, PHYS REV LETT 45, 1233 (1980);
*    BURLESON ET AL, PHYS REV C22, 1180 (1980);
*    GREENE ET AL, PHYS LETT 88B, 62 (1979).
*MO: MORRIS ET AL, PHYS REV LETT 54, 775 (1985)
*
* FORMAT IS: TARGET, INCIDENT PI POLARITY, A(NALOG) OR N(ONANALOG),
* LAB ENERGY, LAB SCATTERING ANGLE, CROSS SECTION, ERROR, SOURCE
* (TWO LETTERS GIVEN ABOVE), AND RESIDUAL EXCITATION ENERGY
* THERE IS (IN SOME CASES) AN AMBIGUITY ABOUT WHETHER THE
* CROSS SECTIONS WERE REPORTED IN LAB OR CM FRAME
* IT IS ASSUMED THAT ALL SIGS ARE CM EXCEPT: BG, LB, RG, SG, PR
*
* SOME NUMBERS WERE READ FROM GRAPHS AND MAY BE INACCURATE
*
* FOLLOWING LINE IS BLANK TO INDICATE START OF DATA FOLLOWS

   9BE + N 140.0  5.0 0.360 0.060 NC  0.00
   9BE + N 145.0  0.0 0.080 0.050 LP  0.00
   9BE + N 162.0  5.0 0.280 0.040 NC  0.00
```

9BE	+	N	162.0	10.0	0.270	0.040	NC	0.00
9BE	+	N	162.0	15.0	0.210	0.030	NC	0.00
9BE	+	N	162.0	18.0	0.200	0.050	NC	0.00
9BE	+	N	162.0	20.0	0.150	0.020	NC	0.00
9BE	+	N	162.0	25.0	0.170	0.020	NC	0.00
9BE	+	N	162.0	26.0	0.170	0.030	NC	0.00
9BE	+	N	162.0	36.0	0.140	0.030	NC	0.00
9BE	+	N	175.0	5.0	0.140	0.030	NC	0.00
9BE	+	N	180.0	5.0	0.150	0.030	SG	0.00
9BE	+	N	238.0	5.0	0.062	0.014	NC	0.00
9BE	+	N	295.0	5.0	0.044	0.012	NC	0.00
12C	+	N	120.0	5.0	0.175	0.043	LB	0.00
12C	+	N	130.0	5.0	0.249	0.051	NC	0.00
12C	+	N	140.0	5.0	0.377	0.072	LB	0.00
12C	+	N	145.0	0.0	0.650	0.200	LP	0.00
12C	+	N	164.0	5.0	0.653	0.071	LB	0.00
12C	+	N	164.0	15.0	0.340	0.068	LB	0.00
12C	+	N	164.0	25.0	0.111	0.023	LB	0.00
12C	+	N	164.0	35.0	0.017	0.004	LB	0.00
12C	+	N	164.0	45.0	0.007	0.004	LB	0.00
12C	+	N	165.0	5.0	0.569	0.061	RG	0.00
12C	+	N	180.0	5.0	0.400	0.050	SG	0.00
12C	+	N	180.0	5.0	0.478	0.100	LB	0.00
12C	+	N	190.0	5.0	0.423	0.064	NC	0.00
12C	+	N	200.0	5.0	0.368	0.050	RG	0.00
12C	+	N	210.0	5.0	0.288	0.047	LB	0.00
12C	+	N	225.0	5.0	0.175	0.026	NC	0.00
13C	+	N	120.0	5.0	0.198	0.034	PS	0.00
13C	+	N	164.0	0.0	0.063	0.021	PS	0.00
13C	+	N	164.0	5.0	0.141	0.021	PS	0.00
13C	+	N	164.0	10.0	0.095	0.016	PS	0.00
13C	+	N	164.0	15.0	0.130	0.019	PS	0.00
13C	+	N	164.0	17.5	0.116	0.020	PS	0.00
13C	+	N	164.0	20.0	0.130	0.018	PS	0.00
13C	+	N	164.0	25.0	0.102	0.017	PS	0.00
13C	+	N	164.0	33.0	0.104	0.015	PS	0.00
13C	+	N	164.0	40.0	0.127	0.017	PS	0.00
13C	+	N	164.0	50.0	0.064	0.011	PS	0.00
13C	+	N	180.0	5.0	0.100	0.030	SG	0.00
13C	+	N	180.0	5.0	0.083	0.019	PS	0.00
13C	+	N	292.0	0.0	0.184	0.044	PS	0.00
13C	+	N	292.0	10.0	0.187	0.032	PS	0.00
13C	+	N	292.0	14.0	0.135	0.025	PS	0.00
13C	+	N	292.0	23.0	0.179	0.019	PS	0.00
13C	+	N	292.0	27.5	0.188	0.020	PS	0.00
13C	+	N	292.0	32.0	0.180	0.016	PS	0.00
	+	N	292.0	41.0	0.153	0.016	PS	0.00
	+	N	292.0	50.0	0.060	0.011	PS	0.00
3C	+	N	120.0	5.0	0.000	0.108	PS	4.21
13C	+	N	164.0	0.0	0.312	0.080	PS	4.21
13C	+	N	164.0	5.0	0.325	0.047	PS	4.21
13C	+	N	164.0	10.0	0.297	0.047	PS	4.21

13C	+	N	164.0	15.0	0.195	0.043	PS	4.21
13C	+	N	164.0	17.5	0.177	0.053	PS	4.21
13C	+	N	164.0	20.0	0.111	0.046	PS	4.21
13C	+	N	164.0	25.0	0.046	0.041	PS	4.21
13C	+	N	164.0	33.0	0.029	0.024	PS	4.21
13C	+	N	164.0	40.0	0.044	0.023	PS	4.21
13C	+	N	164.0	50.0	0.034	0.023	PS	4.21
13C	+	N	180.0	5.0	0.170	0.049	PS	4.21
13C	+	N	292.0	5.0	0.000	0.053	PS	4.21
14C	+	A	49.2	20.3	3.260	0.230	LE	0.00
14C	+	A	49.2	30.4	3.040	0.220	LE	0.00
14C	+	A	49.2	40.5	2.480	0.180	LE	0.00
14C	+	A	49.2	50.6	1.970	0.180	LE	0.00
14C	+	A	49.2	60.7	1.560	0.120	LE	0.00
14C	+	A	49.2	70.8	1.320	0.120	LE	0.00
14C	+	A	49.2	80.8	0.880	0.110	LE	0.00
14C	+	A	49.2	90.8	0.730	0.070	LE	0.00
14C	+	A	49.2	130.6	0.650	0.100	LE	0.00
14C	+	A	50.0	50.0	2.500	0.900	NV	0.00
14C	+	A	50.0	60.0	1.220	0.330	NV	0.00
14C	+	A	50.0	70.0	0.880	0.150	NV	0.00
14C	+	A	50.0	80.0	1.050	0.160	NV	0.00
14C	+	A	50.0	90.0	0.920	0.130	NV	0.00
14C	+	A	50.0	100.0	0.820	0.150	NV	0.00
14C	+	A	50.0	110.0	0.570	0.200	NV	0.00
14C	+	A	50.0	120.0	0.570	0.160	NV	0.00
14C	+	A	80.0	5.5	0.962	0.340	PR	0.00
14C	+	A	100.0	5.5	0.614	0.194	PR	0.00
14C	+	A	120.0	5.0	0.960	0.257	PS	0.00
14C	+	A	140.0	5.0	0.858	0.161	PS	0.00
14C	+	A	140.0	5.5	1.556	0.271	PR	0.00
14C	+	A	140.0	15.5	0.477	0.109	PR	0.00
14C	+	A	140.0	20.5	0.330	0.110	PR	0.00
14C	+	A	140.0	25.5	0.135	0.067	PR	0.00
14C	+	A	140.0	30.5	0.000	0.045	PR	0.00
14C	+	A	140.0	35.5	0.172	0.065	PR	0.00
14C	+	A	140.0	40.5	0.115	0.058	PR	0.00
14C	+	A	164.0	0.0	1.371	0.287	PS	0.00
14C	+	A	164.0	5.5	1.948	0.355	PR	0.00
14C	+	A	164.0	5.0	1.063	0.106	PS	0.00
14C	+	A	164.0	10.0	0.894	0.150	PS	0.00
14C	+	A	164.0	15.0	0.828	0.161	PS	0.00
14C	+	A	164.0	17.5	0.237	0.079	PS	0.00
14C	+	A	164.0	20.0	0.230	0.069	PS	0.00
14C	+	A	164.0	25.0	0.145	0.048	PS	0.00
14C	+	A	164.0	33.0	0.207	0.062	PS	0.00
14C	+	A	164.0	40.0	0.126	0.043	PS	0.00
14C	+	A	164.0	50.0	0.139	0.052	PS	0.00
14C	+	A	180.0	5.0	1.935	0.308	PS	0.00
14C	+	A	200.0	5.5	2.973	0.489	PR	0.00
14C	+	A	200.0	15.5	1.849	0.344	PR	0.00
14C	+	A	200.0	25.5	0.449	0.098	PR	0.00

14C	+	A	200.0	30.5	0.202	0.082	PR	0.00
14C	+	A	200.0	35.5	0.157	0.052	PR	0.00
14C	+	A	200.0	40.5	0.167	0.059	PR	0.00
14C	+	A	220.0	5.0	2.891	0.340	PS	0.00
14C	+	A	230.0	5.5	4.823	0.[illegible]	PR	0.00
14C	+	A	260.0	5.0	4.337	0.553	PS	0.00
14C	+	A	292.0	0.0	4.550	0.787	PS	0.00
14C	+	A	292.0	5.0	4.518	0.585	PS	0.00
14C	+	A	292.0	5.0	4.701	0.555	RG	0.00
14C	+	A	292.0	10.0	2.424	0.446	PS	0.00
14C	+	A	292.0	14.0	1.584	0.340	PS	0.00
14C	+	A	292.0	23.0	0.424	0.131	PS	0.00
14C	+	A	292.0	27.5	0.032	0.032	PS	0.00
14C	+	A	292.0	32.0	0.022	0.022	PS	0.00
14C	+	A	292.0	41.0	0.115	0.057	PS	0.00
14C	+	A	292.0	50.0	0.277	0.075	PS	0.00
14C	+	N	120.0	5.0	0.215	0.107	PS	5.90
14C	+	N	140.0	5.0	0.590	0.134	PS	5.90
14C	+	N	164.0	0.0	0.132	0.066	PS	5.90
14C	+	N	164.0	5.0	0.236	0.047	PS	5.90
14C	+	N	164.0	10.0	0.352	0.108	PS	5.90
14C	+	N	164.0	15.0	0.203	0.087	PS	5.90
14C	+	N	164.0	17.5	0.187	0.094	PS	5.90
14C	+	N	164.0	20.0	0.125	0.041	PS	5.90
14C	+	N	164.0	25.0	0.044	0.021	PS	5.90
14C	+	N	164.0	33.0	0.056	0.038	PS	5.90
14C	+	N	164.0	40.0	0.097	0.038	PS	5.90
14C	+	N	164.0	50.0	0.048	0.032	PS	5.90
14C	+	N	180.0	5.0	0.259	0.087	PS	5.90
14C	+	N	220.0	5.0	0.195	0.078	PS	5.90
14C	+	N	260.0	5.0	0.000	0.072	PS	5.90
14C	+	N	292.0	5.0	0.000	0.062	PS	5.90
14C	+	N	292.0	0.0	0.571	0.286	PS	7.70
14C	+	N	292.0	10.0	0.405	0.162	PS	7.70
14C	+	N	292.0	14.0	0.438	0.188	PS	7.70
14C	+	N	292.0	23.0	0.328	0.089	PS	7.70
14C	+	N	292.0	27.5	0.466	0.117	PS	7.70
14C	+	N	292.0	32.0	0.370	0.083	PS	7.70
14C	+	N	292.0	41.0	0.423	0.105	PS	7.70
14C	+	N	292.0	50.0	0.165	0.070	PS	7.70
14C	-	N	164.0	5.0	0.700	0.184	RG	0.00
160	+	N	101.0	5.0	0.146	0.073	SG	0.00
160	+	N	120.0	5.0	0.273	0.035	RG	0.00
160	+	N	120.0	15.0	0.127	0.018	RG	0.00
160	+	N	120.0	25.0	0.049	0.008	RG	0.00
160	+	N	120.0	35.0	0.013	0.006	RG	0.00
160	+	N	120.0	40.0	0.004	0.006	RG	0.00
160	+	N	120.0	45.0	0.010	0.005	RG	0.00
160	+	N	141.0	5.0	0.348	0.070	SG	0.00
160	+	N	145.0	0.0	0.870	0.210	LP	0.00
160	+	N	164.0	0.0	0.540	0.130	BG	0.00
160	+	N	164.0	5.0	0.500	0.040	BG	0.00

160	+	N	164.0	5.0	0.449	0.049	RG	0.00
160	+	N	164.0	10.0	0.360	0.040	BG	0.00
160	+	N	164.0	15.0	0.225	0.020	BG	0.00
160	+	N	164.0	20.0	0.094	0.010	BG	0.00
160	+	N	164.0	25.0	0.043	0.008	BG	0.00
160	+	N	164.0	30.0	0.008	0.003	BG	0.00
160	+	N	164.0	35.0	0.012	0.005	BG	0.00
160	+	N	164.0	40.0	0.023	0.004	BG	0.00
160	+	N	164.0	45.0	0.023	0.005	BG	0.00
160	+	N	164.0	50.0	0.026	0.005	BG	0.00
160	+	N	182.0	5.0	0.339	0.068	SG	0.00
160	+	N	200.0	5.0	0.222	0.023	RG	0.00
160	+	N	200.0	15.0	0.104	0.010	RG	0.00
160	+	N	200.0	20.0	0.016	0.006	RG	0.00
160	+	N	200.0	25.0	0.000	0.006	RG	0.00
160	+	N	200.0	30.0	0.006	0.003	RG	0.00
160	+	N	200.0	35.0	0.011	0.005	RG	0.00
160	+	N	200.0	43.0	0.012	0.004	RG	0.00
160	+	N	210.0	5.0	0.184	0.020	RG	0.00
160	+	N	211.0	5.0	0.113	0.041	SG	0.00
160	+	N	231.0	5.0	0.087	0.018	SG	0.00
160	+	N	292.0	5.0	0.119	0.022	SG	0.00
160	+	N	120.0	5.0	0.191	0.029	RG	1.80
160	+	N	120.0	15.0	0.156	0.020	RG	1.80
160	+	N	120.0	25.0	0.079	0.008	RG	1.80
160	+	N	120.0	35.0	0.034	0.008	RG	1.80
160	+	N	120.0	40.0	0.036	0.013	RG	1.80
160	+	N	120.0	45.0	0.016	0.006	RG	1.80
160	+	N	164.0	0.0	0.380	0.120	BG	1.80
160	+	N	164.0	5.0	0.330	0.030	BG	1.80
160	+	N	164.0	5.0	0.239	0.034	RG	1.80
160	+	N	164.0	10.0	0.210	0.040	BG	1.80
160	+	N	164.0	15.0	0.155	0.020	BG	1.80
160	+	N	164.0	20.0	0.150	0.015	BG	1.80
160	+	N	164.0	25.0	0.135	0.010	BG	1.80
160	+	N	164.0	30.0	0.076	0.008	BG	1.80
160	+	N	164.0	35.0	0.072	0.008	BG	1.80
160	+	N	164.0	40.0	0.045	0.006	BG	1.80
160	+	N	164.0	45.0	0.044	0.006	BG	1.80
160	+	N	164.0	50.0	0.021	0.005	BG	1.80
160	+	N	200.0	5.0	0.196	0.022	RG	1.80
160	+	N	200.0	15.0	0.118	0.010	RG	1.80
160	+	N	200.0	20.0	0.086	0.011	RG	1.80
160	+	N	200.0	25.0	0.074	0.009	RG	1.80
160	+	N	200.0	30.0	0.053	0.007	RG	1.80
160	+	N	200.0	35.0	0.043	0.008	RG	1.80
160	+	N	200.0	43.0	0.027	0.007	RG	1.80
160	+	N	210.0	5.0	0.215	0.020	RG	1.80
180	+	A	81.0	5.0	0.925	0.308	SG	0.00
180	+	A	95.0	0.0	1.670	0.380	LP	0.00
180	+	A	100.0	5.0	1.058	0.200	PR	0.00
180	+	A	100.0	15.0	0.591	0.139	PR	0.00

180	+	A	100.0	25.0	0.138	0.069	PR	0.00
180	+	A	100.0	40.0	0.000	0.026	PR	0.00
180	+	A	101.0	5.0	0.839	0.168	SG	0.00
180	+	A	117.0	5.0	1.765	0.256	SG	0.00
180	+	A	121.0	5.0	1.342	0.163	RG	0.00
180	+	A	121.0	15.0	0.721	0.081	RG	0.00
180	+	A	121.0	20.0	0.331	0.070	RG	0.00
180	+	A	121.0	25.0	0.058	0.019	RG	0.00
180	+	A	121.0	30.0	0.011	0.011	RG	0.00
180	+	A	121.0	35.0	0.150	0.033	RG	0.00
180	+	A	121.0	43.0	0.257	0.041	RG	0.00
180	+	A	126.0	0.0	2.190	0.440	LP	0.00
180	+	A	130.0	5.0	2.201	0.203	PR	0.00
180	+	A	139.0	0.0	2.000	0.340	LP	0.00
180	+	A	141.0	5.0	1.714	0.203	SG	0.00
180	+	A	148.0	18.0	0.300	0.100	LP	0.00
180	+	A	152.0	5.0	1.406	0.205	PR	0.00
180	+	A	164.0	5.0	1.011	0.116	SG	0.00
180	+	A	164.0	8.0	0.720	0.089	SG	0.00
180	+	A	164.0	13.0	0.323	0.049	SG	0.00
180	+	A	164.0	13.0	0.360	0.065	KS	0.00
180	+	A	164.0	18.0	0.068	0.014	SG	0.00
180	+	A	164.0	18.0	0.069	0.015	KS	0.00
180	+	A	164.0	23.0	0.046	0.014	SG	0.00
180	+	A	164.0	23.0	0.087	0.020	KS	0.00
180	+	A	164.0	28.0	0.178	0.030	SG	0.00
180	+	A	164.0	30.0	0.261	0.045	KS	0.00
180	+	A	164.0	33.0	0.247	0.049	SG	0.00
180	+	A	164.0	45.0	0.202	0.040	KS	0.00
180	+	A	172.0	5.0	0.987	0.172	PR	0.00
180	+	A	172.0	10.0	0.621	0.142	PR	0.00
180	+	A	172.0	15.0	0.174	0.071	PR	0.00
180	+	A	172.0	20.0	0.034	0.034	PR	0.00
180	+	A	172.0	25.0	0.077	0.044	PR	0.00
180	+	A	180.0	5.0	0.615	0.123	PR	0.00
180	+	A	180.0	10.0	0.341	0.074	PR	0.00
180	+	A	180.0	15.0	0.150	0.033	PR	0.00
180	+	A	180.0	20.0	0.063	0.024	PR	0.00
180	+	A	180.0	25.0	0.200	0.047	PR	0.00
180	+	A	180.0	35.0	0.405	0.078	PR	0.00
180	+	A	182.0	5.0	0.876	0.102	SG	0.00
180	+	A	187.0	18.0	0.210	0.080	LP	0.00
180	+	A	190.0	5.0	0.713	0.124	PR	0.00
180	+	A	200.0	5.0	0.964	0.149	PR	0.00
180	+	A	200.0	10.0	0.518	0.102	PR	0.00
180	+	A	200.0	15.0	0.291	0.064	PR	0.00
180	+	A	200.0	20.0	0.145	0.034	PR	0.00
180	+	A	200.0	25.0	0.141	0.031	PR	0.00
180	+	A	200.0	30.0	0.117	0.031	PR	0.00
180	+	A	200.0	35.0	0.144	0.033	PR	0.00
180	+	A	211.0	5.0	0.960	0.129	SG	0.00
180	+	A	230.0	5.0	1.386	0.149	PR	0.00

180	+ A	230.0	15.0	0.621	0.096	PR	0.00
180	+ A	230.0	20.0	0.179	0.052	PR	0.00
180	+ A	230.0	25.0	0.043	0.015	PR	0.00
180	+ A	230.0	30.0	0.018	0.010	PR	0.00
180	+ A	230.0	35.0	0.029	0.012	PR	0.00
180	+ A	230.0	40.0	0.036	0.014	PR	0.00
180	+ A	231.0	5.0	1.079	0.120	SG	0.00
180	+ A	261.0	5.0	1.469	0.160	SG	0.00
180	+ A	292.0	5.0	2.405	0.187	SG	0.00
180	+ A	292.0	5.0	2.141	0.147	RG	0.00
180	+ A	292.0	8.0	1.952	0.378	SG	0.00
180	+ A	292.0	13.0	0.593	0.160	SG	0.00
180	+ A	292.0	18.0	0.177	0.089	SG	0.00
180	+ A	292.0	23.0	0.064	0.012	SG	0.00
180	+ A	292.0	28.0	0.065	0.014	SG	0.00
180	+ A	292.0	33.0	0.103	0.018	SG	0.00
180	+ A	292.0	40.0	0.100	0.024	PR	0.00
180	+ A	310.0	5.0	1.992	0.252	SG	0.00
180	+ N	81.0	5.0	0.243	0.365	SG	1.89
180	+ N	100.0	5.0	0.529	0.141	PR	1.89
180	+ N	100.0	15.0	0.394	0.114	PR	1.89
180	+ N	100.0	25.0	0.620	0.146	PR	1.89
180	+ N	100.0	40.0	0.316	0.091	PR	1.89
180	+ N	101.0	5.0	0.469	0.138	SG	1.89
180	+ N	117.0	5.0	0.197	0.112	SG	1.89
180	+ N	121.0	5.0	0.296	0.076	RG	1.89
180	+ N	121.0	15.0	0.297	0.052	RG	1.89
180	+ N	121.0	20.0	0.158	0.048	RG	1.89
180	+ N	121.0	25.0	0.211	0.037	RG	1.89
180	+ N	121.0	30.0	0.253	0.053	RG	1.89
180	+ N	121.0	35.0	0.293	0.046	RG	1.89
180	+ N	121.0	43.0	0.250	0.041	RG	1.89
180	+ N	130.0	5.0	0.038	0.027	PR	1.89
180	+ N	152.0	5.0	0.000	0.030	PR	1.89
180	+ N	164.0	5.0	0.033	0.049	SG	1.89
180	+ N	164.0	8.0	0.070	0.035	SG	1.89
180	+ N	164.0	13.0	0.083	0.035	SG	1.89
180	+ N	164.0	13.0	0.098	0.030	KS	1.89
180	+ N	164.0	18.0	0.094	0.022	SG	1.89
180	+ N	164.0	18.0	0.155	0.020	KS	1.89
180	+ N	164.0	23.0	0.168	0.028	SG	1.89
180	+ N	164.0	23.0	0.248	0.035	KS	1.89
180	+ N	164.0	28.0	0.158	0.035	SG	1.89
180	+ N	164.0	30.0	0.330	0.050	KS	1.89
180	+ N	164.0	33.0	0.128	0.043	SG	1.89
180	+ N	164.0	45.0	0.087	0.025	KS	1.89
180	+ N	172.0	5.0	0.090	0.052	PR	1.89
180	+ N	172.0	10.0	0.065	0.046	PR	1.89
180	+ N	172.0	15.0	0.174	0.071	PR	1.89
180	+ N	172.0	20.0	0.202	0.082	PR	1.89
180	+ N	172.0	25.0	0.334	0.093	PR	1.89
180	+ N	180.0	5.0	0.148	0.060	PR	1.89

180	+	N	180.0	10.0	0.227	0.061	PR	1.89
180	+	N	180.0	15.0	0.158	0.034	PR	1.89
180	+	N	180.0	20.0	0.190	0.041	PR	1.89
180	+	N	180.0	25.0	0.211	0.048	PR	1.89
180	+	N	180.0	35.0	0.090	0.037	PR	1.89
180	+	N	182.0	5.0	0.022	0.034	SG	1.89
180	+	N	190.0	5.0	0.303	0.081	PR	1.89
180	+	N	200.0	5.0	0.230	0.073	PR	1.89
180	+	N	200.0	10.0	0.220	0.066	PR	1.89
180	+	N	200.0	15.0	0.097	0.036	PR	1.89
180	+	N	200.0	20.0	0.123	0.031	PR	1.89
180	+	N	200.0	25.0	0.135	0.030	PR	1.89
180	+	N	200.0	30.0	0.084	0.026	PR	1.89
180	+	N	200.0	35.0	0.022	0.013	PR	1.89
180	+	N	211.0	5.0	0.316	0.127	SG	1.89
180	+	N	230.0	5.0	0.430	0.083	PR	1.89
180	+	N	230.0	15.0	0.222	0.057	PR	1.89
180	+	N	230.0	20.0	0.209	0.056	PR	1.89
180	+	N	230.0	25.0	0.128	0.026	PR	1.89
180	+	N	230.0	30.0	0.067	0.020	PR	1.89
180	+	N	230.0	35.0	0.096	0.021	PR	1.89
180	+	N	230.0	40.0	0.046	0.015	PR	1.89
180	+	N	231.0	5.0	0.336	0.069	SG	1.89
180	+	N	261.0	5.0	0.238	0.079	SG	1.89
180	+	N	292.0	5.0	0.342	0.086	SG	1.89
180	+	N	292.0	5.0	0.495	0.071	RG	1.89
180	+	N	292.0	40.0	0.050	0.017	PR	1.89
180	-	N	140.0	5.0	0.380	0.105	RG	0.00
180	-	N	164.0	5.0	0.621	0.126	RG	0.00
180	-	N	164.0	15.0	0.369	0.077	RG	0.00
180	-	N	164.0	25.0	0.052	0.021	RG	0.00
180	-	N	164.0	30.0	0.000	0.009	RG	0.00
180	-	N	164.0	35.0	0.026	0.013	RG	0.00
180	-	N	164.0	45.0	0.037	0.017	RG	0.00
180	-	N	180.0	5.0	0.473	0.118	RG	0.00
180	-	N	210.5	5.0	0.301	0.070	RG	0.00
180	-	N	239.5	5.0	0.125	0.041	RG	0.00
180	-	N	140.0	5.0	0.121	0.049	RG	1.55
180	-	N	164.0	5.0	0.199	0.020	RG	1.55
180	-	N	164.0	15.0	0.123	0.044	RG	1.55
180	-	N	164.0	25.0	0.060	0.023	RG	1.55
180	-	N	164.0	30.0	0.053	0.022	RG	1.55
180	-	N	164.0	35.0	0.076	0.022	RG	1.55
180	-	N	164.0	45.0	0.049	0.019	RG	1.55
180	-	N	180.0	5.0	0.191	0.060	RG	1.55
180	-	N	210.5	5.0	0.123	0.044	RG	1.55
180	-	N	239.5	5.0	0.041	0.024	RG	1.55
24MG	+	N	120.0	5.0	0.298	0.069	LB	0.00
24MG	+	N	140.0	5.0	0.405	0.093	LB	0.00
24MG	+	N	141.0	5.0	0.290	0.062	SG	0.00
24MG	+	N	145.0	0.0	0.670	0.200	LP	0.00
24MG	+	N	164.0	5.0	0.305	0.035	LB	0.00

24MG + N	180.0	5.0	0.227	0.041	LB	0.00
24MG + N	180.0	5.0	0.078	0.018	SG	0.00
24MG + N	210.0	5.0	0.094	0.027	LB	0.00
24MG + N	250.0	5.0	0.013	0.007	SG	0.00
24MG + N	292.0	5.0	0.014	0.006	SG	0.00
26MG + A	120.0	5.0	0.385	0.100	SG	0.00
26MG + A	120.0	5.0	0.259	0.078	PS	0.00
26MG + A	140.0	5.5	0.324	0.087	PR	0.00
26MG + A	140.0	15.5	0.099	0.034	PR	0.00
26MG + A	140.0	20.5	0.018	0.018	PR	0.00
26MG + A	140.0	25.5	0.000	0.017	PR	0.00
26MG + A	140.0	30.5	0.110	0.049	PR	0.00
26MG + A	140.0	35.5	0.157	0.043	PR	0.00
26MG + A	140.0	40.5	0.113	0.040	PR	0.00
26MG + A	141.0	5.0	0.338	0.074	SG	0.00
26MG + A	145.0	0.0	0.180	0.100	LP	0.00
26MG + A	164.0	0.0	0.322	0.097	PS	0.00
26MG + A	164.0	5.5	0.482	0.124	PR	0.00
26MG + A	164.0	5.0	0.242	0.054	PS	0.00
26MG + A	164.0	10.0	0.106	0.040	PS	0.00
26MG + A	164.0	15.0	0.028	0.014	PS	0.00
26MG + A	164.0	17.5	0.000	0.018	PS	0.00
26MG + A	164.0	20.0	0.000	0.010	PS	0.00
26MG + A	164.0	25.0	0.086	0.032	PS	0.00
26MG + A	164.0	33.0	0.140	0.038	PS	0.00
26MG + A	164.0	40.0	0.164	0.039	PS	0.00
26MG + A	164.0	50.0	0.016	0.008	PS	0.00
26MG + A	180.0	5.0	0.206	0.061	PS	0.00
26MG + A	200.0	5.5	0.152	0.077	PR	0.00
26MG + A	200.0	15.5	0.030	0.030	PR	0.00
26MG + A	200.0	25.5	0.030	0.018	PR	0.00
26MG + A	200.0	30.5	0.032	0.023	PR	0.00
26MG + A	200.0	35.5	0.041	0.019	PR	0.00
26MG + A	200.0	40.5	0.000	0.010	PR	0.00
26MG + A	211.0	5.0	0.277	0.060	SG	0.00
26MG + A	230.0	5.5	0.423	0.133	PR	0.00
26MG + A	260.0	5.0	0.450	0.098	SG	0.00
26MG + A	292.0	5.0	1.000	0.143	SG	0.00
26MG + A	292.0	8.0	0.684	0.127	SG	0.00
26MG + A	292.0	13.0	0.291	0.065	SG	0.00
26MG + A	292.0	18.0	0.056	0.019	SG	0.00
26MG + A	292.0	23.0	0.035	0.013	SG	0.00
26MG + A	292.0	28.0	0.023	0.015	SG	0.00
26MG + A	292.0	33.0	0.100	0.036	SG	0.00
26MG + A	310.0	5.0	0.922	0.192	SG	0.00
26MG - N	162.0	5.0	0.260	0.070	NA	0.00
28SI + N	120.0	5.0	0.121	0.036	LB	0.00
28SI + N	140.0	5.0	0.191	0.040	LB	0.00
28SI + N	145.0	0.0	0.350	0.100	LP	0.00
28SI + N	164.0	5.0	0.204	0.020	LB	0.00
28SI + N	180.0	5.0	0.214	0.046	LB	0.00
28SI + N	210.0	5.0	0.101	0.028	LB	0.00

32S	+ N	120.0	5.0	0.101	0.027	LB	0.00
32S	+ N	140.0	5.0	0.171	0.036	LB	0.00
32S	+ N	164.0	5.0	0.169	0.024	LB	0.00
32S	+ N	180.0	5.0	0.084	0.025	SG	0.00
32S	+ N	180.0	5.0	0.149	0.032	LB	0.00
32S	+ N	210.0	5.0	0.069	0.019	LB	0.00
40CA	+ N	120.0	5.0	0.109	0.028	LB	0.00
40CA	+ N	140.0	5.0	0.135	0.033	LB	0.00
40CA	+ N	164.0	5.0	0.165	0.022	LB	0.00
40CA	+ N	164.0	15.0	0.058	0.014	LB	0.00
40CA	+ N	164.0	25.0	0.014	0.007	LB	0.00
40CA	+ N	164.0	35.0	0.038	0.010	LB	0.00
40CA	+ N	164.0	45.0	0.015	0.013	LB	0.00
40CA	+ N	180.0	5.0	0.101	0.024	LB	0.00
40CA	+ N	210.0	5.0	0.061	0.015	LB	0.00
42CA	+ A	130.0	5.0	0.406	0.102	MK	0.00
42CA	+ A	163.0	5.0	0.140	0.040	MK	0.00
42CA	+ A	180.0	5.0	0.132	0.028	MK	0.00
42CA	+ A	180.0	15.0	0.008	0.006	SE	0.00
42CA	+ A	235.0	5.0	0.169	0.031	MK	0.00
42CA	+ A	292.0	5.0	0.404	0.061	MK	0.00
44CA	+ A	163.0	5.0	0.181	0.042	RG	9.00
44CA	+ A	210.0	5.0	0.314	0.062	RG	9.00
44CA	+ N	163.0	5.0	0.151	0.034	RG	0.00
44CA	+ N	210.0	5.0	0.034	0.020	RG	0.00
48CA	+ N	130.0	5.0	0.124	0.124	MK	0.00
48CA	+ N	180.0	5.0	0.041	0.041	MK	0.00
48CA	+ N	235.0	5.0	0.000	0.066	MK	0.00
48CA	+ N	292.0	5.0	0.000	0.051	MK	0.00
48CA	+ A	130.0	5.0	0.833	0.296	MK	17.38
48CA	+ A	163.0	5.0	0.290	0.130	NC	17.38
48CA	+ A	180.0	5.0	0.679	0.165	MK	17.38
48CA	+ A	235.0	5.0	1.575	0.310	MK	17.38
48CA	+ A	292.0	5.0	1.746	0.290	MK	17.38
48TI	+ N	130.0	5.0	0.142	0.053	MK	0.00
48TI	+ N	180.0	5.0	0.073	0.029	MK	0.00
48TI	+ N	235.0	5.0	0.031	0.015	MK	0.00
48TI	+ N	292.0	5.0	0.025	0.013	MK	0.00
48TI	+ A	130.0	5.0	0.117	0.078	MK	8.75
48TI	+ A	180.0	5.0	0.093	0.062	MK	8.75
48TI	+ A	235.0	5.0	0.382	0.080	MK	8.75
48TI	+ A	292.0	5.0	0.590	0.103	MK	8.75
56FE	+ N	80.0	5.5	0.035	0.035	PR	0.00
56FE	+ N	100.0	5.5	0.000	0.005	PR	0.00
56FE	+ N	120.0	5.0	0.060	0.015	RG	0.00
56FE	+ N	140.0	5.0	0.075	0.023	PS	0.00
56FE	+ N	164.0	5.0	0.053	0.014	PS	0.00
56FE	+ N	180.0	5.0	0.018	0.005	RG	0.00
56FE	+ N	220.0	5.0	0.014	0.007	PS	0.00
56FE	+ N	230.0	5.0	0.000	0.008	RG	0.00
56FE	+ N	260.0	5.0	0.014	0.014	PS	0.00
56FE	+ N	292.0	5.0	0.000	0.011	RG	0.00

56FE	+	N	292.0	5.0	0.000	0.013	PS	0.00
56FE	+	A	80.0	5.5	0.931	0.537	RG	9.60
56FE	+	A	100.0	5.0	0.035	0.026	RG	9.60
56FE	+	A	120.0	5.0	0.062	0.035	RG	9.60
56FE	+	A	140.0	5.0	0.033	0.027	PS	9.60
56FE	+	A	164.0	5.0	0.032	0.018	PS	9.60
56FE	+	A	180.0	5.0	0.041	0.012	RG	9.60
56FE	+	A	220.0	5.0	0.161	0.036	PS	9.60
56FE	+	A	230.0	5.0	0.110	0.039	RG	9.60
56FE	+	A	260.0	5.0	0.390	0.081	PS	9.60
56FE	+	A	292.0	5.0	0.290	0.068	RG	9.60
56FE	+	A	292.0	5.0	0.323	0.077	PS	9.60
56FE	-	N	164.0	5.0	0.038	0.038	RG	0.00
58NI	-	N	164.0	5.0	0.025	0.018	RG	0.00
80SE	+	N	100.0	5.0	0.070	0.050	RG	0.00
80SE	+	N	130.0	5.0	0.120	0.035	RG	0.00
80SE	+	N	164.0	5.0	0.060	0.014	RG	0.00
80SE	+	N	190.0	5.0	0.054	0.031	RG	0.00
88SR	+	N	180.0	5.0	0.041	0.011	SE	0.00
88SR	+	N	292.0	5.0	0.000	0.004	SE	0.00
88SR	+	A	180.0	5.0	0.245	0.036	SE	17.20
88SR	+	A	292.0	5.0	0.797	0.052	SE	17.20
90ZR	+	N	164.0	5.0	0.032	0.023	RG	0.00
90ZR	+	N	180.0	5.0	0.006	0.006	SE	0.00
90ZR	+	N	211.0	5.0	0.034	0.034	RG	0.00
90ZR	+	N	292.0	5.0	0.000	0.007	SE	0.00
90ZR	+	A	164.0	5.0	0.240	0.089	RG	13.90
90ZR	+	A	180.0	5.0	0.155	0.025	SE	13.90
90ZR	+	A	211.0	5.0	0.209	0.089	RG	13.90
90ZR	+	A	292.0	5.0	0.572	0.058	SE	13.90
118SN	+	A	165.0	5.0	0.000	0.118	RG	21.90
118SN	+	A	212.0	5.0	0.350	0.157	RG	21.90
118SN	+	N	165.0	5.0	0.037	0.037	RG	0.00
118SN	+	N	212.0	5.0	0.120	0.084	RG	0.00
208PB	+	A	292.0	5.5	1.090	0.290	MO	32.46
209BI	+	A	292.0	5.0	0.460	0.150	SG	30.80

REFERENCES

[Be-71] F. Becker and Yu. A. Batusov, Riv. Nuo. Cim. 1, 309 (1971).

[Be-75] M. Beiner, H. Flocard, N. van Giai, and P. Quentin, Nucl. Phys. A238, 29 (1975).

[Bo-68] P. E. Boynton et al., Phys. Rev. 174, 1083 (1968).

[Co-68] C. J. Cook, M. E. Nordberg, Jr., and R. L. Burman, Phys. Rev. 174, 1374 (1968).

[Co-79] Martin D. Cooper in Lampf Workshop on Pion Single Charge Exchange, Los Alamos National Laboratory Report LA-UR-7892-C, 194 (1979).

[Co-80] W. B. Cottingame and D. B. Holtkamp, Phys. Rev. Lett. 45, 1828 (1980).

[Cr-70] G. M. Crawley et al., Phys. Rev. C 2, 1071 (1970).

[Da-64] R. E. P. Davis et al., Bull. Am. Phys. Soc. 9, 627 (1964).

[Fo-83] H. T. Fortune, S. J. Greene, C. F. Moore, and C. L. Morris, Phys. Rev. C 25, 2142 (1982).

[Fo-84] H. T. Fortune and R. Gilman, LAMPF proposal #906 (1984).

[Ge-80] William J. Gerace, Morton M. Sternheim, Kwang-Bock Yoo, and David A. Sparrow, Phys. Rev. C 22, 2497 (1980).

[Gi-65] L. Gilly et al., Phys. Lett. 19, 335 (1965).

[Gi-85a] R. Gilman et al., Nucl. Phys. A432, 610 (1985).

[Gi-85b] R. Gilman et al., submitted to Phys. Rev. Lett

[Gr-82a] Steven J. Greene, Ph.D. dissertation, University of Texas (1981); Los Alamos report LA-8891-T (1981).

[Gr-82b] S. J. Greene et al., Phys. Rev. C 25, 924 (1982).

[Gr-84] S. J. Greene et al., Phys. Rev. C 30, 2003 (1984).

[Ho-83] Pervez Hoodboy, Roger A. Freedman, Gerald A. Miller, and Ernest M. Henley, Phys. Rev. C 27, 277 (1983).

[Ja-74] C. W. de Jager, H. de Vries, and C. de Vries, At. Data and Nucl. Data Tables 14, 479 (1974).

[Ja-75] F. James and M. Roos, Comp. Phys. Comm. 10, 343 (1975).

[Jo-80] Mikkel B. Johnson, Phys. Rev. C 22, 192 (1980).

[Jo-83a] Mikkel B. Johnson and E. R. Siciliano, Phys. Rev. C 27, 1647 (1983).

[Jo-83b] Mikkel B. Johnson and E. R. Siciliano, Phys. Rev. C 27, 730 (1983).

[Jo-84] M. B. Johnson, E. R. Siciliano, H. Toki, and A. Wirzba, Phys. Rev. Lett. 52, 593 (1984).

[Jo-85] M. B. Johnson et al., work in progress.

[Ka-74] William B. Kaufman, Jane C. Jackson, and W. R. Gibbs, Phys. Rev. C 9, 1340 (1974).

[Ka-83] W. B. Kaufmann and W. R. Gibbs, Phys. Rev. C 28, 1286 (1983).

[Ka-85] T. Karapiperis, talk given at LAMPF Workshop on Pion Double Charge Exchange, January 10 - 12, 1985.

[Ki-55] L. Kisslinger, Phys. Rev. 98, 761 (1955).

[Ki-83] Leonard Kisslinger, private communication.

[Ki-84] R. R. Kiziah, Ph.D. thesis, University of Texas (1984); Los Alamos Report LA-10257-T, (1984).

[Ki-85] L. Kisslinger and M. B. Johnson, unpublished.

[La-84] Lampf Users Handbook, Clinton P. Anderson Meson Physics Facility, report MP-DO-3-UHB (Rev.) (1984).

[Le-77] T.-S. H. Lee, D. Kurath, and B. Zeidman, Phys. Rev. Lett. 39, 1307 (1977).

[Li-75] L. C. Liu and Victor Franco, Phys. Rev. C 11, 760 (1975).

[Li-81] Guang-Lie Li, Chu-Hsia Li, and T.-S. H. Lee, Phys. Lett. 99B, 200 (1981).

[Li-83] L. C. Liu, Phys. Rev. C 27, 1611 (1983).

[Ma-77] T. Marks et al., Phys. Rev. Lett. 38, 149 (1977).

[Mi-74] G. A. Miller and J. E. Spencer, Phys. Lett. 53B, 329 (1974).

[Mi-76] G. A. Miller and J. E. Spencer, Ann. Phys. (N.Y.) 100, 562 (1976).

[Mi-84] Gerald A. Miller, Phys. Rev. Lett. 53, 2008 (1984).

[Mo-80] C. L. Morris et al., Phys. Rev. Lett. 45, 1233 (1980).

[Mo-82] C. L. Morris et al., Phys. Rev. C 25, 3218 (1982).

[Mo-84] C. L. Morris et al., Los Alamos report LA-UR-84-3934, submitted to Nucl. Inst. Meth. (1984).

[Mo-85] C. L. Morris, work in progress.

[Oo-76] M. Oothoudt, "Two-Body Relativistic Kinematics Code, KINREL," (1976) unpublished.

[Os-77] E. Oset, D. Strottman, and G. E. Brown, Phys. Lett. 73B, 393 (1978).

[Os-83] E. Oset, D. Strottman, M. J. Vicente-Vacas, and Ma Wei-Hsing, Nucl. Phys. A408, 461 (1983).

[Qr-83] Q Release Notes, Los Alamos document MP-1-3413-2 (1983).

[Ro-71] E. Rost and G. W. Edwards, Phys. Lett. 37B, 247 (1971).

[Ro-78] G. Rowe, M. Salomon, and Rubin H. Landau, Phys. Rev. C 18, 584 (1978).

[Se-84] K. K. Seth et al., Phys. Rev. Lett. 52, 894 (1984).

[Sp-78] D. A. Sparrow and A. S. Rosenthal, Phys. Rev. C 18, 1753 (1978).

[Th-77] H. A. Thiessen et al., Los Alamos report LA-6663-MS (1977).

[Un-84] J. E. Ungar et al., Phys. Lett. 144B, 333 (1984).

[Wi-85] A. Wirzba, H. Toki, E. R. Siciliano, an Mikkel B. Johnson, unpublished.

[Xi-81] Liu Xianhui, Wu Zongen, Huang Zhaohui, and Li Yangguo, Sci. Sin. 24, 789 (1981).

[Ya-75] Li Yang-Kuo, Liu Hsien-Hui, and Ma Wei-Hsing, Sci. Sin. 18, 38 (1975).

INDEX

☆ U S GOVERNMENT PRINTING OFFICE:1985—676-034 / 20150